MICROSTRUCTURE DESIGN OF POROUS BRITTLE MATERIALS

by

Frederick George Haubensak

S.M., Massachusetts Institute of Technology, 1991
S.B., University of California at Berkeley, 1988

Submitted to the Department of Materials Science and Engineering
in partial fulfillment of the requirements for the degree of

Doctor of Philosophy

at the

MASSACHUSETTS INSTITUTE OF TECHNOLOGY

September 1994

Author .....
Department of Materials Science and Engineering
August 5, 1994

Certified by .....
Dr. Ali S. Argon
Quentin Berg Professor of Mechanical Engineering
Thesis Supervisor

Accepted by .....
Carl V. Thompson II
Professor of Electronic Materials
Chair, Departmental Committee on Graduate Students

MICROSTRUCTURE DESIGN OF POROUS BRITTLE MATERIALS

by

Frederick George Haubensak

Submitted to the Department of Materials Science and Engineering
on August 5, 1994, in partial fulfillment of the
requirements for the degree of
Doctor of Philosophy

Abstract

Extrapolations can be made to intermediate porosities from the dilute porosity and cellular material extremes with some limited success, however, there is a fundamental lack of understanding of the fracture behavior of materials within the intermediate range of porosities ($15\% < p < 85\%$). Given a prescribed level of porosity, we would like to discover the relevent measures, such as the pore shape, size distribution and degree of spacial homogeneity, in order to optimize the crack propagation resistance of this class of materials. We have studied the porous ceramic system reaction bonded silicon nitride in order to observe toughness controlling behavior at an average porosity at the transition from dilute to intermediate porosity. At this porosity the structure can be considered to have randomly distributed pores which have significant elastic interaction. We have demonstrated a technique whereby virtual microstructures are designed and analyzed by computer simulation and the results can be used to guide the processing of unique microstructures with optimum properties. The unique elements of the technique are the consideration of the pore population as intrinsic ingredients of the microstructure such that the microstructural details are smeared out and replaced in the stress field of the macroscopic crack tip by the equivalent properties. In addition, the interactions of competing toughening mechanisms are allowed and the destructive or synergistic behavior can be observed. The fracture model is compared with the observations of cracks produced by Vickers indentation in microstructures of RBSN, both qualitatively for crack morphology and quantitatively with a novel technique for measuring the fracture toughness. Both simulations and experimental observations show small variations in toughness, but indicate improvement is possible with the observations of crack bridging ligaments by locally tough elements.

Thesis Supervisor: Dr. Ali S. Argon
Title: Quentin Berg Professor of Mechanical Engineering

Contents

List of Figures

List of Tables

Acknowledgments

I would like to take the opportunity to thank all of those generous souls who have contributed to my professional development over the past six years here at MIT. Over all thanks go to Professor Ali Argon who unwaveringly defined a standard of excellence that will remain as an example for me for many years to come. Thanks to Dr. John Haggerty who taught me how to be critical scientifically, and for his generosity in supplying RBSN material. Thanks also to Professors Yet Chiang and Stu Brown for many positive comments and for educating me on how to keep a 30 minute presentation to an hour. Special thanks to Dr. Vasily Bulatov for many hours of discussions and for the significant contributions to this work, and for his friendship.

To my office mates who probably know me better than anyone on the planet, who have had to endure my bad sense of humor and my obnoxious side, and who have served as good sounding boards and bad players at horse, Christine Allan, Ellen Arruda, Srihari Balasubramanian, Curt Bronkhorst, Brian Gally, Mehrdad Haghi, Surya Kaladindi, Manish Kothari, Leo Lev, John Zaroulis, and Antonios Zavaliangos, thanks guys.

To my good friends I've made at MIT, the Rick-man and the Rick-man, the most excellent drinking buddies and sometimes partners in (wholesome) crimes, Livia Racz and Alice Lin my two outstanding (singing) female friends who put up with my flirting ways and still kept me as a friend, you guys made my tenure in Boston worth it. I learned the precise definition of the scientific proof and how my thesis related to this from the singularly most underrated intellect at MIT, Jack Smith, thanks Jack. I learned the subtleties of hydraulic car jacks and other middle aged man trivial from one of the best house mates one could ask for, Ralph Mason. I learned the subtleties and fine character of good diet pepsi and jack daniels from the messiest, but coolest roomate Francis Hodsoll. I learned that it is possible to work endless hours in the lab and still have a life from my good friend Paul, although I'm still trying. To Larry B. and Ann S., thanks for the great rap sessions. And then there are all my singing pals who made it possible to go out for beers nearly every Monday and Thursday evening at the Ear, I couldn't have done it alone, Steve, Matt, John, Bill, Chris, and of course the evanescent and effervescent John Oliver. I will also warmly remember Sossina Haile, my first pal in Boston who educated me as to where Davis Square was and where the other exciting locales around Boston were, Mike Frongillo for kicking my butt occasionally and some great (Somerville brand) banter, the beautiful Judy who always had a smile, and the warm hearted Jeannie, you guys are synonymous with my Boston experience.

Finally, thanks to my family. My father Otto, sister Karen, and aunt Emmy, thanks for all the long distance encouragements. Special thanks to my mother whose spirit was with me every day.

Thanks to all who made my experience at MIT so rich.

Chapter 1

Introduction

The cause-effect relationship between microstructure and mechanical properties of materials has been of interest for several decades. In particular, the characterization of the mechanical behavior of heterogeneous, and specifically, porous materials, has recently become of technological interest. Research has typically concentrated on materials with highly porous cellular microstructures [35] with relative densities as low as 0.3% and on materials with dilute porosity. For each extreme of porosity there are models of mechanical behavior with good predictive properties that are based on engineering assumptions about the microstructural morphology. In each case, extrapolations can be made to intermediate porosities with some limited success, however, there is a fundamental lack of understanding of behavior of materials within the intermediate range of porosities.

In the science of processing high technology ceramics, much success has been had in manufacturing these materials and much is known about the resulting mechanical behavior of both fully dense and cellular foams. Therefore, materials at both ends of the porosity scale, that have unique properties have been exploited: cellular materials for their low density and thus low thermal mass, and insulating properties, as well as applications for filtering molten metals or impact energy absorption; fully dense materials for their higher modulus, fracture toughness and creep resistance on an absolute scale. But because the limiting factor for the use of ceramics in structural applications has been their low fracture toughness, and because defects are the sources

of fracture, it has been the aim of ceramists to produce structural parts with a minimal number of defects in otherwise fully dense materials, thus naturally avoiding the development of porous ceramics.

However, there exist materials that have intrinsic populations of defects due to their processing. This fact requires the ceramist to accept the existance of defects and rely on other means to increase the toughness, such as through martensitic transformation of second phase particles, the incorporation of whiskers into the material, or the promotion of microcrack formation and crack branching.

Reaction bonded silicon nitride is one of these porous materials, and though processes exist to produce fully dense silicon nitride, such as including a hot hydrostatic compaction in the processing steps or adding densification additives, there are significant advantages to porous materials and the elimination of densification steps. (see figure 1-1). In dynamic applications such as turbine blades, where the applied stress is linearly proportional to the mass of the material in motion, the inherent low density of porous materials implies lower operating stresses. In addition, the economies of the low processing temperature of the reaction bonding process are obvious. This processing temperature is often lower than the target service operating temperature for high temperature diesel or gas-turbine engine hot zone components[1] [90]. These beneficial reaction kinetics allow for the incorporation of SiC whiskers with minimal interaction with the matrix and complete nitriding in less than 10 hours at 1400^{o}C [98]. Another practical advantage is the fact that many reaction bonding processes have nearly negligible dimensional change during the reaction phase due to the fact that little or no sintering densification occurs. Consequently, cracking associated with differential shrinkage is avoided, and the produced part will have the same size and shape as the precursor green body. This is an advantage if the final part can then avoid final machining steps, and the consequential introduction of surface defects that are well known for being the source of failure of ceramic parts.

As a price for these benefits, though, the final microstructure is left with a residual porosity. The consequence of this porosity as a first order effect is to reduce the

[1]Gas inlet temperatures approach 1370^{o}C for engine designs suitable for trucks and automobiles.

modulus and fracture energy, both of which have been observed to be related to the volume fraction of porosity: the modulus goes to zero for an ideally random distribution of porosity at approximately 85%, the three dimensional elastic percolation limit[2], and the fracture energy is linearly proportional to the fracture surface area, which for a planar fracture surface implies a linear dependence on porosity. Thus, one might infer that mechanical properties are inferior at high porosities.

However, materials have been produced that, on mass specific bases, have fracture properties that are comparable to fully dense materials. There are some indications that the fracture energy may be substantially increased at higher porosities due to induced crack branching, as has been observed by Rice[89], and grain bridging as observed by Lawn in fully dense, heterogeneous material [103].

The opportunity to study the effects of processing on the mechanical behavior of a material, like most ceramics, that are so sensitive to their processing provides a unique chance to better understand the structure-property relationships, and specifically to characterize the strength controlling defects. The effects of all steps in the processing are therefore valid candidates for detailed study. For example, in the first stages of processing the RBSN material as produced here, after the conversion of powder from Silane gas with a laser process, the spherical silicon particles are packed together by first dispersion in a slurry with an organic solvent followed by pressure infiltration casting. This process which lays down an approximate template for the morphology of the final material is a critical step in terms of determining the character of the spacial network of porosity. The concept of understanding processes such as this as they affect the mechanical properties is therefore integral to the mechanical modelling.

As models are developed to correlate mechanical response to microstructural features, a strong emphasis will be placed on the well known paradigm of structure-property relationship, as it seems clear that more is at work in these porous materials

[2]The critical volume fraction at the percolation threshold for a variety of three dimensional lattices ranges from 0.143 to 0.163. Although the continuum percolation critical volume fraction in two dimensions (exactly 1/2) cannot be extended directly to three dimensions, the conjecture that the critical volume fraction is comparable to the three dimensional packing of spheres ($\sim$ 0.15) is consistent with Monte Carlo computations [111].

than merely variations in density. For example, a model based on information on the distribution of defect sizes and spacings can be simplified to a relationship based on a porosity parameter, only at the expense of information on the microstructural influence. Because of the high level of porosity in RBSN materials, the pores cannot be considered as merely defects or sites of stress concentrations, but as an integral part of the microstructure, requiring instead an understanding of the specifics of the microstructure such as the nature of the interparticle ligaments that form the three dimensional foam network.

1.1 Background Literature Review

1.1.1 Influence of Porosity

In the cases where the effects of porosity have been investigated, often the study relates to relatively isolated pores (and consequently low levels of porosity) acting as strength reducing defects. For example, MacKenzie has derived the shear and bulk moduli of a solid containing a small fraction of spherical pores [86]. On the opposite end of the porosity spectrum, Gibson and Ashby have assessed the field of cellular materials ($P < 30\%$)[35]. These density trends in properties can be extended beyond their applicable range with some agreement. But generally, in the intermediate porosity range, the mechanical properties of ceramics are often described in terms of an empirical exponential function of porosity. Figure 1-2 schematically illustrates the boundaries of intermediate porosity. Rice [87] has suggested that the fracture toughness and moduli of low porosity, brittle materials can be described this way. However, although these descriptive equations can be fit to experimental data, they do not provide pertinent information for the improvement of properties through microstructural control.

Fracture of intermediate porosity materials

The close connection of material processing and mechanical properties especially in brittle heterogeneous materials is recognized but poorly understood. This lack of understanding stems from the fact that the interaction of a macroscale crack with the highly heterogeneous microstructures is typically beyond the scope of analytical solutions. For a planar crack in a glassy material in the dilute porosity extreme, two first order porosity effects reduce the fracture toughness. The relationship, $K = \sqrt{EG}$, implies that the toughness is related directly with E, the elastic modulus, and G, the energy release rate. The average elastic modulus typically observed to follow the form $E \sim E_o e^{-b^E p}$, where p is the average porosity and b^E is dependent on the specific porosity shape and spacial distribution and is found experimentally to range from 2-5 over many material systems, as is seen in the compilation of data by Rice [86]. The energy release rate for a planar crack in the dilute porosity range is proportional to the fracture surface area such that $K \sim \sqrt{(1-p)} e^{-b^E p/2}$. Expanded around p = 0, $K \sim 1 - (b^E/2 + 1/2)p$. Data compiled for SiC in the porosity range of 0 to 16 % show this connection for which $(b^E/2 + 1/2) = 2.9 \pm .1$ as compared to the measured dependence, $K \sim e^{\hat{b}p}$, where $\hat{b} = 2.7 \pm 1.3$

Any crack interaction with the porosity which produces non-planar fracture, such as microcracking, crack bridging, and three dimensional crack configuration effects will modify this relationship. In mono-phase porous materials, the list of toughening mechanisms includes geometrical processes such as crack deflection and the intersection of the crack with locally tough elements or the potentially more potent shielding mechanisms such as microcracking and crack bridging.

As porosity increases and the elastic interaction of pores becomes important, the approximation of isolated pores breaks down. This is likely to occur near 15% porosity, the percolation threshold of randomly distributed porosity in three dimensional structures. Beyond this range of dilute porosity, we may expect stronger interaction between pores and additional crack complexity due solely to the increase in the degree of heterogeneity. X-ray microradiography evidence has shown that the presence of enhanced microcracking, branching and increased crack complexity occurs with

increasing porosity[108].

1.1.2 Microstructure Design for Fracture Toughness

The typical methodology for microstructure design, in most instances, is an iterative process involving the production of material in the laboratory which is then studied with a number of conventional mechanical tests, and key microstructural features are determined, as outlined schematically in Evans, 1991 [25], and shown in figure 1-3. The results are then related through a mechanistic model based on micromechanical model analysis. The mechanistic model is then used to create different microstructures which should have better properties. In a complementary approach, that is usually only taken on paper, more ideal microstructures are considered which through the existing models should lead to superior performance. The justification of this second approach is usually the inadequacy of the available degrees of freedom in processing to achieve the sought after microstructures. In a hybrid approach which is taken here, the microstructure-property connection is studied experimentally while in a parallel computer simulation the processes that control the microstructure and the mechanisms that control the property are modelled. This is ideally pursued until a close correspondence is reached with the actual experimentally probed system through a systematic variation of the parameters that control the simulated microstructures. Once a proven cause-effect relationship is reached in the simulations that parallel the experimental one, it becomes possible to use the computer simulations to explore other microstructure-property connections and to determine the possible benefits of pursuing new developments in processing to achieve such microstructures.

Porosity models - self-consistent techniques

Two diametrically opposite approaches present themselves as techniques to be used to model the behavior of intermediate porosity materials. From the dilute porosity approximation is a technique to smear out the effects of porosity by averaging out the pore interactions. Specifically, the self-consistent technique provides a framework to relate porosity with properties. The solution was first suggested by Roscoe who

extended the result of Einstein's solution of an incompressible Newtonian fluid filled with a dilute concentration of rigid spherical particles. This method allows one to adequately calculate the average modulus of a composite two phase material.

In effect, this method approximates interactions between the two phases by computing the interaction of one phase as an inclusion in a matrix with the average properties of the composite. By replacing the surrounding composite with a smeared out homogeneous material, the interactions are therefore approximated, but this allows one to calulate the fourth order tensor, P_{ijkl}, relating the average inclusion strain with the average matrix strain. The composite average moduli are therefore functions of the moduli of the two individual phases and their respective volume fractions, and P_{ijkl}:

$$\overline{C_{ijkl}} = C^{(2)}_{ijkl} + c_1(C^{(1)}_{ijpq} - C^{(2)}_{ijpq})P_{pqkl} \tag{1.1}$$

where C^1 and C^2 are the moduli of phases 1 and 2, c_1 is the volume fraction of phase 1. The fourth order tensor P_{ijkl} is the measure of the average interaction between the two phases.

The analytical model from Chow [15] captures in an approximate manner the interaction of a finite concentration of ellipsoidal inclusions. When taken to the limit of spherical pores, the solution reduces to the Kerner solution [53],

$$E/E_o = 1 - \phi\left[\frac{1}{3(1+(\phi-1)\alpha)} + \frac{2}{3(1+(\phi-1)\beta)}\right] \tag{1.2}$$

where ϕ is the porosity and α and β are weak functions of Poisson's ratio, ν,

$$\alpha = \frac{1}{3}\left(\frac{1+\nu}{1-\nu}\right), \quad \beta = \frac{2}{15}\left(\frac{4-5\nu}{1-\nu}\right) \tag{1.3}$$

This solution has been shown to fit well with experimental data [49],[51],[52].

These models assume that the two phases have no unique structure, or in effect, are distributed randomly, and in quasi-equiaxed form, and that one phase concentration is larger than the other. For a composite material with voids as the inclusion phase,

the self consistent methods which assume dilute concentrations predict a modulus of zero at 50% volume fraction, which is the critical volume fraction for percolation in two dimensions, and is thus an approximation at larger porosity. In addition, the occurance of materials with truly random microstructures is rare, because most materials have some form of internal structure due to their processing. For example, a porous material with regularly spaced voids has an internal structure unaccounted for by the self-consistent scheme and should be expected to have pore interactions that are not random.

Porosity models - periodic arrays of unit cells

Approaching the problem from a discrete point of view, the material can be modelled with a periodic array of unit cells corresponding to the microstructure, as is illustrated in figure 1-4. This approximation has some conceptual advantages because the assumptions of a periodic array can be customized to fit the microstructure of interest. In the case of the Gibson and Ashby cellular foam developments[35], the highly porous materials are modelled after the periodic array of a unit cell composed of slender beams and struts, and the large scale material response is obtained from the analytical solutions of the mechanical response at the representative unit cell level. As an example of the power of this approach, the results of an analysis using a three dimensional unit cell corresponding to a foam material gives:

$$\frac{E^*}{E_s} \sim \left(\frac{\rho^*}{\rho_s}\right)^2 \tag{1.4}$$

$$\left(\frac{K^*_{Ic}}{K_{Ic_s}}\right) = C\left(\frac{\rho^*}{\rho_s}\right)^{\frac{3}{2}} \tag{1.5}$$

where (*) represents quantities for the porous material, and (s) for the solid phase.

The benefit of this approach is that analytical solutions can be readily obtained for many mechanical properties such as modulus, crushing strength and fracture toughness all as functions of material parameters, and unit cell geometry. Numerical simulations for more complex geometries are simple to generate with finite element

methods. One drawback to these solutions is that they tend to predict unrealistically anisotropic behavior, but if the real material is isotropic, appropriate averaging can produce useful results.

1.1.3 Micromechanics of Toughening Mechanisms

In order to improve the potential viability of intrinsically brittle ceramic materials in structural applications, many mechanisms of toughening have been developed. In contrast to the *flaw control* approach which accepts the inherent material brittleness and seeks to control the flaw population (keeping in mind the importance of weakest link statistics), a significant emphasis has been placed recently by the ceramics community on the toughening approach. Although in most cases more than one toughening mechanism will be in effect [46], microstructural design for improved toughness is typically based upon the identification of the single dominant toughening mechanism. These mechanisms include crack tip shielding by martensitic transformation of partially stabilized zirconia under stress[75,11,26], controlled microcracking[45,94,29], fiber fracture and pull out[30,5], and grain localized bridging [103].

Dissipative processes, such as fiber pull out and analogous grain pull out, and others like microcrack rubbing, are potentially powerful, however, the occurance of these in primarily linearly elastic, single phase materials is less frequent. Most of the developments put forward are theoretical in nature, although some preliminary data suggests that frictional tractions are important elements in toughening by grain-localized bridging [103].

Though there are issues still to be resolved in the use of linear elastic fracture mechanics for polycrystalline ceramics, continuum based models are used in the literature to correlate structure with property. Rice and Lewis[88] discuss a variety of problems in the mechanics of ceramics for which more understanding is required, such as the statistical effects of distributions of porosity, and microstructural stresses such as thermal misfit stress arising from the reaction bonding. Other questions arise such as the degree of deflection of cracks in polycrystalline ceramics during fracture. Wu[109,108] et. al. demonstrate, by use of an x-ray microradiographic technique, for

example, the tendency for crack twisting, wandering and branching in ceramics over various grain sizes and materials including Si_3N_4.

Role of microcracking

The pre-existence and formation during fracture processes of microcracks can have a significant effect on material properties. Usually, the occurance of microcracks has been associated with general microcracking due to thermal mismatch stresses and the deterioration of the material integrity. Studies have suggested that in certain cases however, frontal-zone microcracking or a microcrack cloud around the main crack can be beneficial, by reducing the local stress intensity[43,24,18,28,16]. The phenomenon of microcracking has been observed to occur in the stress concentrations of macro-scale cracks in cases generally associated with favorable stress states. For example, in transformation toughened alumina, with zirconia inclusions, the highly localized residual stresses due to the tetragonal to monoclinic transformation in the zirconia create microcracks[17]. The release of elastic energy has the effect of postponing the unstable crack propagation to failure in brittle materials. In effect, the stress fields near the crack tip have the same classical form, but the stress intensity factor is reduced in the damage zone.

In the division of toughening mechanisms between crack wake phenomenon, and crack frontal process zones, microcracking is the only likely viable candidate for crack frontal zone toughening in non-transforming ceramics. In order to model this mechanism, various authors[11,45,28,12,58] have produced useful solutions for transformations appropriate for microcracking. These solutions are based on the efforts to model transformation toughened materials which take into account both shear and dilatational character of the irreversable transformation and consequential redistribution of stresses around a macrocrack tip. One such development is that of Hutchinson[45], which assumes that the process zone is large enough to include a 'cloud' of microcracks so that the microcracked material is isotropic and the strain due to the release of residual stress is purely dilatational. The solution indicates the beneficial shielding of the microcracks on the macro-scale crack is derived from two effects: the release of in-

ternal stresses and a reduction in the effective moduli near the crack tip. Specifically, the dependence of K_{tip} on modulus differences, the volume average dilatational transformation strain, θ_T, associated with the release of residual stress, and the process zone shape is:

$$\frac{K_{tip}}{K} = 1 + (k_1 - \frac{5}{8})\delta_1 + (k_2 + \frac{3}{4})\delta_2 + \frac{1}{3}\left(\frac{2}{\pi}\right)^{\frac{1}{2}} \frac{E\theta^T}{(1-\nu)K} \int_0^{\pi} [R(\theta)]^{\frac{1}{2}} \cos(\frac{3}{2}\theta) d\theta \quad (1.6)$$

where, the terms k_1 and k_2 are the integrals which account for the process zone shape which is represented by $R(\theta)$, and δ_1 and δ_2 are dimensionless moduli which vanish for no change in modulus for the transformation (see appendix). The parameter θ^T is the volume average of the dilatational strain in the process zone, thus is proportional to the microcrack density. The term that includes the integral represents the contribution from the dilatational transformation due to the release of residual stresses, and is process zone size dependent. This dilatation effect is thought to have the major impact on toughening, as well as being the primary reason for the existance of R-curve behavior. The modulus effect is small, and process zone size independent.

The solution of the problem of a steadily growing macrocrack with a simple microcrack nucleation criterion of $(\sigma_{matrix})_{max} > \sigma^c_{matrix}$ reveals:

$$\frac{K_{tip}}{K} = 1 - 1.278\epsilon - 0.3215 E\theta^T \frac{\sqrt{H}}{K} \quad (1.7)$$

where ϵ is the microcrack volume fraction, σ^c_m is the critical level of mean normal stress to initiate a transformation, and H is the damage zone half height,

$$H = \frac{\sqrt{3}(1+\nu)^2}{12\pi} \left(\frac{K}{\sigma^c_m}\right)^2 \quad (1.8)$$

The microcrack strain arises from the elimination of local stresses that are commonly attributed to thermal misfit or elastic anisotropy of neighboring grains. In intermediate porosity materials, however, it is more likely that the microcracking would be derived from locally weak ligaments. It appears that cracked ligaments

would have a stable configuration if the ligaments are spacially isolated, a necessary condition for effective toughening, but these hypotheses have yet to be proved.

However, experimental evidence for this crack tip frontal zone toughening mechanism in non-transforming ceramics is sparse or altogether lacking [60,103,102]. Some suggestions have been made that more likely, microcracks ahead of the crack tip play a role in inducing crack branching and deflection. The analysis by Lawn [60] on the conditions necessary for the creation of microcrack clouds is based on fully dense periodic structures with the spacial distribution of weak ligaments linked with the microstructural scale, as would be the case for fully dense, polycrystalline monophase material. The result of the analysis is that the microcrack cloud radius scales strongly with microstructural scale such that the optimal spacial distribution of microstructural dimensions (or weak ligaments) for maximum toughening due to microcracking is restrictively small.

Crack bridging

The effect of crack bridging by such elements as unfractured grains (as is observed for high aspect ratio grain microstructures) or by fibers or whiskers is expected to significantly increase the toughness. The effects of crack bridging and grain pull out are expected to add to both the macro-scale crack propagation resistance as well as microcrack stability. In effect, where excessive microcracking causes microcrack linkage and failure, stronger elements will essentially hold the material together, and provide additional dissipative processes in the crack tip damage zone. In situ observations of crack growth in a coarse grained alumina have revealed the presence of grain-localized bridging, which provide for stable fractures, typical of material with R-curve behavior [103]. This mechanism has been suggested as a general phenomenon in non-transforming ceramics.

The idealized models based upon the notion of uniaxial aligned continuous fibers predict that toughness increases with the length of the bridging zone, strength and volume fraction of the bridging elements. If we make the assumption that the bridging stress increases from zero at the crack tip to its maximum value at D_B, we can estimate

the increase in toughness due to crack bridging:

$$\Delta K^{wr} = \frac{2}{3}\sigma^c\sqrt{\frac{2D_B}{\pi}} \tag{1.9}$$

where $\sigma^c = V_f \times \sigma^{frac}$, V_f is a volume fraction associated with the bridging species, and σ^{frac} is the bridging stress of one bridging element at the point of impending element rupture.

Qualitatively, as the crack propagates through the material, a bridging zone is developed, in which stronger elements remain intact behind the crack tip. This zone can be divided into three regions (see figure 1-5) such that at very short distances behind the crack tip (typically$< 5\mu$m) the stronger element carries the load. If this element is a grain properly aligned that serves as a whisker like ligament, then once the shear tractions along the grain boundary exceed its fracture stress, debonding occurs. The characteristic length of debonding, λ, is inversely related to the grain boundary strength. This debonding distributes the crack opening displacement strain over a longer length of grain, thus reducing the bridging stress. If the interface fracture strength is small enough, debonding can occur at the crack tip, therefore locally eliminating the stress singularity and arresting the crack. Because with increasing distance away from the crack tip, the crack opening displacement increases, the required grain elongation increases as well. The maximum length of debonded grain, 2λ, occurs where $\sigma_c = \sigma_{fc}$. Once this point is reached, the grain cleaves. A significant fraction of bridging grains may fracture away from the main crack, and will therefore participate in pull out in the third region of the bridging zone, providing additional toughening. By using the Budiansky et. al.[11] approach to estimating the debond length, λ, for whisker toughened microstructures ($\lambda/d \sim \frac{1}{12}\gamma^m/\gamma^i$, where d is the diameter of the whisker, γ^m is the matrix energy release rate, and γ^i is the interface energy release rate), the length of the bridging zone, D_B can be estimated by setting the crack opening displacement equal to the displacement for the strong element at the point of fracture:

$$D_B = \frac{\gamma^m E^c}{\gamma^i E^w}\left[\frac{\pi d}{24}(1-\nu^2)V_f\right] \tag{1.10}$$

Here, E^c and E^w are the elastic moduli of the composite and whisker material respectively. This result emphasizes the importance of the role of the interface fracture strength, a somewhat ill defined and difficult quantity to measure, having influences from surface roughness, and the degree of mode 'mixity' (shear and opening) effects[31].

Crack Roughness and Tortuosity

Generally speaking, only truly isotropic materials like glasses or extremely fine grained materials exhibit ideally single, planar cracking. Thus, thermal expansion differential, elastic anisotropies, and stress concentrators like pores are suspected to be the heterogeneities necessary for departure of the crack from planar form in monophase materials.

The initiation of crack bifurcation is not currently understood, however the role of microcracking in the initiation of crack branching is prominent[109,108]. The microcracked material, having expended its ability to dissipate energy, and having a reduced modulus reduces the local stress intensity, and produces potent heterogeneities in the stress field of the crack tip. This now less isotropic material can thus provide alternate preferential pathways for the macroscale crack. In all cases, it is expected that the extent of any branching or wandering, as a result of microcracking produced, should be well within the damage zone of half height, H.

A study by Wu and Rice et. al.[108] concludes that in non-cubic or two-phase, polycrystalline ceramics, where elastic and thermal expansion anisotropies can produce microcracks at grain boundaries, crack branching occurs on a multi-grain scale and is attributed to the generation of microcracks around the main crack. For large grained material, the linking of microcracks results in less branching and more wandering, or single crack propagation along grain boundaries or through grains by cleavage, naturally following a topology on the grain size scale.

As an illustration of this microcrack effect, the fracture energy of Al_2O_3 is shown to pass through a maximum with grain size. The increase in grain size produces more local anisotropies with a given amount of stress and thus the increased extent of microcracking produces an increase in crack wandering and branching. The crack resulting deflections reduce the driving stress intensity, and increase the total fracture surface area and thus fracture energy, especially for branching. As grains get larger, however, fewer grains lie in the high stress intensity zone of the macroscale crack, and thus the fracture process becomes more of a linking up of microcracks such that their effect is a deterioration of fracture energy.

A final influence to be considered is the effect of the quantity and spacial distribution of porosity on crack branching. It is suspected that the pore size and spacial distribution, instead of grain size, plays a more prominent role in the higher porosity regime. Rice shows crack branching in other RBSN material, at higher porosities in material produced at Boeing[89] which exhibit relatively high energy release rates, $G = 12$ [J/m^2]. Microradiographic studies of material with a porosity of 51% indicate a substantial branching width on the order of 100μm, and wandering from planar form on the order of 100-300μm, which are approximately the dimensions of the large pores and particles used to fabricate the material, as can be seen in figure 1-6. The material was processed with particles of sizes 20-200 μm, and microradiographs show large pore sizes in the range 100-150μm. The observations that the crack appears to propagate from large pore to large pore and that the fracture surface reveals predominantly transgranular fracture suggest that the spacial distribution of pores plays a strong role in branching, and grain size and morphology are of secondary importance.

1.1.4 Multiple Mechanisms

As stated by Lewis[46], most processes of toughening result from a combination of processes of crack tip shielding and dissipative work. The interactions between mechanisms can be either cooperative and produce a synergistic effect, or they can interact deleteriously. Synergistic behavior has been shown to exist when both bridging and process zone mechanisms, like microcracking, operate simultaneously[1]. A multi-

plicative combination of effects occurs in this case because the tractions on the crack faces in the bridging zone serve to increase to process zone height behind the crack tip.

1.2 Outline of Thesis

The outline of this thesis is as follows. Chapter 2 explores the microstructural details in terms of pore and grain morphology as observed by micrographical sectioning and observation in the electron microscope. In this chapter we also include experimental use of the acoustic wave as a microstructural probe. With this gathered information about the microstructure of real porous media, a model for simulating realistic microstructures in the computer is presented in Chapter 3 and compared quantitatively with real pore size and shape distributions. These microstructures are then mapped onto a discrete spring mesh with corresponding properties and placed under load in order to observe the fracture behavior in Chapter 4. Microstructural images from electron micrographs are similarly mapped onto the fracture mesh for comparitive purposes. In the first case, sections of simulated microstructure of dimension corresponding to the representative volume element are probed in uniaxial strain to observe crack nucleation mechanisms and the influence of specific microstructural details such as grain boundary strength. The observations of microcrack nucleation and coalescence are used to extend the modelling of fracture to crack propagation of much larger dimensions of material. In essence, the microstructural details are smeared out and the local material properties, local elastic modulus and strength, (probed on the scale at which fracture takes place, i.e. on the pore size scale) are used at the mesoscopic scale of crack propagation. In this manner, a connection is made between local micromechanical property variability and such macroscopic level crack behavior as crack deflection, bridging phenomena by locally tough elements and redundant cracking in the stress field of the sharp crack.

In Chapter 5, cracks emanating from Vickers microhardness indentations are observed qualitatively for identifying toughening mechanisms such as crack tortuosity,

and a method for measuring the fracture toughness parameter from crack opening displacements is described. Comparisons of the experimental observations and simulated crack propagation are enumerated and described in the concluding chapter.

The studies performed here demonstrate the following.

- The ability to simulate the fracture of microstructures in the intermediate regime of porosity from the processing stage to crack propagation is demonstrated and some key qualitative toughening mechanisms are observed. With the qualitative and semi-quantitative comparison of the simulated crack propagation and experimentally observed cracks, we have demonstrated a connection which suggests this model as a tool for microstructural design

- A new technique for measuring fracture toughness in brittle media is developed and demonstrated to have good accuracy, based upon measurements of toughness in well characterized materials, and the fundamental nature of the connection between the crack opening displacements and crack length with stress intensity. This technique is based on the measurable quantity, crack opening displacement, is naturally a lower bound, and does not rely on empirical connections between load and crack length with toughness.

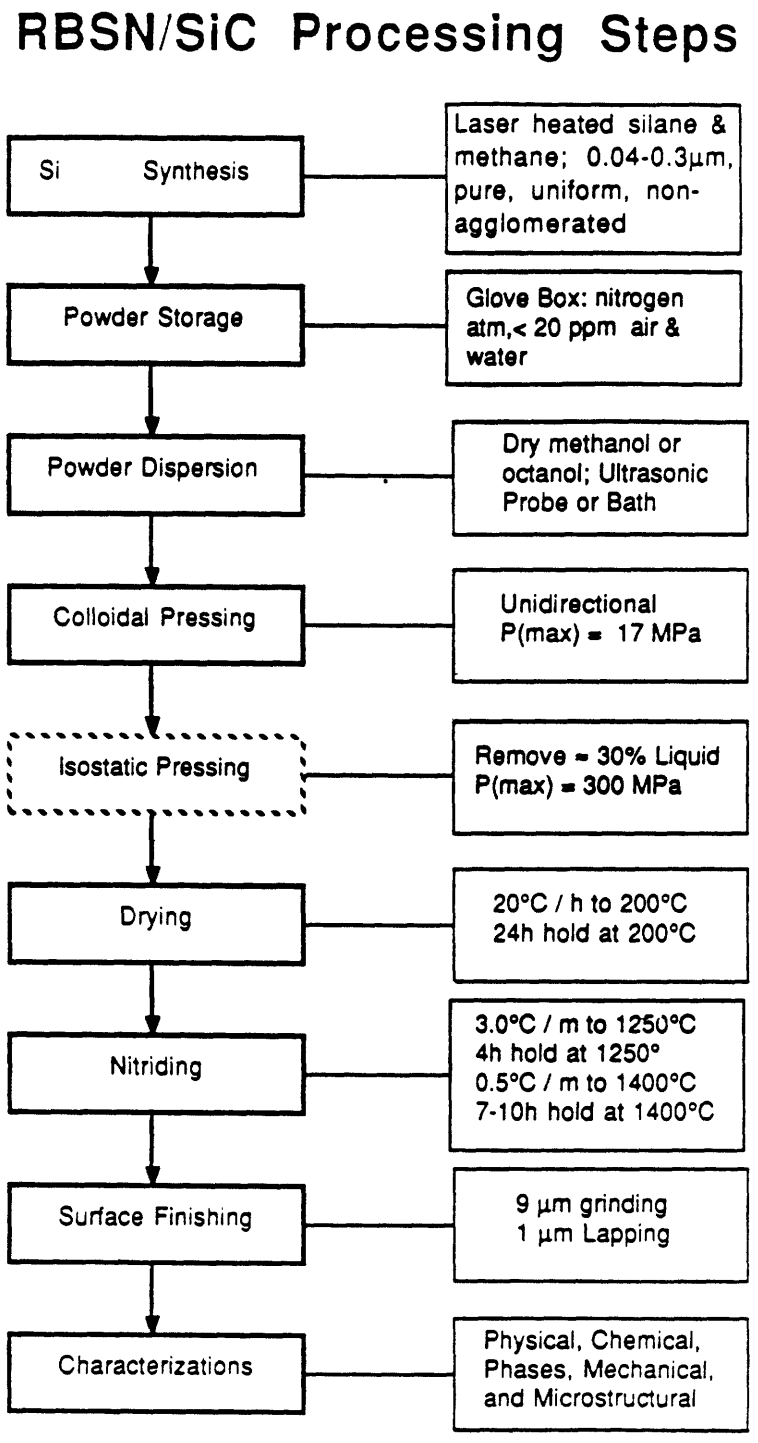

Figure 1-1: Processing steps for RBSN.

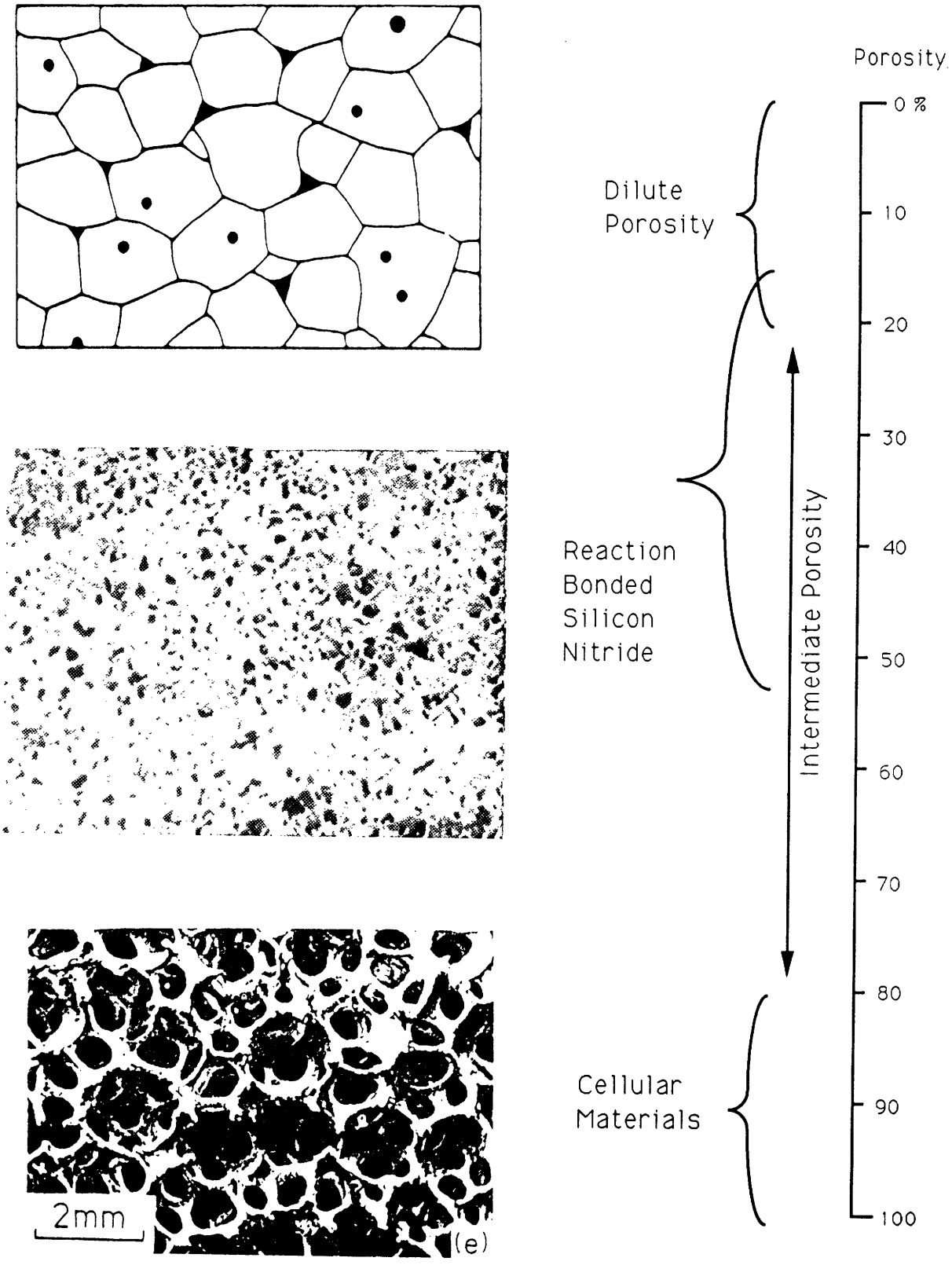

Figure 1-2: Material classification based upon average porosity.

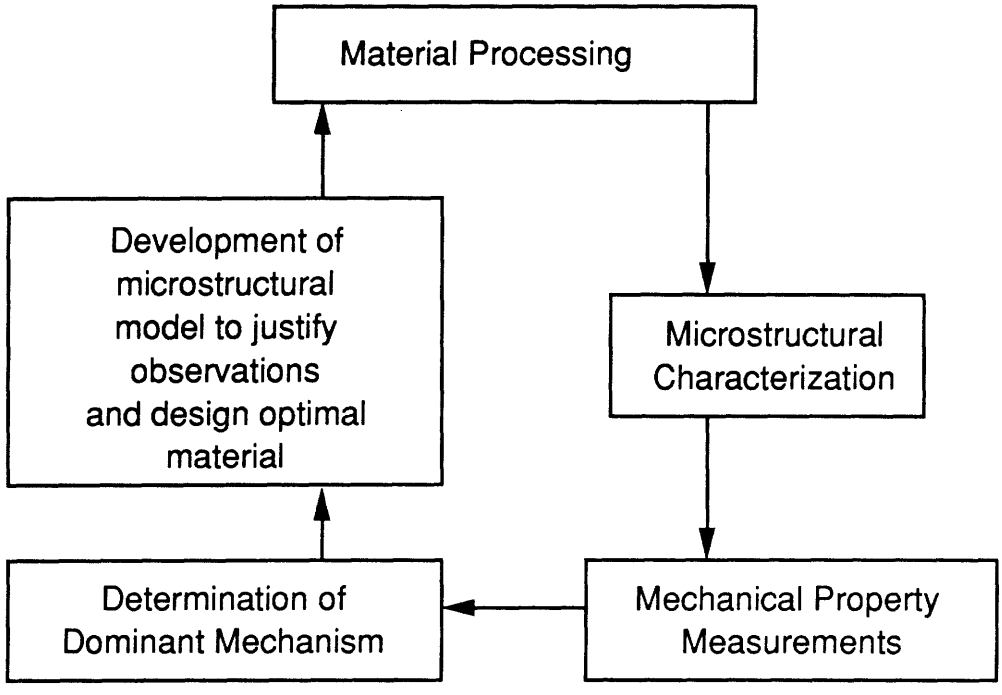

Figure 1-3: Typical methodology for microstructure design is an iterative process involving material production and evaluation.

(a)

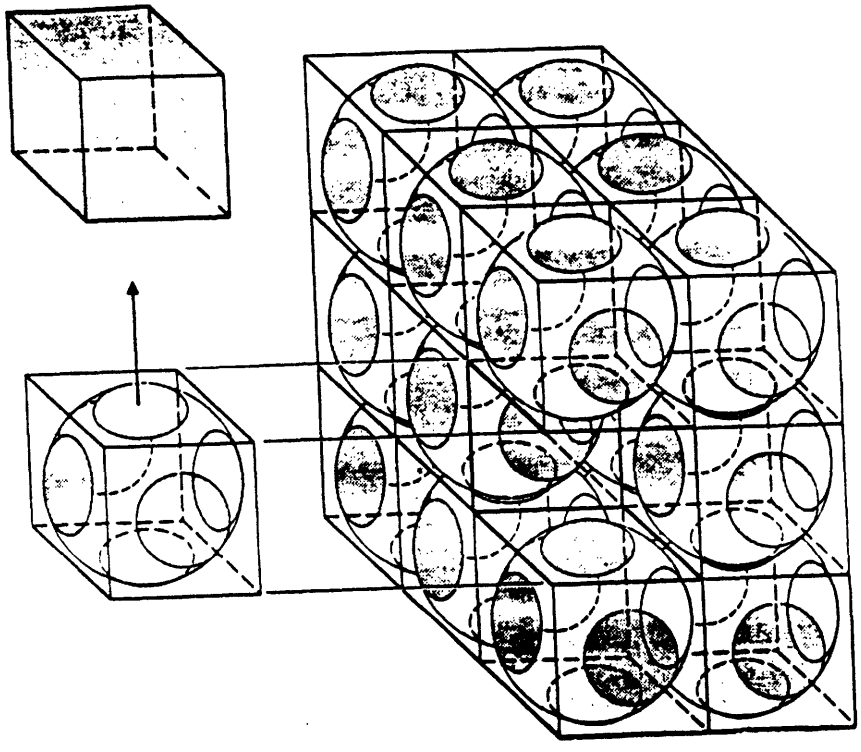

(b)

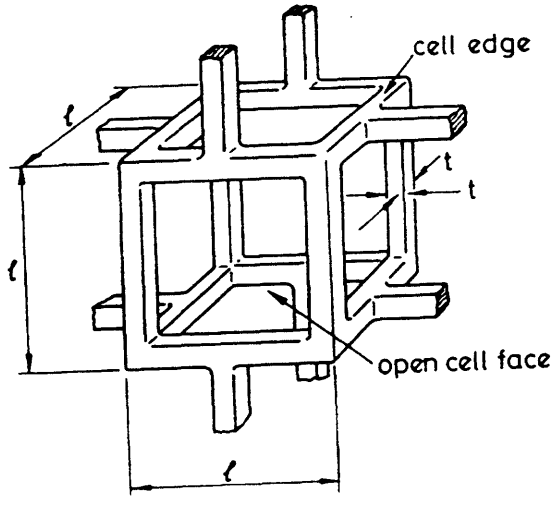

Figure 1-4: (a) Schematic of periodic array of unit cells (from R.W. Rice, 1990), (b) unit cell used for cellular material models (from Gibson and Ashby, 1988).

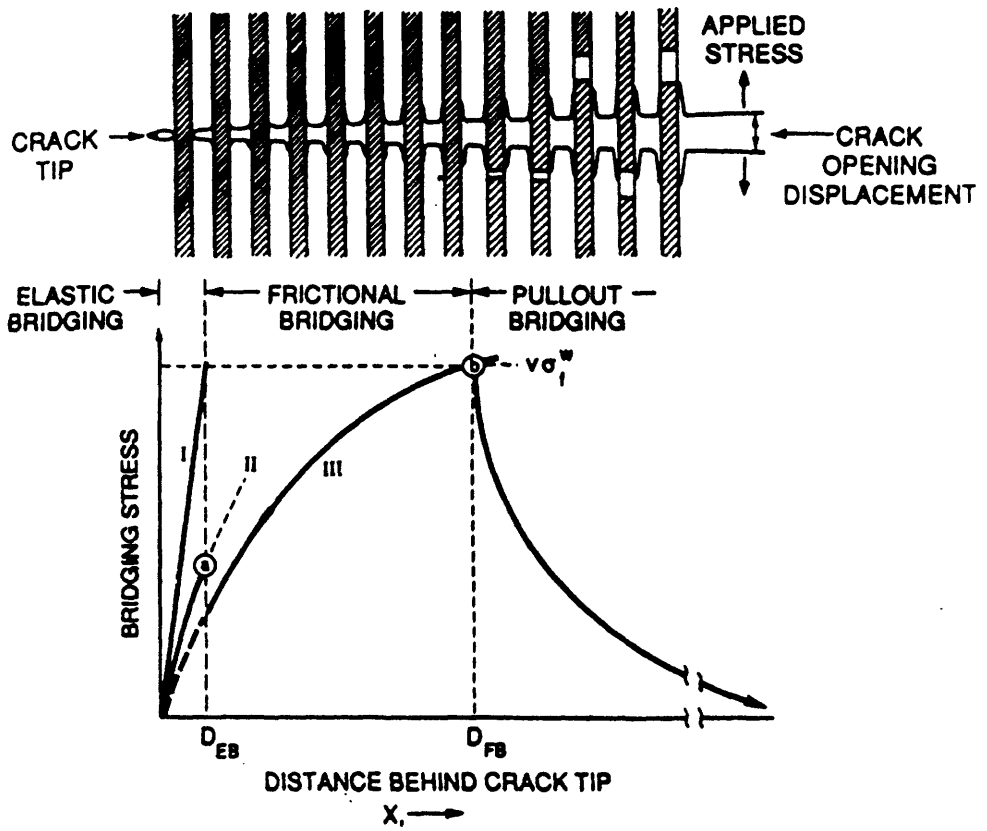

Figure 1-5: Crack bridging zones (from Becher, 1990).

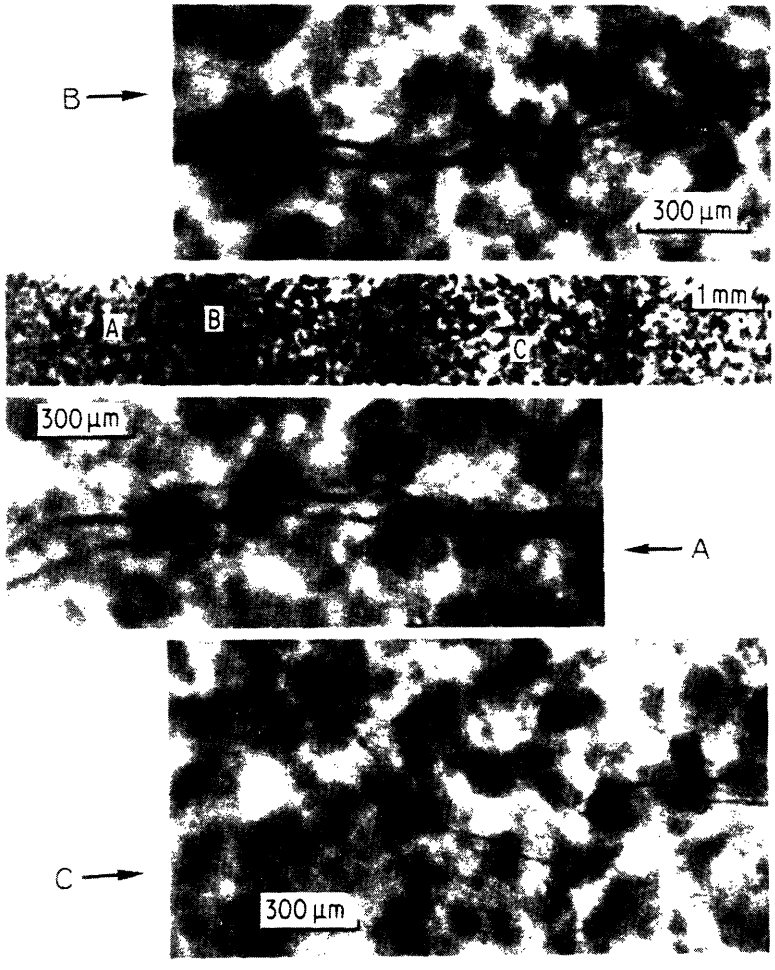

Figure 1-6: Microradiograph of RSSN with porosity of 51%, exhibiting an unusually high fracture energy of 12 J/m^2 (from R.W. Rice, 1985).

Chapter 2

Microstructure of RBSN

In order to provide comparisons of the microstructure and fracture properties between experimentally produced material of the model material system, reaction bonded silicon nitride, RBSN, and the modelling results of fracture in subsequent chapters, we provide here some microstructural analysis from a fracture mechanics perspective. To ascertain properties critical to mechanical response, a combination of methods is often used. It was found to be most practical to use the electron microscope to measure the submicron porosity length scales, and to probe the average elastic properties with a long wavelength acoustic wave, in relation to average microstructural dimensions, to ascertain the degree of variation of the porosity distribution. In addition, scanning acoustic microscopy is employed to obtain information about elastic property gradients on the micron length scale.

2.1 Introduction

The scalar quantities of pore size and shape distributions as measured by such quantities as the pore diameter and aspect ratio as well as grain size and shapes serve as simple descriptors of the microstructure and as references for differentiation between materials of varying properties. More importantly, these measures can buttress the degree of similarity between real microstructures and the simulated microstructures in the related mechanical modelling in the following chapters.

However, the transformation from the two dimensional representation of the microstructure as obtained ideally by sampling a planar section to the size distribution function is not necessarily a reversible process. The spacial distribution and other details of porosity is lost with the stereological procedures of measuring microstructural feature sizes. Because this information is central to the determination of the stress distribution in the loaded microstructure, microstructure size distributions are helpful, but generally insufficient to predict fracture properties.

In Chapter 4 an alternate method for describing highly complex probing the pertinent local properties is described. In essence, small, localized regions in the microstructure of both simulated and real material are sectioned and sampled for their mechanical response including elastic modulus and strength. In the analysis here, attention is paid to quantifying the specific functions of size and shape distributions of the porosity.

2.2 Experimental Procedures

2.2.1 Microstructure Characterization

In order to objectively determine approximate pore sizes and shapes in highly complex nano-scale microstructures, two complementary procedures of image analysis on metallurgically prepared surfaces were undertaken in parallel. Stereoscopic scanning electron microscope images of the microstructure in the first case were hand edited to differentiate solid from pore. In the second case the images were digitized by an optical scanner and pore boundaries were determined by a contrast threshold criterion. In both cases the images were statistically analyzed with a numerical image analysis system. Pore size was measured by pore area and the dimensions of an equal area ellipse. The shape of the fitted ellipse was determined in such a way that maximum overlap occured with the pore image. The pore aspect ratio was characterized by the ratio of the equal area ellipse major and minor axes and the surface roughness was determined by the measured pore circumference, C, normalized by the circumference

of the equivalent area circle, $C/(2\sqrt{\pi A})$, where C is the circumference and A is the pore area. The circumference was measured at a resolution of 8.5nm. Average grain size was determined by TEM observation and x-ray line broadening in a separate study [68].

Microstructure image acquisition

Specimen sectioning is critical to obtaining stereologically valid sampling of the microstructure. Specifically for submicron scale pores, the filling-in of pores during grinding and lapping is problematic. In preparation of the porous RBSN ceramic, standard diamond lapping produced surfaces with many filled-in pores. However, a final ion plasma etch for 30 minutes at 6kV removed sufficient material to reveal the sub-micron pores. Figure 2-1 shows the surface morphology of the same specimen before and after ion milling. Figure 2-2 shows the surface roughness after ion milling. Stereoscopic observation of the produced surface at 5000 magnification revealed a nearly flat surface on a scale larger than the submicron pores, with a deviation from planar in a wave like form of wavelength of approximately 15 microns and an amplitude of 0.2 microns, as in figure 2-3. The roughness described here is attributed to the combination of lapping and ion milling and is deemed to be acceptable for the analysis of the pore features which are substantially smaller than the surface roughness wavelength.

Obtaining high magnification SEM images of non-conducting specimens presents special challenges. Conducting the excess charge from the specimen without obscuring fine features is the primary problem. Because standard gold coating requires 10-30 nm to create a contiguous conducting layer, features in this range are obscured, and larger features may be distorted. It was found that depositing a 30nm carbon coating allowed for good high voltage microscopy and resolution of sub-micron features. Because carbon is a light element, the interaction with the electron beam is weak, and this layer is mostly penetrated by a high energy electron beam of 10-30kV accelerating voltage. Objects of 20nm dimension on a C coated, micrographically prepared, and ion milled surface have been resolved with a high resolution field emission SEM (FESEM), as

seen figure 2-4). The point to point resolution of the images is approximately 5nm. In contrast, for uncoated specimens of RBSN, field emission source SEMs resolve 20nm features well with minimal charging at 2.0kV, (see figure 2-5).

An additional technique used for observing uncoated specimen surfaces was the environmental scanning electron microscope (ESEM). This microscope operates with 3 to 10 torr of water vapor pressure, instead of vacuum, which serves to carry away the excess charge buildup. In this manner, high accelerating volatages can be used to probe non-conducting specimens without standard coatings. Resolution obtainable is approximately 20nm, as seen in figure 2-6, which is somewhat larger than by using the optimal techniques of coating with FESEM. The additional feature this technique provides is the sampling of a subsurface layer of material in which the high energy electron beam penetrates to a depth which is a function of the material properties. This effect can be seen in figure 2-7. The same specimen surface is imaged in the ESEM, with and without 20nm Au coating. The uncoated image reveals a texturing of the contrast attributed to density fluctuations. These large pore channels have been observed previously [68], and can also be seen in figure 2-8.

Observation of pore shape and size distribution

The hand edited micrographs of stereoscopic images and digitized images directly from micrographs were analyzed by an image analyzing system, a Macintosh Quadra 950 operating the application Image 1.41. In this procedure, each individual pore is measured for its various dimensions described above. In the case of the hand edited micrographs, pore boundaries are determined subjectively. This data is compared with the unedited, digital images for which the pore boundaries were determined by a contrast threshold.

2.2.2 Acoustic Response

In addition to observing pore size and shape distributions, the acoustic wave as a probe of the microstructure is an effective means for obtaining reliable and non-destructive average mechanical response. The measurement of acoustic wave velocity

is typically an indicator of average microstructural morphology[22,32], due to the fact that elastic waves need to be larger than the microstructural scale for transmission beyond a few microstructural dimensions. Other acoustic non-destructive techniques are used to resolve elastically active defects like small cracks[7] which are larger than the probing wavelength.[1]

The acoustic pulse echo technique

In order to probe for microstructural differences between samples, the Young's Modulus was measured by an ultrasonic pulse-echo technique. Microstructural morphology such as pore aspect ratio has been shown experimentally to relate to average elastic response [22]. The experimental approach used here is to mount a thin specimen to a gold coated piezoelectric single crystal quartz transducer for acoustic transmission (see figure 2-9). The optimal specimen thickness was determined to be 1mm, thick enough to contain one wavelength of the acoustic pulse ($\lambda = 200$ μm), and thin enough so that minimal attenuation of the acoustic wave occurred. The acoustic wave was generated by a laser pulse focused on the gold film which creates a thermal expansion and a quasi-planar compressive acoustic wave [64]. The coupling of the rate of change of the integrated strain in the volume of the transducer with the closed circuit current produces a signal when the wave enters and exits the specimen. In this way, the time of the transmission of the stress wave into the specimen, (and out of the transducer), and the time of transmission back into the transducer can be obtained. The difference in time between these two events is the time of travel of the

[1]The impediments to resolving submicron pores acoustically in stiff ceramic materials are the requirements of a high frequency of approximately 90 GHz, and the strong level of disorder in the material. The practical limitation is that severe attenuation occurs from thermal phonon interaction above 1 GHz in quartz at room temperature[105,8], a common transducer material, and requires cooling to liquid helium temperatures[104]. The other difficulty for intermediate porosity materials is the high level of disorder. The interaction of a plane wave scattered by a single spherical pore in an elastic medium can be solved explicitly by standard differential equation methods[110]. These solutions can be extended to complicated shapes for waves larger than the pore size by an order of magnitude, by using integral methods[37]. For more complex interactions, solutions become very difficult[100]. The possibility eexists to exploit mode localization phenomenon, termed Anderson localization, where there is no long range propagation of vibration. Recent efforts[83,106] have shown progress in providing interpretive models to deconvolute structural information from the acoustic data.

acoustic wave through the thickness, reflection at the free surface and travel back to the specimen/transducer interface. The plane strain wave velocity is thus obtained and is related to the Young's Modulus by:

$$E = F(\nu)\rho v^2 \tag{2.1}$$

where ρ is the material density, v is the wave velocity, and

$$F(\nu) = (1+\nu)(1-2\nu)/(1-\nu) \tag{2.2}$$

is a weak function of Poisson's ratio, ν.

Scanning acoustic microscopy

Scanning acoustic microscopy has been used to provide information about elastic gradients on scales larger than the surface acoustic wave, approximately 2 microns. SAM contrast is formed by the interaction of leaky acoustic Rayleigh surface waves with the microstructure. The acoustic lens focuses a pulsed wave on the specimen surface which produces the surface wave. Contrast arises from changes in the phase and amplitude of this wave and the interference this produces with the reflected wave. Specimen elastic gradients can produce these phase and amplitude changes, thus a region of high microcracking density ideally can be resolved for microcracks of dimension less than the acoustic wavelength. Since surface waves cannot be transmitted well across fluid filled (typically water) surface cracks of more than a few nanometers, cracks larger than the acoustic wavelength can be resolved [70]. SAM images were obtained for mechanically polished surfaces as before and indented by the Vickers microhardness indenter such that radial cracks were produced. The Vickers indentation experiment is described more fully in Chapter 5.

2.3 Model Material Description

A series of specimens were examined in this thesis of the model porous material system, reaction bonded silicon nitride, as were produced at MIT [66]. Specimen choice was made based upon extremes in porosity as produced by characterizable differences in processing. The unique reaction kinetics and processing methods of the RBSN material which were produced from high purity, submicron scale (average particle dimension = 250nm) Si powder synthesized from silane gas with a laser process have been studied elsewhere[91,97,38]. Results show that the material can be fully reacted at uniquely low temperatures, and in relatively short times. Because the material is processed with high purity Si particles, and the process eliminates the need for densification additives, brittle glassy phases are eliminated, thus a high level of strength at operating temperatures is retained, and improved oxidation resistance is attained[34]. It appears that the maximum relative density is approximately 85%, which provides the minimum required pathway for the nitrogen gas to reach the unreacted silicon.

Table 2.1 summarizes the description of materials analyzed here. Nominally, all the materials were produced in the same manner with differences arising in the organic solvent used in the pressing of unreacted green bodies, and the addition of binders in some instances. The porosity measurements were performed by simple mass and volume measurements.

2.4 Results

2.4.1 Pore Size and Shape distributions

Figure 2-6 shows a typical microstructure of porous RBSN as produced at MIT. The pores appear somewhat equiaxed with relatively smooth surfaces indicating that during the formation of the RBSN there is a finite amount of time for smoothing of the surfaces by diffusion. The pore size distribution for the typical microstructure is usually narrow, and in the range of 50-300 nm, as shown in figure 2-10. Pore aspect

Material	Processing	p
K	Octanol w/o CIP	22.0%
H	Octanol w/o CIP	23.9
G	Octanol w/o CIP	25.5
D	Octanol w/o CIP	26.9
E	Octanol w/o CIP	25.8
I	Octanol w/o CIP	23.1
J	Methanol w/CIP	23.0
L	Methanol w/CIP	19.1
N	Methanol w/CIP - oxidized 1000°C, 1hr	23.0
M	6-8% polysilazane binder	17.0
C	1.5% polystyrene binder, colloidal pressed	27.0
F	1.5% polystyrene binder, colloidal pressed	25.8
A	5% polystyrene binder, warm isopressed	30.5
B	5% polystyrene binder, warm isopressed	29.0

Table 2.1: Summary of RBSN specimen key material processing descriptions.

ratios are found to be between 1 and 4 and circumferences normalized with the equal area circle are between 1 and 2, as shown in figure 2-11. These measures reinforce the qualitative observations of relatively homogeneous, equiaxed porosity which appear to have smooth surfaces.

As can be seen in figures 2-12 and 2-13, a comparison of pore size distributions as determined by the equal area ellipse major axis between the two methods of hand edited stereo pair micrographs and digital contrast threshold revealed no significant differences in average dimension and the spread of the population size. Hand editing produced fewer very small size pores, less than 50nm, as would be expected that pores of dimension 50nm at 20,000 magnification is 1mm or the typical limit of resolution of visual observation.

In addition, the pore size distribution has relatively low sensitivity to the chosen threshold contrast. As the choice of threshold contrast is varied, in figure 2-14, the measured pore size distribution is relatively unaffected. This effect is explained by the fact that the strong contrast gradients which defined pore boundaries are often at relatively different absolute values of contrast, implying that at one average threshold contrast chosen to obtain correct average porosity for one entire image, certain pore boundaries will be underestimated, and others will be overestimated, while a large

fraction will be accounted for accurately.

All measured pore size distributions over the porosity range of 18 to 30% were alike within experimental error, with variation arising from limited sample size, typically 250 pores sampled over an area of 30[μm^2], as seen in Figures 2-10a - 2-10n. In a few instances there was found to be a presence of a larger pore population labelled as pore channels, see Table 2.2. The larger pores, as seen in figures 2-15, 2-16, and 2-7 appear as high aspect ratio channels of approximately 200 nm in width and typically more than 1 micron long, and form an apparent cell-like network with a periodic length scale of approximately 2-5 microns. In addition, the difference in area fraction of micron size scale pores between the two nominally identically processed materials, one which had the large pore population, specimen G, and the other for which the porosity was distributed homogeneously, specimen H, suggests that the volume fraction of these large pore channels is approximately 7% (Figure 2-8). Line profile height measurements of the sectioned surface revealed a 5% proportion of the surface sampled was a large dimension pore. The profilometry was performed by a scanning laser confocal microscope which has a height resolution of 0.25μm and a vertical resolution of 1μm. Qualitative observation suggests that these larger pores are interconnected, providing an easy fracture path. The observations in Chapter 5 of cracks propagating through this microstructure reveal that indeed there is a tendency for the crack to deflect and sample these large pores and reduce the fracture toughness.

Both methods for obtaining pore dimensions, although complementary, have approximations. The uncertainties of the hand editing of micrographs relates to the subjective nature of the process of editing and comparison between 3 operators reveals the subjective nature with regard to what constitutes solid matter or pore. The average porosity is a function of the subjective judgement of the operator, and is not directly controllable from the outset. Average porosities for hand edited micrographs ranged from 19-40%, for microstructures which had nominal average porosity of 24%. For the above analysis, the comparison with the hand edited micrographs was made with the edited microstructure for which the average porosity was measured to be

Specimen	Young's Modulus	Pore channels
A	135 GPa	no
B	157 GPa	yes
C	149 GPa	yes
D	169 GPa	no
E	161 GPa	no
F	168 GPa	no
G	164 GPa	yes
H	193 GPa	no
I	175 GPa	no
J	182 GPa	no
K	193 GPa	no
L	185 GPa	no
M	215 GPa	yes
N	182 GPa	no

Table 2.2: Summary of elastic properties.

24%, close to the actual porosity. In the case of the digitized micrographs, the choice of contrast directly relates to the average porosity, and can be chosen arbitrarily. By choosing a lower contrast, or level of pixel brightness, more of the image will be classified as porosity. However, the determination of pore boundaries is left to the image contrast, which to a first order is related to the morphology of the sectioned surface. Other second order effects which produce more or less interaction with the electron beam modify the contrast, such as height, the angle of incidence with the electron beam, the surface material density or thickness, and charging effects such as for sharp pore edges.

2.4.2 Grain Size and Shape

In a separate experimental study [66], TEM and SEM observations indicate that the fractures follow a predominantly intergranular fracture path, which implies that the grain size and shape, in relation to the porosity, are important parameters to the fracture behavior. In reference [68], the grain size and phase content are determined by TEM and xray techniques. Grain size was deterimined to be approximately 45-115nm. The predominant phase is the α phase, at 75-80%, which in some other cases

tends to form whisker-like shapes, however TEM observations indicate that here, the grains are more equiaxed. The other phase, β Si_3N_4, is typically larger and more rod-like in morphology in material where liquids are present during processing, which is not the case here; TEM observations reveal only equiaxed grains. A discussion of the crystal chemistry of the two phases if Si_3N_4 is given is Section 3.2.2.

2.4.3 Elastic Properties

The Young's modulus in similarly produced reaction bonded silicon nitride over the range of 17-31% porosity depend strongly on the average porosity, implying a similarity of microstructural morphology. The modulus data tends to follow typical trends of the self-consistent models for randomly distributed spherical pores, as seen in figure 2-20. In comparison with an exponential curve fit,

$$E = E_o \exp(-bp) \tag{2.3}$$

where E_o is the modulus of fully dense material and p is porosity, the best fit for parameter b is 2.23 ± 0.17 as compared to published values for many varieties of silicon nitride of 2.4 ± 0.4[86], and 3.7 for a variety of reaction sintered silicon nitride [89]. Uncertainty for measured values of E with this technique is estimated to be 4%, and is associated obtaining a uniform thickness specimen and measuring this dimension.

Moreover, statistically small deviation from the fitted exponential curve was found, indicating small microstructure variation other than average porosity. This similarity of microstructural morphology over the range of porosity is found again by the quantitive microstructure analysis.

Direct comparisons are difficult between materials produced with different methods, such as for the addition of binders, however, in the nominally identical materials, G and H, a variation in modulus was seen to arise from observed porosity features. The microstructure of material G exhibited a larger sized pore population, and a lower modulus, as shown in Table 2.2. As seen in figure 2-15, material H has a homo-

geneous character, whereas material G, exhibited contrast gradients of approximately 2-5 microns which were attributed to fluctuations in density. However, the existance of these cell-like porosity fluctuations did not always produce a reduced elastic modulus. In the case of material B and C which exhibited this large scale pore correlation of somewhat reduced magnitude, as can be seen in figures 2-7, and 2-16, the elastic modulus was not strongly affected, as the data fall along expected porosity trends for randomly distributed pores.

Acoustic Microscopy

Scanning acoustic microscopy was used to determine the existance of elastic gradients due to microcracking in the crack wake and at the crack tip of the Vickers indentation induced cracks. Although the resolution is less than the electron microscope, the key observation is that there is no obvious region of differing contrast around the crack tip, near the center of the image in figure 2-21. The image from the 1 GHz acoustic lens which produces a surface wave of approximately 2 microns graphically shows contrast gradients on the scale of about 5 microns. These apparent pores are likely to be height variations in the surface of the specimen, which is a primary determinant of the contrast of the SAM image. This is consistent with other microstructural images of this specimen, which show no large scale variations in porosity.

2.5 Discussion

The microstructures observed here of RBSN prepared under careful conditions have a high degree of uniformity based on the microstructural observations and the minimal scatter of the elastic modulus data. In addition, the similarity of pore size distributions implies a degree of qualitative similarity in microstructural features. Although there are uncertainties associated with each separate procedure in obtaining distributions of the pore population measurements, the marked agreement between the methods and the low sensitivity of the choice of threshold contrast suggests that these data have some reasonable degree of accuracy.

Microstructural homogeneity was frequently found except in a few cases where porosity existed on a scale much larger than the intrinsic pore scale, of a volume fraction of approximately 5-7% in the extreme case of material G. The processing steps which produced these defects were not identified. However, the length scale of the porosity which is much larger than the initial silicon particle size suggests that the source of inhomogeneity is associated with particle packing defects.

The average elastic modulus was strongly dependent on the average porosity, except in the case where the microstructure included a population of larger pores, which tended to produce a lower modulus. This close dependence on average porosity is found for many other materials [86], and implies a similarity of structure. The degree of agreement with the finite porosity model by Chow [15] (see equation 1.2), for the case of randomly distributed spherical pores, reinforces the notion of a quasi-random, low aspect ratio pore population of uniform dimensions. This similarity and the relatively low value of the pre-exponential factor b^E of 2.2, as compared to the range of values of 1.7 to 6.6, in which the large majority of polycrystalline materials fall, implies that for the isotropic RBSN, the elastic properties cannot be substantially increased, given a level of average porosity[2].

2.6 Conclusions

The high degree of homogeneity of microstructures on scales larger than the average sub-micron pores implies that these materials are a good choice for modeling fracture of intermediate porosity for which the porosity has a quasi-random spacial distribution, from near the dilute porosity range, into higher porosity level materials.

[2]A lower value of b implies less dependence on the average porosity, i.e. less reduction in E for a given porosity level.

Lapped to 1μm diamond

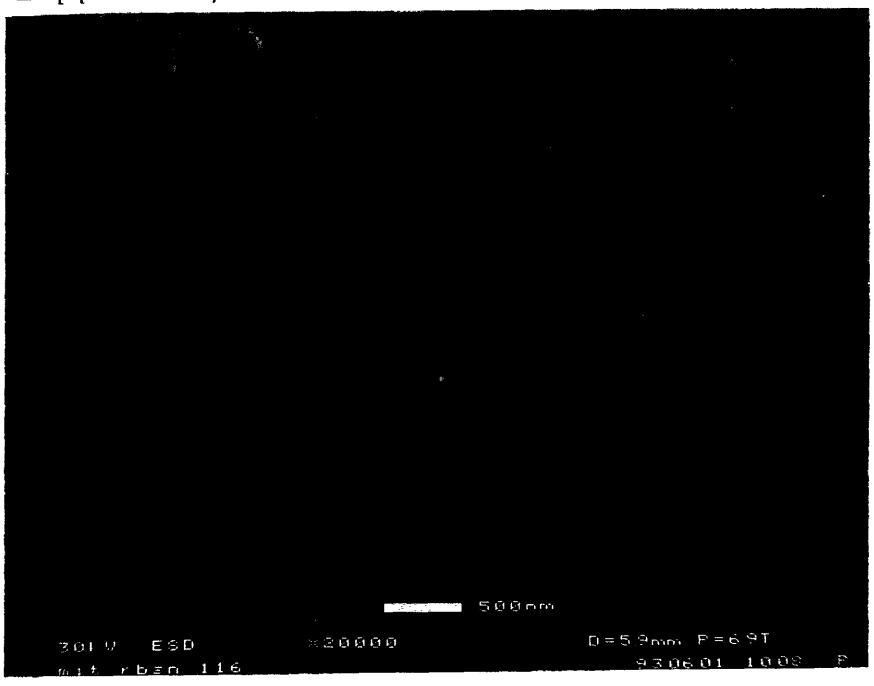

Lapped and ion milled 30 min

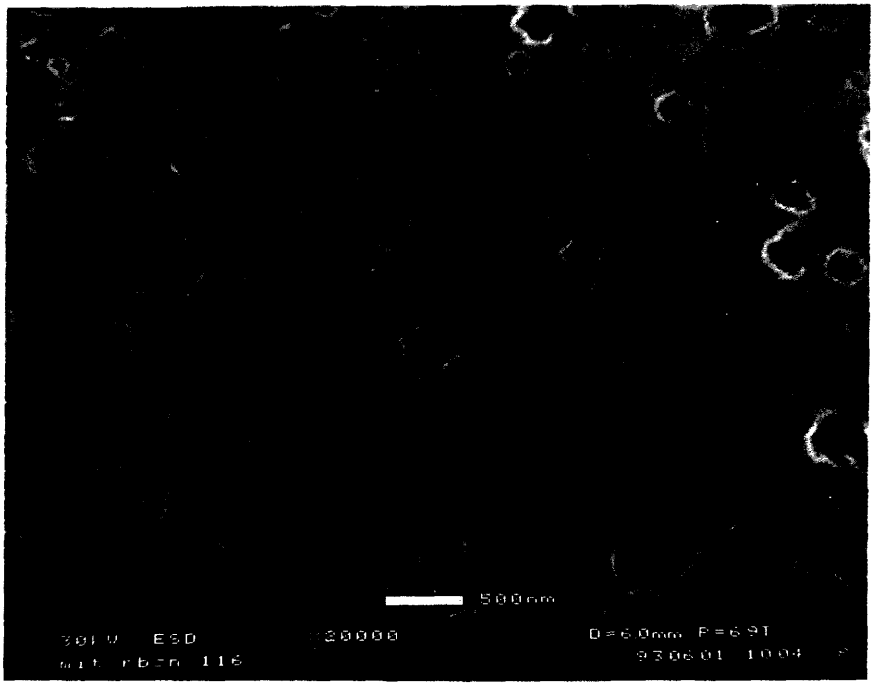

Figure 2-1: Typical micrograph of the ground and lapped surface to 1 micron diamond before and after ion milling step. (Material G)

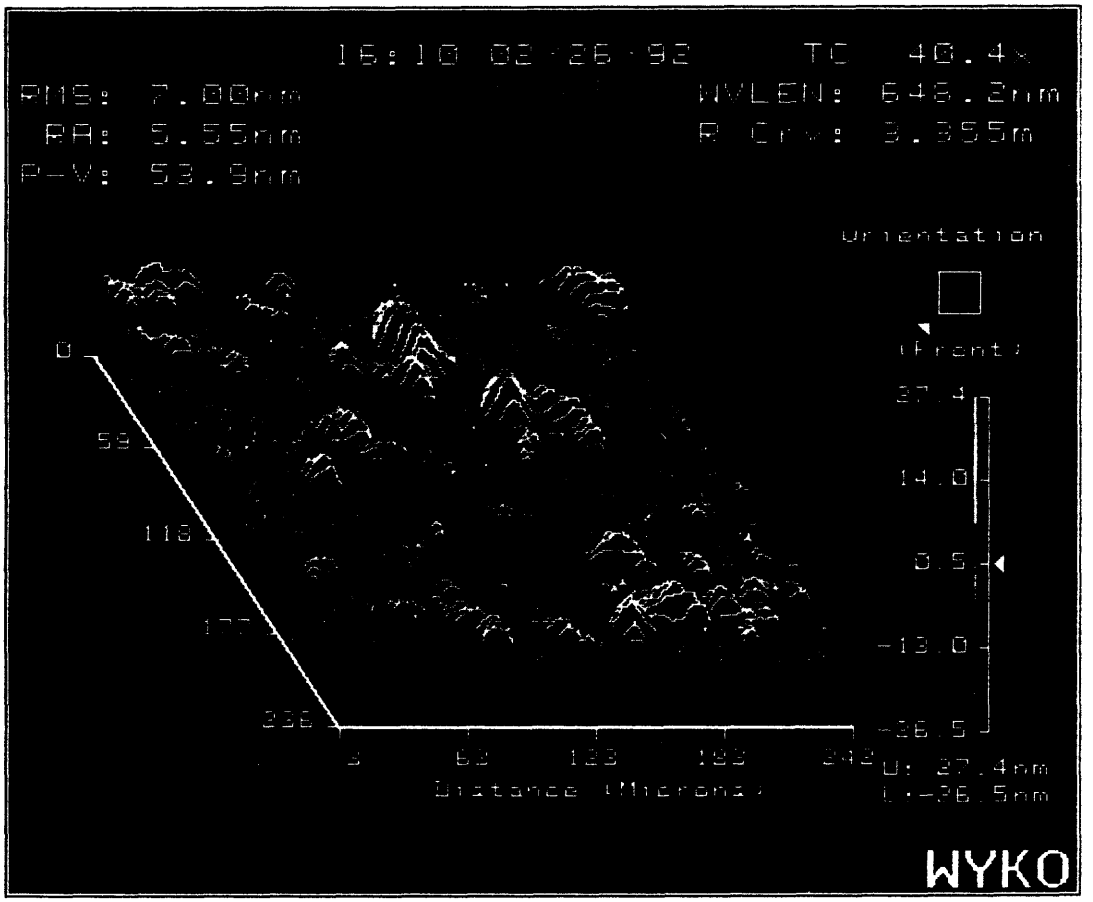

Figure 2-2: Surface roughness of lapped surface as determined by optical profilometry. The height scale on the right is in nanometers.

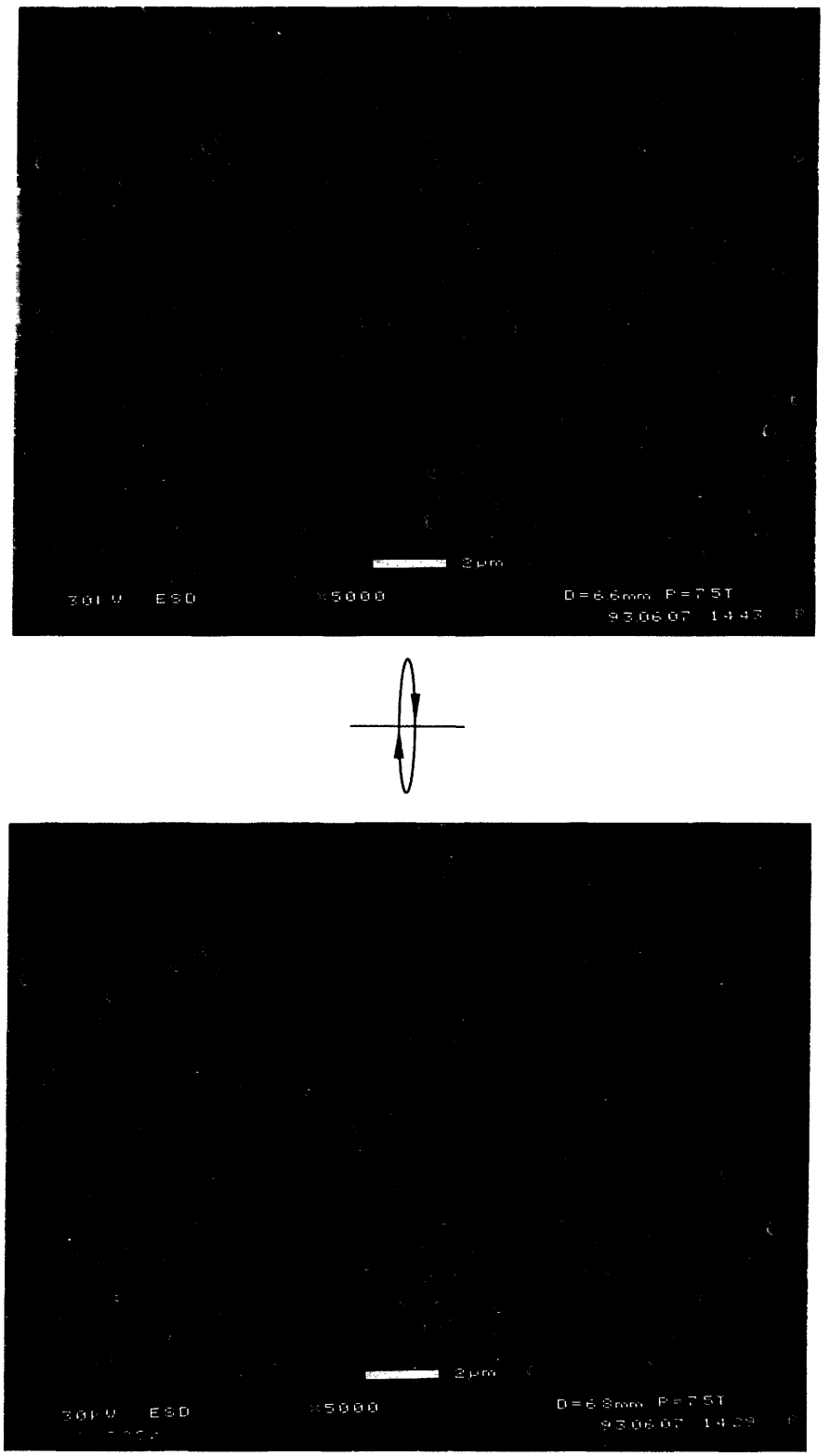

Figure 2-3: Stereo pair micrographs of the prepared surfaces suggesting the quasi-planar topology of the section. (Material H)

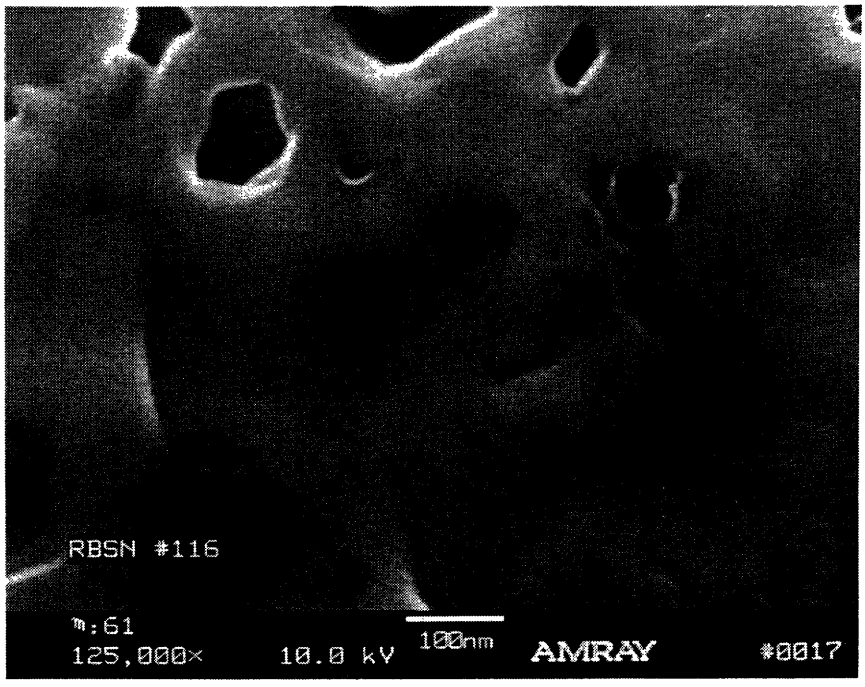

Figure 2-4: High magnification image of the microstructure of RBSN showing small scale (20nm) pore in the center of the image, and the relatively smooth pores surfaces. The image was generated with a field emission SEM at 10 kV accelerating voltage; the surface has a 30nm C coating. (Material G)

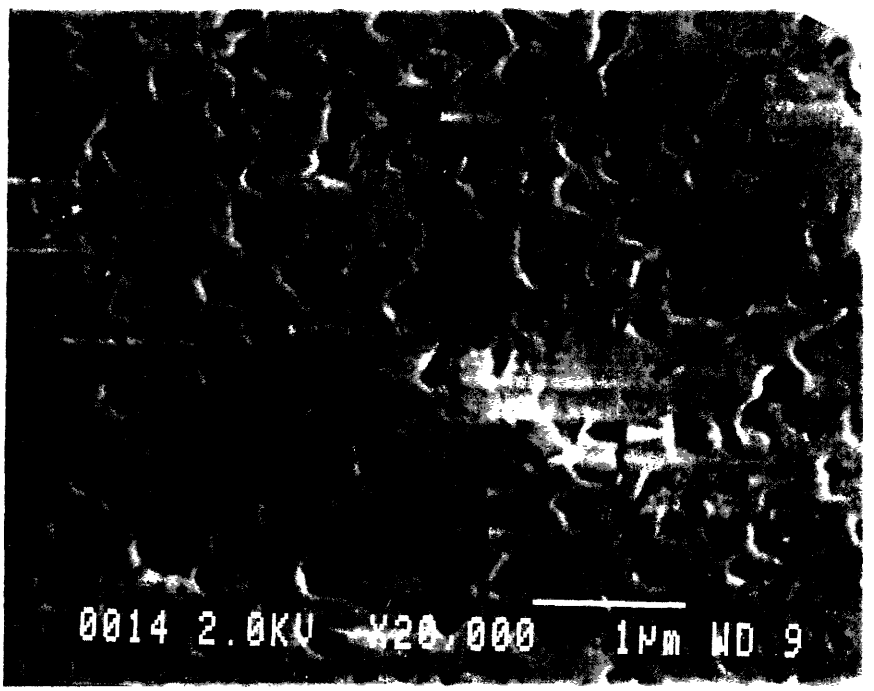

Figure 2-5: Micrograph for uncoated surface of RBSN obtained with low current field emission SEM.

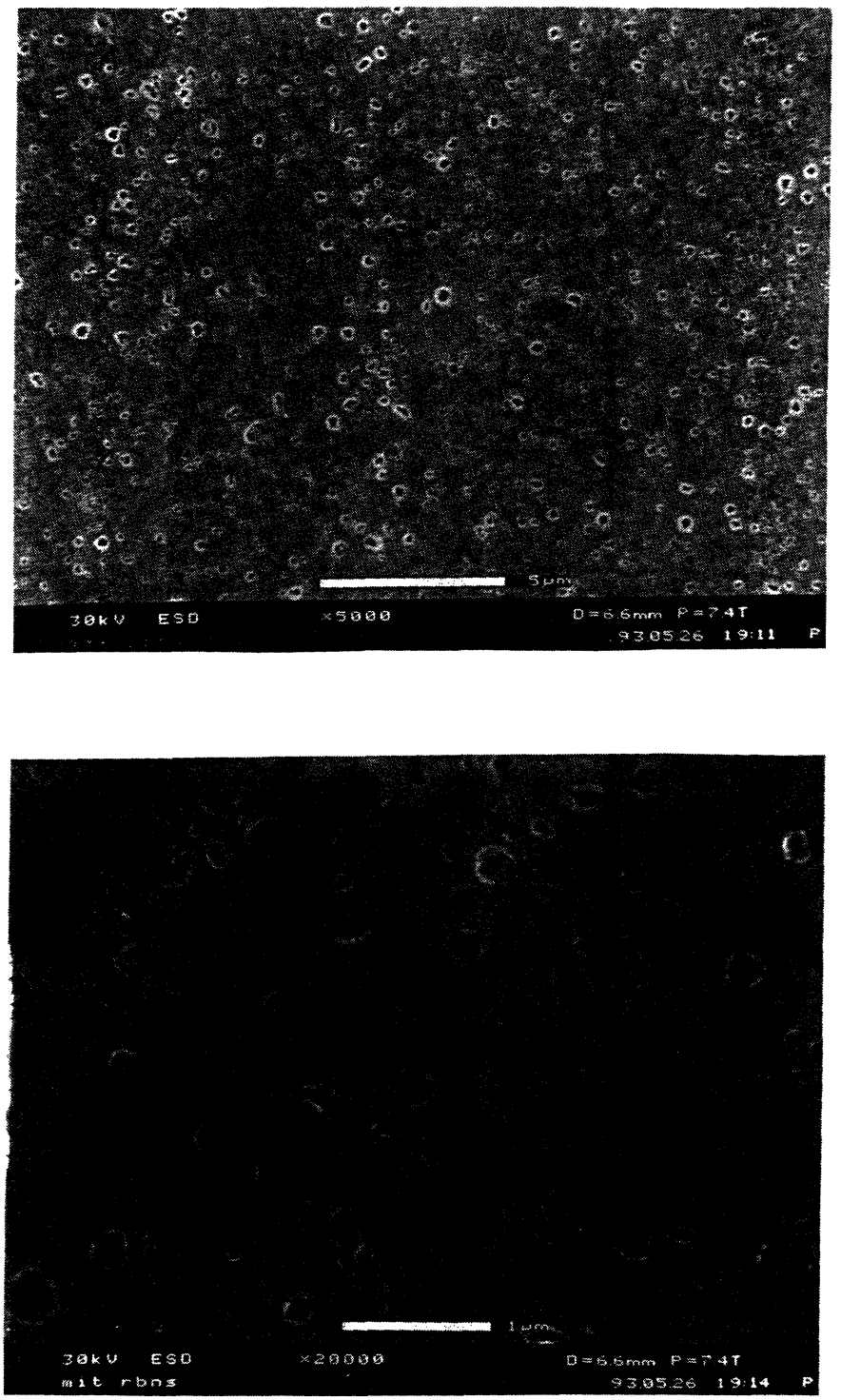

Figure 2-6: Typical microstructure of RBSN showing submicron scale porosity and relative homogeneity of spacial pore distribution. The upper micrograph is for a gold coated surface. (Material C)

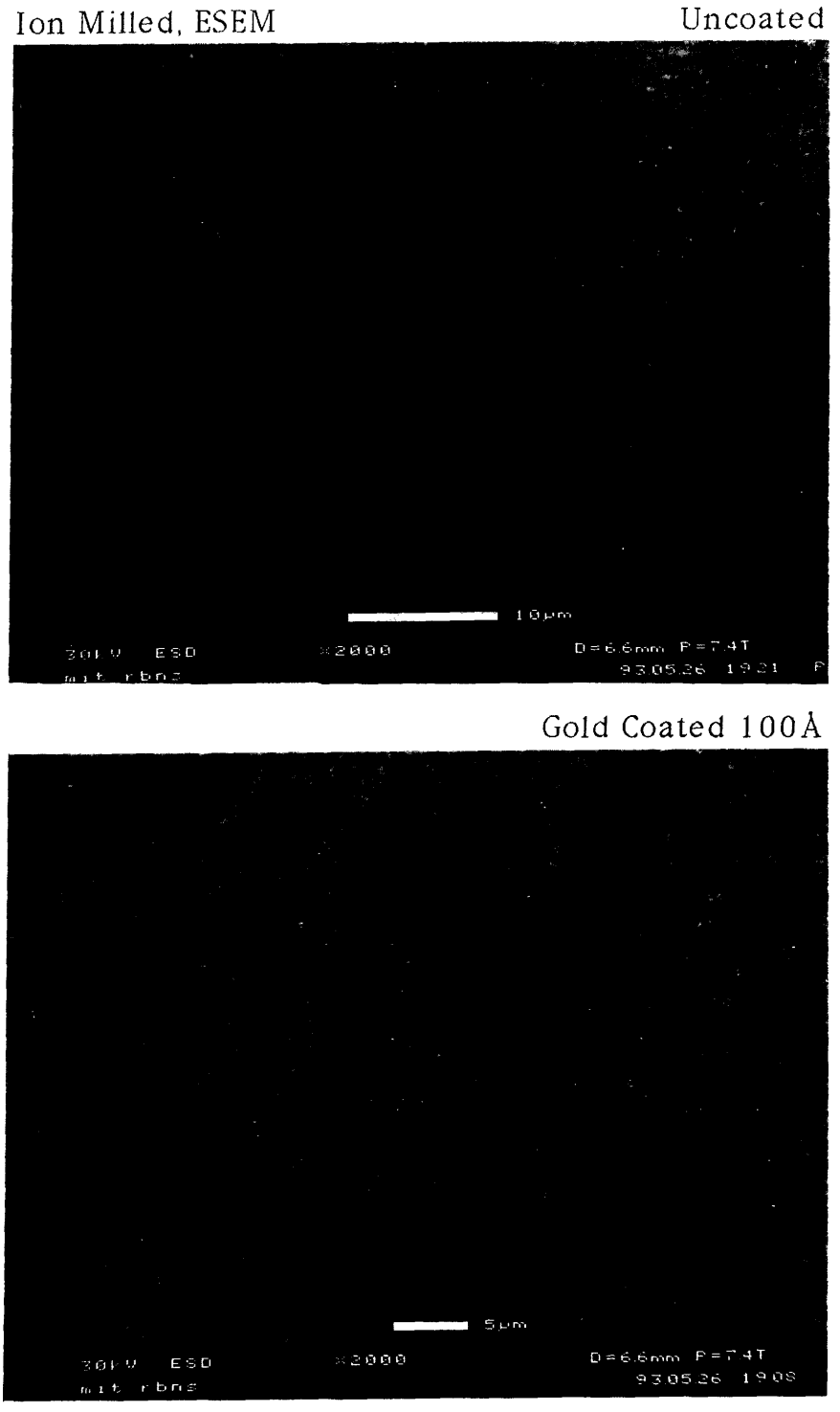

Figure 2-7: Material C in the Environmental SEM uncoated (above) and coated with approximately 20nm Au (below) showing the effect of the electron beam penetration for the uncoated surface.

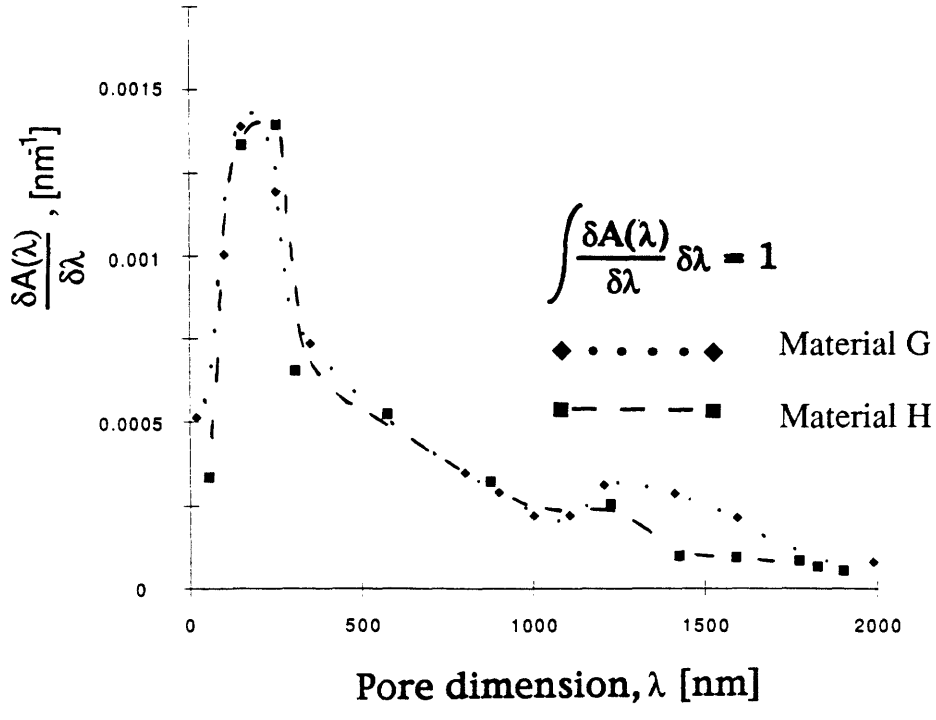

Figure 2-8: Pore area distributions of two similarly produced materials (G and H). Material G exhibits 7% volume fraction of pores between 1 and 2 micron dimension, as determined by the equal area ellipse major axis method.

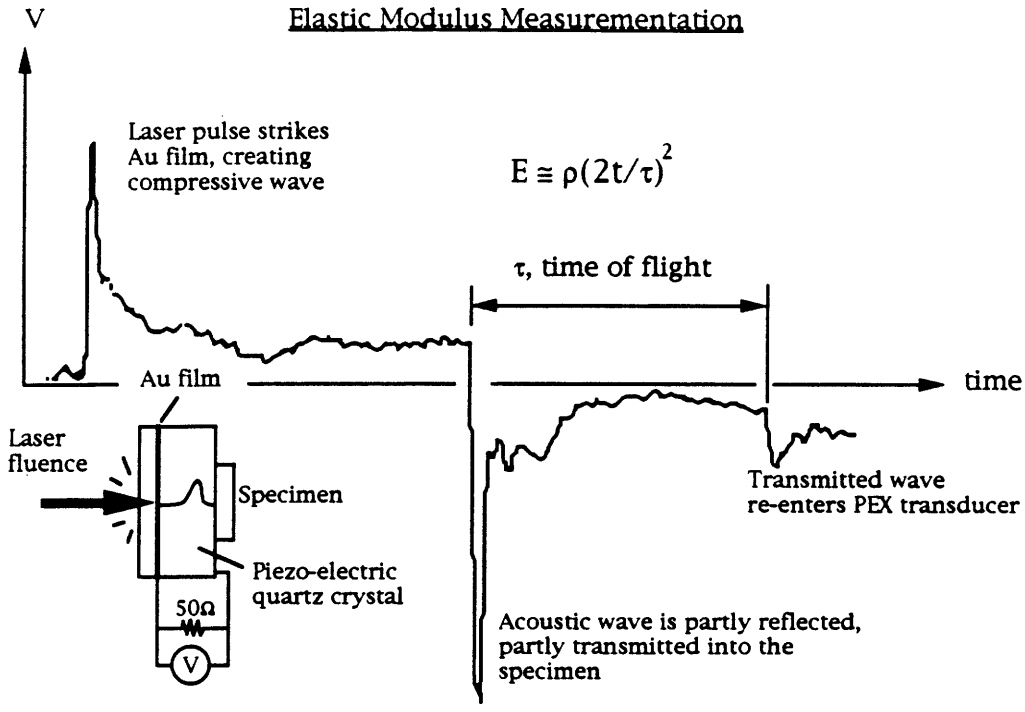

Figure 2-9: Typical piezoelectric transducer voltage, V(t), for elastic modulus measurement.

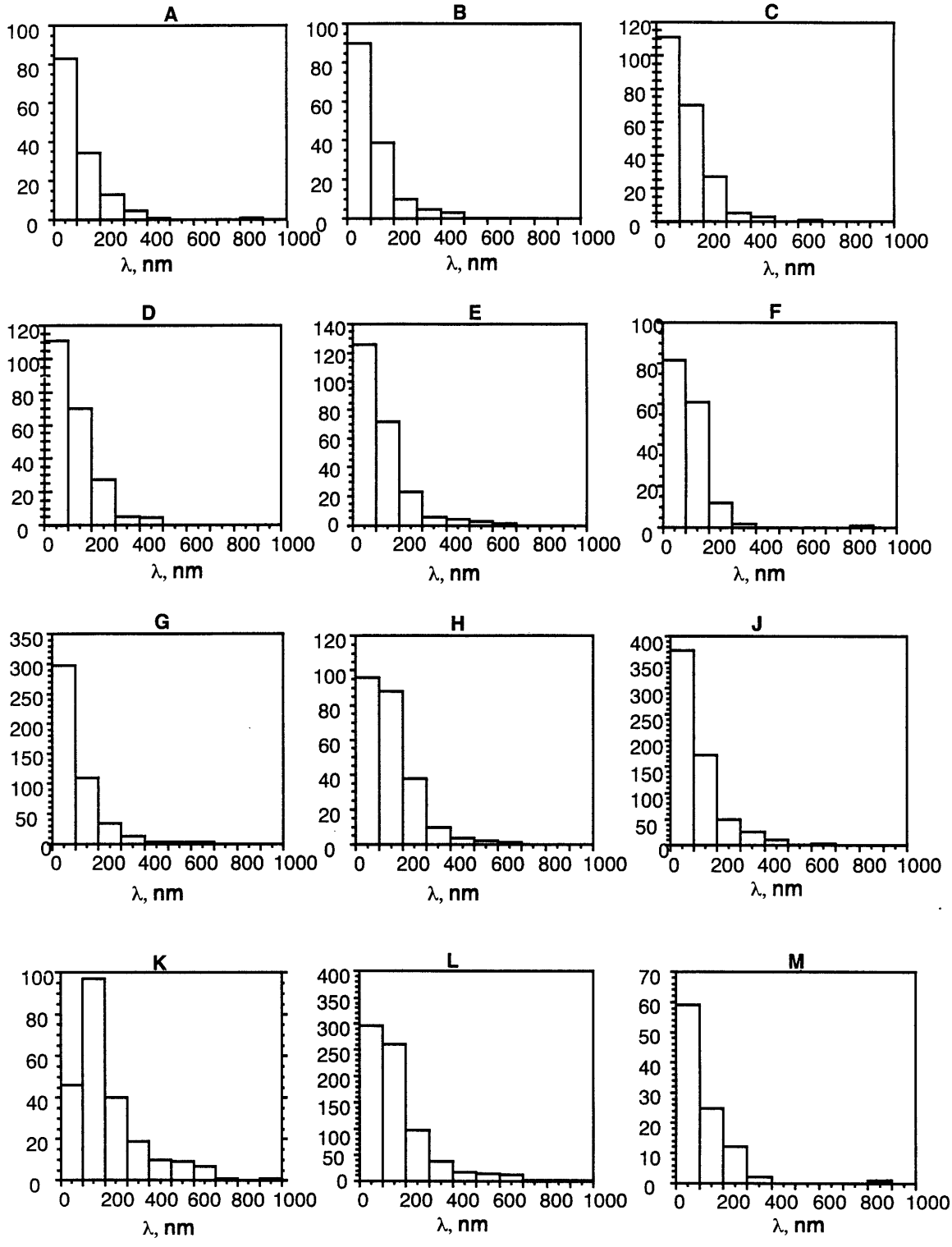

Figure 2-10: Pore size distributions obtained from digitized micrographs of real microstructures over the range of porosity from 17 to 31%. The pore dimension is obtained by fitting an equal area ellipse with maximum overlap.

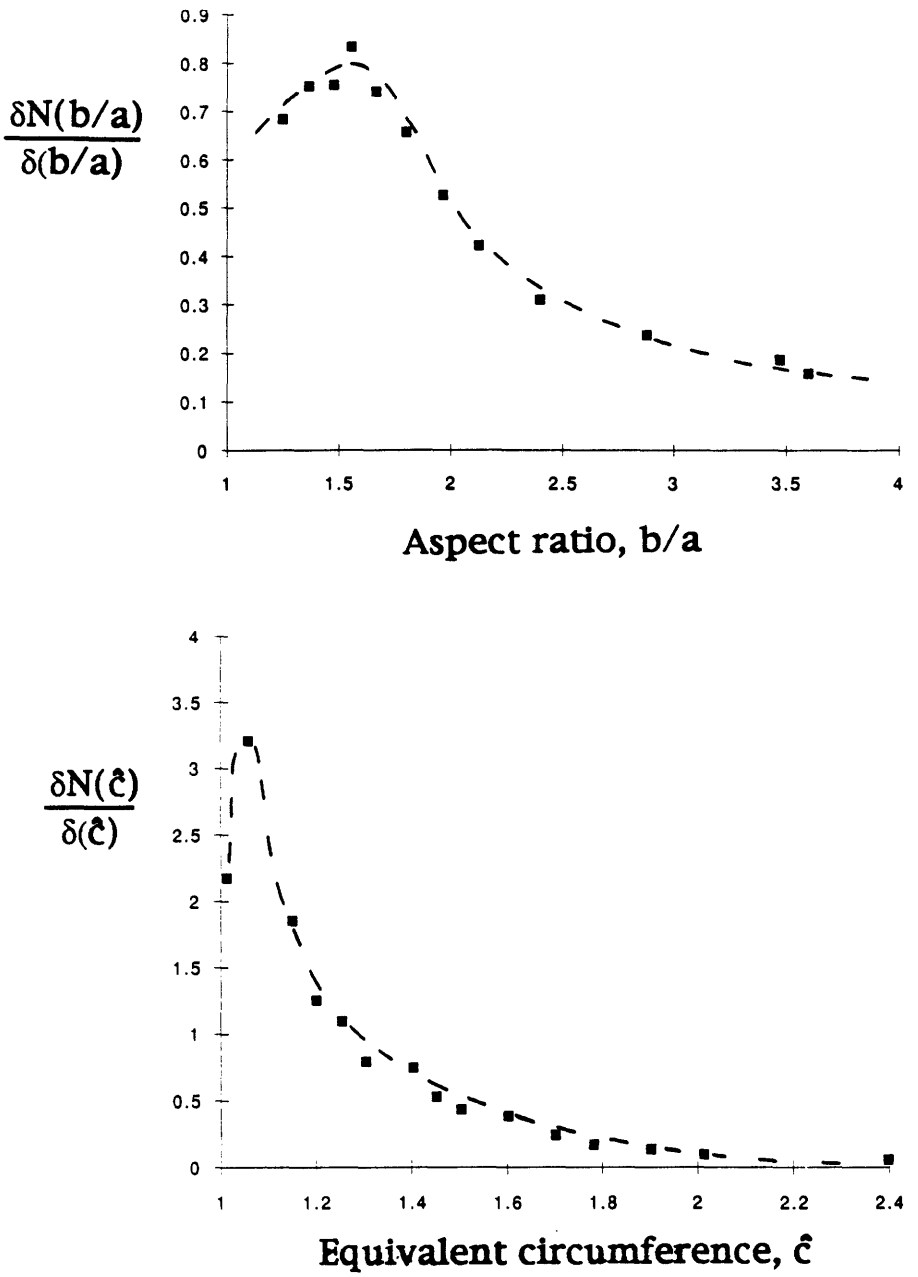

Figure 2-11: The typical distributions of pore equal area ellipse aspect ratio and pore circumference normalized by the equal area circle circumference. The equivalent ellipse is fitted such that the overlap of the pore is maximized. Circumference values are measured by computer from digital images with a resolution of 8.5nm.

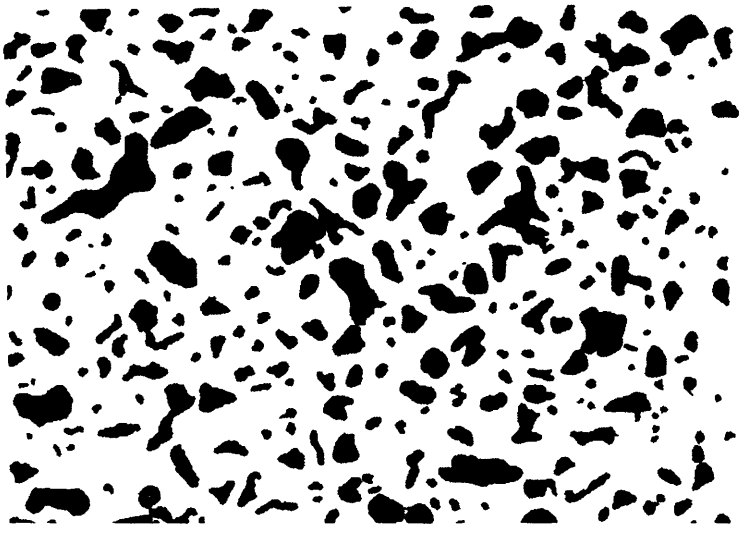

POROSITY = 24% HAND EDITED MICROGRAPH

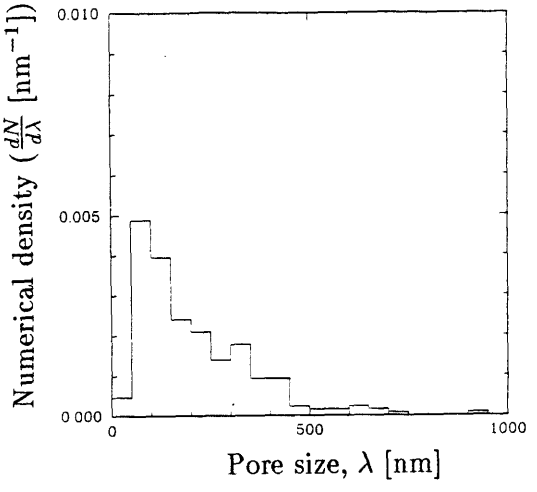

Figure 2-12: A microstructure of RBSN hand edited by observation of stereo pair micrographs, and the corresponding pore size distribution. (Material H)

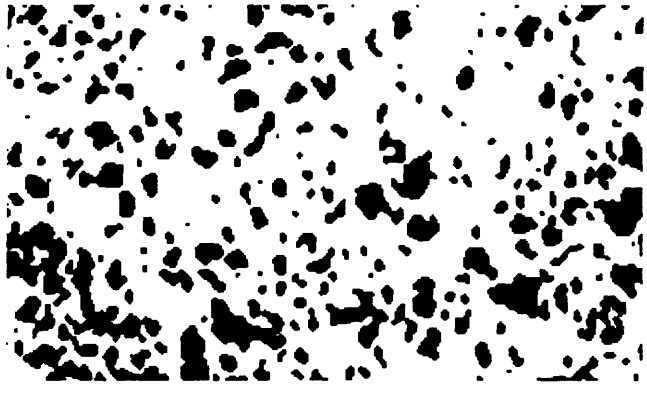

POROSITY = 24%

THRESHOLD = 128/255

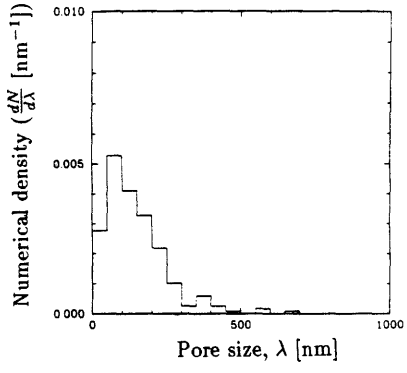

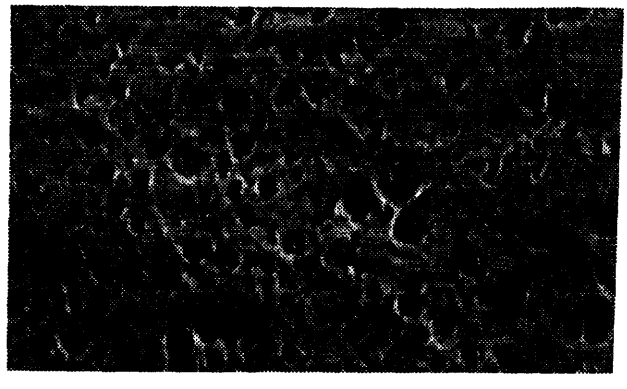

1 micron

DIGITIZED MICROGRAPH

Figure 2-13: Typical digitized micrograph of RBSN, and the pore size distributions for a choice of contrast threshold which produces an effective porosity which is equal to the true porosity. (Material H)

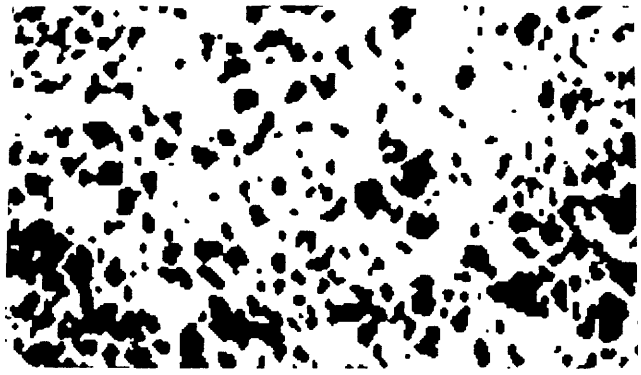

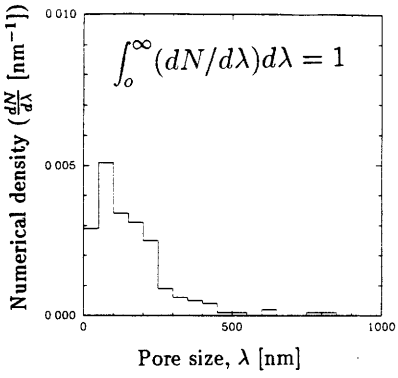

POROSITY = 29% THRESHOLD = 125/255

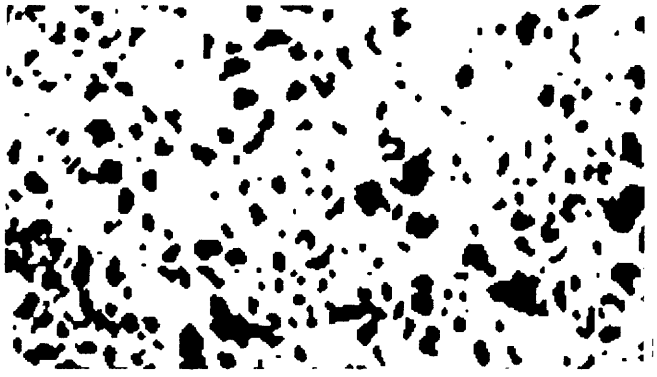

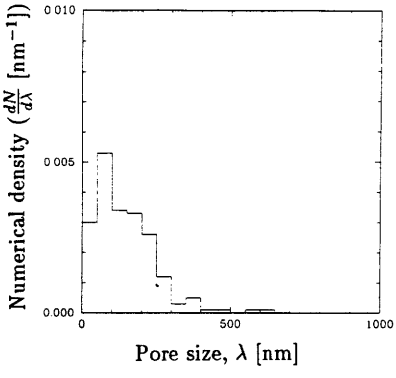

POROSITY = 21% THRESHOLD = 130/255

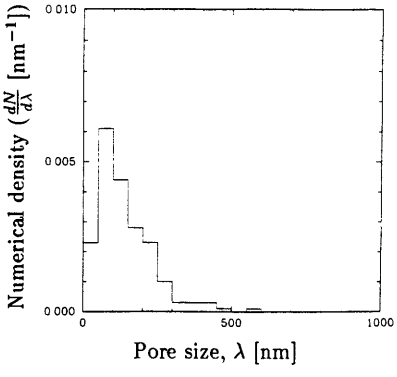

POROSITY = 15% THRESHOLD = 135/255

Figure 2-14: Pore size distributions of a digitized micrograph of a typical microstructure of reaction bonded silicon nitride as a function of contrast threshold. The choice of threshold determines the proportion of the total image which is classified as pore or solid. (Material H)

Material H

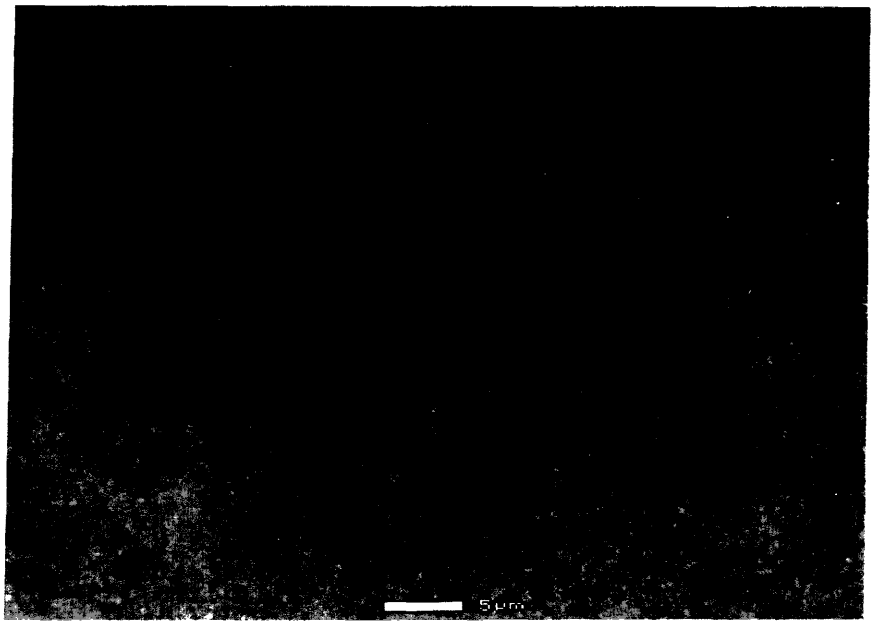

Material G

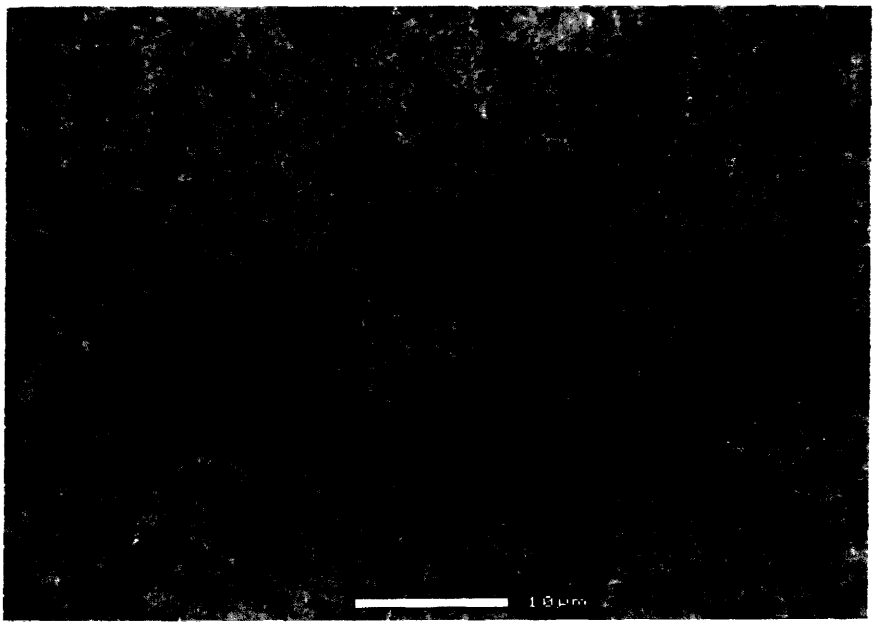

Figure 2-15: Uncoated Environmental SEM images showing the homogeneity of material H and the fluctuations in contrast in similarly processed material G associated with density fluctuations.

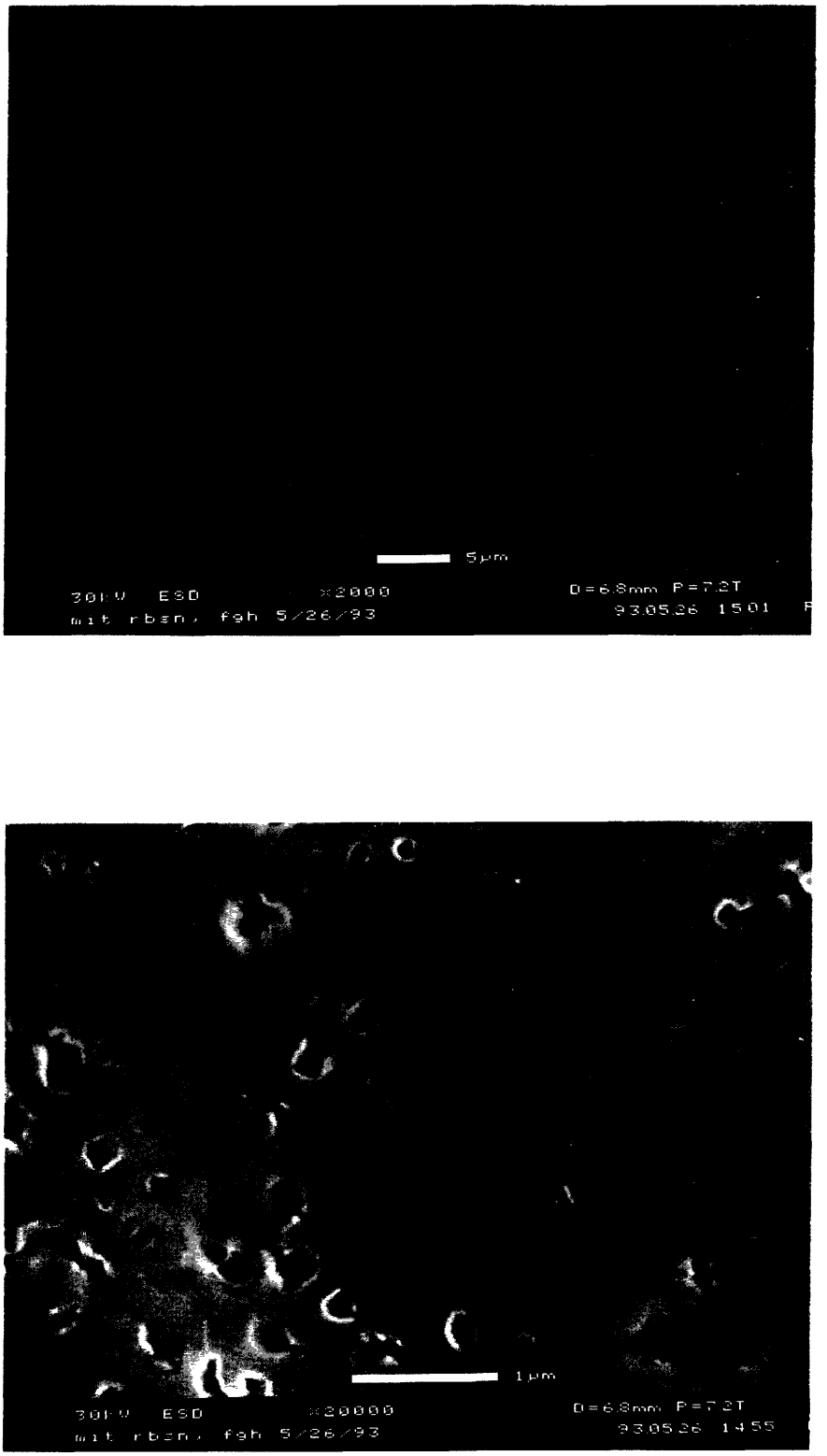

Figure 2-16: Micrographs of uncoated surfaces of materal B in the Environmental SEM.

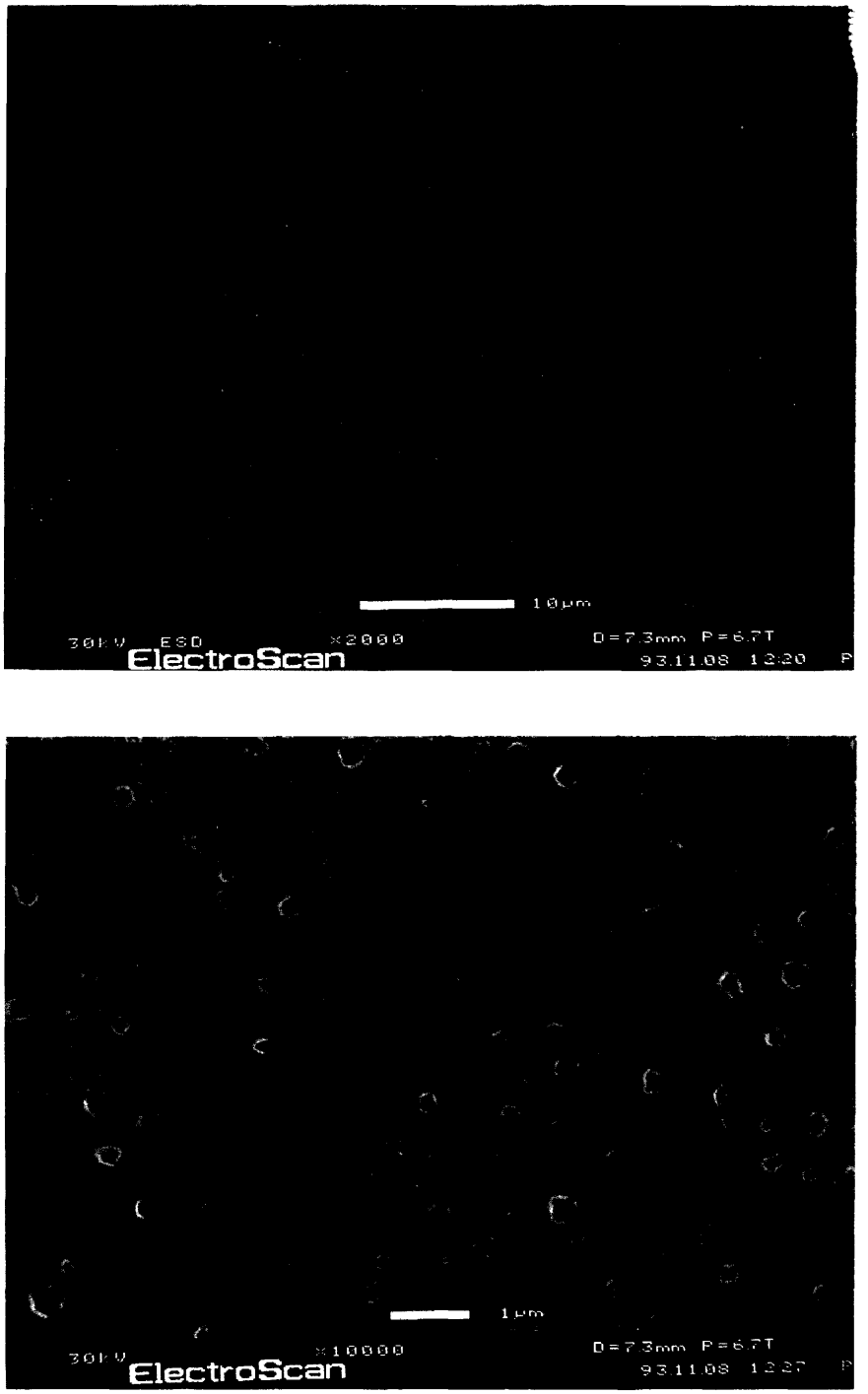

Figure 2-17: Micrographs of uncoated surfaces of materal J in the Environmental SEM.

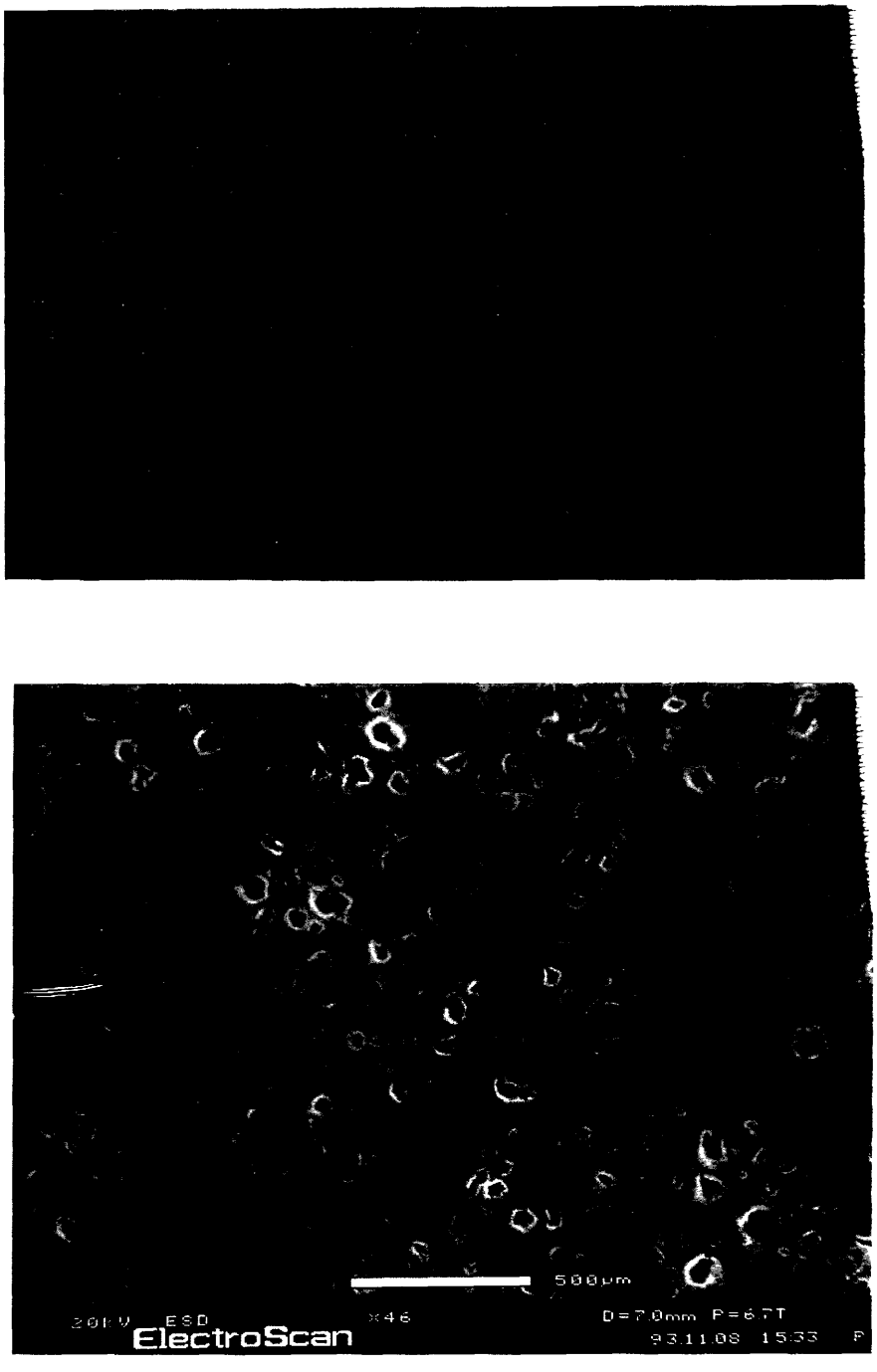

Figure 2-18: Micrographs of uncoated surfaces of materal K in the Environmental SEM.

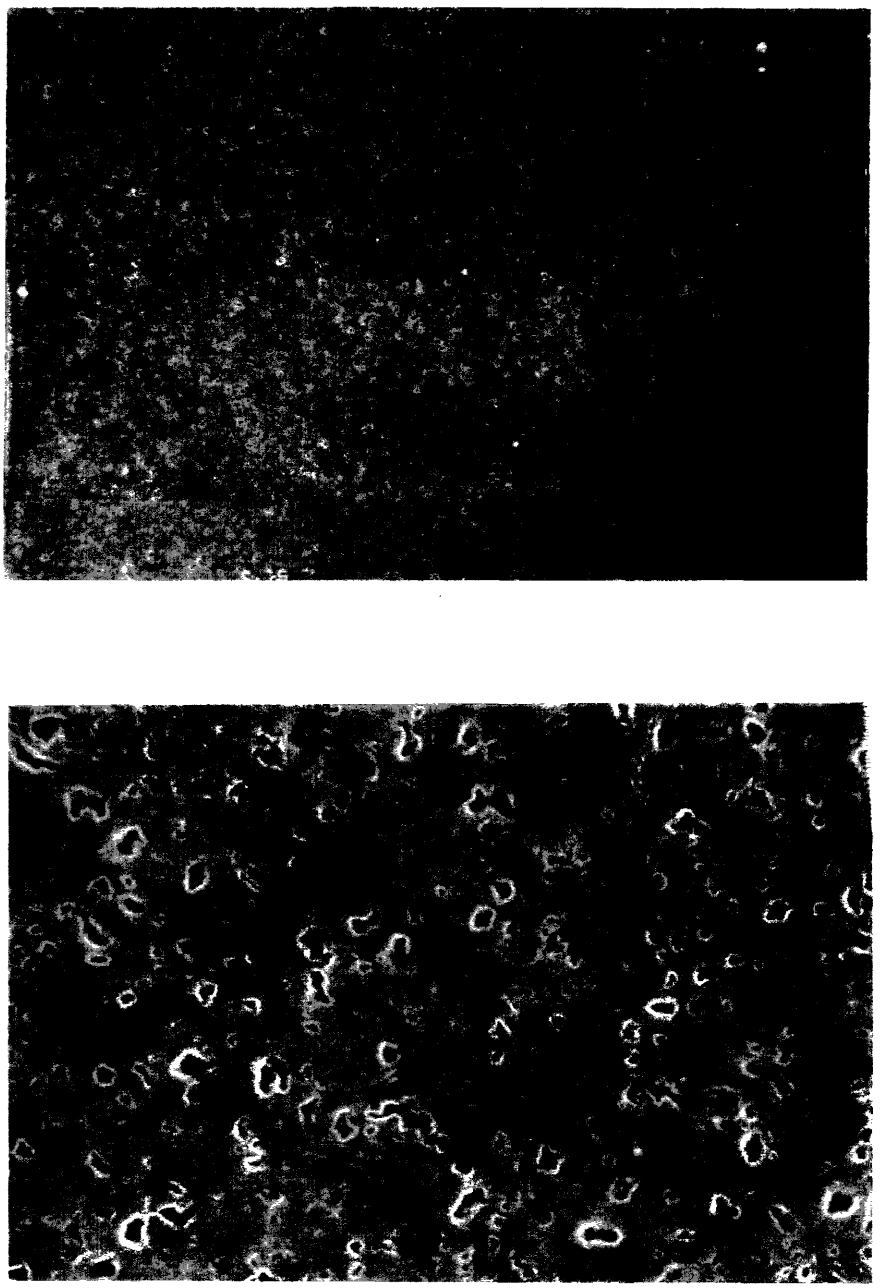

Figure 2-19: Micrographs of uncoated surfaces of materal L in the Environmental SEM.

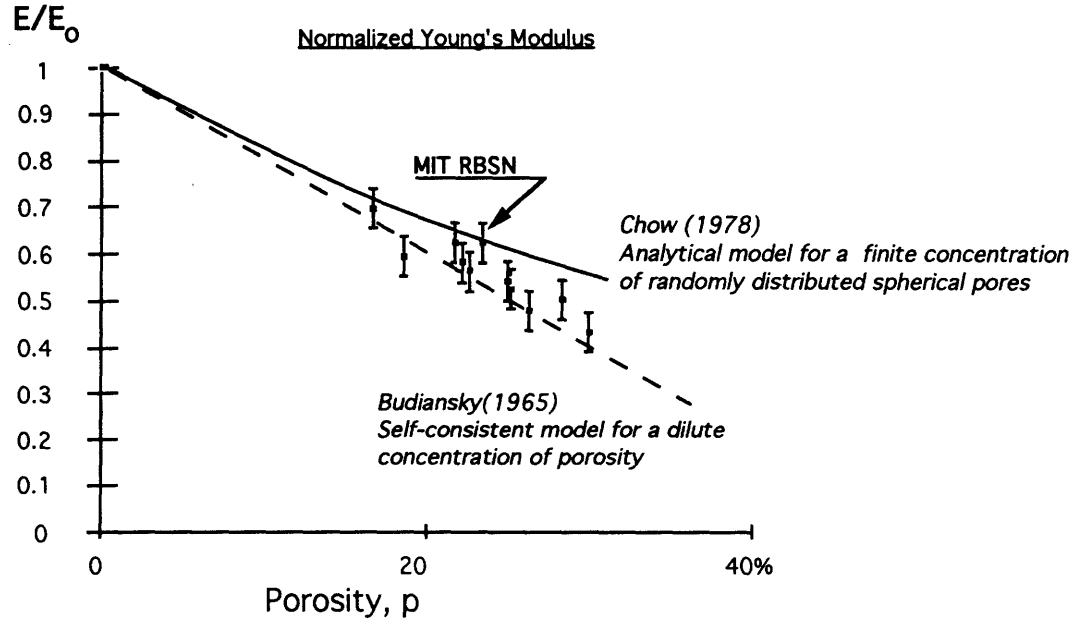

Figure 2-20: Normalized Young's Modulus for RBSN samples.

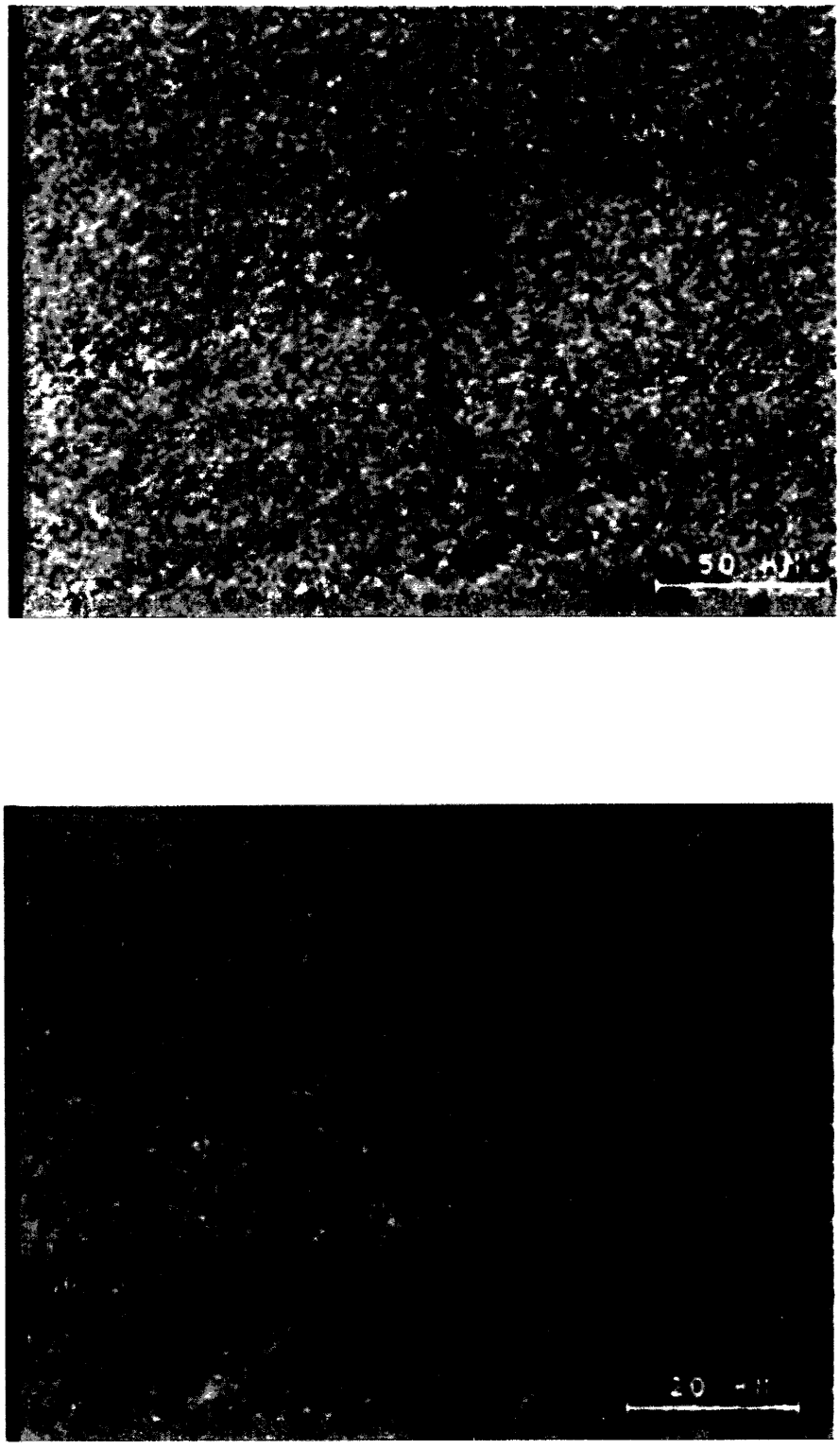

Figure 2-21: Scanning acoustic microscopy of a surface of RBSN indented by the Vickers microhardness stylus with a load of 10N.

Chapter 3

A Simulation of the Reaction Bonding Process

3.1 Introduction

In this chapter we develop a numerical model for the gas phase reaction that results in the porous RBSN for the principal purpose of generating non-arbitrary microstructures that are topologically similar to those of the real RBSN, that have been reported by Haggerty and co-workers [97,68,40]. In the following chapter, we explore the fracture resistance of these computer generated microstructures by means of a separate simulation of crack propagation through these porous microstructures to develop the microstructure-property connection.

With this premise, the primary use of the simulated reaction is the generation of realistic microstructures incorporating the major features of reaction bonding. In this manner we generate objective, systematic variation of microstructures. Ideally, we can then observe crack nucleation and propagation mechanisms and identify the processing parameters which control fracture toughness.

In the following discussion, we outline the details of the model, and demonstrate its ability to generate realistic microstructures, specifically in terms of the pore size and spacial distribution in addition to the placement of grain boundaries. Finally, some additional observations are reported for some topological reaction phenomena

such as those which control the formation of large pores in the final structure. In Chapter 2 we presented the microstructures of the actual RBSN. We will use these findings of the latter here for making some comparisons between the real and simulated microstructures.

3.2 Methodology

3.2.1 Background

Typically, probabalistic cellular automata methods developed for modeling microscopic physical processes have been used to study fluid dynamics[48,57], solid state diffusion[14] and critical points in phase transitions[6]. Recently, this technique has addressed the issues in the complex reaction/diffusion coupled problems associated with materials processing. The investigators Dab and Boon [21] have presented results for a more sophisticated microscopic process than the simple collisions in previous models, by introducing the existance of chemical reactions in the medium. The model of an autocatalytic reaction with the presence of diffusion displayed essential features in qualitative agreement with non-discrete reaction-diffusion systems as described by what is known about them from analytical solutions. The Potts model has been shown to yield realistic grain size distributions [108]. More recently, the treatment Srolovitz has demonstrated good agreement between experiment and three dimensional Monte Carlo simulated structures obtained by grain coarsening [2].

3.2.2 Reaction chemistry

In order to generate realistic porous microstructures of RBSN, it is important to include all the major features of consequence of the reaction bonding process in the simulation. The reaction begins with the formation of discrete Si_3N_4 nuclei which happens over an initial incubation period [97]. These nuclei grow at the expense of the evaporating silicon and form individual grains in the final microstructure. Under typical processing conditions[97], the chemical pathway for the formation of

silicon nitride is elemental silicon undergoing sublimation and a subsequent gas phase reaction with nitrogen:

$$3Si_g + 2N_{2,g} \rightarrow (Si_3N_4)_s \tag{3.1}$$

This process is essentially similar to a chemical vapor deposition process with product formation on previously formed silicon nitride. The free surface of silicon nitride serves as a reaction catalyst. Although the complete reaction may include intermediate reactions such as formation of silicon monoxide vapor which then acts as a silicon carrier, here those details are not considered but rather a single all-encompassing composite reaction is developed. The formation of a reaction product on previously existing silicon nitride gives rise to a growing product front which is in competition for space with the silicon particles in the process of receeding by evaporation. The balance between these two processes is one of the phenomena which most strongly affects the reaction rate and morphology of the unique reaction bonded porous microstructure.

Silicon transport by solid state diffusion has been suggested by some investigators[79] however this is kinetically unfavorable. Solid state diffusion is too slow to account for the observed 'fast' reaction rates[54,97] in the material studied here and described in Chapters 2 and 5. In addition, it has been pointed out that the silicon vapor pressure of 10^{-3} atmospheres at typical processing temperatures for most processing routes for RBSN, is more than adequate to sustain the observed nitridation rates[90].

The assumption of fast nitrogen vapor transport has been observed experimentally[97] for the MIT produced material. For 1 atmosphere N_2 and samples two millimeters thick, complete nitridation is observed at the center of the samples of average thickness in the millimeter range for temperatures from 1150 to 1350°C over typical reaction periods of 5 to 60 minutes [98]. Therefore in our simulation, a constant partial pressure of nitrogen is used, and the silicon vapor is the rate limiting medium, adjusting to new conditions instantaneously.

Popper and Ruddlesden[84] recognized that the exothermic nature of the reaction could cause melting of the unreacted silicon unless the heating rate was carefully

controlled. However, melting effects are not currently incorporated in the model, and isothermal conditions are assumed.

Lastly, acknowledging the possibility that silicon nitride grains exhibit anisotropic growth in some instances, we have allowed preferential growth directions in some cases. The degree of anisotropy is dependent upon which of two silicon nitride phases dominate, α or β, and the kinetics of formation. Of these two hexagonal crystal structures, the β phase has a layered structure of hexagonal basal planes, where the distorted α phase consists of a unit cell whose bottom half is the same as β but the top half is related to the bottom by a c-glide plane. While the precise control of phase content is currently a topic of debate, it has been observed that the α phase is favored for vapor phase reaction processes at lower temperatures, less than $1350^{o}C$[77], and for relatively pure silicon powders. Its morphology has been observed to range from equiaxed to whisker-like. The β phase has an elongated morphology, though not whisker-like, and is typically larger in size. It is prominent in materials processed with either impurities such as iron or at higher temperatures where liquids are prevalent.

3.2.3 Model Material Specimen Processing

The model material RBSN as described in Chapters 2 and 5 were produced from high purity Si powder synthesized from silane gas with a laser process, and the reaction kinetics and processing methods have been extensively studied[91,97,38]. Results show that the material can be fully reacted at uniquely low temperatures, and in relatively short times. In addition, the material exhibits superior fracture toughness on a per unit weight basis, and unequalled oxidation resistance[34]. Because the material is processed with high purity Si particles, and the process eliminates the need for densification additives, brittle glassy phases are eliminated, thus a high level of strength at operating temperatures is retained. It appears that the maximum relative density is approximately 85%, which provides the minimum required pathway for the nitrogen gas to reach the unreacted silicon.

The condition of high purity and contamination free processing is central to the

superior reaction kinetics. Conventional processing techniques employ a 1°C/min ramp to 1200°C followed by a 0.5°C/min ramp from 1200 to 1400°C and a 1 hour hold, often totaling more than 20 hours. The reduction to a 1 hour step at 1150°C (or 10 min at 1250°C) represents a major improvement in processing economy[97]. The use of a pre-nitriding nucleation step allows complete conversion in 1 hour at 1050°C.

3.2.4 Numerical technique

The modeling of the reaction has been performed in the spirit of the cellular automata approach, where the simulation volume is divided into cells, each of which is allowed to exist in one of few discrete states. The state of a given cell changes in steps, as determined by its current state and that of its nearest neighbors. However, unlike the classical cellular automata approach, where evolution of states is deterministic, here the cell in any given state has more than one possible transformation alternatives.

To choose between the several possible outcomes in the reaction, a random number generator was employed. Thus, the approach used here has features common to both cellular automata and Monte Carlo algorythms. However, deterministic cellular automata evolutions may be thought of as a limiting case of the present stochastic simulation, when probabilities of all but one outcome are set to zero. This is why we associate our present simulations with the cellular automata approach.

The reaction model that has been used is a 2-D cut out of a 3-D dense random packing of spheres in space as will be expanded on below in Section 3.2.5. The choice of resolution of the mesh was based on maintaining equiaxed particle shapes, therefore, the cell dimension was a small fraction of the initial silicon particle size. The total mesh dimension was limited only by computational resources. At maximum resolution, we have obtained fully reacted structures spanning 1000 by 1000 cells or approximately 130 partical diameters. A typical example of a reacting particle field is shown in figure 3-1. In order to expedite generation of larger numbers of structures, a mesh of an edge length of 64 cells was chosen for most simulations. This ensures the packing of enough silicon particles into the mesh (about 100) and provides an

acceptable representative volume element.

3.2.5 Motivation and limitations of the model

As already stated, the motivation for developing the present numerical model was to generate microstructures for subsequent fracture studies, rather than to develop a fully realistic study of the reaction kinetics. The limitations of the model, primarily its two dimensional nature and its fixed resolution, restrict our conclusions to indications of trends. However, it has been possible to obtain meaningful trends of fracture toughness that could be identified with specific processing parameters. In addition, it appears possible to obtain some insight into such complex phenomena as the spacial competition between the growing silicon nitride particles and the silicon particles receding by evaporation silicon, and the effects these processes have on the fracture toughness of the material.

In our model any internal stresses arising from such effects as sintering densification or volume changes arising from the reaction other than from the stoichiometry of the chemical process is not specifically considered. Incorporation of this effect, however, would have required a substantial expansion of the model to include simulataneous considerations of mechanical equilibrium and elastic strain energies. We counteract this ommision by assuming certain parameters governing the strength of interfaces in our fracture simulation [41].

3.3 The Model

3.3.1 Overall Outline

The following features of the model will be described operationally: the packing of the unreacted green body; the placement of initial silicon nitride nuclei which become single grains in the final microstructure; and finally the chemical conversion into reaction bonded silicon nitride.

3.3.2 Packing of Unreacted Silicon Particles

To avoid artificial clustering phenomena arising from the two dimensional nature of our model, the initial unreacted silicon particles are actually modelled as a three dimensional random close packed structure of uniform sized spheres. This approximation is well suited to the actual spherical Si particles used in the RBSN and for its qualitative similarity to the usual green body packings (i.e. the existance of expected naturally occuring packing defects and lack of long-range periodicity[33]) and for its similar packing density[1], (62%).

The particle coordinate data was generated by a molecular dynamics (MD) technique using periodic boundary conditions. Many methods can be utilized to generate dense random packings, but the MD technique is efficient and provides packings which have the spacial distribution of the random close packed structure (see figure 3-2).

This 3-D structure of dense random packed spheres was subsequently sectioned to obtain a two dimensional arrangement of circles of a well known size distribution. This information was then discretized on a hexagonal planar net.

Figure 3-3 shows a typical planar section through the 3-D initial dense random packing of spheres which was taken for the 2-D model. Figure 3-3 shows schematically how the 2-D plane arrangement of material in circular disc form and surrounding voids are discretized for the reaction model.

3.3.3 Nucleation of Silicon Nitride

Once the particle disc geometry is mapped on the 2-D mesh, the cell sites of the mesh that represent surface sites of Si particles are located (i.e. Si cells with at least one neighboring empty site). A given number of these surface sites were randomly chosen to be initial silicon nitride nuclei and were replaced by silicon nitride. The number of such nuclei was small (typically 100-1000 or 1-10 per particle), compared to typically 10,000 total cells (100x100 mesh).

[1] Dense random structures have the most efficient packing of uniform sized particles without long range periodicity.

In some instances, a given proportion of these were assigned to have preferential growth directions to simulate anisotropy of grain growth. Growth directions were chosen randomly from among three discrete directions corresponding to the mesh three-fold symmetry.

3.3.4 Conversion Reaction to Si_3N_4

Basic Components

Given the green structure of Si particles, the probabilities are computed for each of the following possible events at each individual surface cell site: (a) the evaporation and condensation of silicon; (b) the reaction and growth of silicon nitride; (c) grain coarsening and surface diffusion.

The condensation and evaporation of silicon vapor to and from free silicon surfaces.

For every site that represents Si, each nearest neighbor is checked for an empty cell. If one exists, the Si site is labeled as a surface Si site, and is a possible candidate for evaporation. The incremental probability for evaporation, δP_{evap}, was taken to be proportional to the increment in time, δt, chosen for all processes, i.e.

$$\delta P_{evap} = E \cdot \delta t, \tag{3.2}$$

where E is a kinetical rate constant discussed further below. Because the incremental probability for evaporation relates directly to the proportion of available candidates for transformation, δP_{evap} is equal to the rate of the process at the given time in the simulation, and thus both sides of the equation have units of rate. If evaporation is deemed to occur, the cell is transformed into an empty cell and the silicon vapor pressure is incremented.

Condensation is taken to be the reverse of evaporation for which an empty cell located next to a Si cell is a candidate for condensation, where the probability for the

condensation transformation is taken to be proportional to the silicon vapor pressure[2].

The conversion reaction and growth of Si_3N_4 silicon nitride from previously grown free Si_3N_4 surfaces.

In a similar manner as for the evaporation and condensation processes presented above, empty cells neighboring on silicon nitride are allowed the possibility of transformation to silicon nitride, extending the growth front. The incremental probability of growth of silicon nitride, $\delta P_{reaction}$, is taken to be proportional to the partial pressure of silicon vapor, p_{Si_v} (the rate limiting species), a rate constant R, and the time step, δt:

$$\delta P_{reaction} = R \cdot p_{\mathrm{Si}_v} \cdot \delta t \tag{3.3}$$

Once growth occurs, the vapor phase is reduced in a stoichiometrically appropriate way[3].

It is important to note that this generic growth law does not specify the mechanism of growth. Only that previously grown Si_3N_4 is allowed to continue to grow, and that the rate is proportional to the concentration of the critical vapor species, silicon, and the reaction constant R. It is assumed that N is present in abundance as an infinite reservoir, requiring no separate N balance.

Grain boundries and surface tension.

Surface tension and 'grain boundary tension' are incorporated into the model in order to give more realistic appearing structures. Although sintering processes are thought not to be very influential in the low temperature processing regime ($T < 1350^oC$), micrographs (both TEM and SEM) give the impression of smooth grain and pore surfaces. Therefore, surface tension and boundary tension parameters are introduced

[2]The amounts of silicon evaporation and condensation are implicitly a function of the amount of silicon free surface because each individual surface particle is given a chance to evaporate or adsorb silicon vapor

[3]see Appendix B

for the silicon nitride material. For grain boundary motion, the silicon nitride cells with neighboring cells of silicon nitride of another grain orientation are given a finite probability to transform to the other grain's orientation. In the case of the free surface, a surface cell is allowed the possibility of translating to a neighboring empty surface site that is adjacent to the same grain of silicon nitride. The specific details are presented in Appendix C.

Implementation of the Reaction Model

In practice, the simulation is initially prepared by sectioning of the 3-D particle packing and mapping onto the 2-D mesh followed by the placing of the silicon nitride nuclei. Once this is prepared, the global variables, time t, and silicon vapor pressure, p_{Si_v} are initialized to t = 0 and $p_{\mathrm{Si}_v} = 0$. After initialization, the time is incremented by δt. The choice of δt is made by computing probabilites for all processes and by scaling δt to the fastest process. In this manner, all processes are scaled such that the criterion is maintained of having the transformation of a particular cell be exclusively a function of the current state of its surrounding neighbors. With this choice of δt, for each cell all transformation probabilities are computed and certain events are chosen to take place based upon the use of a random number generator. In the cases of evaporation, condensation and reaction of Si_3N_4, the mass balance of Si is accounted for by appropriately incrementing and decrementing the parameter p_{Si_v}. As already stated, the transport of N is assumed to be easy in comparison to Si, so no mass balance is kept for this species. Also, isothermal conditions are assumed so no energy balance is undertaken.

3.4 Results

3.4.1 Overview of results

Many features of the reaction kinetics process are mirrored in these simulations. For example, the basic trends of the reaction extent with time and the pore to particle

size are in quantitative agreement with experiments as we will demonstrate below. Moreover, the effect of initial Si particle positions and final pore positions are also in qualitative agreement with experimental observations.

We utilize the fact that the simulations presented here have some connection with the real process, although with some noted assumptions, to report observations of the effects of the reaction process on microstructure. Throughout the discussion below, attention will be paid to microstructural features as they relate to the various reaction parameters, in particular grain and pore size and shape as well as the effect of packing defects on the final microstructure.

3.4.2 Comparison with experimental observations

The comparison of the pore size distribution for the simulated and actual microstructures reveals comparable average dimension and qualitative agreement between the size distributions (figure 3-4). The ratio of average grain size, D, to the initial Si particle size, d, in the simulated microstructures with nuclei density per Si particle, N, appropriate to experimentally observed values, is 0.45 compared to the expected ratio of 0.439 [4]. The experimentally determined grain and Si particle sizes were determined with a combination of electron microscopy and x-ray techniques [67]. In addition, the pore aspect ratio and circumference normalized with equal are circle are shown to match well between real and simulated microstructures in figure 3-5.

Additional agreement between the model and actual reaction kinetic behavior can be found in the time dependence of the extent of the reaction. The simulated extent of the reaction follows the Johnson-Mehl-Avrami form:

$$X = 1 - \exp\left(\alpha N t^n\right) \tag{3.4}$$

where X is the amount transformed, N is the constant density of nuclei, α includes the growth rate constant and geometric factors, t is time, and n is the time exponent, established here to be 1.5 (see figure 3-6). Figure 3-7 shows this data in comparision

[4] see Appendix D

with thermogravometric data by Sheldon[97]. One key difference in the simulation is in the nucleation regime of varying waiting times, followed by the sigmoidal trend of the JMA model. The mechanisms for nucleation have been discussed by Sheldon and Haggerty[98]. In a possible further refinement of the model such waiting times representing nucleation barriers could be readily incorporated. Here this was not of interest. The fact that this simple model follows this form and produces realistic microstructures reinforces the notion that the model incorporates key features of the reaction bonding process - albeit without a realistic nucleation barrier.

In the following sections the trends of pertinent microstructural features obtained by the simulation are presented with dimensionless ratios of the reaction parameters, followed by a discussion of the mechanisms which appear to control the formation of large pores in the final microstructure.

3.4.3 Reaction of Si_3N_4 to Evaporation of Si Rates

The competition between the reaction rate of Si and N and the silicon evaporation rate on active surfaces is the most relevent consideration in the topological competition of growing silicon nitride and the receding, evaporating silicon particles. A large ratio of reaction rate constant, R, to evaporation constant, E, subsequently referred to R/E, indicates immediate reaction of silicon nitride and a high degree of impedence on the kinetics from purely geometrical impingement of the silicon nitride on the more slowly receding silicon.

For this reason of increased impingement of reaction product on the Si particles at high reaction rates, there is a marked correlation between the positions of the initial silicon particles and final pores of sizes comparable to the initial particle size. This is illustrated in figure 3-8 for two extreme R/E ratios of 0.3 and 300. The above replacement of particles with pores effect is evident in the case of R/E = 300.

Large pores in the initial packing are observed to be the locations of large final pores for both high and low reaction rates. The packing of the initial particles in figure 3-8, unlike in the other simulations, were performed in two dimensions instead of in three dimensions. This is done to illustrate the conglomerating effects of packing

equal diameter circles in 2D, and the associated larger packing defects which arise. However, the high reaction rate microstructure to some extent has 'healed' the largest pores associated with the large packing defects. This is because the Si_3N_4 growth has been stifled by its impingement with neighboring Si particles everywhere but where the growth front had ample space to grow, i.e. the large packing defects. Thus, conditions with large R/E provide for high growth rates for those nuclei which are growing unimpeded in the space of the large void. This effect is shown clearly in the shrinking of the large pore in the upper right quadrant of figure 3-8 and qualitatively in 3-9, and 3-10.

Finally, the amount of trapped silicon is increased for high R/E ratio conditions due to increased impingement of Si_3N_4 and the evaporating Si also due to the reduced silicon surface available for evaporation, as in the case of figure 3-8 for R/E = 300. Note that the unreacted silicon is located in the most densely packed region of the initial particle packing, where impingement is expected to be the greatest. Conversely, a low value of R/E ratio implies that ample silicon vapor is created and impingement is reduced. Both of these effects enhance the reaction rate. Figure 3-11 shows the separate process evolution plots for R/E of 0.3 and 300. Is it clear that a decrease in the R/E ratio by 1000, which spans the transition from impinging to non-impinging reactant/product fronts, results in radical differences. For the case of R/E = 0.3, the copious production of Si vapor, and the temporary high porosity state, are results of the entire process being reaction limited. For the case of R/E = 300 where Si evaporation is followed by immediate consumption by the silicon vapor starved reaction, the time for complete reaction is completed in 1/4 of the time for R/E = 0.3.

3.4.4 Evaporation to Condensation rates

A high evaporation to condensation rate ratio produces higher vapor pressures and a proportionately higher reaction rate. This effect is quite strong as seen in figure 3-12. For a 100 fold increase in the evaporation/reaction parameter, with all other parameters held constant, the time for reaction completion is smaller by a factor of three

hundred. The amplification of this effect appears to be due to reduced impingement of growing silicon nitride interfaces with the silicon particles. Impingement can be reduced if the silicon reactant can be effectively 'stored' in the mobile vapor phase. Notice the unreacted silicon in figure 3-12 implying increased impingement for a low evaporation rate.

3.4.5 Density of Nuclei on Particles

The number of initial reactive nuclei on particles, N, influences the reaction rate, the amount of unreacted silicon and the size scale and homogeneity of the final microstructure. At the initial stages of the reaction, a large number of nuclei per particle, N, will increase the reaction rate due to the larger amount of reaction sites. However, once a comparable amount of Si_3N_4 is generated, the growth rates are equivalent. This effect is shown in figure 3-13 for two different cases of the initial number of Si_3N_4 nuclei per particle for the same R/E and E/C ratios of 30 and 1, respectively. Extremely high nuclei density for which the silicon evaporation is blocked, stops the reaction prematurely.

For the case of low nuclei density, N, there is an increased incidence of impingement of the growing Si_3N_4 interfaces, because the fewer nuclei grow locally in a quite unrestrained manner with the receding silicon, while the evaporation of silicon remains homogeneous throughout. This causes geometrically restricted growth and additional entrapped silicon.

If the nuclei density, N, is low enough, fewer than 10 per particle in our observations, and the nuclei are distributed randomly, there is a statistically relevent probability for forming green structure regions with zero nuclei, resulting in large voids in the final reacted structure. Such a case is shown in figure 3-14 with large pores with tortuous borders. Conversely, a large nuclei density, N, reduces this probability and distributes the reaction product more uniformly. Note that the number of grains or nuclei per particle in real microstructures is observed to be approximately 7 in 2-D cross section, which is close to the critical density for formation of large scale voids.

Finally, with fewer nuclei, the final average grain size is larger, because each nucleus at the initial stage represents a grain in the final stage, with the total amount of reacted material divided among those fewer grains. Quantitatively, the pore size scales with grain size, which becomes evident by the average grain to pore size ratio which remains constant (roughly at a level of 2) over a range of nuclei density, N, from 1.0 to 10.0 nuclei/particle.

3.4.6 Packing Defects

Shapes of larger pores are observed to be related to three types of defects in the unreacted particle packing. These defects can be: 1) regions of high density of packing, where there is highly restricted growth (see figure 3-15), 2) large scale pores, on the order of multiple particle diameters, or 3) low density of nuclei which is discussed above. All three types of defects have been observed in the simulations to produce large pores in the final microstructure. The first and third cases have been observed to coexist, i.e. locally high packing density regions with low nuclei density, due to the reduced free surface area per unit volume where particles are in contact.

There is reason to believe that the large scale packing defects in the green structure such as cases 1 and 2 above exist in real structures. Large samples of uniform size powders are likely to be aggregates of dense and highly ordered crystalline domains, with a lower density of randomly packed particles in between[85,4]. A key difference between the ideal random close packing procedure and the real pressed green compacts is that these experience interparticle hydrostatic and shear stresses and therefore possible localized densification.

In addition to these high density regions, there exist naturally occuring interstitial voids in ideal random closed packed structures. According to the analysis by Frost [33], the volume per cent of polyhedral voids decreases rapidly with the number of faces. At an average neighbor distance of 1.3 particle diameters in a uniform size packing of spheres, the volume fraction of 20 sided polyhedra is $2-4\%$, however, $20-25\%$ of the volume is represented by larger shapes. These large voids cannot contain a unit sphere, so they are elongated regions where the packing is less dense.

3.5 Discussion

The model presented here primarily provides an objective means for providing arguably realistic appearing microstructures of porous reaction bonded silicon nitride. The fact that the grain and pore sizes and shapes appear to match those of real microstructures and that the simulation mirrors other features of the reaction process places an arguably sufficient degree of reliabilty on this technique. Moreover, the physical basis of the model implies that these microstructures can be altered in an objective manner by varying parameters which are identifiable with physical quantities. In addition, it can be noted that, it is possible to obtain some insight into such complex phenomena as the spacial competition between the growing silicon nitride and the receding, evaporating silicon. The observed reaction mechanisms depend not only on elementary reaction rates, but on these structural effects.

The most prominant parameters in the model which govern the microstructural homogeneity, pore and grain shape and size are the reaction to evaporation ratio (R/E), the evaporation to condensation ratio (E/C), and the initial silicon nitride nuclei density. All of these parameters directly affect the degree of product/reactant impingement, the time for reaction completion and the homogeneity of the microstructure. Specifically, for the cases of low nuclei density, high reaction to evaporation and low evaporation to condensation parameters, product impingement is found to occur. In this regime, the following effects are observed: reduced overall reaction rates, a high correlation between initial Si particle positions and final pores positions, and a tendency for faster product growth in regions of lower packing density, i.e. packing defect 'healing'.

Several severe assumptions limit this method of modelling complex reaction processes to the creation of schematic processing maps. Foremost is a lack of specific functional forms for reation rates. We consequently tailored the analysis in terms of non-dimensional ratios of specific reaction constants and limited the results to trends. Also, the limit of resolution of the mesh and the two dimensional nature place some degree of artificial constraints on the simulated processes. The resolution of the mesh

is less problematic if the continuum processes can be thought of occuring smoothly during the discrete time increments and if the typical microstructural feature is sufficiently larger than the mesh resolution. The two dimensional nature of the simulation has been compensated for partly by using a 2D section of a true 3D packing of particles and by appropriately adjusting the Si_3N_4 nuclei density to conserve the grain to Si particle size[5]. Although the microstructure is certain to evolve in all three dimensions, we have compensated for the lack of three dimensionality in an effective manner in the simulation of crack propagation through the microstructure.

Other less severe approximations of not considering the mechanical equilibrium of stresses generated during the reaction and gradients of the various material species have already been discussed. The only situations which are too complex to simulate are the isolation of large regions to either Si vapor or nitrogen gas reactants. The approximation of small Si vapor gradients is valid when the evaporation if the Si particles occurs homogeneously throughout the reaction. However, if structurally, a reaction product (or unreacted Si) barrier forms around a volume larger than one particle (the simulation can account for this case) the reaction within will naturally be choked off. Because in the typical reaction case, nearly complete nitridation is reached [98], the likelihood of the occurance of many reactant starved regions is minimal.

With these observations and the ability to generate unique microstructures which would be difficult if not impossible to generate precisely in the laboratory, we can then proceed to sample the fracture properties of these microstructures. Not only can we then obtain trends of fracture toughness with processing variables, but we can bring a mechanistic understanding of the reasons for the trends to the material design problem and introduce preconceived microstructural design criteria to the subsequent material processing iteration.

[5]See Appendix D.

3.6 Conclusions

The kinetics model presented here captures many of the salient features of the reaction bonding process in terms of considerations for determining fracture toughness. Primarily, the generated microstructures resemble actual reaction bonded silicon nitride microstructures, in terms of the grain and pore to particle size ratio. The observed microstructural evolution mechanisms depend not only on elementary reaction rates, but on such complex spacial, structural phenomena such as the competition between the growing silicon nitride and the receding, evaporating silicon, which are summarized here.

- Key dimensionless reaction variables control the competition between the growth of the product and the receding reactant, specifically the reaction to evaporation ratio, the evaporation to condensation ratio, and the ratio of Si_3N_4 nuclei to initial silicon particles.

- The final pore positions are related to the particle positions in the unreacted green structure when the product growth is inhibited due to impingment of growing Si_3N_4 with the silicon reactant.

- Three types of packing defects may give rise to large pores in the final structure:

    1. Packing flaws on the scale of multiple particle dimensions will tend to remain large pores in the final microstructure. This effect can be reduced, and defects can be 'healed' to some extent, if the reaction takes place in a regime where reaction rate limit is related to spacial competition of the reactant and product species and not of a chemical kinetics nature.
    2. Densely packed regions, which are known to exist in real structures, retard growth at the early stages due to strong impingement of the reaction product with the silicon reactant particles.
    3. Regions of low nuclei density may form statistically if the average nuclei density is low enough. Interstitial regions which have no nuclei associated with them will be shielded from the growing reaction product.

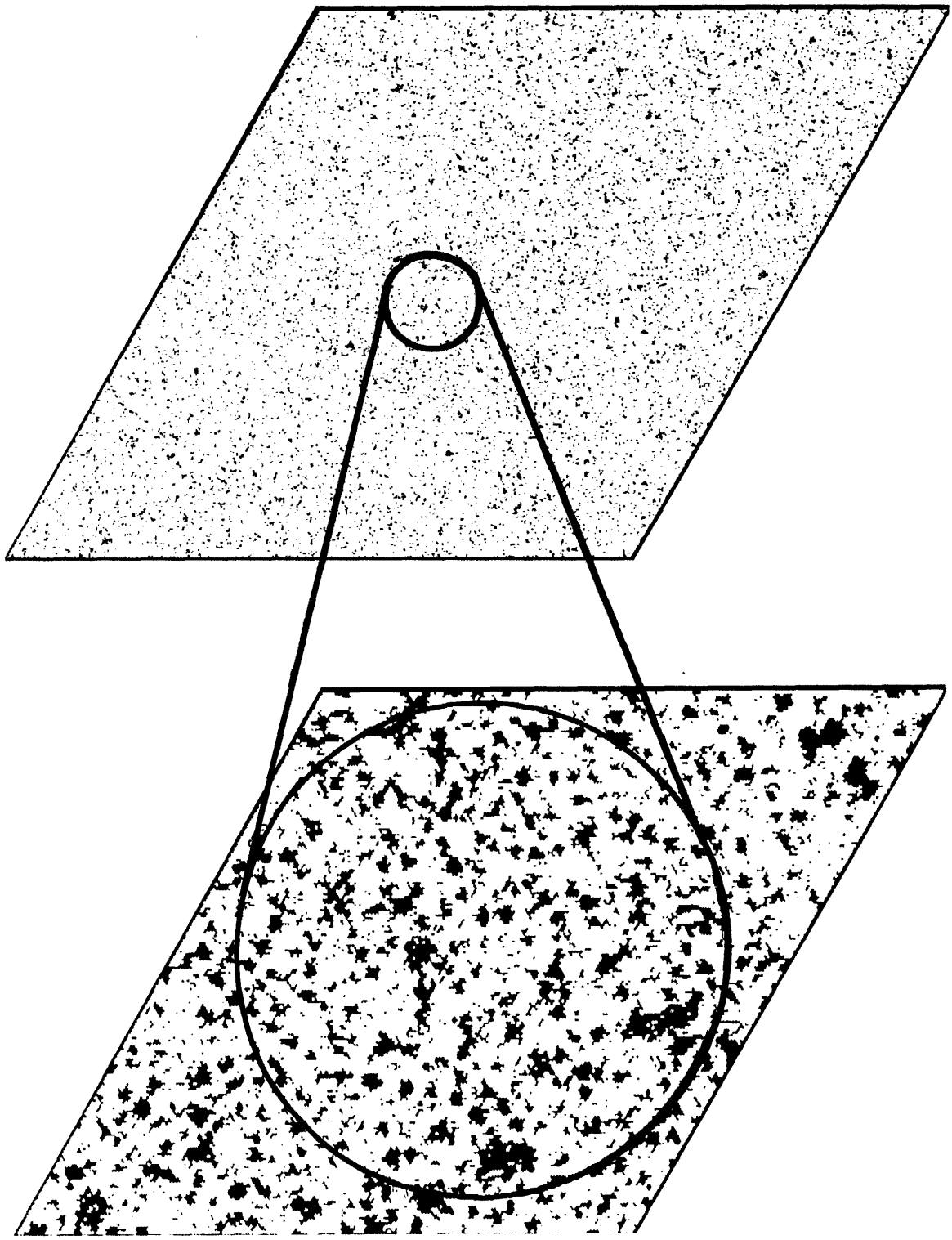

Figure 3-1: Large simulated structure. E/C = 1 , R/E = 300 , N = 1.1

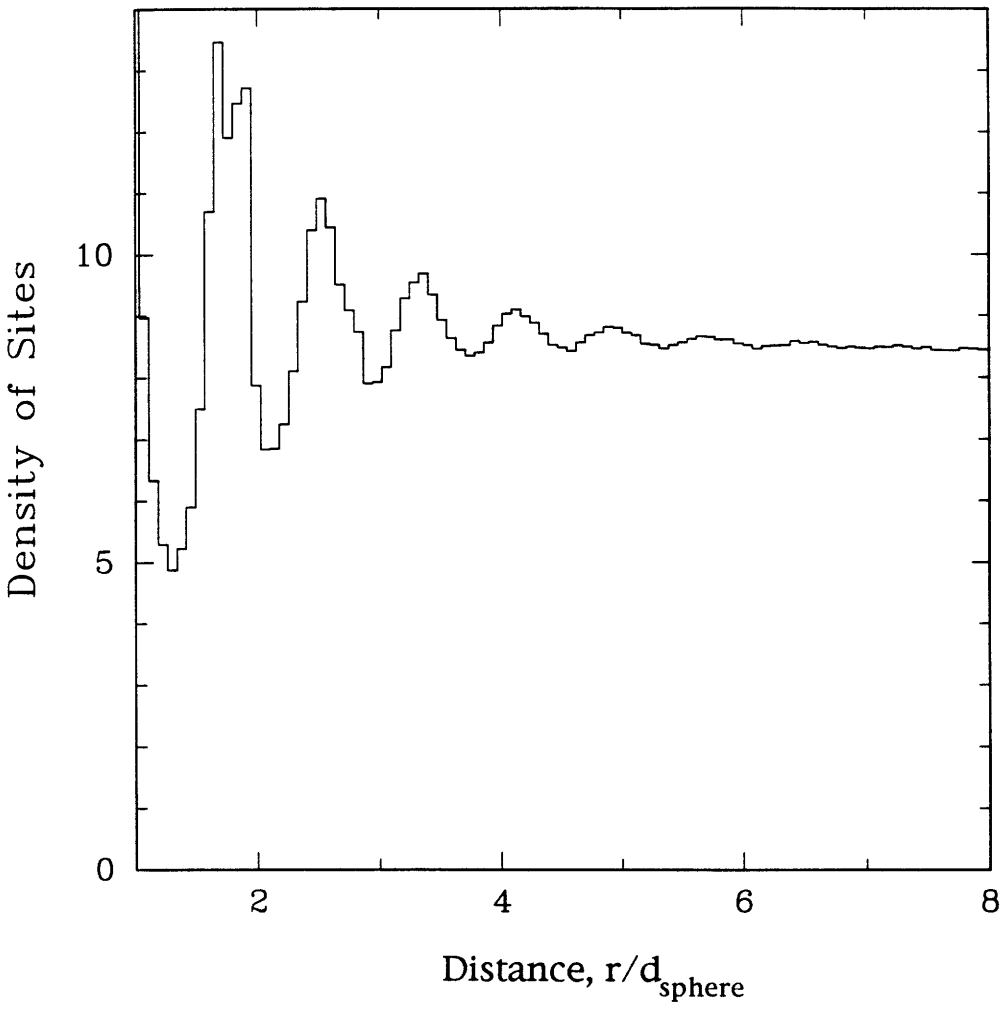

Figure 3-2: Radial distribution function of coordinates from the molecular dynamic simulations from Finney (1970) for 8000 spheres indicating the lack of crystallinity, and the characteristic distribution of dense random packings.

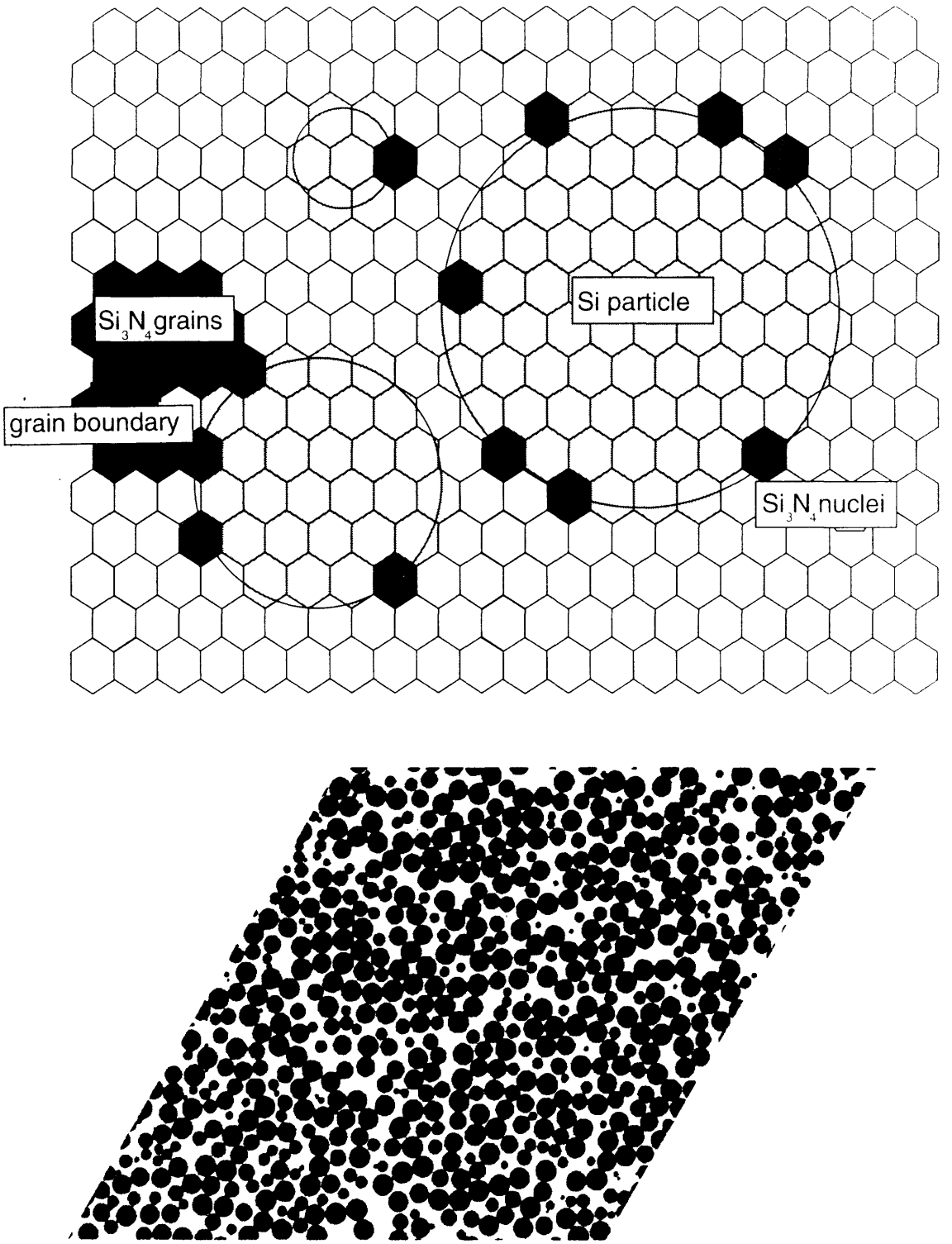

Figure 3-3: Schematic of the discretization procedure and a 2D section of a 3D random close packed structure with 8000 particles

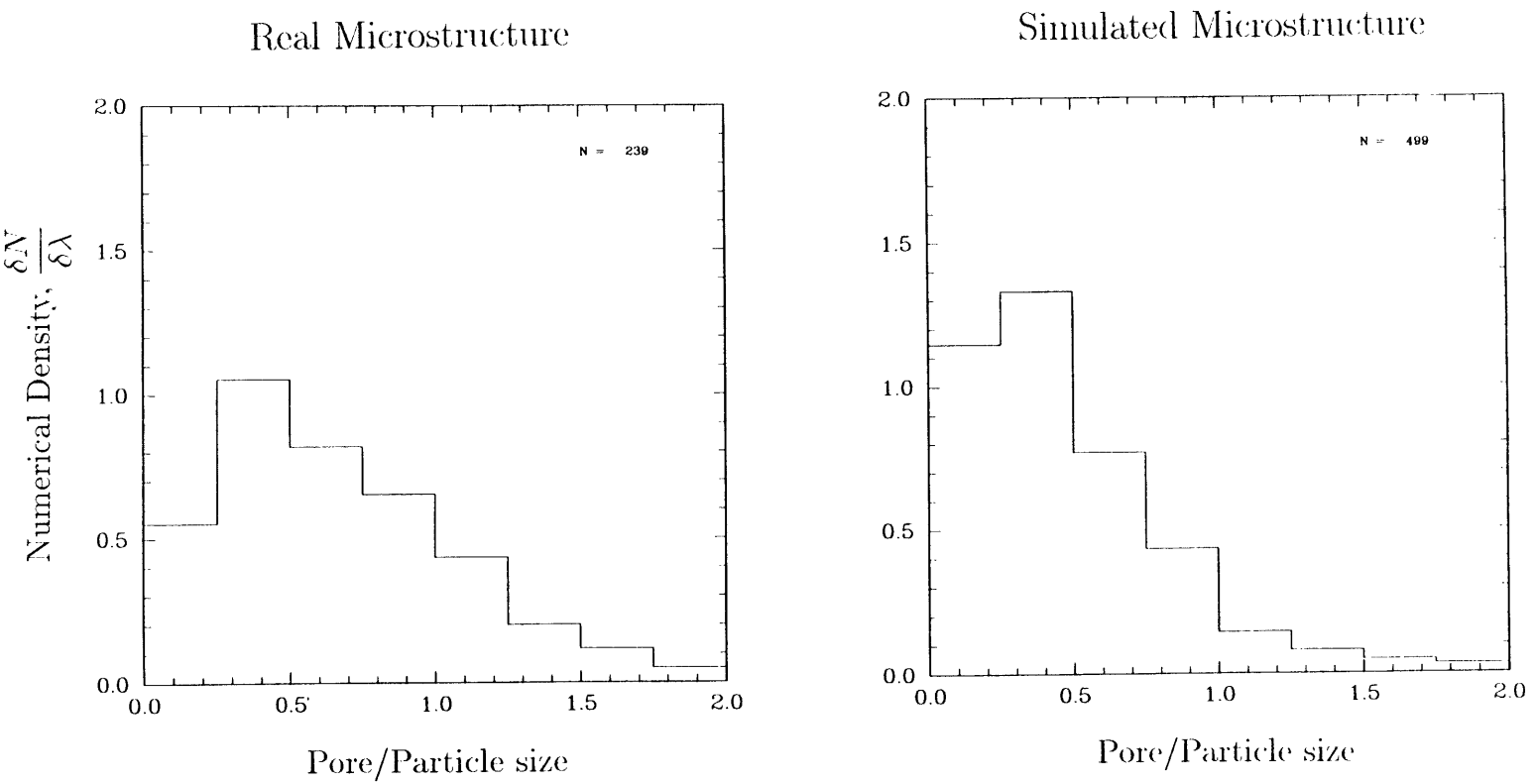

Figure 3-4: Pore size distributions for real and simulated microstructures. The simulated structure had reaction parameters as follows, R/E = 0.3, E/C = 1, N = 7.6

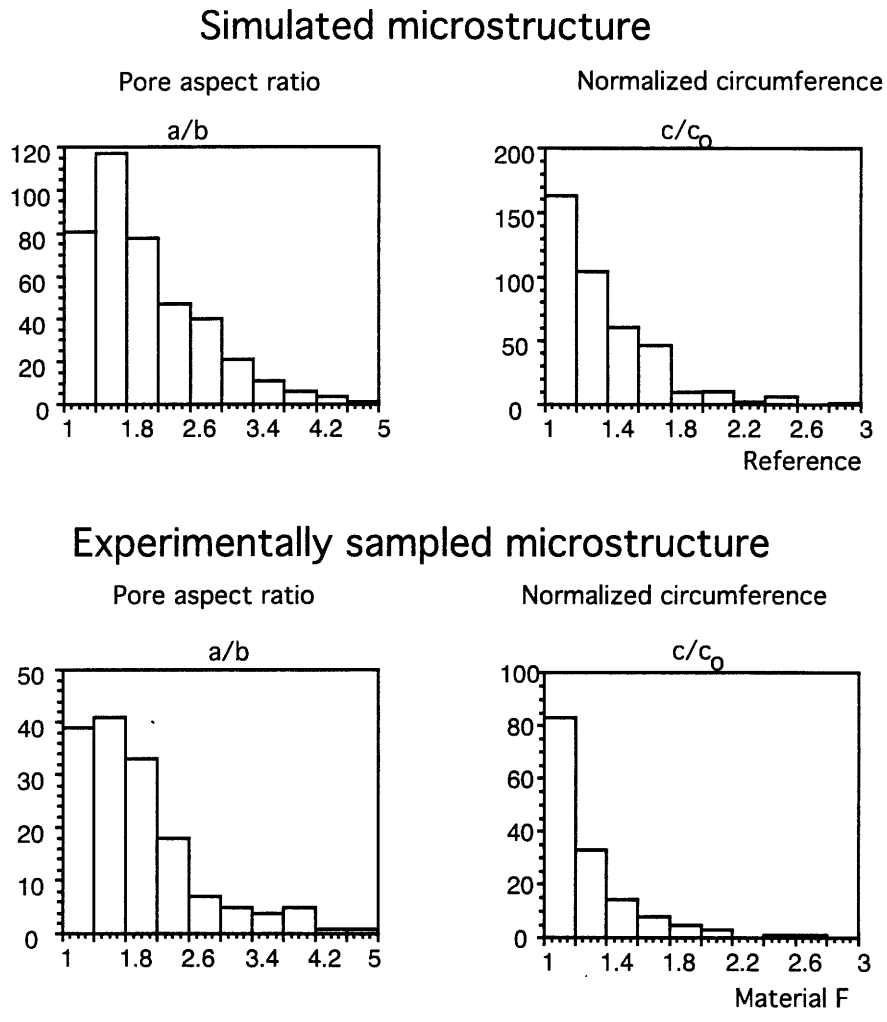

Figure 3-5: Pore shape distributions for real and simulated microstructures. The simulated structure had reaction parameters as follows, R/E = 0.3, E/C = 1, N = 7.6

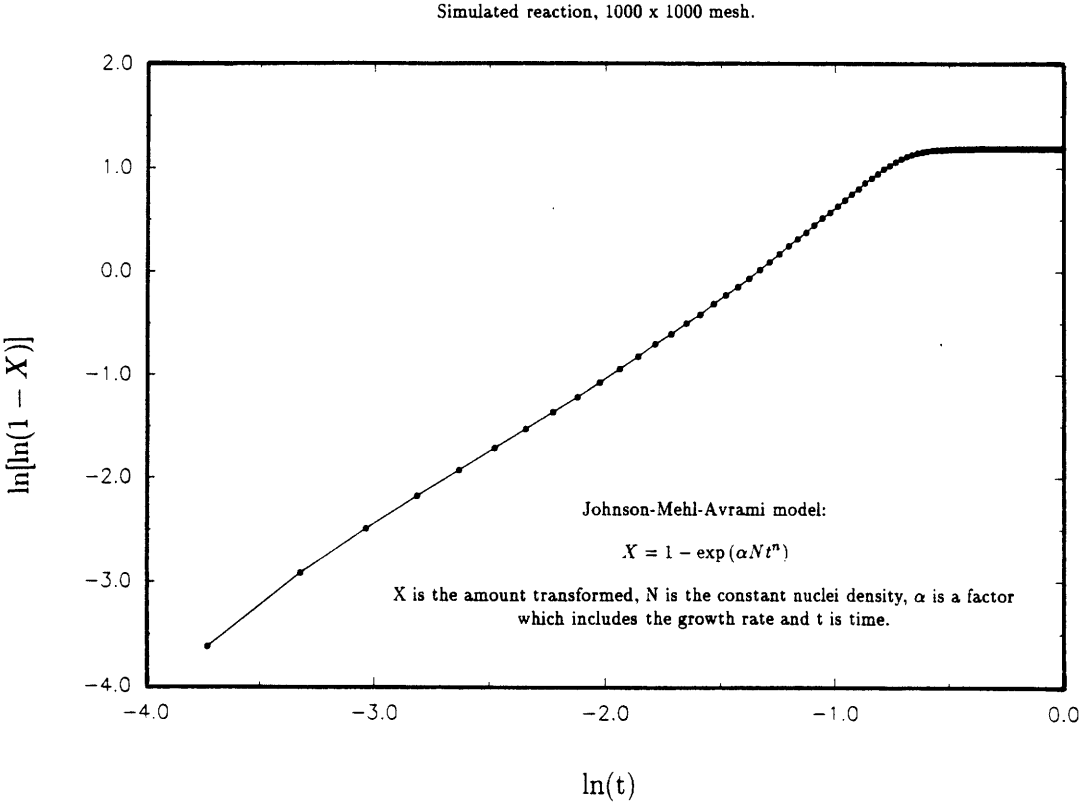

Figure 3-6: Time dependence of growth kinetics law.

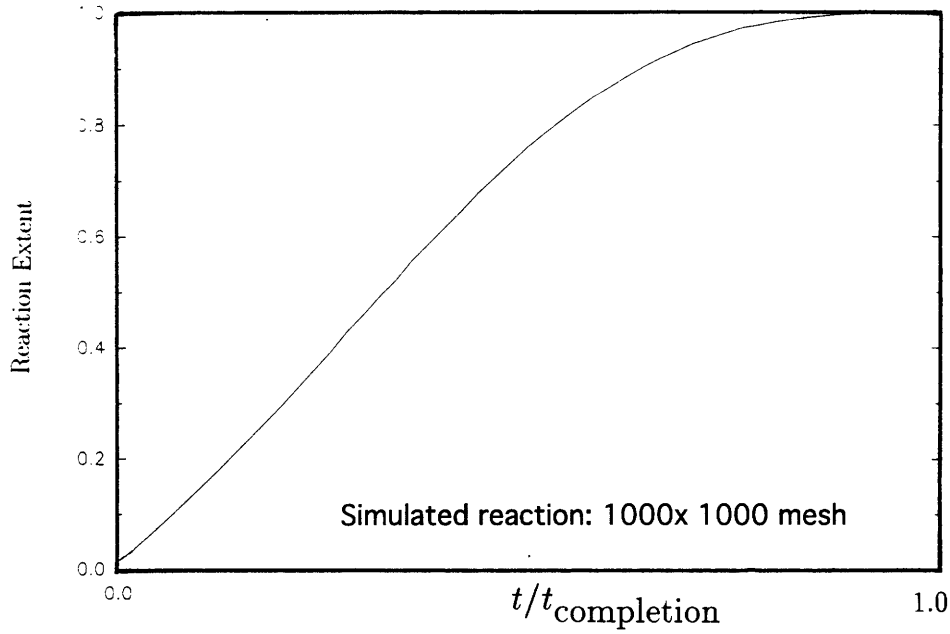

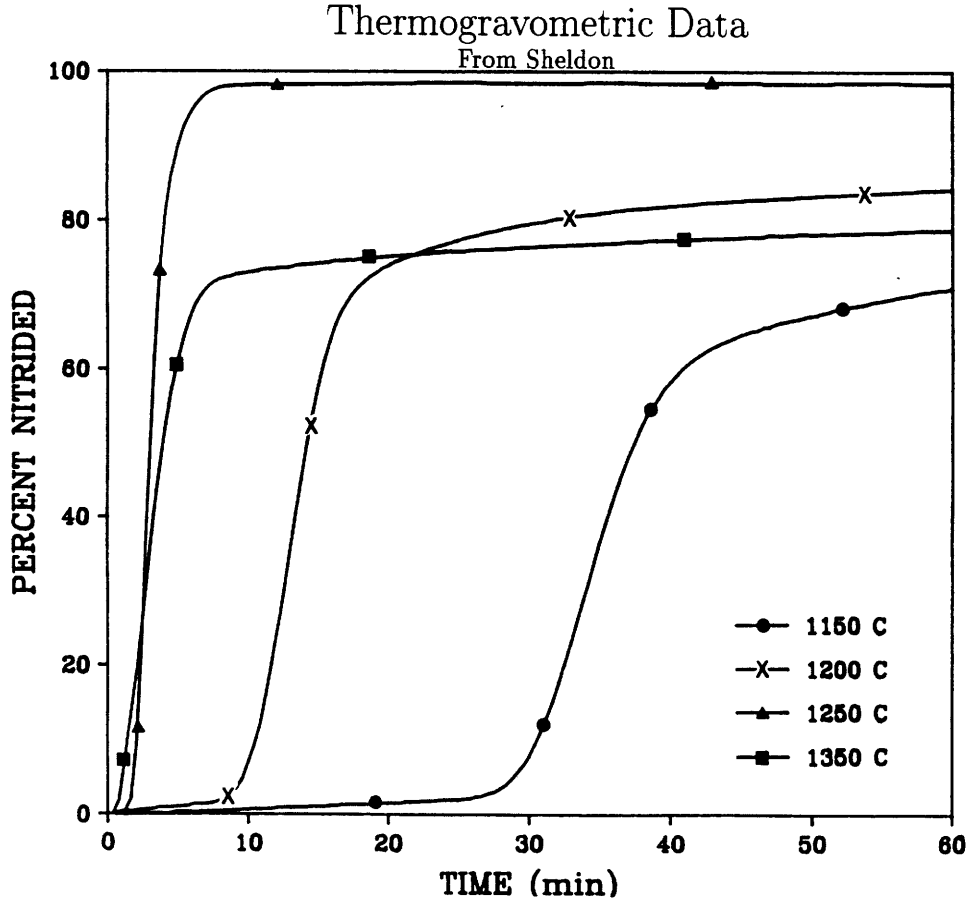

Figure 3-7: Reaction extent in simulated and real reaction.

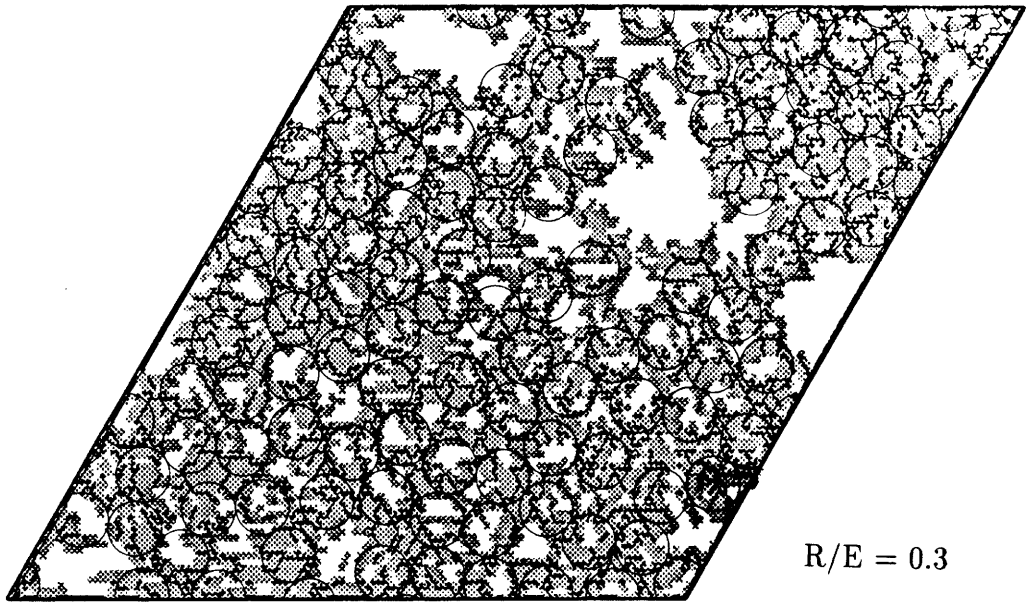

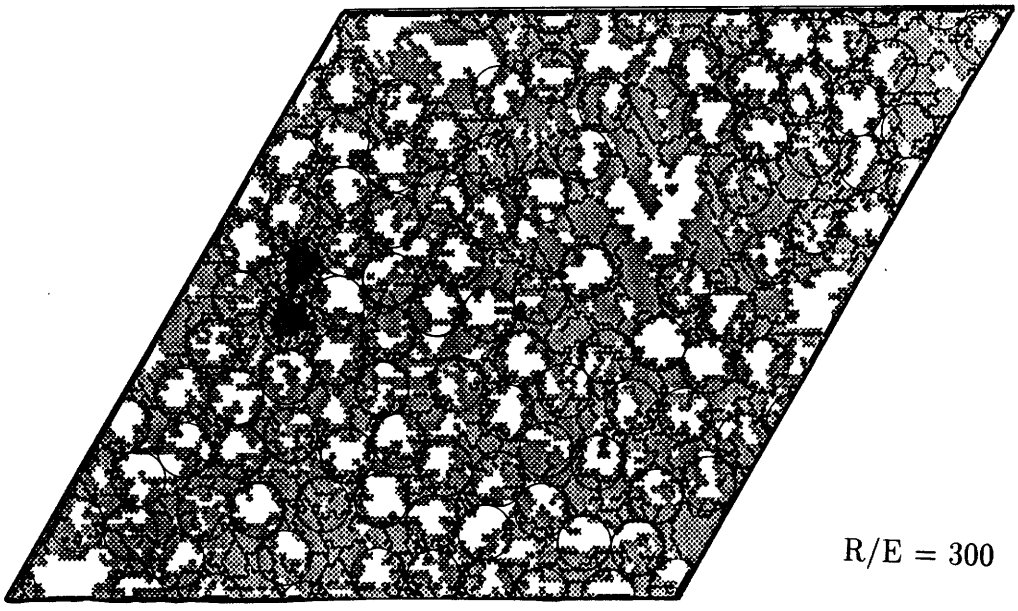

Figure 3-8: Microstructures of low and high reaction / evaporation rates showing positions of initial packed particles. Packed particles were equal diameter discs packed in 2D to illustrate conglomeration effect and the tendency of the high R/E simulation to 'heal' packing defects. (E/C = 1, Nuclei density, N = 10.)

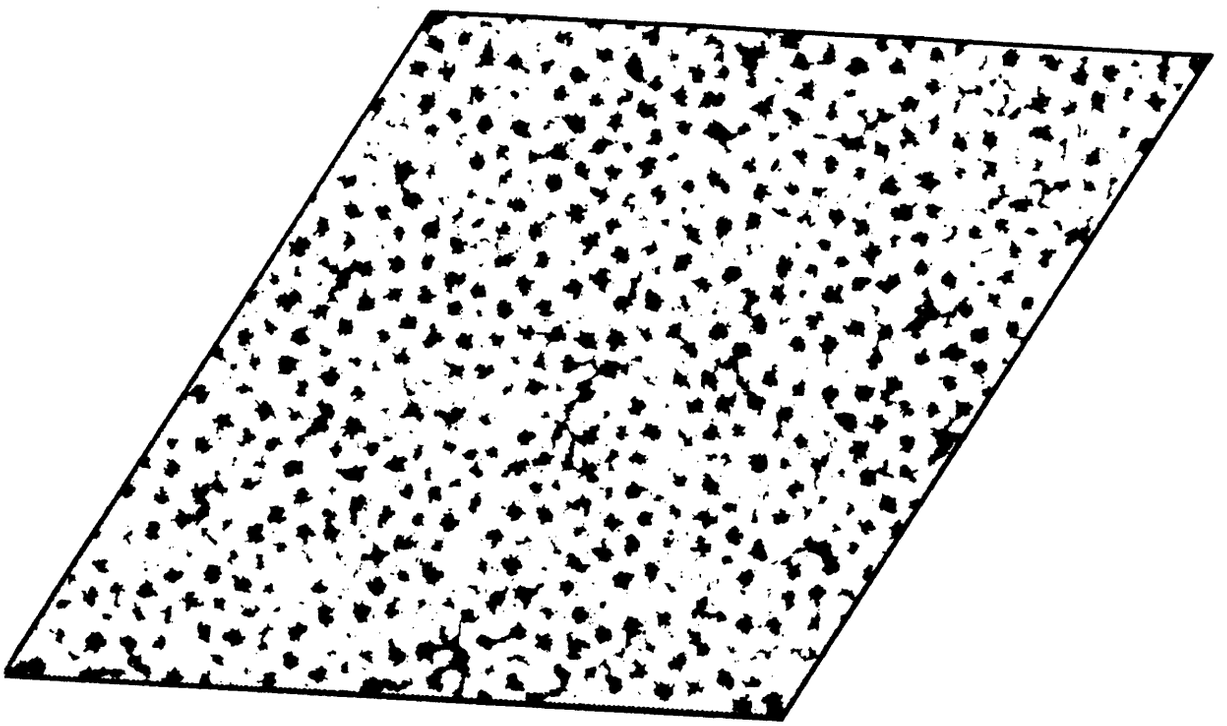

Figure 3-9: Simulated RBSN microstructure, R/E = 300, E/C = 1, N = 25

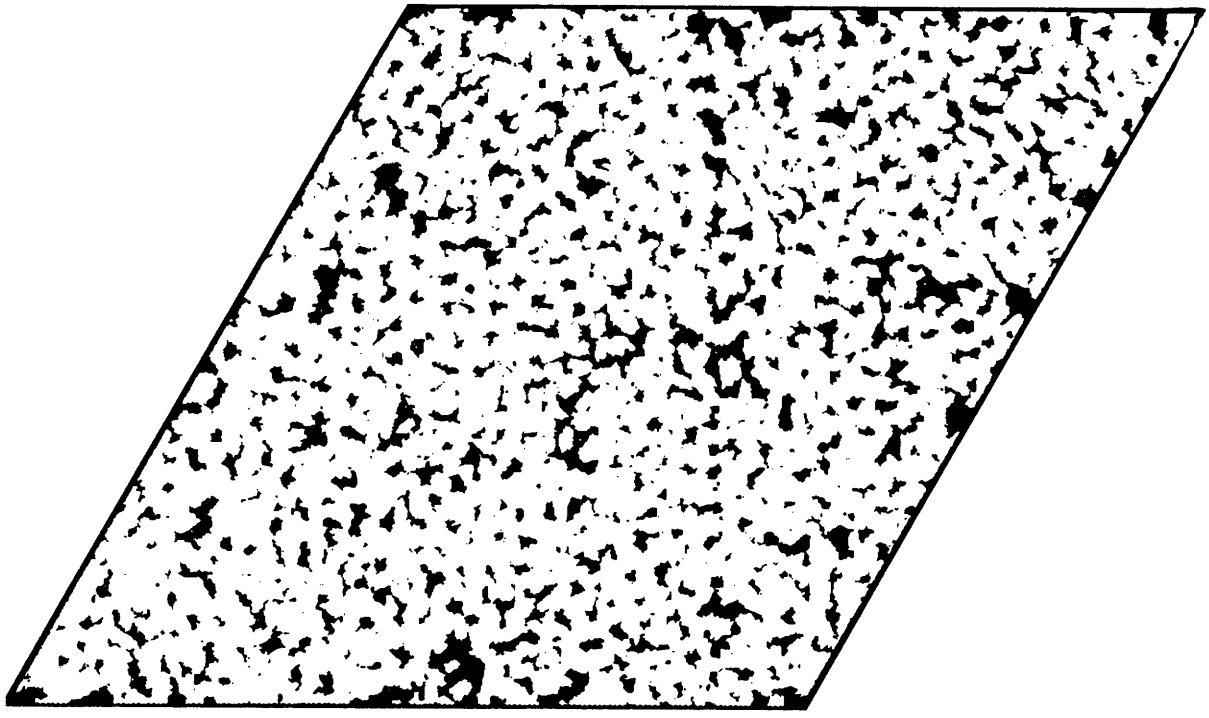

Figure 3-10: Simulated RBSN microstructure, R/E = 0.3., E/C = 1, N = 25

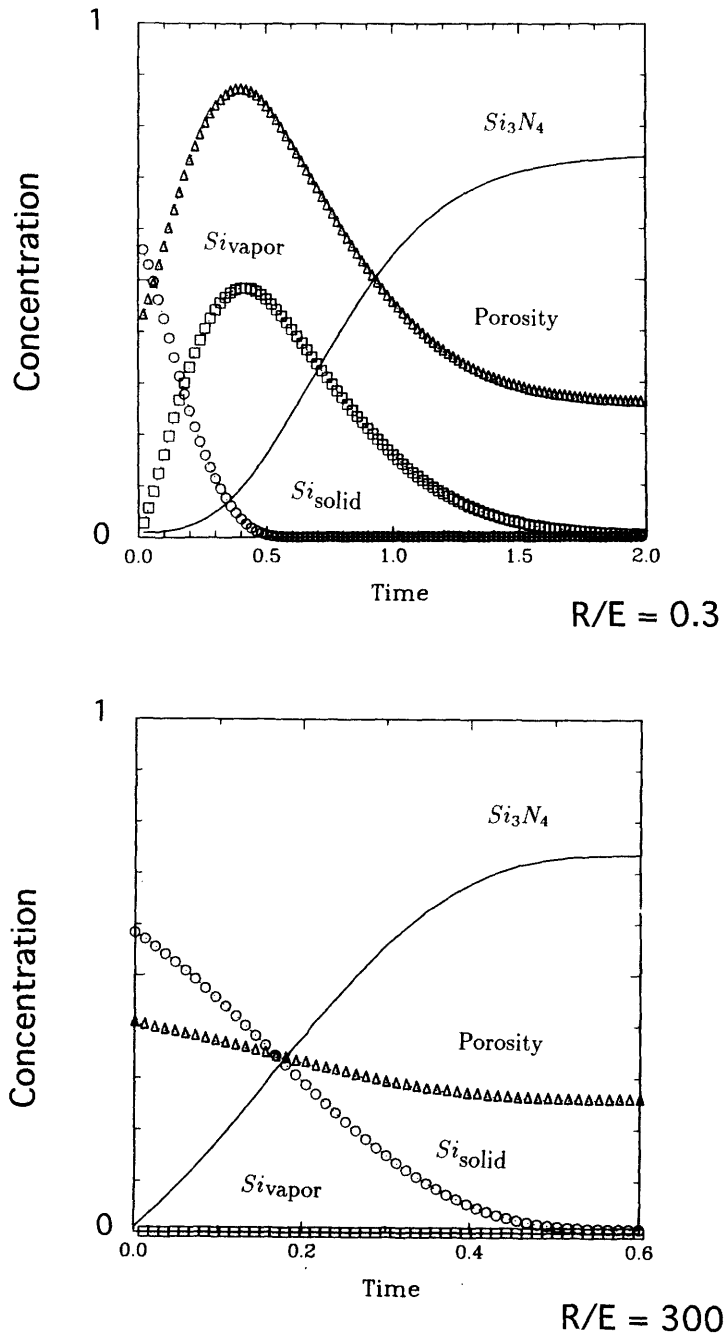

Figure 3-11: Relative densities of various reaction species for low and high reaction/evaporation parameter (R/E = 0.3, 300., E/C = 1, N = 25, mesh dimension = 1000 x 1000)

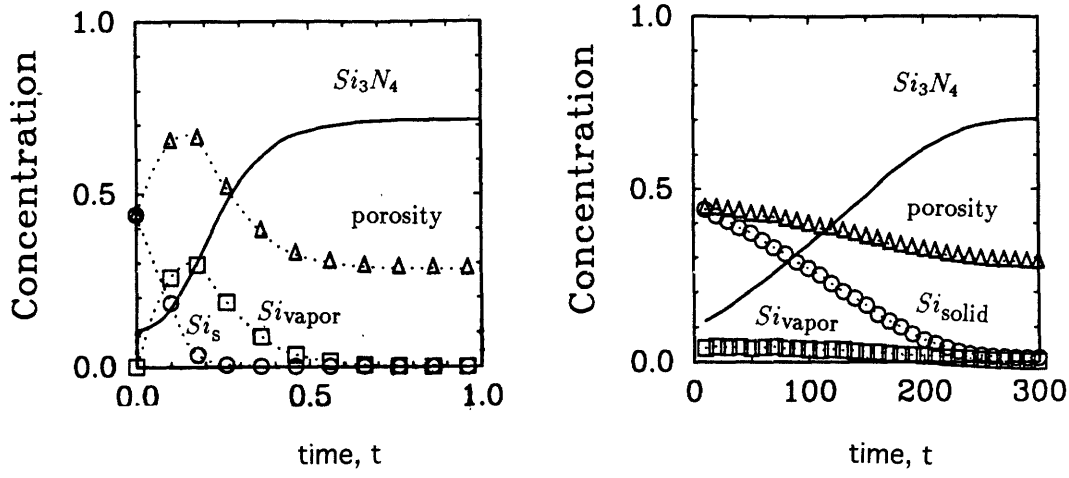

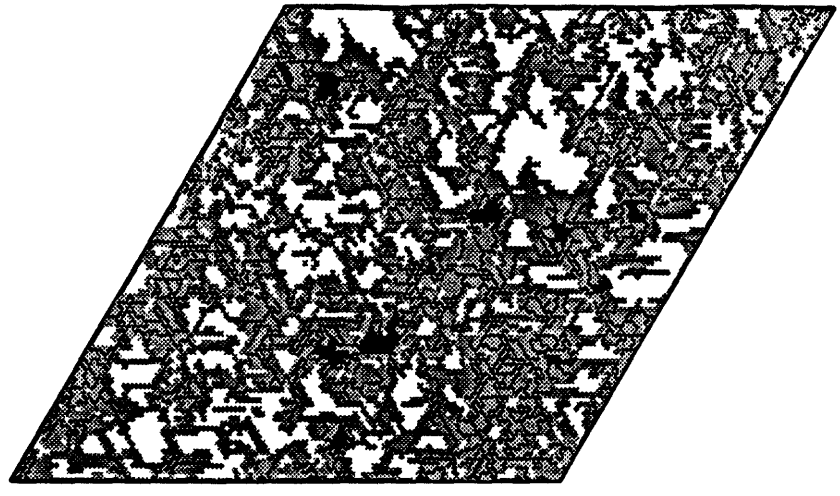

Figure 3-12: Simulated microstructure for low evaporation to condensation parameter showing unreacted silicon, and kinetic curves for low and high values of E/C (E/C = 0.1, 10). (R/E = 3, N = 10)

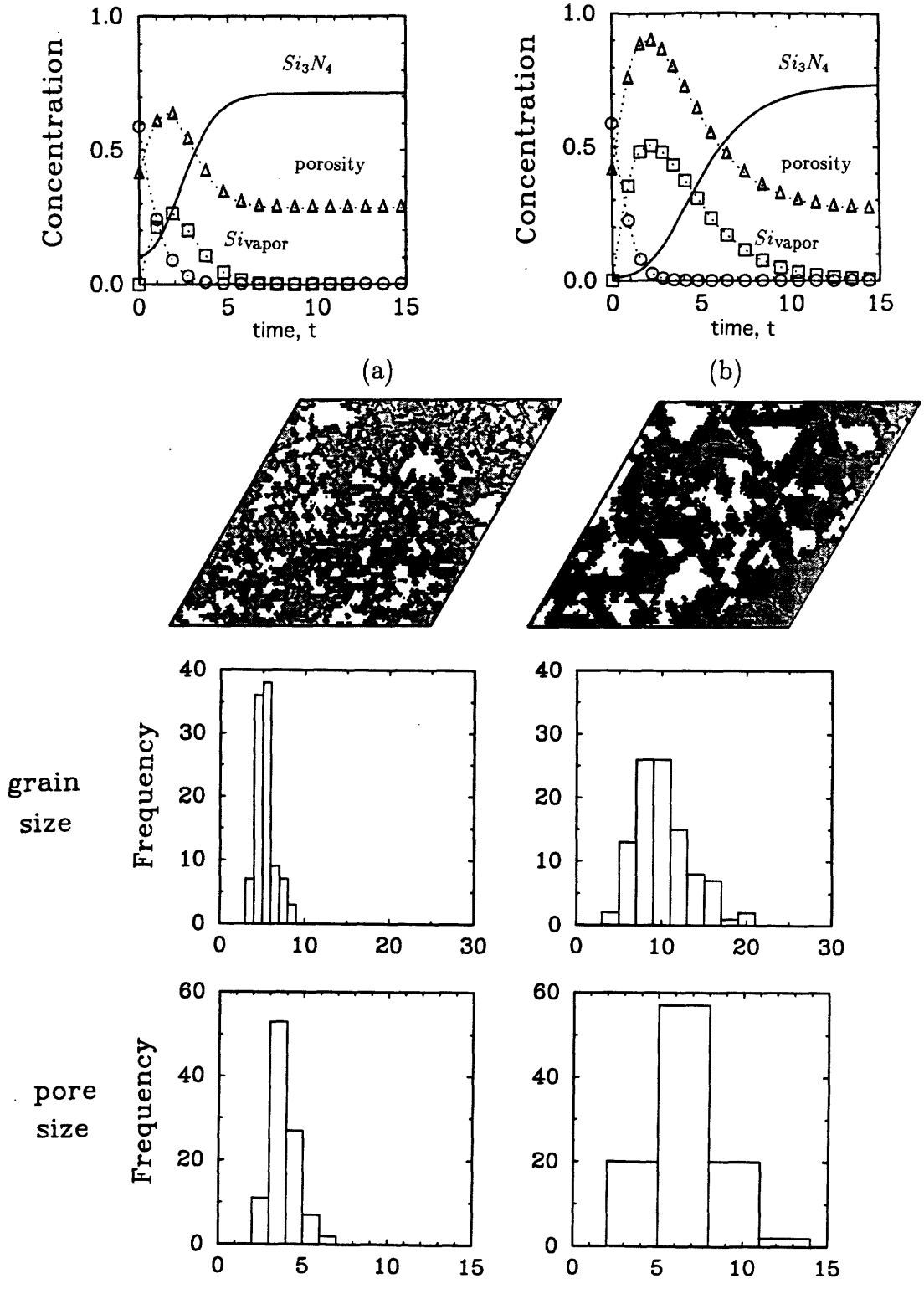

Figure 3-13: Micrographs and statistical distributions for grain and pore sizes for (a) high (10 nuclei per particle) and (b) low (1 nucleus per particle) nuclei densities. (R/E = 3, E/C = 1)

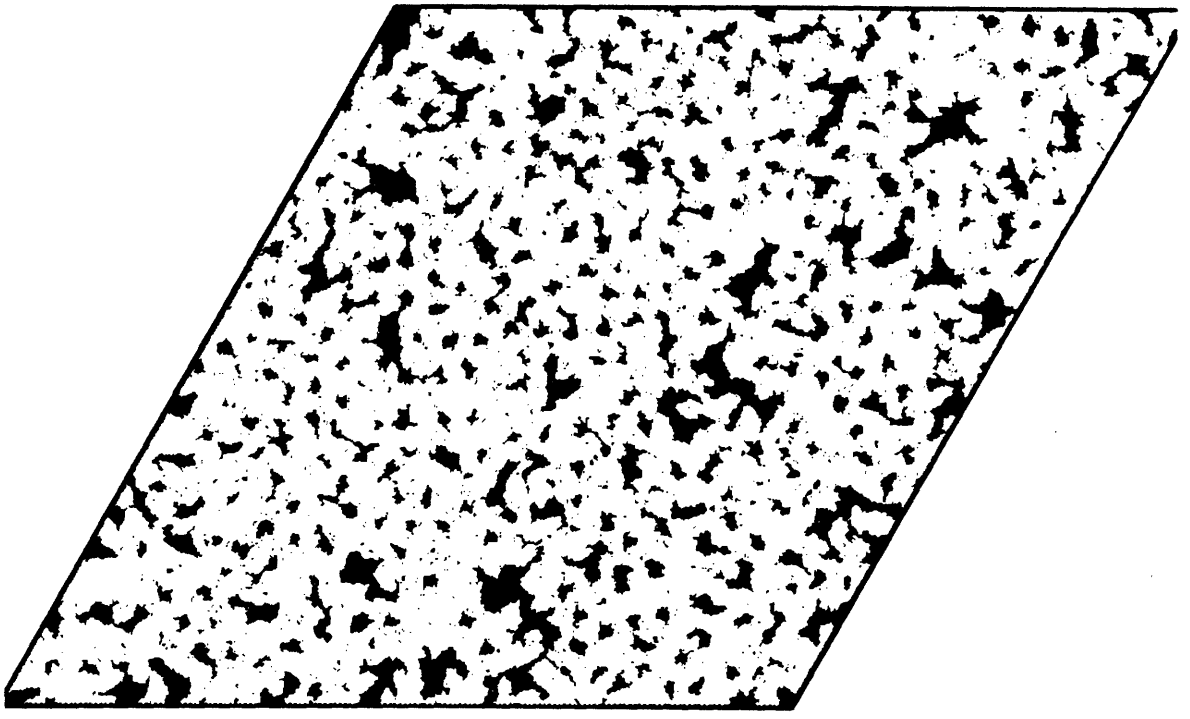

Figure 3-14: Simulated microstructure with nuclei density, N = 7.3, R/E = 300, E/C = 1

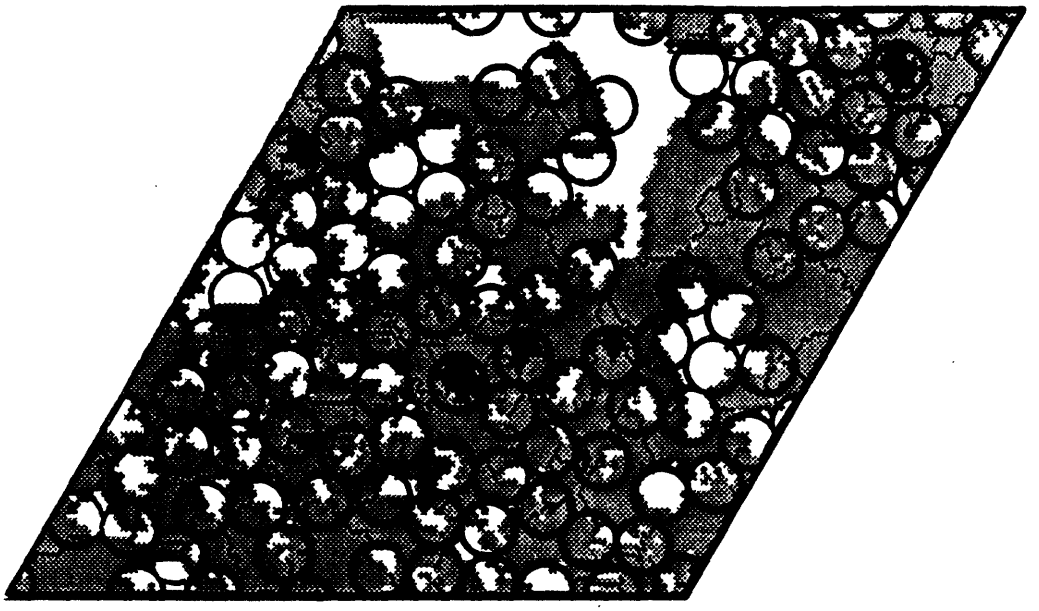

Figure 3-15: Microstructure of high reaction to evaporation parameter and low nuclei density. Notice the large pores in regions of high packing density, upper left and center right.

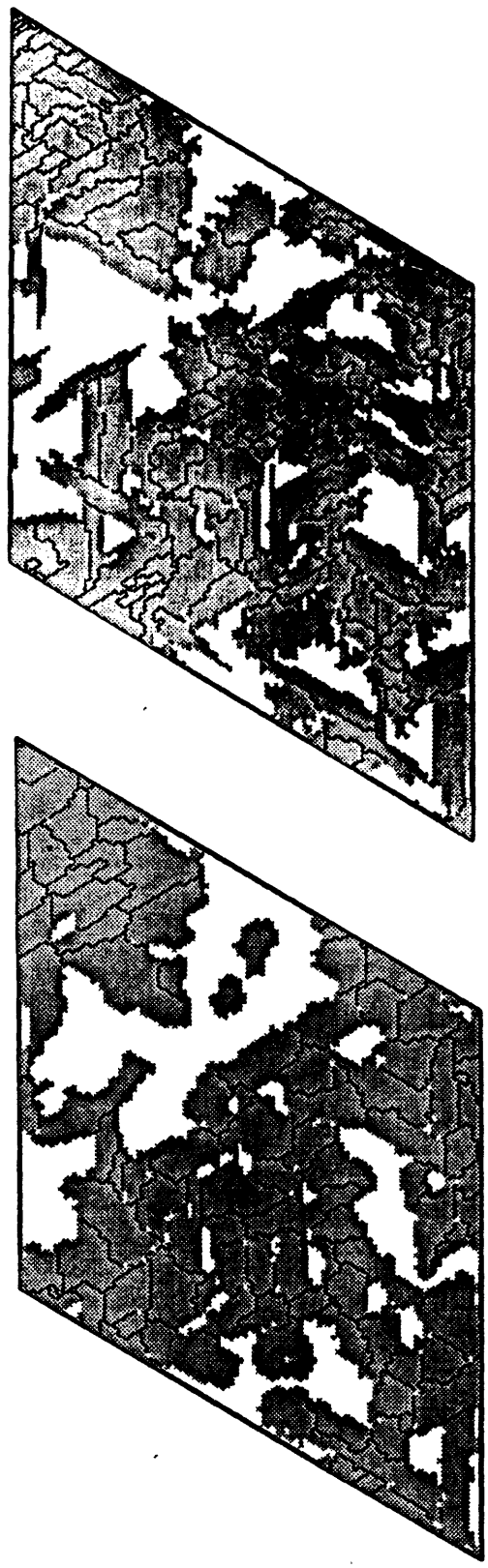

Figure 3-16: High and low surface tension microstructures.

Chapter 4

Simulating Fracture in Porous Media

4.1 Introduction

In Chapter 3 a separate but related reaction kinetics model was presented for the production of porous Si_3N_4 to establish the important reaction parameters that give rise to microstructures similar to the real microstructures presented in Chapter 2. In the present simulation we have explored the fracture processes in such computer generated microstructures with the goal of determining the causal and mechanistic connection between microstructures and toughness which can be translated to the real RBSN system, and perhaps guide the processing.

A numerical procedure is developed here for sampling the local tensile toughness and the crack propagation resistance of highly heterogeneous microstructures. Specifically, we have investigated porous brittle materials in the range of porosity less than cellular materials and greater than microstructures which fall under the category of dilute porosity. Explicit microstructural details are incorporated into a finite difference type simulation under a uniaxial strain condition in order to investigate the mechanisms of sub-critical damage evolution leading to fracture. In order to investigate material strength and stiffness variability on scales larger than the representative volume element in a crack tip stress gradient, we have incorporated the

explicit microstructural results into a simulation with boundary conditions of the displacement field of an infinite crack. Lastly, we have investigated the transition between high porosity cellular material fracture behavior and that for fully dense material by considering the potency or sharpness of the crack tip.

The approach taken here is to consider the details of the microstructure explicitly on a representative volume element scale, then to homogenize the material around the crack tip and apply the constitutive behavior that characterizes the material. In addition, the issue of the transition from cellular fracture behavior to the development of crack propagation in fully dense material is investigated.

We use the following notation throughout the analysis.

SYMBOL	DEFINITION
A	fracture surface area including only solid portion
A_o	total fracture surface area
E	Young's modulus
E_o	Young's modulus for fully dense material
G_c	critical energy release rate of porous material
G_{co}	critical energy release rate for fully dense material
K_c^*	fracture toughness of effective 3D super element
$K(\sigma, k)$	fracture toughness of a microstructure having element strength σ and stiffness k
N	number of nodes in simulation
$\mathcal{N}$	population size
U^e	elastic strain energy of bond extension
U^w	elastic strain energy associated with flexture of the angle between bonds ij and ik
a_o	equilibrium bond length
b	empirical exponential prefactor relating porosity and elastic modulus
b_o	equilibrium bond angular position
c	angular bond stiffness
$c(x)$	coefficient of variation

f	crack tip potency
$\vec{f}$	force on nodes due to pairwise and 3 fold interactions
f_b^*	grain boundary bond strength
f_m^*	bulk (matrix) bond strength
g_i	energy release rate of RVE, (= wr_u)
k	two node bond spring constant
$\overline{k}$	population average value of bond spring constant k in large assemblies
k_o	peak stiffness of a microstructural element
p	average porosity
r_{ij}	scalar distance between nodes i and j
r_u	size of the RVE chosen to derive properties of effective 3D super element
u_{ij}	unit vector connecting nodes i and j
w	tensile toughness, fracture work per unit volume of microstructural element tested in ten
Φ	total elastic strain energy
Ω	area associated with one node or a Voronoi polyhedon
ϵ_c	rupture strain of an indivual matrix bond
ν	Poisson's ratio
ρ	radius of curvature
σ	strength of an individual bond
σ_{ij}	element of second rank stress tensor
σ^*	strength of an effective 3D super element
σ_c	strength of individual matrix bond in the porous microstructures
σ_o	peak strength of a microstructure element
χ	two variable correlation parameter

4.2 Modeling Fracture in Brittle Porous Material

4.2.1 Outline of the Numerical Model

The model used in the simulations described here is based on the properties of a network of springs, and is similar to the models first used by Kirkwood[55] and of Keating[50] and most recently by Srolovitz [63,107], Curtin [20] and others [78,95]. The network is composed of a two dimensional, 6 fold coordination lattice whose points are connected by bonds. These bonds consist of extensional springs connecting nearest network nodes and three body angular stiffness springs referred to as 'watch' springs associated with pairs of two springs coming together at a network node as shown in figure 4-1. The nature of the physical bond model of interlocking linear bonds used here is is capable of solving general problems in plane isotropic elasticity, and is uniquely able to capture the displacement field solution for strongly heterogenous systems. Discussions of this and related types of modelling can be found in references [47] and [93] including comparisons with finite element techniques.

In brittle materials with quasi-homogeneously dispersed porosity the list of possible fracture toughening mechanisms include microcracking, and other crack shielding mechanisms like crack deflection, crack branching, and crack bridging analogous to fiber reinforcement by locally tough elements. Therefore, we exclude any dissipative or non-linear effects such as stress induced phase transformation, fiber pull out and large scale plastic deformation for the present study and consider only variations in strength and stiffness of the representative elements.

The elastic strain energy, Φ, is the 2-D hexagonal network is partly in the form of bond stretch and partly in the form of bond angle flexure:

$$\Phi = \frac{1}{2}\sum_{i}^{N}\sum_{j=1}^{6} U^e(r_{ij}) + \sum_{i}^{N}\sum_{j,(k=j+1)}^{6} U^w(r_{ij}, r_{ik})$$

where r_{ij} represents the scalar length between the center node 'i' and any one of its nearest neighbor nodes 'j', U^e represents the elastic strain energy of bond extension, and U^w represents the elastic strain energy associated with the flexure of the angle

between bonds ij and ik. The factor 1/2 in the first term accounts for the double counting over all nodal points N in the entire field. The bond stretching and angular flexing functions are chosen to represent the energy of the linear and watch springs. These functions are:

$$U_{ij}^{e} = \frac{1}{2} k_{ij} (r_{ij} - a_o)^2$$

$$U_{ijk}^{w} = \frac{1}{2} c_{ijk} \left(\vec{u_{ij}} \cdot \vec{u_{ik}} - b_o \right)^2$$

where $\vec{u_{ij}}$ and $\vec{u_{ik}}$ are unit vectors connecting node point i with its nearest neighbors j and k, $(\cdot)$ represents a dot product, a_o and b_o represent measures of the equilibrium bond length and angles in the unstressed network, and k and c represent the extensional and watch spring constants of the stretch and angle flexing interactions of the network nodes.

We note that the watch spring interactions have been included in the field response to account for non-central interactions permitting a full range of isotropic 2-D elastic response with arbitrary Poisson's ratio. The hexagonal symmetry assures isotropy [73]. To relate the spring network response to the actual material elastic properties we note that the isotropic elastic properties of a homogeneous network can be given by its Young's modulus E and Poisson's ratio ν as [107]:

$$E = 3ka_o^2 \frac{2ka_o^2 + 7c}{6ka_o^2 + 7c} \tag{4.1}$$

$$\nu = \frac{2ka_o^2 - 7c}{6ka_o^2 + 7c} \tag{4.2}$$

The stress tensor can be computed for a given tesselation of the mesh with the following general functional form:

$$\Omega_i \cdot \sigma_{ij} = \frac{1}{2} \left(\vec{r} \otimes \frac{\partial \Phi}{\partial \vec{r}} + \frac{\partial \Phi}{\partial \vec{r}} \otimes \vec{r} \right) \tag{4.3}$$

where σ_{ij} is one component of the 2-D stress tensor and Ω_i is the area of the invariant

locality of the element, usually chosen to be the Voronoi polyhedra surrounding one nodal point. Earlier models for obtaining stress solutions which incorporated central forces alone [10] can be shown to be a special case of equation 4.3 [69].

In Appendix A the basic conjugate gradient energy minimization technique that we use in obtaining equilibrium, together with the generalized local stress definition given above is demonstrated to constitute a fully flexible method of obtaining solutions of boundary value problems of stress distributions. The attractive feature of this network field method of solutions of problems of the types that we will be presenting below for RBSN, is a ready and flexible introduction of material properties of internal heterogeneities and cohesive properties of interfaces in the material.

4.2.2 Method of Implementation of the Model

In order to probe the energy absorbing capacity of a given microstructure, its elastic and strength properties are assigned to the spring mesh. The mesh is then placed under a prescribed loading condition, and is equilibrated with a conjugate gradient method until the energy function, Φ, is minimized for a unit level of boundary displacement which serves to scale the internal field distribution. Stresses are computed and the bond with greatest tensile stress is identified and is elevated to the level of a pre-determined critical fracture criterion by re-scaling the boundary displacements. The stiffness of this bond is broken by setting the associated spring stiffnesses to zero. The fracture criterion of maximum stress is chosen over other criteria, such as maximum energy density, for the fact that brittle materials fracture when local tensile stresses exceed the intrinsic material strength. Upon fracture, the mesh is re-equilibrated to identify the next highest bond that can be broken, and so on, until the entire cross section of the microstructural element is severed. In the process the overall system stress and system extension is recorded to construct a characteristic stress strain curve for the volume element.

4.2.3 The Fracture of Porous Microstructures

In the first simulation, the constituitive behavior is sampled of material sections which are large enough to encompass many multiples of the microstructural features. In doing so, the processes of crack nucleation and damage accumulation are studied and key parameters are measured, such as the tensile toughness, maximum strength and the evolution of the elastic modulus. The microstructures sampled are obtained from the reaction kinetics simulation described in Chapter 3 and are also obtained from digitized microscopy images.

The microstructural volume element to be used in the simulation is mapped onto the two dimensional lattice as follows. Solid elastic elements of the microstructure are differentiated from pores such that solid bonds have full stiffness and pores have zero stiffness. The fracture properties are incorporated by assigning bond strengths. Here the bulk matrix bonds were differentiated from the intergranular bonds by assigning boundary bonds f_b^* to have lower strength , i.e. $f_b^* = 0.75\ f_m^*$ where the latter stands for the strength of a bulk (matrix) bond. This value of boundary bond strength was chosen as an upper estimate of the strength necessary to permit intergranular fracture in polycrystalline solids as simulated also by Srolovitz et al [107]. Intergranular fracture has been observed in high purity RBSN manufactured by Haggerty and coworkers [67] whose research has been closely linked with the present simulations. The dimension of the bond is defined to be equal to a fraction of the grain size in order to capture some aspects of the intergranular fracture. The specific fracture criterion used here is the maximum traction on the surface normal to the linear bond orientation, in order to approximate grain boundary surfaces. Once the spring mesh is assembled, the spring network is placed under a state of uniaxial strain, and periodic boundary conditions are imposed so the specimen is essentially infinite with no free surfaces.

Other possible features that could be incorporated into the model were separate properties for distinct phases, and the imposition of eigenstrains by appropriately altering a_o and b_o, the equilibrium bond parameters. The scale chosen for the mesh of the large scale microstructural unit was 64x64 node dimensions, approximating a

nominal dimension of 2 microns, and incorporating 10-20 pores of 0.1 micron dimension, i.e. a field of roughly 25 RVEs.

4.2.4 Variability of Strength and Stiffness

In order to capture the interaction of a crack with strongly heterogeneous microstructures on scales larger than individual microstructural features, a second set of simulations are performed in the stress gradient of a Mode I crack. In this case, each bond represents a larger volume of material. Before the question of the dimension of the bond is addressed, a series of fracture simulations are performed with increasing bond strength and stiffness variation to obtain some idealized trends.

In this approach the mesh is precracked and is placed in a strain gradient field solution of the crack tip singularity for an infinite Mode I crack. This approximates to a part of infinite dimensions. Beyond the border of the cracked domain the solution applies exactly. Inside the domain, the variations due to individual bond properties were solved explicitly, and care was taken to minimize the effective variation at the boundary by keeping the mesh larger than any crack tip process zone. The local fracture criterion was again taken as a maximum principal stress, and no internal interfaces are presumed.

To explore the effect of variability of bond stiffness or strength, the bond properties are chosen to have a value between a maximum (1.0) and a minimum value determined by a varience which was defined by a coefficient of variation, i.e. the standard deviation divided by the mean, where the frequency distribution was taken to be constant over the range of values defined by a minimum and the maximum (1.0). In this manner, the coefficient of variation $c(x)$ in the variable x is defined as:

$$c(x) = \frac{1}{\sqrt{3}}\left(\frac{1}{\overline{x}} - 1\right) \tag{4.4}$$

where $\overline{x}(= (x_{max}+x_{min})/2)$ is the mean of the distribution in which $x_{max} = 1$. Thus, a variance ranging from values of 0 to 1.0 results in a coefficient of variation of 0.577. In the simulation each parameter was varied either independently, or the two parameters

of strength and stiffness were chosen together with a prescribed correlation.

4.2.5 Incorporating Microstructural Information into Stress Gradient Simulation

To remove the arbitrariness of the independent variabilities of local strength and stiffness, explicit microstructural stiffness and strength were generated by developing statistically significant combined strength and stiffness variability information and introduced into the stress gradient model. This was accomplished by testing a significant number of small microstructural units as representative volume elements (RVEs) extracted from a very large field of a porous microstructure by a random selection process followed by testing these under uniaxial stress to obtain their initial elastic stiffness and their fracture peak stress. This is described in detail in Section 4.4 below.

Moreover, to introduce an element of 3-D realism where porosity in a real structure is randomly distributed into the third dimension rather than being columnar as implied in a 2-D model, a special three dimensional element was constructed by averaging the properties of three neighboring simulations of small representative volume elements with pre-determined different stiffness and strength properties in a row, to constitute a strip of arbitrary crack front. The effective stiffness of the equivalent 2-D 'super-element' with the desired 3-D relevence was then taken as the upper bound average of the three units. The effective strength σ^* of the super element was obtained on the argument that of Rose [92] that the average energy release rate of a strip of crack front with heterogeneities is approximately equal to the line average of the local energy release rates, g, along the crack front, s:

$$\sigma^* = \frac{K_c^*}{\sqrt{\pi r_u}} = \frac{\sqrt{E(\sum_{i=1}^{3} g_i \Delta s)/3\Delta s}}{\sqrt{\pi r_u}} = \sqrt{\frac{E\sum_{i=1}^{3} g_i}{3\pi r_u}} \tag{4.5}$$

where r_u is the size of the microstructural RVE used in the preliminary simulations to gather statistical data, g_i is the energy release rate (area under the stress-strain simulation of the RVE times r_u, the size of the RVE) of an individual unit considered

in the 3 unit average. This effective solution is compared below in figure 4-2 to a more exact result obtained by Bower and Ortiz [9] for a crack pinned at two heterogeneities and bowing into a region with decreasing toughness. The solutions match well for ratios of the minimum to maximum toughness of the three averaged elements larger than 0.2, at which point the error is approximately 6%.

4.3 Results

4.3.1 The Evolution of Damage Under Uniaxial Tensile Loading

The damage evolution in homogeneously stressed microstructures is characterized by cascades of individual element (bond) fracture events with the fracture process always initiating at a pore surface and developing into a succession of breaks which comprise the evolution of a crack. The nature of fracture is predominantly intergranular, with 75 - 100% of the breaks occuring along the lower strength grain boundary bonds. The cascade of breaks commonly represents the sequential breaking of elements in a ligament between two pores, which is generally the smallest dimension between two adjacent pores. This is evidenced graphically and by the fact that the number of breaks in the cascade correlates with the number of mesh elements that make up a ligament. These fracture cascades are separated by single stable breaks at pore surfaces which, however, do not continue to grow.

Figure 4-3 shows in considerable detail the response of a stressed microstructure obtained from the digitized image of a real RBSN sample. The figure identifies the connection between the features on the stress strain state with events on the stressed microstructure.

During the simulation when a local break is obtained, such as at the point near A, between the two central pores, the system registers a slight decrease in elastic stiffness. At this stage, for operational purposes the system is unloaded and subjected to the same unit border displacement to seek a new level of internal equilibrium, and is then

reloaded until the second break is registered (at point A). The decreased stiffness (increased compliance) of the system manifests itself by an elastic loading line, with reduced slope, connecting the origin to point A (not shown in the stress strain curve). The second break at point A in the newly re-equilibrated microstructure occurs at a system stress less than the first break. After this break the continued loading of the system (following the usual re-equilibration) produces a third break which now exceeds the stress of the first break. All other dotted lines falling inside the outer envelope of the stress strain curve represent such virtual re-equilibration and reloading processes probing the system in the computer. In a real system loaded by border displacements or imposed external strain increments there would be no retraction of strain, but the system response would be given by vertical stress drops as the outer envelope stress strain curve indicates. In this case, all individual fracture events represented by crosses falling inside the stress strain curve would represent unstable fracture cascades, as those identified by A-I in the stress strain curve and located correspondingly on the microstructure.

During the evolution of damage leading progressively to increasing concentration of fractured ligaments the overall system modulus systematically decreases, shown by the ever decreasing slopes of the lines connecting the origin to the new fracture events. This progressive decrease in stiffness of the structure accumulating increasing levels of breaks is summarized in figure 4-4.

Uniaxial Fracture Behavior of a Series of Microstructures

A series of porous microstructures which were produced under systematically varied conditions with the associated reaction kinetics simulation mentioned above were probed for their quasi-homogeneous fracture properties in uniaxial loading. The microstructures shown in figure 4-5a were deemed to be realistic in appearance as can be qualitatively verified by a visual comparison of the computer generated microstructures with the real microstructures of RBSN shown in Chapter 2. In addition, quantitative measures of real microstructural features, such as average porosity levels and pore size distributions, are comparable with the simulated structures. Of the mi-

crostructures shown in figure 4-5 the first represents a typical control microstructure of 25% porosity; the second and third microstructures are for a higher porosity of 31% and a lower porosity of 20.5% respectively. The fourth microstructure is for a case of a significantly anisotropic growth condition, while the fifth and sixth microstructures are for a low reaction to evaporation ratio in the reaction kinetics simulation from Chapter 3 producing a controlled variation in porosity distribution and finally a case of the addition of a population of small diameter (one tenth of the normal diameter) silicon particles. This last case was undertaken as a comparitive simulation with the experimental observation of a measured fracture toughness reduction with the addition of smaller Si particles, and was thought to arise possibly from pre-nitridation particle packing effects.

The results of these simulations in the form of stress strain curves are shown in figures 4-5b - 4-5h, together with a representative microstructure of the individual cases. In all cases the stress strain curves presented are the composites of four separate simulations. In the final phases of a simulation history when the microstructure becomes increasingly compliant the re-equilibration times of such structures becomes quite long. Thus, to economize on computational effort the forms of the declining parts of several stress strain curves, such as the ones of figures 4-5b and 4-5d were obtained by an empirical fit. This same termination form was then applied to all other simulations.

Perusal of the composite stress strain curves of those simulations shows many similarities in their shapes. Apart from the case of the anisotropic microstructures which show marked increased tensile toughness all other cases show few quantitative differences apart from the primary effect of changes in porosity.

Figures 4-6,4-7 and 4-8 summarize the principal results of these simulations: for the Young's modulus (figure 4-6), the peak strength (figure 4-7), and the tensile toughness (fracture work per unit volume, figure 4-8). In the latter the beneficial effect of the anisotropic grain morphology stands out. This effect can be accounted for by the increased strength of this microstructures by a factor of approximately 1.3, which is comparable to the relative increase in toughness compared to the control

microstructure. In all other cases the porosity level is clearly the most important structure characterizing parameter.

In the simulation, the tensile toughness, w, is obtained as the area under the individual stress strain curves, i.e.:

$$w = \int_0^{\epsilon_m} \sigma d\epsilon \tag{4.6}$$

where w is the energy per unit volume required to completely fracture the microstructure to a state of zero load support under uniaxial strain, and ϵ_m is the strain for complete fracture. Typical energy densities normalized by the energy to fracture a perfect solid of bulk material, $\sigma_c \epsilon_c/2$, are in the range of 0.1-0.2; as figure 4-8 shows. The terms σ_c and ϵ_c are the strength and strain to fracture a fully dense matrix bond in uniaxial tension.

The restriction of the uniaxial strain condition may produce additional load support at the end of the simulation due to the absence of stress relaxation perpendicular to the loading direction. However, the magnitude of the energy contribution under the tail for strains between 0.5 and 1.0 ϵ_c, the critical strain to failure under uniaxial strain, is not a major portion of the work of fracture and scales with the total energy, $w_{\text{tail}} = (0.3 - 0.4) w_{\text{total}}$.

4.4 Fracture of Homogenized Material with Prescribed Variability

4.4.1 Uncorrelated Strength and Stiffness Variation

The investigation of the properties of porous microstructures in uniaxial tension, the results of which we have discussed above, revealed that because of the porosity and the variability introduced through lower bond strengths for boundaries in comparison with the strength of the bulk matrix, damage accumulation was strongly clustered. This effect, which was discussed in detail in connection with figure 4-3 manifests itself in the form of cracking cascades and implies that for purposes of simulating crack

growth the material can be divided up into smaller representative volume elements. We have followed this approach in two separate but related simulations of crack growth.

In the first of these simulations which we will discuss in this section we have considered the material to have uniform density, i.e. to be free of pores, in which the expected clustered growth of a crack was taken to result from material heterogeneities in either strength or stiffness, and where the variabilities in either property are uncorrelated. In the second simulation the strength and stiffness of the heterogeneities were correlated on the basis of a separate uniaxial tensile simulation of the fracture behavior of RVE's of the size of the cracking cascades of the type observed earlier in connection with figure 4-3. The results of this second simulation are discussed in Section 4.4.3 below. In both simulations we have utilized the same hexagonal network structure discussed above, where however the individual bonds were now interpreted to be the heterogeneities resulting in the clustered cracking behavior noted in the fracture response of larger microstructures. The propagation of Mode I cracks through such uniform density material with prescribed heterogeneities was then investigated in a manner described in Section 4.2.5 above.

The degree of variation of both the bond strength and stiffness affects directly the extent of microcracking, crack deflection, branching and bridging behavior. For small variability, the crack path is planar, the crack samples on average the population average of element strength, and the average fracture toughness is that of a homogenized structure with the average properties, $K(\overline{\sigma}, \overline{k})$, where $K_c = \sigma_o\sqrt{\pi a_o/2}$ has been taken as the unit of toughness measure. As the variation of local properties increases, the crack path becomes more tortuous, and the number of redundant breaks increases. This trend is shown in figures 4-9a - 4-9f for increasing coefficients of variation in strength and in figures 4-10a - 4-10e for increasing coefficients of variation in bond stiffness. The effect of the increasing variabilities on tortuosity of crack path is shown under each figure. With this increase in crack complexity comes increased toughness in comparison to the homogenized structure as shown in figure 4-11. In the case of largest strength variation ($c(\sigma) = 0.52$), the advancing crack splinters into an un-

bounded growing cloud of microcracks, characterizable as generalized microcracking, and material degradation.

The increase in toughness due to material variability correlates with the crack complexity or degree of deviation from planar form. This is measured by the calculated root mean square of the height coordinate of the breaks away from the median plane of the crack which comprise the crack profile, and naturally includes effects of crack tortuosity and redundant microcracks. Figure 4-12 shows the positive correlation of the crack height deviation from planar form with the relative toughness, $\Delta K/\overline{K}$. The parameter ΔK is defined as the difference between the average K sampled and the toughness of a homogeneous material with average properties, $\overline{K} = \sqrt{\overline{E} \times \overline{g}}$. Here, the term g stands for the energy release rate of one severed bond, $(1/2)\sigma\epsilon a_o$, where a_o is one cell dimension. Higher complexity crack configurations due to crack tortuosity and microcracking produce higher crack propagation resistance, as expected.

In the case of stiffness variation, the effective toughening is due to microcracking and bridging effects as in the case of strength variation, and some additional toughness is derived from some elastic crack tip shielding effects due to stiffness variation. The toughening effect increases monotonically with stiffness variation (as is shown in figure 4-13) but is delayed in its effect with increasing coefficient of variation as compared to the strength variation case. However, since the stiffness variations produce less crack tortuosity and redundant breaks, the toughening effect is more potent for a given crack profile roughness. The average stiffness of the broken bonds is equal to the average of the total population suggesting no favoring of high or low stiffness bonds for fracture. Thus, any elastic shielding is due to a favorable stress redistribution arising from a broader spacial distribution of bond stiffnesses. In comparison with a homogenized material where all bonds have the same average stiffness, the maximum toughening effect is 1.34 for a coefficient of variation of 0.520 in bond stiffnesses. The homogenized material also has constant toughness by the argument that a more compliant bond absorbs proportionally more energy, yet the surrounding material has a reduced elastic modulus which is related to the bond stiffness (see Section 4.2.1). The relation

$$K_c = \sqrt{(\overline{k}/a_o)g} = \sqrt{(\overline{k}/a_o)(\sigma_o^2 a_o^2/2\overline{k})} = \sigma_o\sqrt{a_o/2} \tag{4.7}$$

where $\overline{k}$ is the average stiffness, and g is the energy release rate for a unit of crack length a_o, implies that the toughness of a brittle material whose energy release rate is inversely proportional to its macroscopic stiffness is independent of the elastic properties, for a stress based fracture criterion.

The quantitative toughness measured in these simulations is possibly an underestimate in the cases where crack face bridging elements produce crack tip shielding. This may occur when the bridging zone is truncated due to the finite dimension of the simulation. The estimation of the potential bridging zone can be made by setting the crack opening displacement equal to the displacement for the strong element at the point of fracture. Long bridging zones can be seen therefore to be created by elements with high strain to failures, a criterion that is difficult to meet with the high correlation of the strength and stiffness of the microstructures studied here. Therefore, it is unlikely that extensive bridging zones could form in the idealized microstructures simulated here.

4.4.2 Correlated strength and stiffness variation

The consideration is taken that with high probability, material elements will have a closer correlation between strength and stiffness than the somewhat artificial cases above in Section 4.4.1 for independent variations of strength and stiffness. Here, the strength and stiffness of individual elements are varied together in perfect correlation and then independently for a coefficient of variation of 0.346 of the correlated properties. The results are summarized in Fig. 4-14. The expected value of toughness for a cooperative effect between strength and stiffness variability is $K^{\text{expected}}/K(\overline{\sigma},\overline{k}) = K(\overline{\sigma}+d\sigma,k_o)/K(\overline{\sigma},k_o) \times K(k_o,\overline{k}+dk)/K(\sigma_o,\overline{k}) = 1.25 \times 1.09$ or 1.37 ± 0.04 when normalized with the homogeneous equivalent material toughness. The result for perfect proportionality between strength and stiffness is a crack configuration of reduced toughness as compared to the homogenized equivalent material,

$K(\overline{\sigma} + d\sigma, \overline{k} + dk)/K(\overline{\sigma}, \overline{k}) = 1.04 \pm 0.01$. The uncertainty value is the standard deviation of the mean, $\delta = s/\sqrt{\mathcal{N}}$, where s is the population standard deviation and $\mathcal{N}$ is the population size.

The conclusion is that the perfect correlation of strength and stiffness effectively transforms the fracture criterion into a critical strain criterion, with some effects of elastic shielding. These effects produce weaker microcracking and crack diffuseness and less toughness than either toughening effect of strength or stiffness variation, alone.

The opposite case of independent strength and stiffness variation produces increased tortuosity, microcracking and higher toughness. The relative toughness is then $K(\overline{\sigma} + d\sigma, \overline{k} + dk)/K(\overline{\sigma}, \overline{k}) = 1.34 \pm 0.013$, which is an effect comparable in magnitude to the expected effect. Qualitatively, the crack configuration appears similar to the highly correlated case but has more surrounding microcracks[1]. This is confirmed by a nearly equal crack profile height (r.m.s. height of 3.0 compared to 2.6 cell dimensions for the uncorrelated and correlated cases respectively). The increased toughness for the cooperative interaction is due to two new effects. The elements with high stiffness and low strength serve as potent microcracking sources, and those with low stiffness and high strength have a significantly higher energy absorbing capacity.

4.4.3 Crack Propagation with Realistic Distributions of Strength and Stiffness

In the light of the abstract exercise of the effects of strength and stiffness variations presented in Section 4.4.2 above, we now apply more realistic distributions of strength and stiffness as derived from explicit microstructural simulations of the properties of RVE's of small specific microstructure units. For this purpose a large (1000x1000) Monte Carlo simulated microstructure was sectioned into 10 x 10 cells and tested individually for their elastic modulus and strength in uniaxial tension. This cell size is equal to a small multiple of the interpore ligament length which corresponds roughly

[1]This explains the shorter crack for the same number of breaks

to the size of the microcracking cascades observed in the explicit microstructural simulation discussed in Section 4.3.1. This choice of scale corresponding to the interpore ligament allows the criterion of fracture (maximum tensile traction) to match the consequencial material response (breaking of the bond of length scale of the interpore ligament) [2].

These simulated strength and stiffness distributions (shown in figure 4-16) replace the artificial strength and stiffness distributions in the simulation of a macroscopic scale crack growing in an appropriate Mode I stress field. In order to introduce a three dimensional effect to the macroscale crack growth, we have fashioned an effective 3D element, as already described in Section 4.2.5 above. Figure 4-17 shows the effective strength and stiffness distributions, and the crack that propagates through the structure, having these local correlated distributions, and the resulting local K values of toughness that are sampled.

The generated crack paths exhibit roughness and bridging behavior, though minimal redundant microcracking. The fracture toughness normalized with that of the homogeneous equivalent microstructure is 1.15 ± 0.02 for the control[3] microstructure described previously, indicating a modest increase in toughness in the light of the maximum expected cooperative toughening ($K(\overline{\sigma}+d\sigma, \overline{k}+dk)_{\max} = (1.34 \times 1.26) K(\overline{\sigma}, \overline{k}) = 1.69 K(\overline{\sigma}, \overline{k})$).

As found in Section 4.4, the measure of local variability and correlation of the local strength and stiffness are the key determinants of the fracture behavior. The variability of strength and stiffness as measured by the coefficient of variability is found in Table 4.1, which statistically summarizes the population of local micromechanical properties for a series of large (10^4 RVE's) simulated microstructures, as studied and

[2]The choice of dimension for probing local properties has a strong dependence on the measured stiffness and strength distribution. A larger dimension of sampled microstructure tends to produce a reduced variation of the population as the values converge to the ensemble average, as seen in figure 4-15. In addition, this effect can be seen to reduce the mean value of the normalized elastic modulus, and normalized strength with respect to the fully dense values. This is an expected effect as larger sampled sections of material have a greater likelihood for containing larger flaws with associated reduced strength and stiffness

[3]The control microstructure was deemed to have many of the features of real RBSN as in Chapter 3, with a grain boundary strength equal to 75% of the full strength bulk matrix material.

discussed in Section 4.3.1. The correlation between the sampled strength and stiffness parameters, as seen in figure 4-18, is measured by the two variable correlation parameter,

$$\chi = \frac{\overline{\left[(\sigma(\vec{x}) - \overline{\sigma}) \times (k(\vec{x}) - \overline{k})\right]}}{s_\sigma(\vec{x}) s_k(\vec{x})} \tag{4.8}$$

Here σ and k are bond strength and stiffness, $\vec{x}$ is the location of an element, and s_σ and s_k are the standard deviations of the respective distributions. The value of χ is computed to be 0.84 to 0.93 for typical simulated microstructures. A value of 1.0 implies perfect correlation, and 0 independent populations. The high value of χ implies a tendency towards a critical strain criterion response with an associated reduced toughness. In addition, the variability of strength and stiffness are seen to be relatively insensitive to the details the different microstructures generated here. Although the coefficients of variability are relatively large in comparison with the variabilities obtained in the previous section for independent prescribed variations in Section 4.4.1, they range from 0.59 to 0.68 and from 0.56 to 0.77 for strength and stiffness coefficients of variability respectively. The strongest dependence of variability was seen to be on the average porosity, as porosity increases, the variability increases for both strength and stiffness.

In addition to the close correlation between local peak strength and stiffness, the close connection between local stiffness and porosity on the scale of the RVE indicates a small and relatively constant effect of the typical factors other than average porosity which govern elastic properties in porous solids, such as pore size, shape and spacial distribution. This same result was obtained in Section 4.3.1 for larger sections of microstructure, implying that over the range of scale from the interpore ligament to a scale five times larger, the simulated microstructures exhibit a limited elastic modulus sensitivity to pore shape and spacial distribution, and strong sensitivity to average porosity.

The strength and local porosity are seen to be less correlated than stiffness and porosity. The previously mentioned factors for variability of stiffness associated with

pore morphology and spacial distribution in addition to the increased variability generated by reduced grain boundary strength are assumed to be the major contributors.

The effect of grain boundary strength is also seen to be a large factor in the de-coupling of local strength and stiffness, as seen in the decrease in correlation parameter, $\chi(\sigma, k)$, from 0.951 to 0.854 for the introduction of grain boundary strength of 75% of full strength (Control), from full matrix (bulk) strength (Control, g/b = 1.0). This reduction of all grain boundary strengths, as was seen to produce a high proportion of intergranular fractures in Section 4.3.1, serves also to de-couple the local strength from local porosity as evidenced by the decreased correlation measure, $\chi(\sigma, p)$, from 0.800 to 0.684. The fact that the average local strength is reduced from 0.287 to 0.267, yet the toughness measured explicitly by propagating a crack through a microstructure through the respective populations of strength and stiffness is relatively unaffected demonstrates the potency of the variability of the local strength.

Despite the high correlation found between strength and stiffness values at the local, RVE scale, the effect of amplified variability is seen with increasing local porosity. As the porosity increases, the spread of values increases, as quantified by the coefficient of variability in figure 4-19. One important contribution is that higher porosity elements manifest higher numbers of possible configurations, within the restrictions of the reaction kinetic simulation model which produced these microstructures. This result suggests that microstructures with a higher frequency of high porosity elements, e.g. high average porosity microstructures, have the potential for higher local variability and consequential increased crack tortuosity, and associated energy release rate.

The major result of crack propagation of microstructures in a stress gradient of a large crack with element properties obtained by sampling of RVE scale sections of simulated microstructures is that the measured toughness is relatively unaffected by variables associated with pore size and shape distributions, and most strongly determined by the average porosity. The simulated fracture paths were of a similar planar character with minimal microcracking and some limited bridging ligaments.

The limits of pore size and spacial distribution imposed by the reaction kinetics model used to generate these microstructures serve to place bounds on the strength and stiffness variations available for optimal microstructure design. One case for which some insight can be made is the high porosity microstructure with associated higher variability. This demonstrates the competition between the increase in toughness due to higher variability in strength and stiffness with the reduction in toughness due to the relatively strong dependence of the elastic properties on average porosity.

4.4.4 The Transition from Cellular to Fully Dense Fracture

The transition from fracture behavior in dilute porosity to the development of cellular fracture behavior occurs over the range of intermediate porosity. Experimentally, it has been observed that the presence of enhanced microcracking, branching and increased crack complexity occurs with increasing porosity[108]. At dilute porosity the crack interacts with pores infrequently and retains its integrity and sharp radius of curvature over much of the crack front. At some level of porosity however, the ability of the material to 'transmit' the sharp crack tip is restricted by an increased concentration of crack front length with small curvature as is found in cellular material. The fracture of cellular structures in tension is the succession of ligament bending and fracture in a local field better characterized by an ellipsoidal discontinuity rather than a stress singularity. The transition between this behavior and the propagation of a crack with a well defined crack tip singularity is investigated here. The method is to use a modified fracture criterion for the purpose of varying the potency of the crack tip stress field.

Because of the limitations in computing crack tip stresses in the discrete bond model, the propensity for bond breakage at the crack tip is considered to be determined by the average stress in the crack tip element. This produces a fracture criterion based on local stress that fits the flaw severity of the long crack to the resolution of the mesh, which is interpreted to represent the scale of the cellular material. It is the very potency of the crack tip singularity to translate far field loading into high crack tip stresses that gives homogeneous brittle materials their unique character. For high

porosity microstructures, the potency or the sharpness of the crack tip is crucial in determining the crack morphology and fracture toughness.

Specifically, the competition between crack tip advance and fracture processes that occur away from the crack tip, such as independent microcrack nucleation, is crucial in determining the crack morphology. The ratio of the propensity for crack advance in the element containing the stress singularity to that for microcracking, etc. in the surrounding stress field is key to this competition. In this light, we have applied a modified fracture criterion at the crack tip to explore this ratio.

Assuming that the stress field in the element just ahead of the crack tip follows the form[4] of $\sigma \sim 1/\sqrt{r}$, we can apply the fracture criterion of stresses at closer dimension to the overall element strength by extrapolation. The method for doing this is to record the previously broken bonds and to modify the fracture condition for bonds surrounding the crack tip. The modification effectively changes the element strength by a factor $f(=\sqrt{\frac{\rho_{\text{mesh}}}{\rho^c}})$, where ρ_{mesh} is the radius of curvature of the mesh, and ρ_c is the position ahead of the ghost crack where a quasi-homogeneous material fracture criterion is to be applied. The term f thus relates the scale of the mesh to the desired radius of curvature.

The effect of increasing the effective crack tip sharpness was explored for a crack sampling a structure with an idealized distribution with strength variation ($c(\sigma)$=0.52) and constant stiffness, k_o. Toughness values which are normalized with the properties of the homogenized equivalent material allow comparisons to be made for highly variable material over the range of crack tip sharpness factors. The toughness of the equivalent homogenized material is $K(\overline{\sigma}, k_o) = (\overline{\sigma}/\sigma_o)K(\sigma_o, k_o)$ and for the modified fracture criterion, the homogeneous equivalent toughness is $K(\overline{\sigma}, k_o)^{amplified} = (\overline{\sigma}/\sigma_o)K(\sigma_o, k_o) \times f$. The factor f must be accounted for in this manner in order to maintain normalization with fracture toughness of the same reference configuration having uniform values of strength and stiffness, $\sigma_o = k_o = 1$. Figure 4-20 shows the relative toughness, $\Delta K/K(\overline{\sigma}, k_o)^{amplified}_{0.52}$, with the average deviation of the crack from planar or profile width, where $\Delta K = (\overline{K}_{measured} \times f - K(\overline{\sigma}, k_o)^{amplified}_{0.52})$ for various

[4]To first order terms this will be the nature of stress concentration in front of an elliptical hole

values of f.

As the effective sharpness increases, the crack configuration becomes less diffuse, and the main crack path becomes better defined, as seen in figure 4-21. A definite main crack is observed for f = 4, with a crack profile zone width of 12.6 cell dimensions, and little increase in toughness as compared to a microcrack cloud radius of 35 cell dimensions for f = 1. With the case of f = 9, minimal microcracking is observed, however the crack path has substantial roughness with a profile zone width of 10.2 cell dimensions, and some bridging ligaments. The relative toughness is a factor of 2.1 higher than the homogenized equivalent material, which indicates that the typical toughening trends with increasing crack complexity do not apply. The increased toughness is observed to be due to crack bridging elements created by the nucleation of microcracks ahead of the main crack tip, and growth and coalescence of these independent cracklets with the main crack. For amplification factor f above 20 ($1/\sigma_{min}$), sufficient to guarantee the fracture of the crack tip element, the crack path is flat and the toughness is equal to the average toughness of the homogenized material.

By biasing the fracture processes from the stress field around the crack to the crack tip by effectively reducing the crack tip radius, some light is shed on the transition from cellular fracture behavior where the crack tip is ill defined and without a stress singularity to a sharp, potent, crack tip that is easily transmitted through the material. The results here indicate one character of the transition between cellular and fully dense fracture in highly variable microstructures is the decrease in microcracking zone size and increase in the number of bridging events. Thus there is a competition between the toughening by microcracking of isolated ligaments which are intrinsically stable due to surrounding pores, and bridging effects which on a normalized basis have the potential for toughening by a factor of 2.1.

4.4.5 Spacial Correlation of Element Properties

The preceding analyses for the fracture of structures with prescribed variabilities in local strength and stiffness are for distributions of element properties which are distributed randomly in space. The justification for this is that in most experimentally

observed structures the porosity is distributed homogeneously on scales larger than the representative volume element described here (see figure 2-15). In the ideal simulated structures, the radial correlation function is measured, and approachs zero at the dimension corresponding to a small multiple of the average pore size, as seen in figure 4-22. In some cases, apparent fluctuations were seen in density in experimentally observed microstructures in the form of slender pore channels forming a cell-like structure with periodicity of approximately 2-5 microns or 10 RVEs, as described in Chapter 2. In order to explore the effect of spacial correlation, an artificial correlation length is imposed on a structure of given variability. For simplicity, a periodic function with wavelength to cell size ratio of 10 and amplitude of 0.35 of the mean was multiplicatively superimposed on a microstructure with perfectly correlated strength and stiffness with a coefficient of variability of 0.231. As seen in figure 4-23, the crack propagates through the structure with periodic spacial correlation with reduced deflection and toughness by a factor of 1.35. The crack has deflected to the path of least fracture resistance as allowed by the spacial correlation of local fracture properties.

4.5 Discussion

4.5.1 Fracture of Porous Microstructures

We have demonstrated a connection between pertinent microstructural features and crack propagation resistance of porous heterogeneous materials by simulating the fracture process in computer generated microstructures. However inexact the solutions may be, by associating the development of microstructural features and the resulting heterogeneities in local stiffness and strength with processing parameters, the gap can be bridged between the manner of processing a material and mechanical properties. This is especially relevent for fracture toughness which is particularly sensitive to microstructural heterogeneities. For example; the variability in local strength and stiffness affects the fracture toughness more strongly than average properties such as the elastic modulus.

The two dimensional fracture simulations for representative microstructures with 21-31% porosity exhibit a stable ligament microcracking behavior which results in the evolution of sub-critical damage leading to an eventual fracture instability. In the tensile simulation under displacement control no instability develops, but rather characteristic stress strain curves with long tails are obtained for material degeneration. The tensile toughness values are significant in comparison with those of a perfect homogeneous material, $w = \int \sigma d\epsilon \sim 0.15(\sigma_c \epsilon_c/2)$, where w is the tensile toughness and subscript c indicates critical stress and strain values of a reference homogeneous material. Paradoxically, an otherwise perfect solid with a stress amplifying defect will have less energy absorbing capacity than the porous microstructures analyzed here if the stress concentration is more than approximately, $k_{\text{amp}} = \sqrt{(\sigma_c \epsilon_c/2)/\int \sigma d\epsilon} \sim 3$.

However, the frequency and potency of this beneficial microcracking mechanism is strongly determined by the blunting ability of the surrounding pores. For three-dimensional microstructure, the possibility exists for crack growth in the third dimension, and the blunting effect may be diminished. A fully three dimensional treatment of crack interaction with porosity is needed to fully evaluate this effect.

This discreteness result of the fracture behavior, as is found in other systems such as coarse grained alumina [103], was utilized in the development of the next stage of modelling of propagation of a large crack through the microstructure. The homogenization of the microstructural details and replacement with elements which have the equivalent properties on the scale of the microstructure fracture discreteness allows for the crack growth increment to match this length scale.

4.5.2 Toughness Dependence on Local Material Variability

Crack propagation in simulated microstructures

The results of crack propagation in a stress gradient of simulated microstructures indicate that the measured toughness is relatively unaffected by the details of the pore population size and shape, and most strongly determined by the average porosity. The limits of pore size and spacial distribution imposed by the reaction kinetics model used

to generate these microstructures place bounds on the strength and stiffness variations available for microstructure design. The simulated crack paths were of a similar character, qualitatively planar with few redundant cracks and few bridging elements. These results can be rationalized by examining the sampled properties of the local strength and stiffness of simulated microstructures on the scale of the porosity. This reveals a high correlation between the microstructural element strength and stiffness as measured by the two variable correlation parameter, χ, defined in equation 4.8, which ranged from 0.81 to 0.93, between the two extremes of 0 and 1 but closer to the less potent toughening of the critical strain criterion behavior.

Design of tough microstructures

The design of tough porous materials, like the RBSN microstructures studied here, then reduces to the introduction of variability in properties on the length scale of the fracture discreteness and decoupling of local strength and stiffness. Variability of elastic stiffness and strength on scales larger than individual pores give rise to increasing crack tortuosity, microcracking, bridging and associated R-curve behavior. Optimal toughness was obtained with strength and stiffness variability sufficient to create a cooperative toughening effect from crack bridging and microcracking effects with an otherwise minimal microcrack cloud extent. The transition to generalized microcracking, and associated material degradation, which should be avoided, was found to occur at high values of the coefficient of variability of strength and occurred over a small range. This suggests the avoidance of excessive strength variability, and a practical difficulty in producing microstructures toughened by the microcrack toughening mechanism.

Independent assignment of strength and stiffness (correlation of 0) produces a cooperative effect and a structure which is tougher than the equivalent homogenized material and also in comparison with the case of proportional strength and stiffness (correlation of 1). This latter distribution of element properties effectively produces a critical strain fracture criterion and a reduced toughening effect.

4.5.3 Sources of Variability

The correlation of strength and stiffness was found to be the average porosity, on both a local representative volume element scale, and on a larger scale encompassing 25 representative volume elements. On the scale of the RVE, typical correlation parameters for stiffness and strength on porosity are 0.84 and 0.70, so that the remaining variability must arise from expected effects as variations in pore geometry and spacial distribution, and grain morphology. In real materials, additional variation arises potentially from effects not explicitly considered in the model here, such as from effects of thermal mismatch residual stresses and elastic anisotropies, which are considered potent heterogeneities in the nucleation of microcracks. In addition, the limitations of the simulated microstructures sampled here, the two dimensional character and limited resolution may restrict the degree of microstructural variations.

The elastic properties were found to be more correlated with the average porosity on the RVE scale, than on the strength which has the additional variability contribution of the grain boundary strength. The introduction of weaker grain boundary interfaces to 75% of the bulk strength, sufficient to produce predominantly intergranular fracture, produced minimal reduction in average strength, presumably due to a transition to intergranular fracturing at lower stressed locations in the microstructure, and this produced an increase in the coefficient of strength variability sufficient to increase the fracture toughness. Further reduction in grain boundary strength reduced the average strength and toughness.

An additional source of variability was found to exist at higher levels of porosity. Although a high correlation of strength and stiffness on porosity was generally found, the dependence is weakened at higher porosities. The direct implication is of increased variability at higher porosity and a de-coupling of local strength and stiffness. These trends illustrate the competition between the increase in toughness due to higher variability in strength and stiffness at higher porosity with the reduction in toughness due to the relatively strong dependence of the average elastic and strength properties on average porosity.

4.6 Conclusions

The substantial tensile toughness of the porous microstructures studied here has been shown to be due to stable ligament microcracking behavior which results in the evolution of sub-critical damage, with characteristic stress strain curves with long tails.

The variability of localized micromechanical parameters of strength and stiffness on scales of the representative volume element produced crack paths with tortuosity on scales larger than the RVE. By assessing this variability and incorporating three dimensional effects associated with crack growth restraint into weak elements by the interaction of surrounding tougher elements, minimal microcracking and a weak propensity for bridging effects was demonstrated. An optimal toughness was obtained with uncorrelated strength and stiffness variability to harness the synergism of crack bridging and microcracking effects with an otherwise minimal microcrack cloud extent. At high porosity, higher variability and a decoupling of local strength and stiffness was found indicating potential for increasing toughness at higher average porosity levels. Therefore the design of tougher microstructures in the highly heterogeneous porous microstructures examined here involves the incorporation of sufficient variability in strength and stiffness at the scale of the discrete fracture events, here at the inter-pore ligament dimension, sufficient to produce tortuous crack paths and bridging ligaments with only minimal redundant cracking.

Simulation	strength	stiffness	porosity	c(σ)	c(k)	CORRELATION			K/Ko
Description	σ/σ_o	k/k_o	p			σ-k	σ–p	k–p	
Control	0.27	0.32	0.25	0.61	0.68	0.85	-0.68	-0.84	0.65
(1)	0.23	0.32	0.25	0.64	0.66	0.93	-0.77	-0.84	0.50
(2)	0.21	0.24	0.31	0.68	0.75	0.81	-0.60	-0.81	0.67
(3)	0.32	0.43	0.19	0.60	0.56	0.93	-0.79	-0.87	0.82
(4)	0.22	0.30	0.25	0.59	0.63	0.93	-0.75	-0.81	0.57
(5)	0.25	0.29	0.28	0.66	0.77	0.84	-0.65	-0.83	0.65
(6)	0.26	0.32	0.24	0.62	0.68	0.85	-0.67	-0.85	0.65
Control	0.29	0.32	0.25	0.64	0.68	0.95	-0.80	-0.84	0.63
(no grain boundaries)									

Table 4.1: Statistical Summary of Local Micromechanical Variability for Simulated Microstructures.

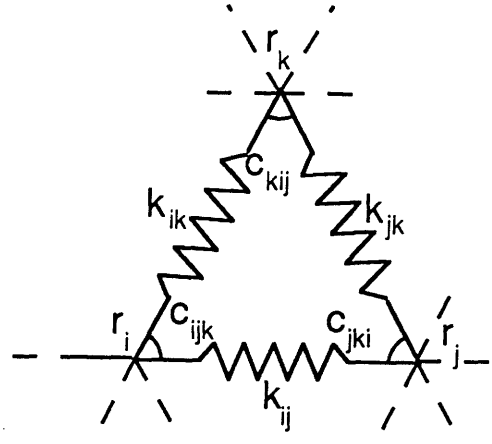

Figure 4-1: The configuration of the linear and watch springs in the mesh

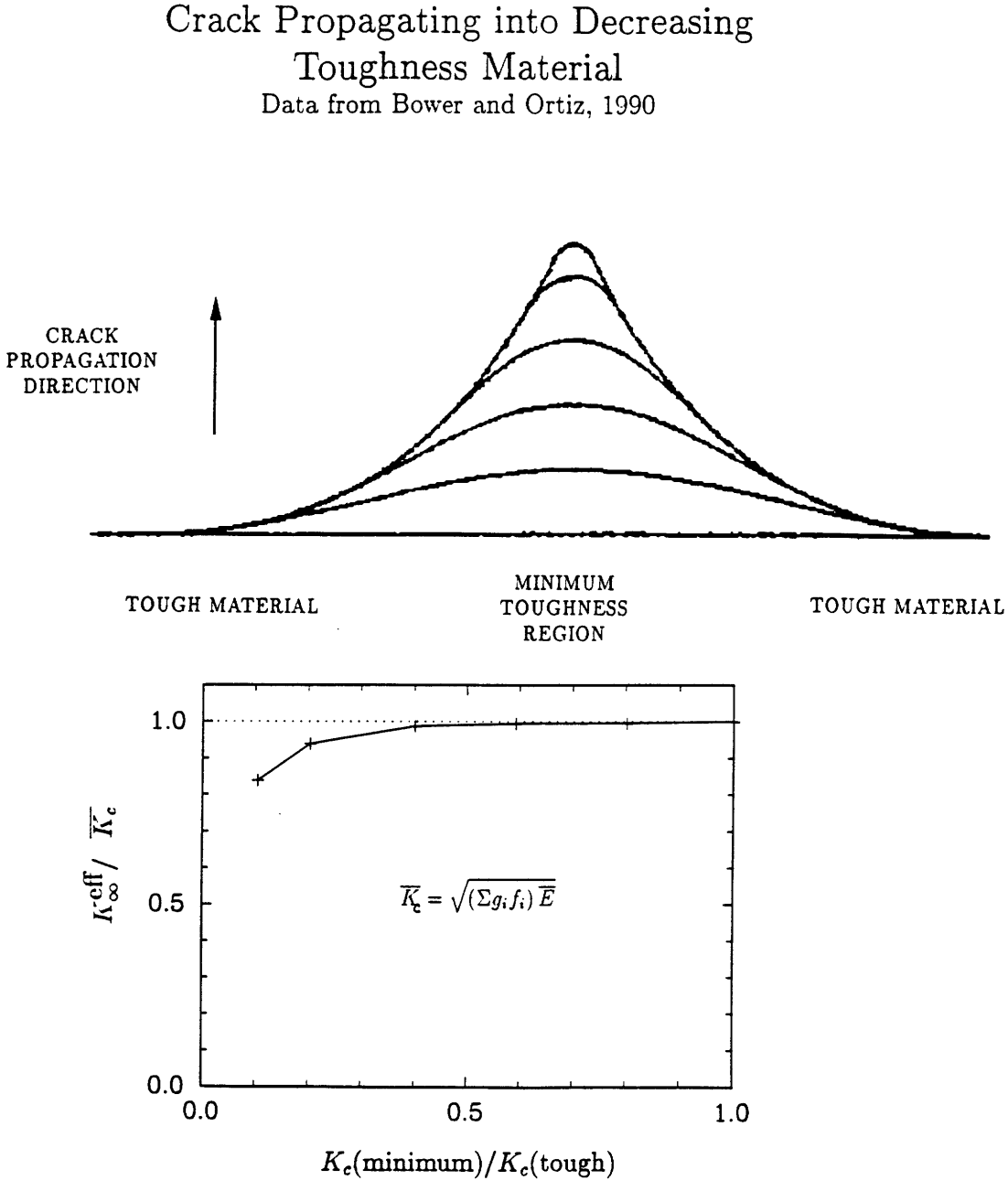

Figure 4-2: A comparison between an effective stress intensity based upon the line integral of g, energy release rate, and the more accurate solution from Bower and Ortiz, 1990.

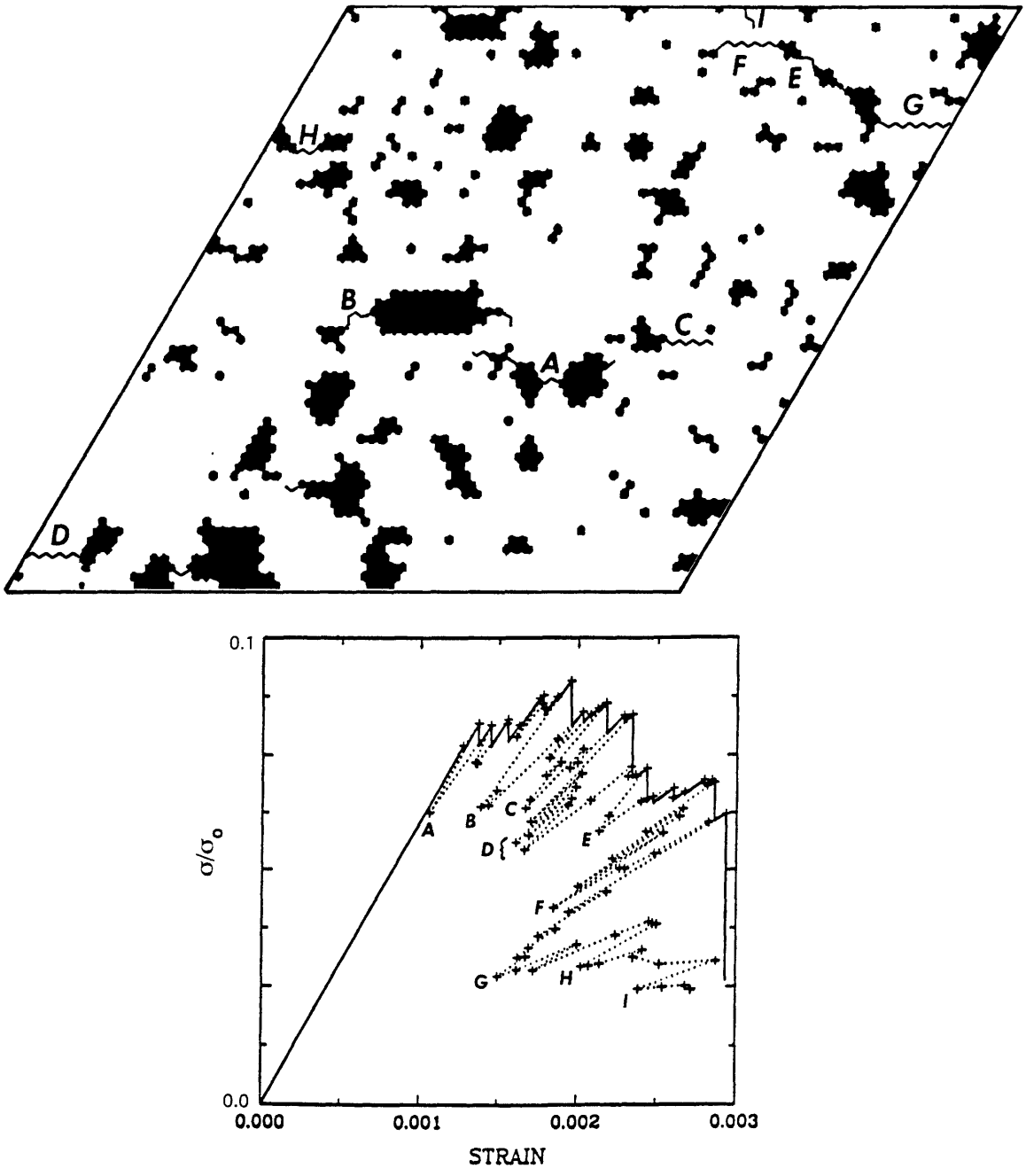

Figure 4-3: Constitutive behavior and associated microstructural features of a microstructural section from a digitized micrograph of RBSN.

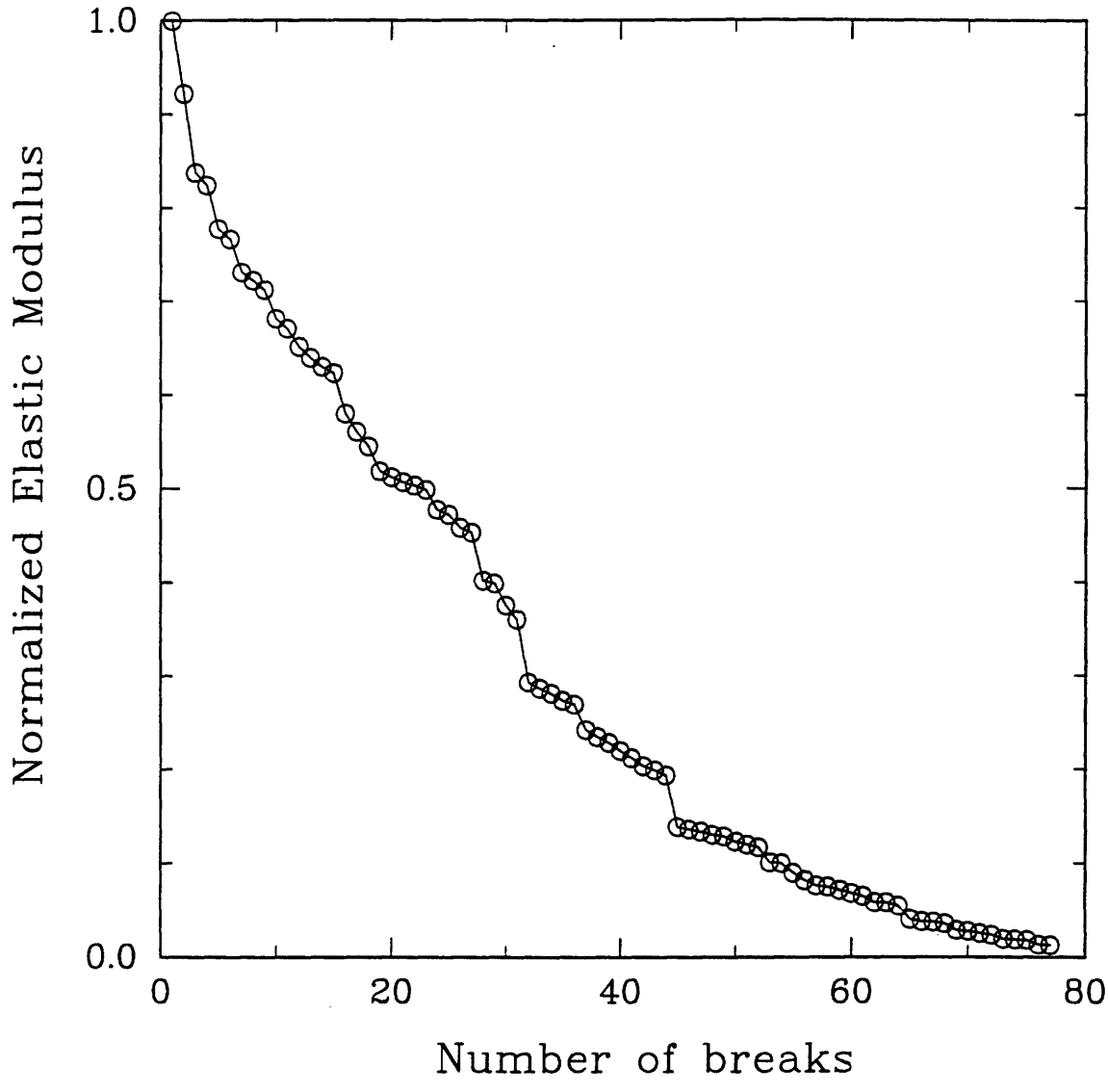

Figure 4-4: The elastic modulus is a smooth function of damage accumulation. Note the jumps associated with pore linkage and subsequent nucleation of a microcrack elsewhere.

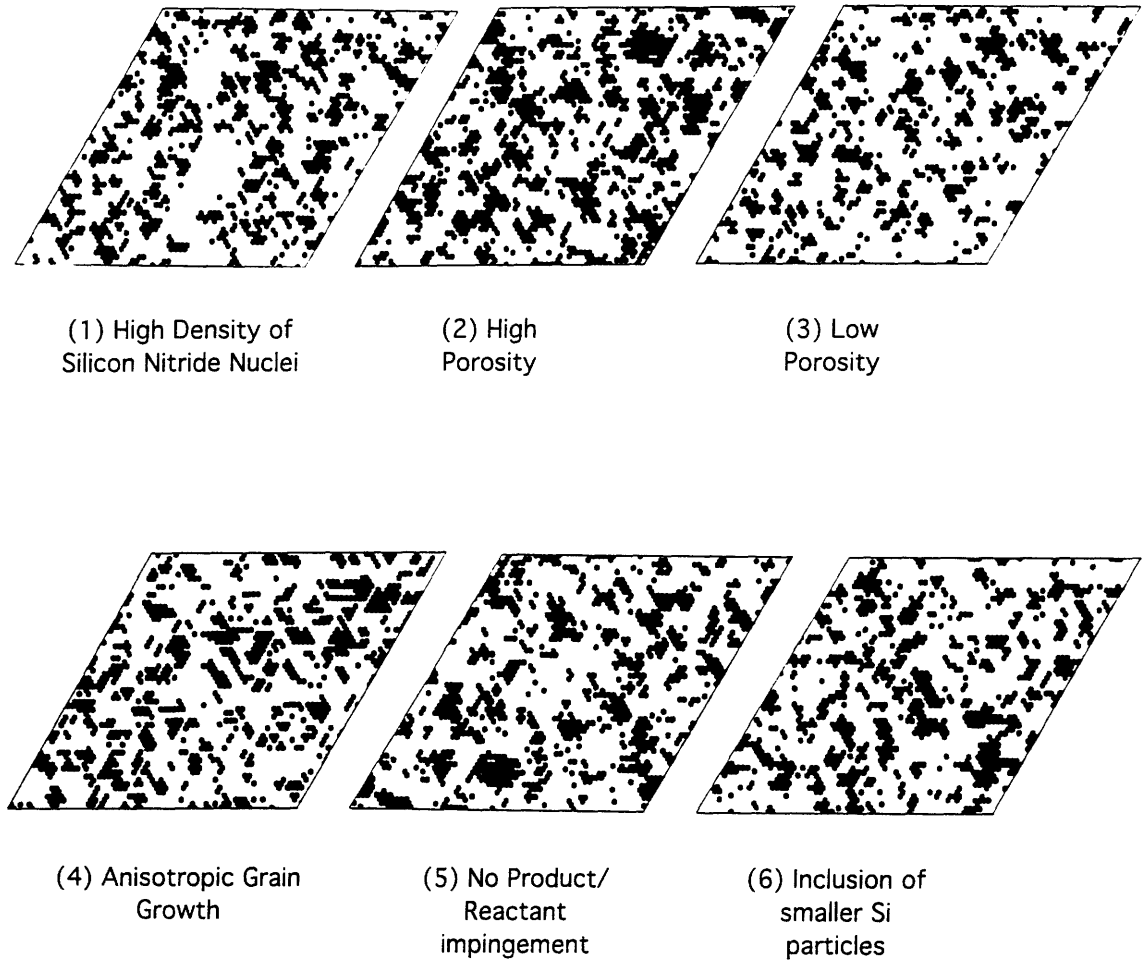

Figure 4-5: Summary of the variety of microstructures produced under different simulated conditions.

Control Microstructure, (c)

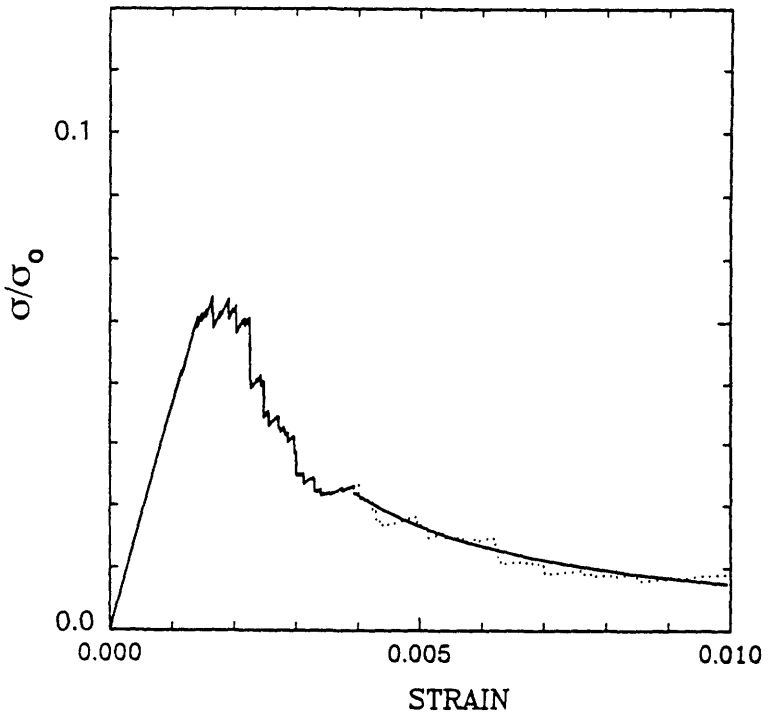

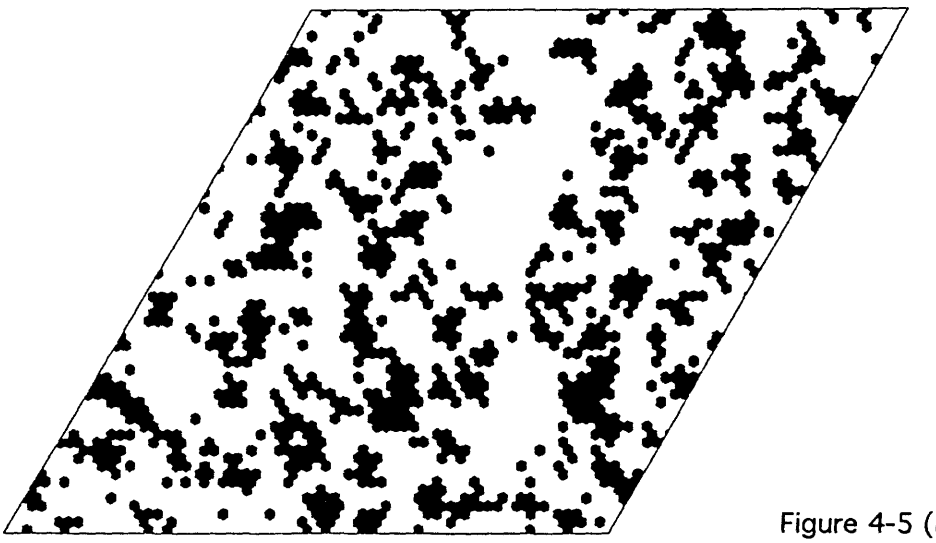

Figure 4-5 (b)

High Silicon Nitride Nuclei Density

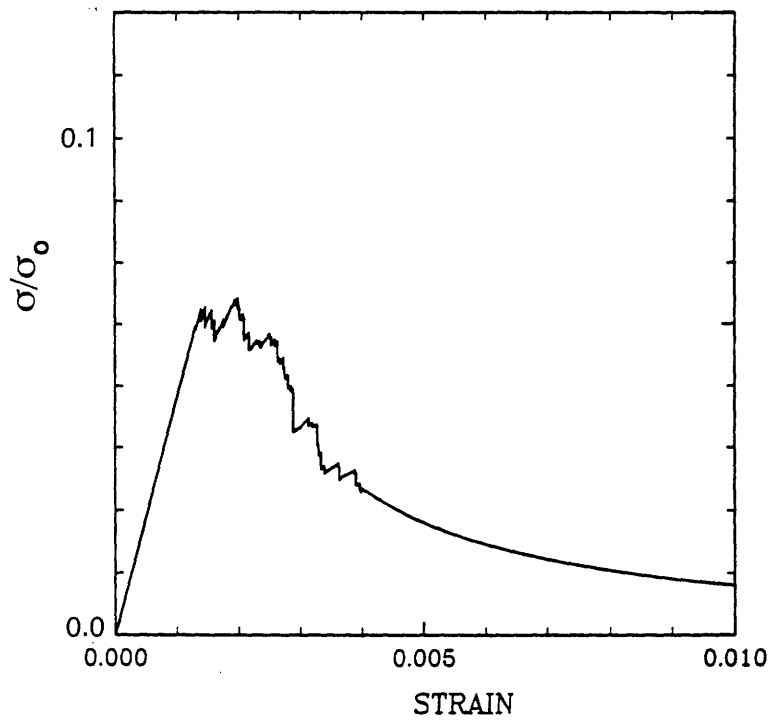

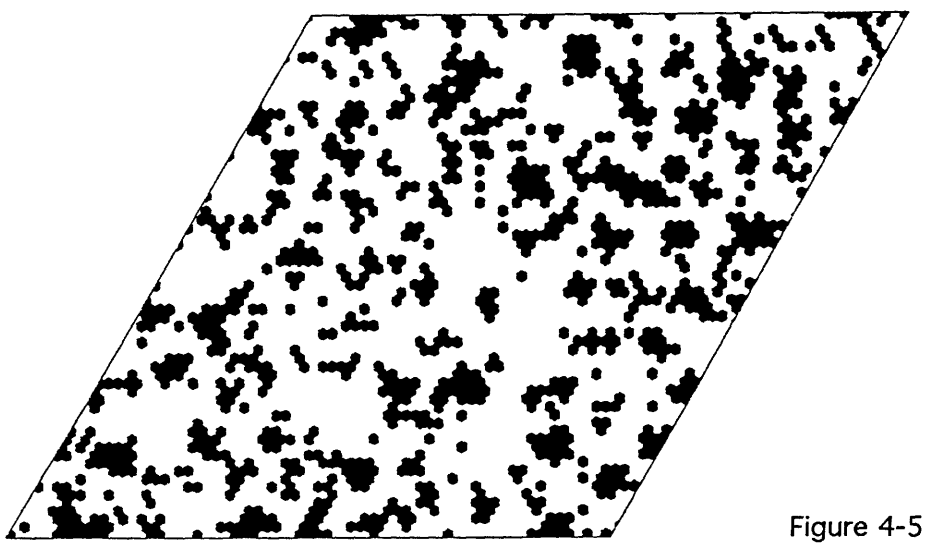

Figure 4-5 (c)

High Porosity

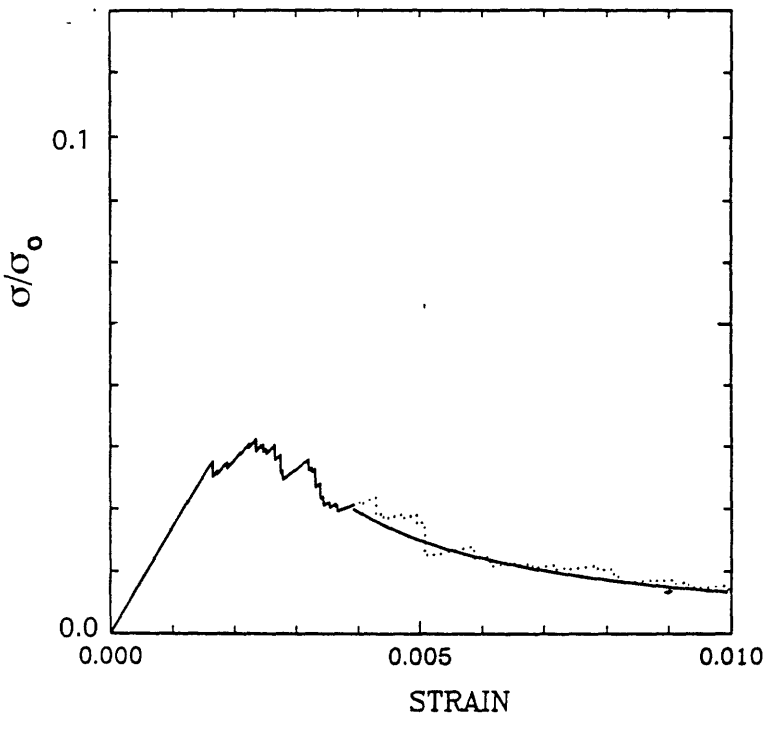

Figure 4-5 (d)

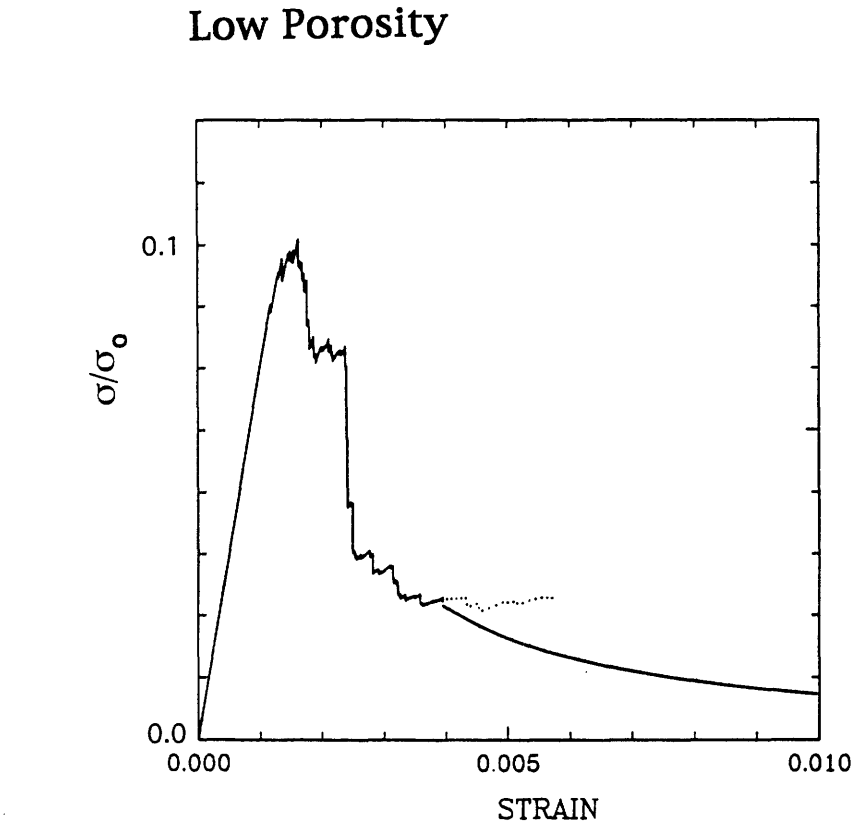

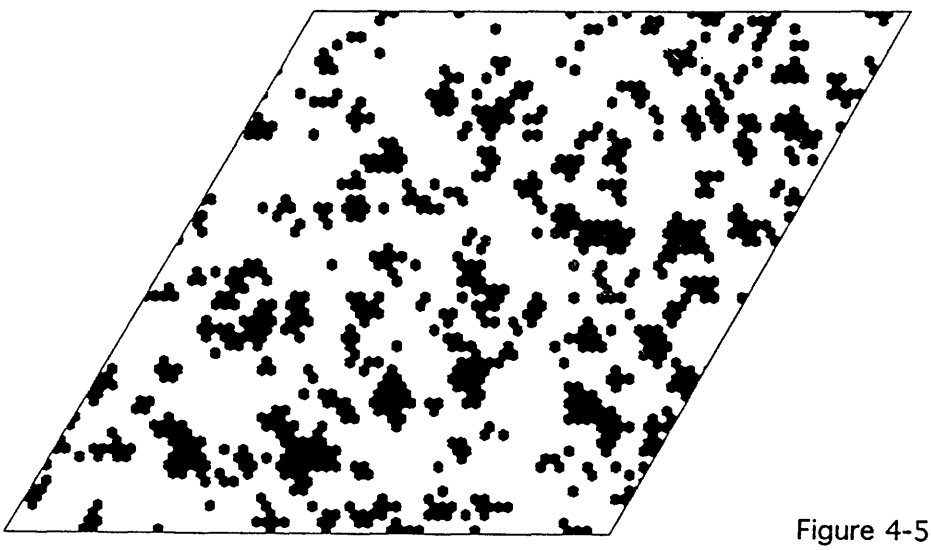

Figure 4-5 (e)

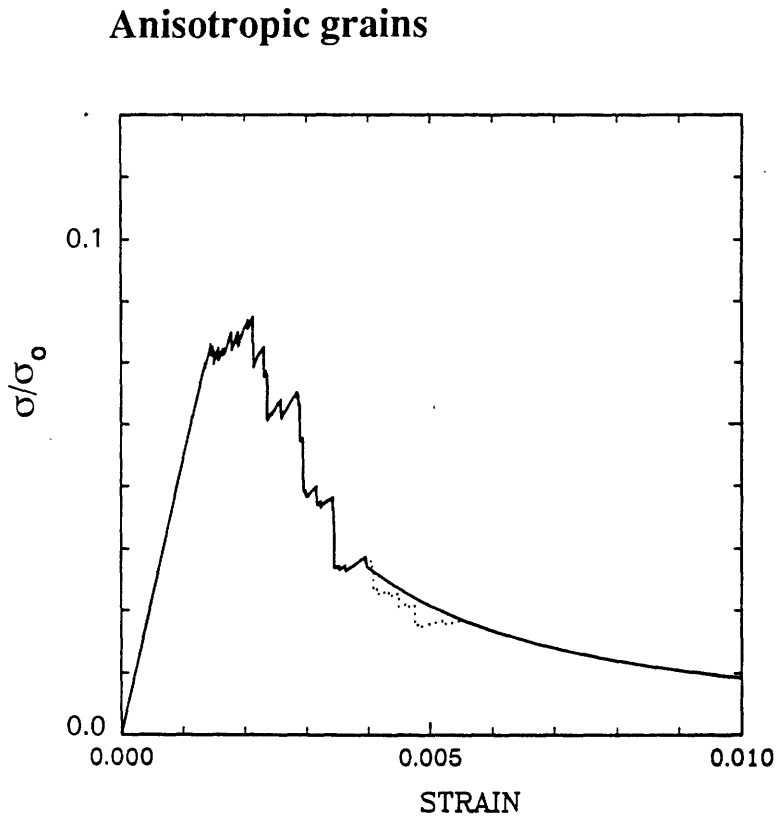

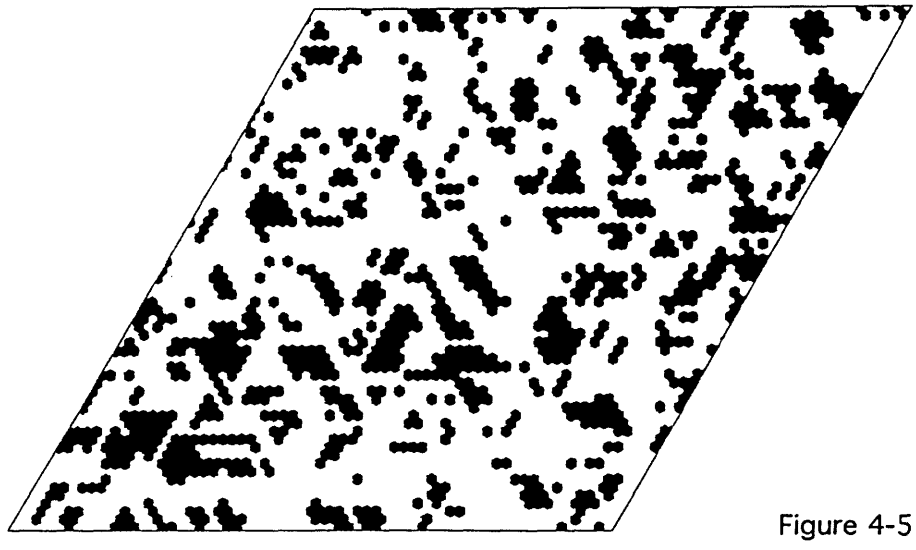

Figure 4-5 (f)

No product / reactant impingement

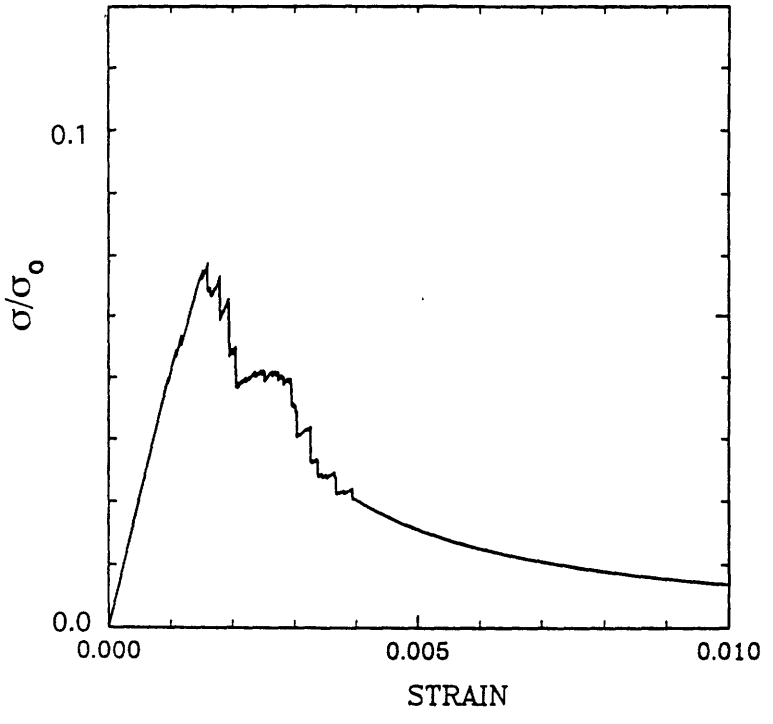

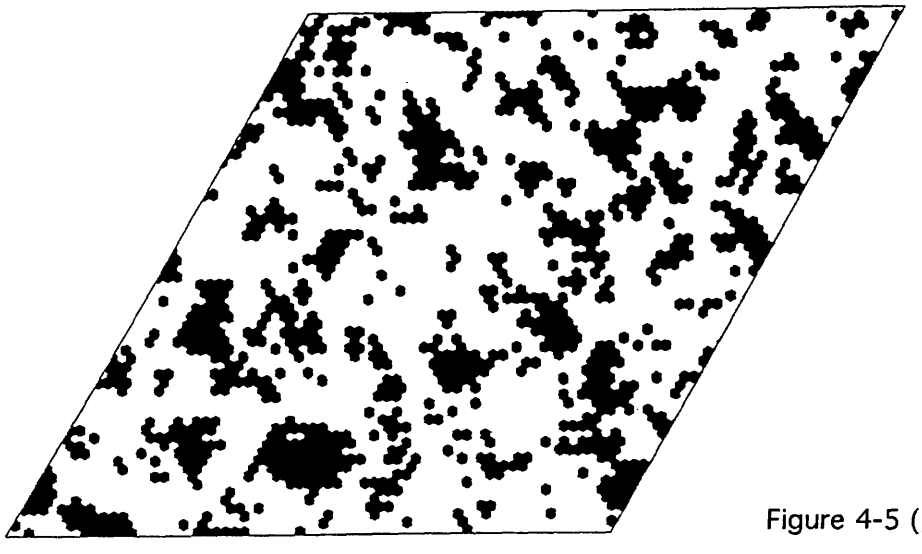

Figure 4-5 (g)

4 wt% Smaller Si Particle Population

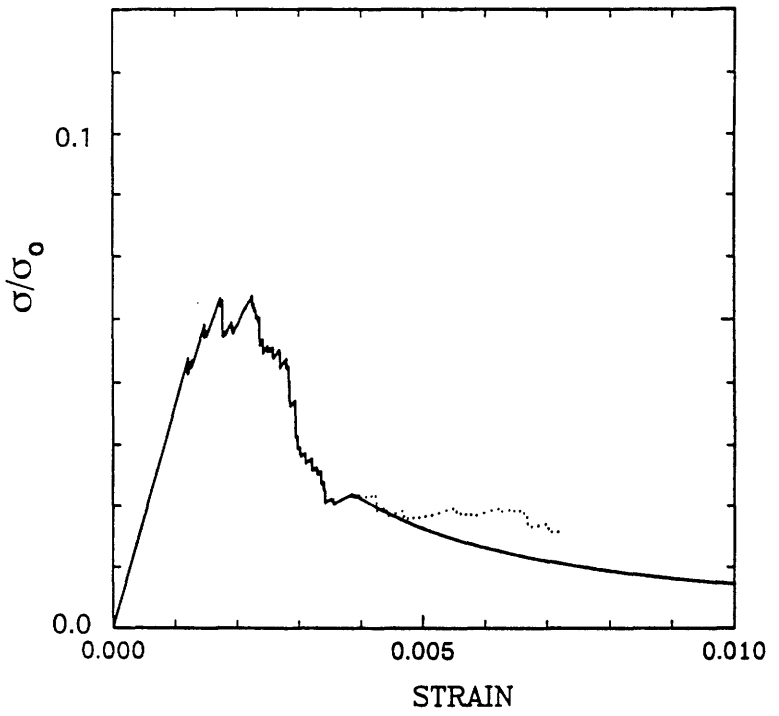

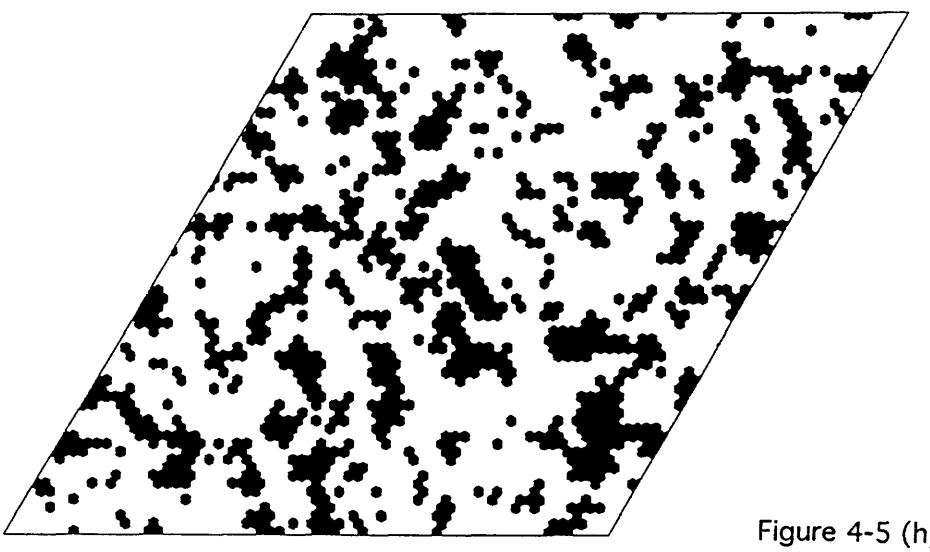

Figure 4-5 (h)

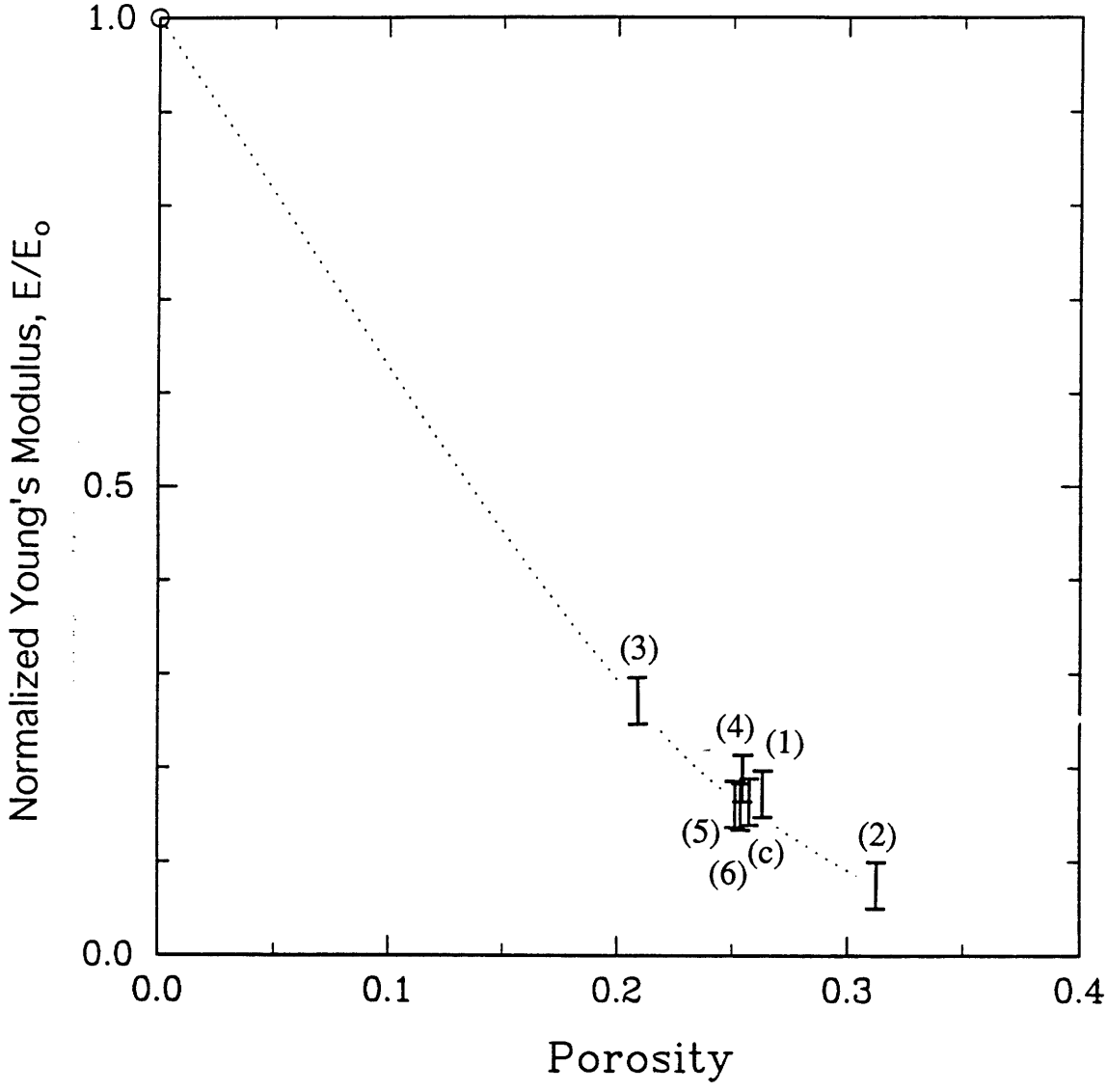

Figure 4-6: Young's modulus for large microstructural segments encompassing 25 representative volume elements

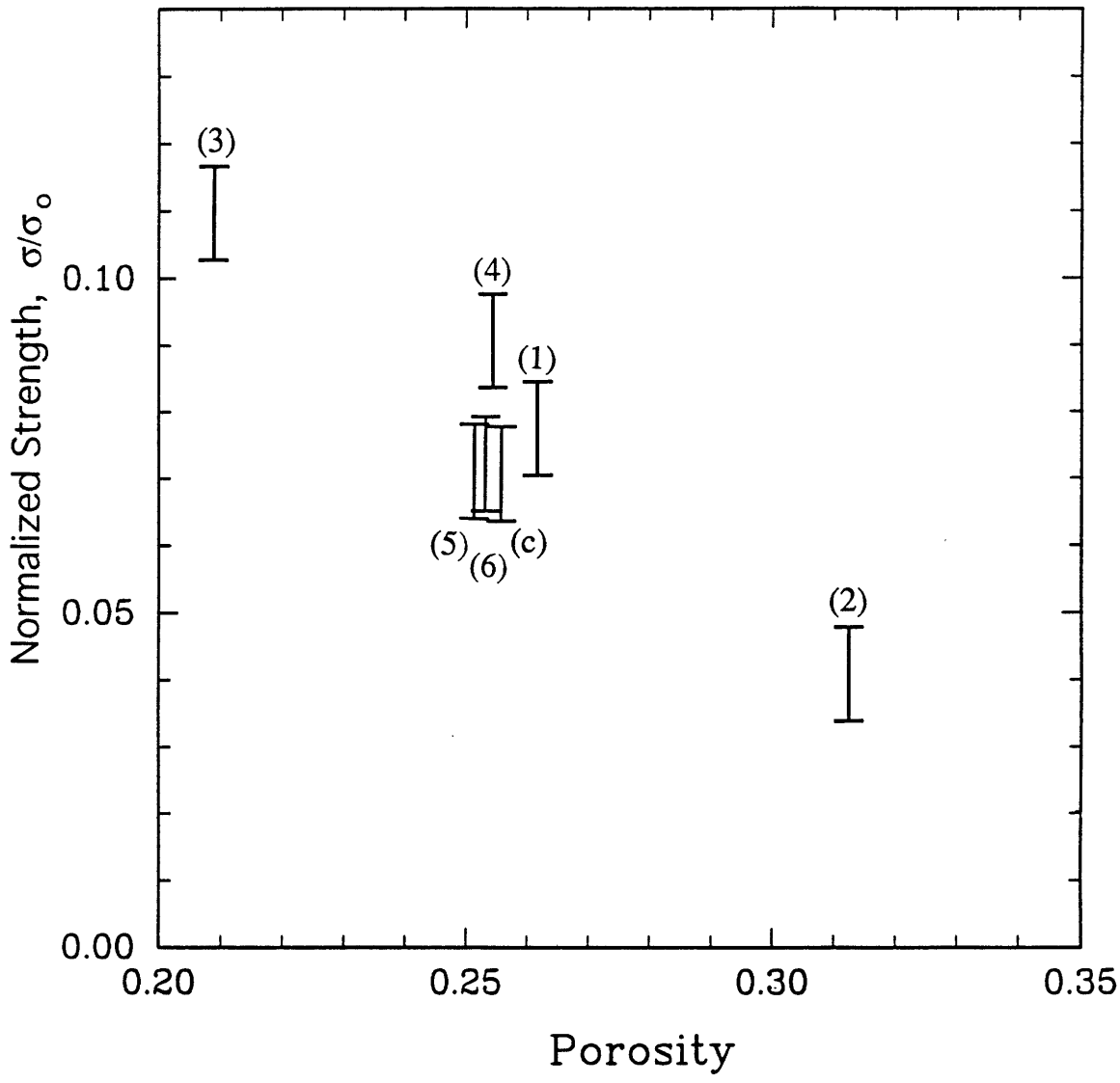

Figure 4-7: Maximum strength for representative volume elements normalized with bulk bond strength

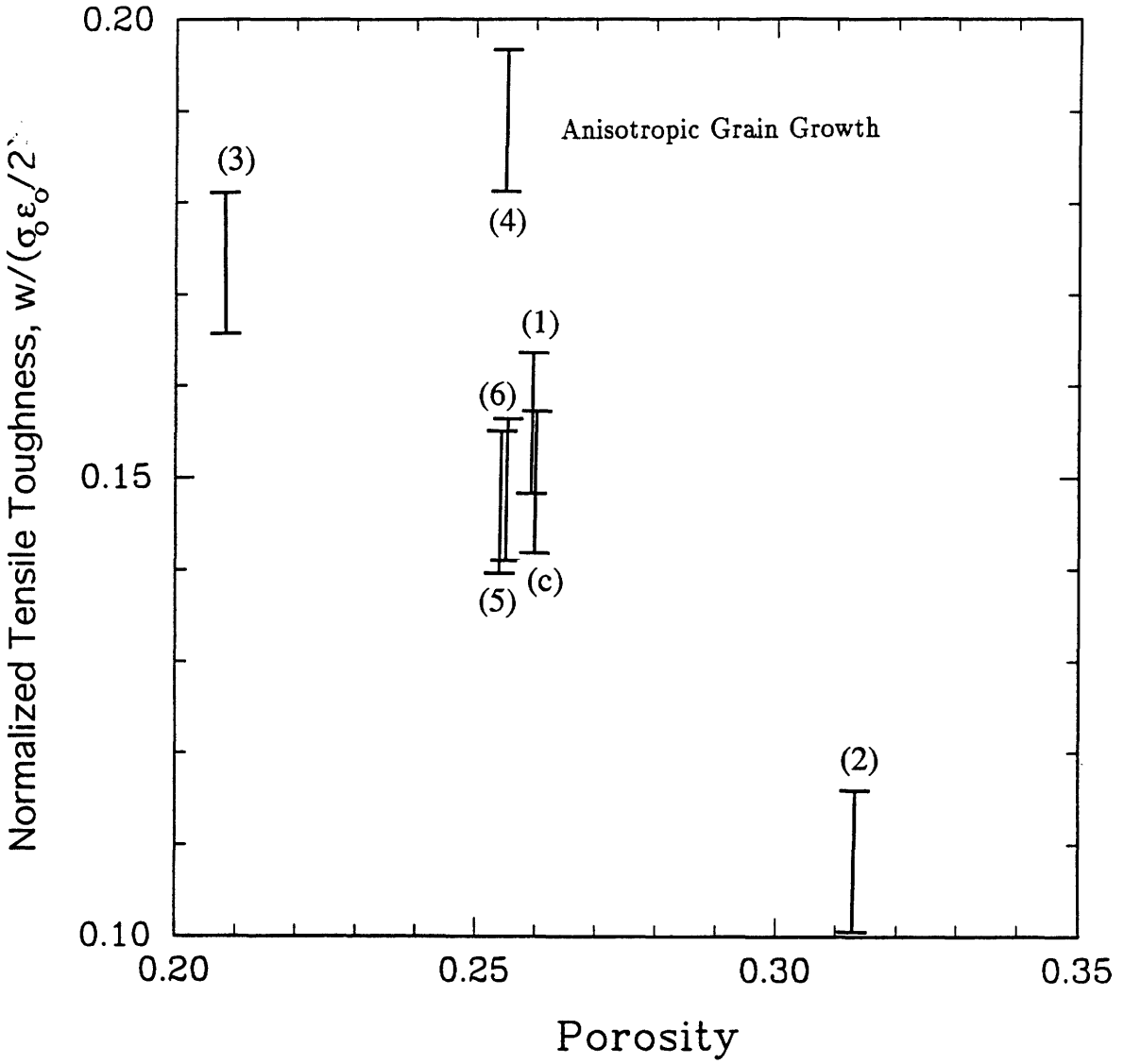

Figure 4-8: Tensile toughness for various microstructures

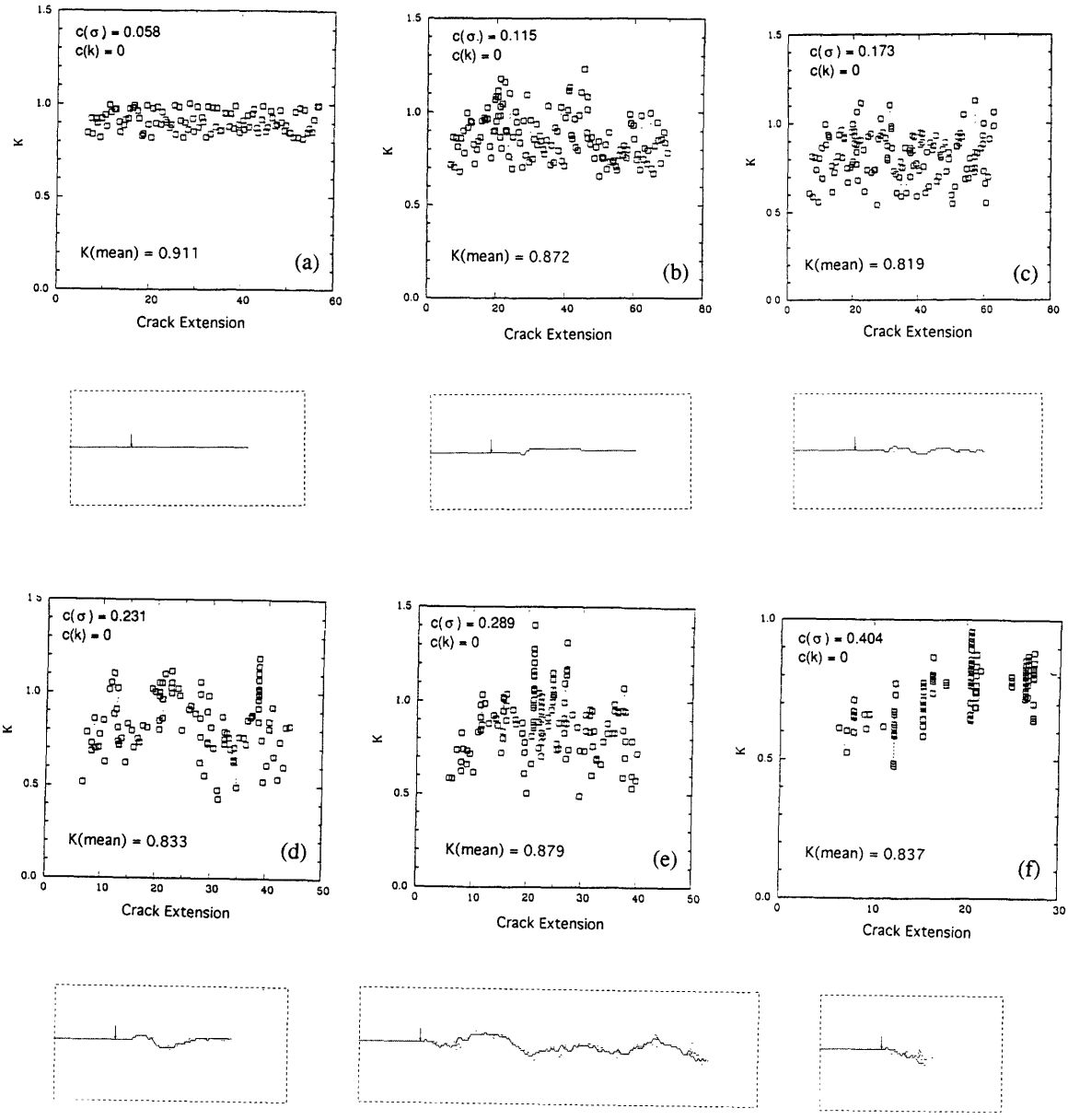

Figure 4-9: Experiments on homogenized microstructure with variability in bond strength with constant, maximum stiffness.

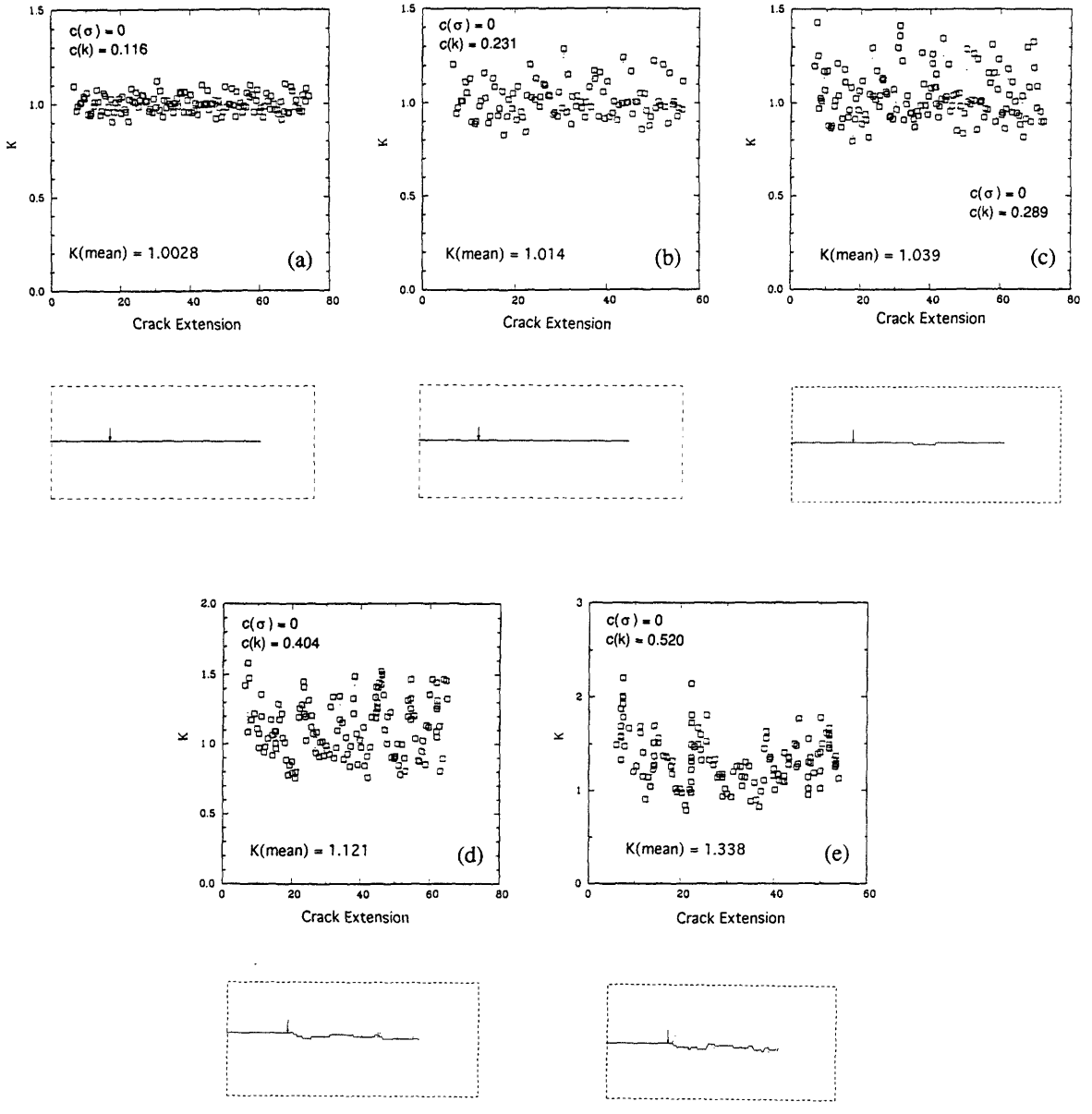

Figure 4-10: Experiments on homogenized microstructure with variability in bond stiffness with constant, maximum strength.

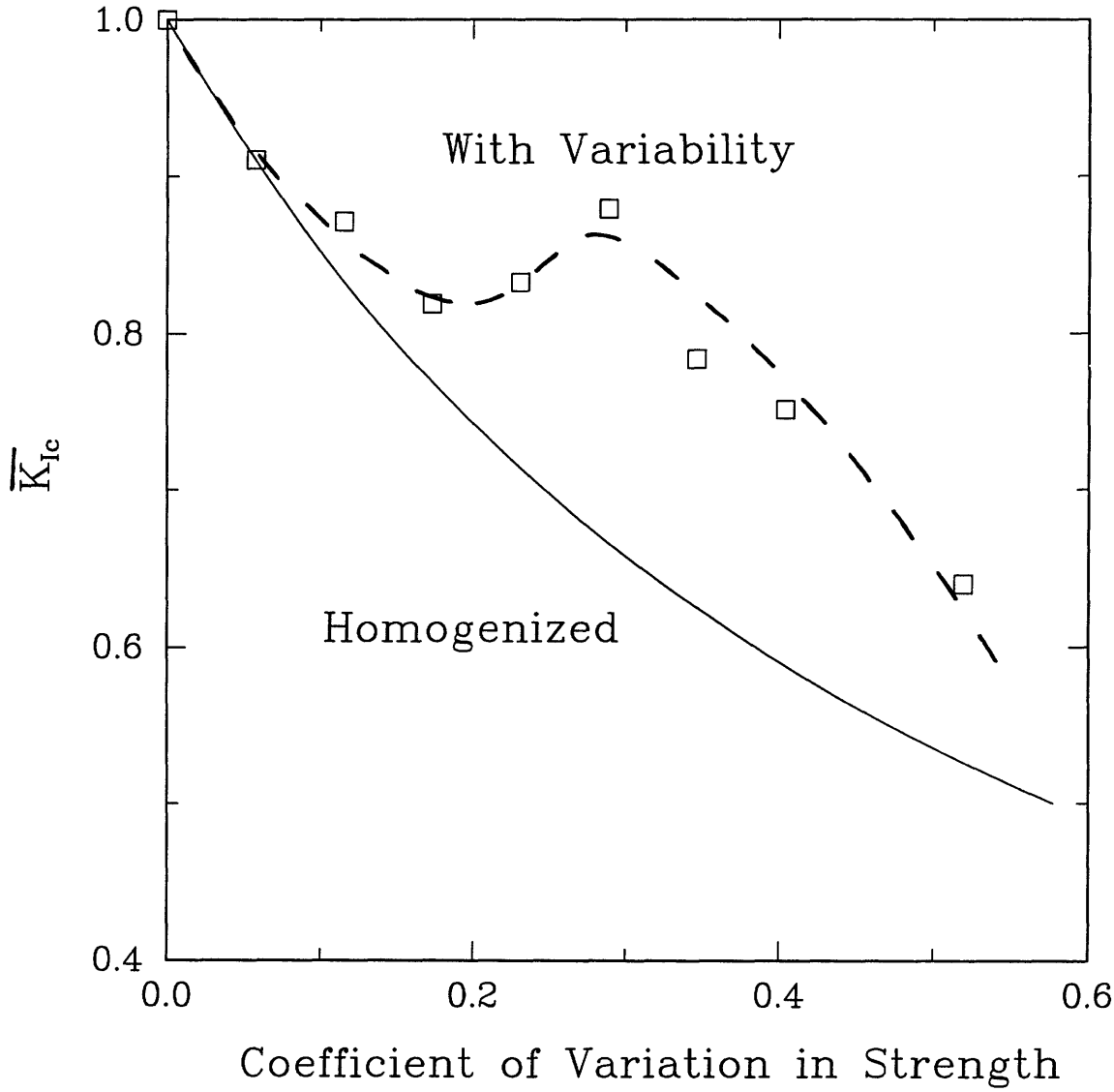

Figure 4-11: Variability in simulation bond strength in comparison with homogenized equivalent material.

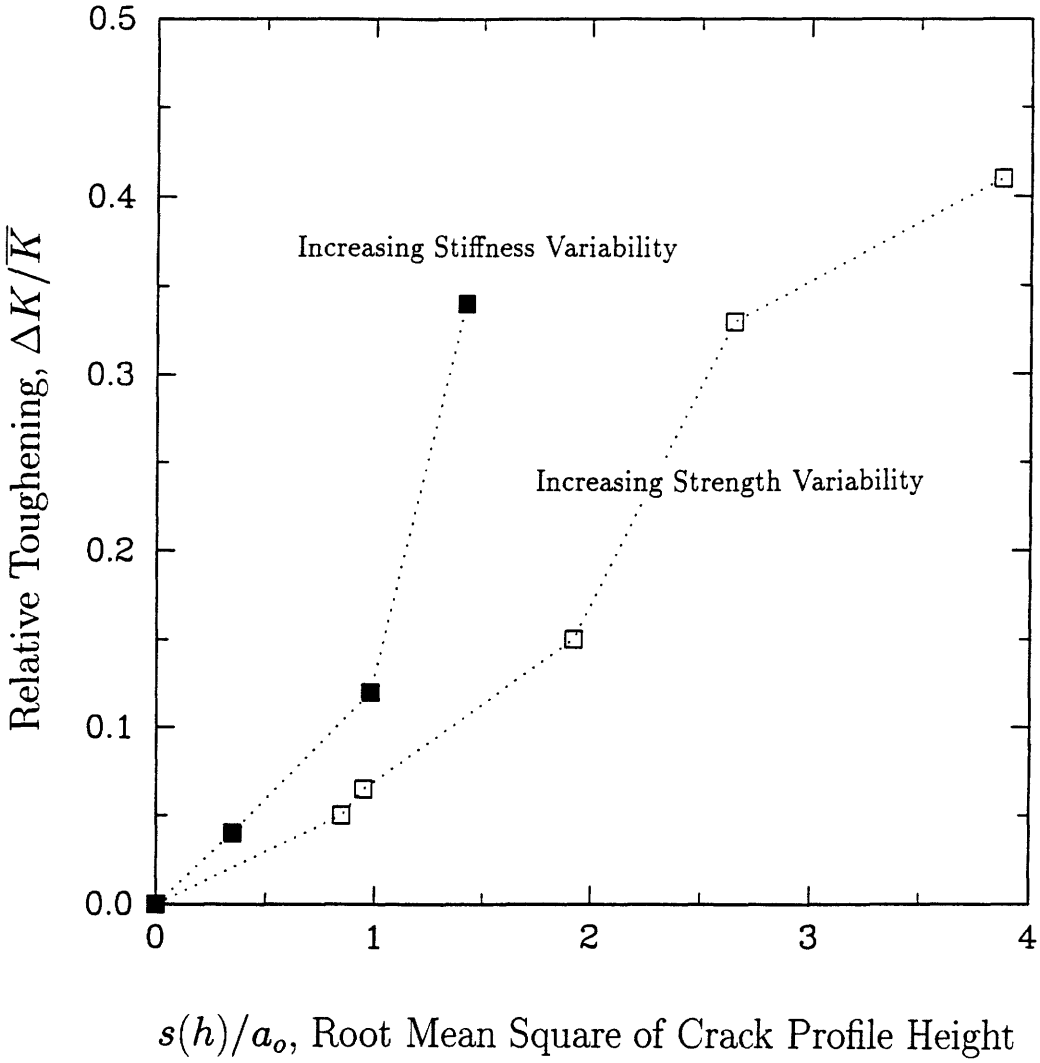

Figure 4-12: The correlation between crack profile height (rms of crack profile height coordinate) and the relative toughness indicates crack deviation from planar morphology relates to measured toughnening due to such effects as crack deflection and microcrack shielding.

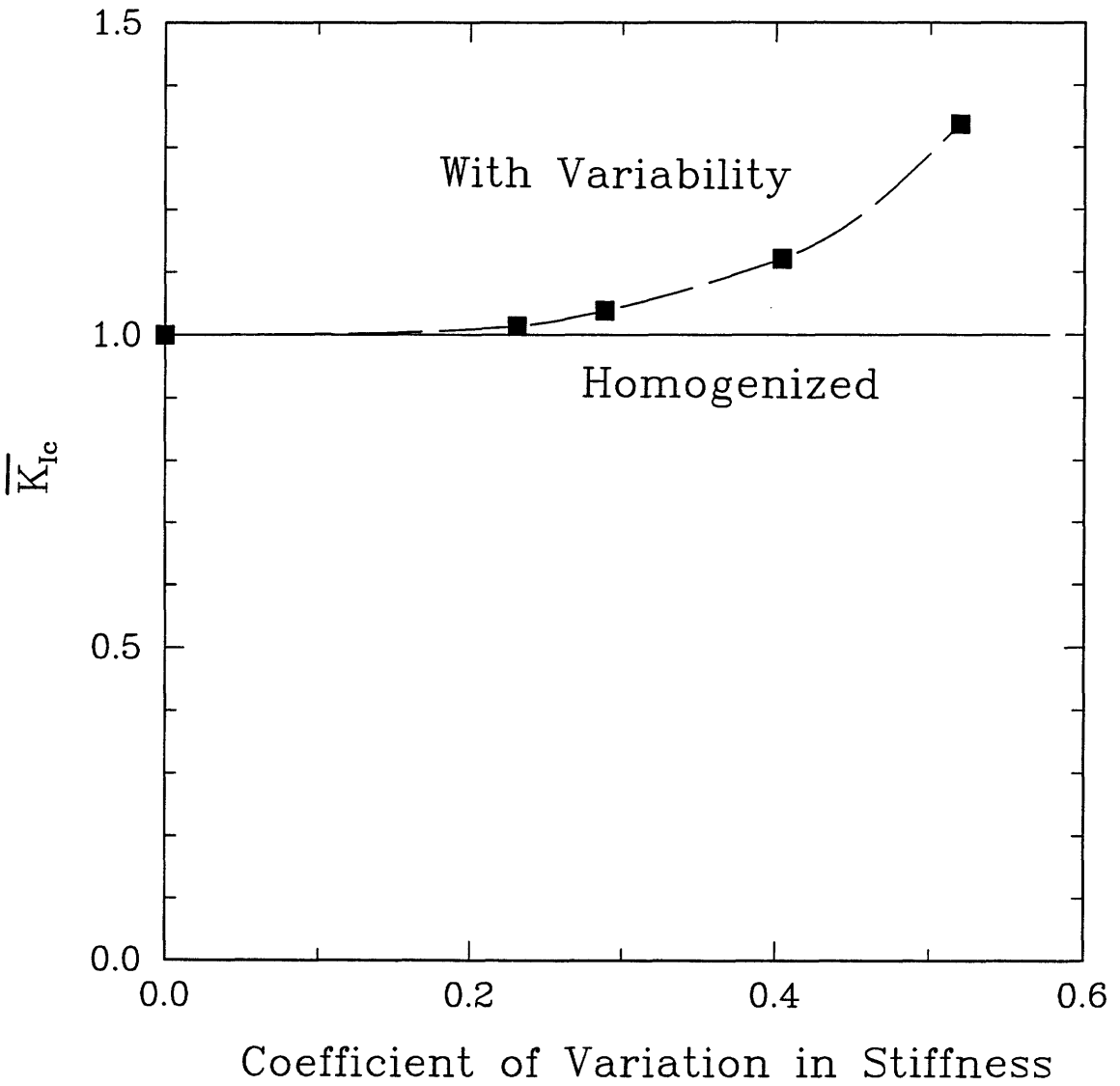

Figure 4-13: Variation in simulation bond stiffness in comparison with homogenized equivalent material.

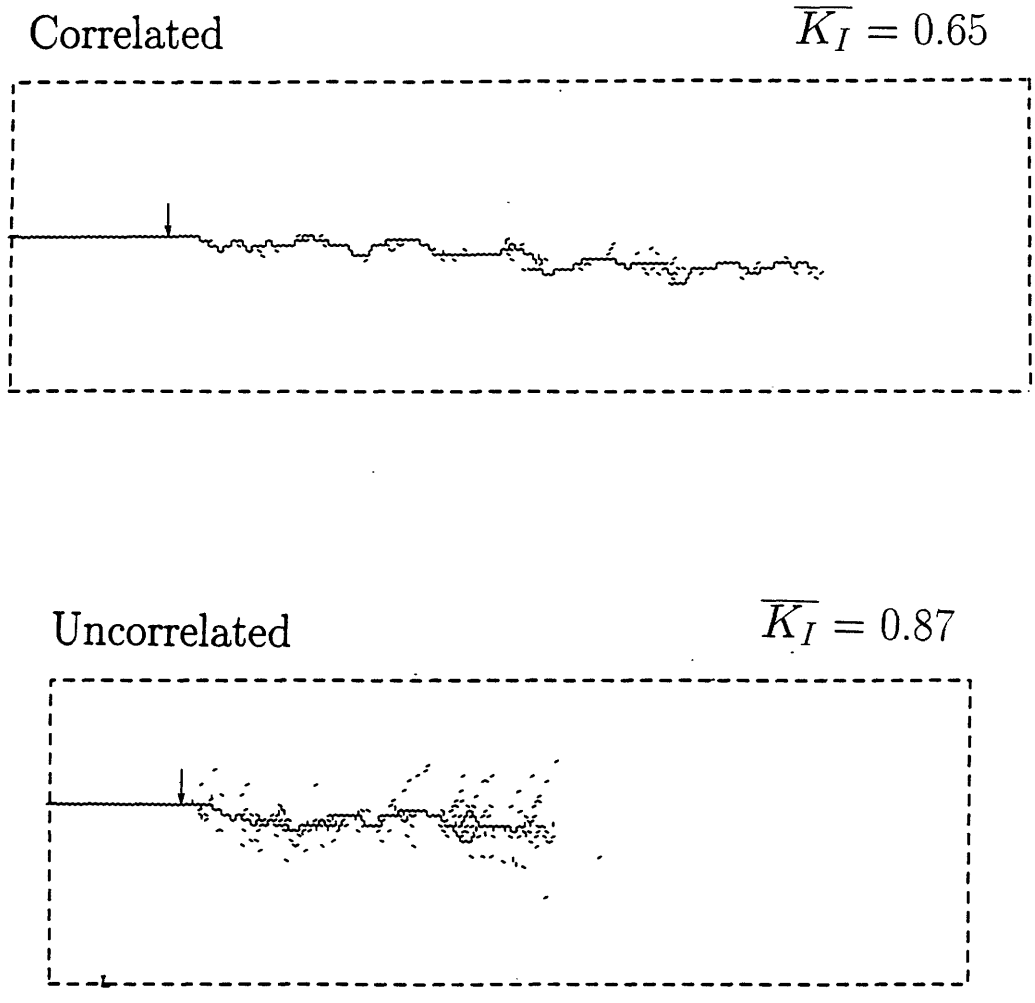

Figure 4-14: The effect of the correlation between bond stiffness and strength for a coefficient of variability of 0.346

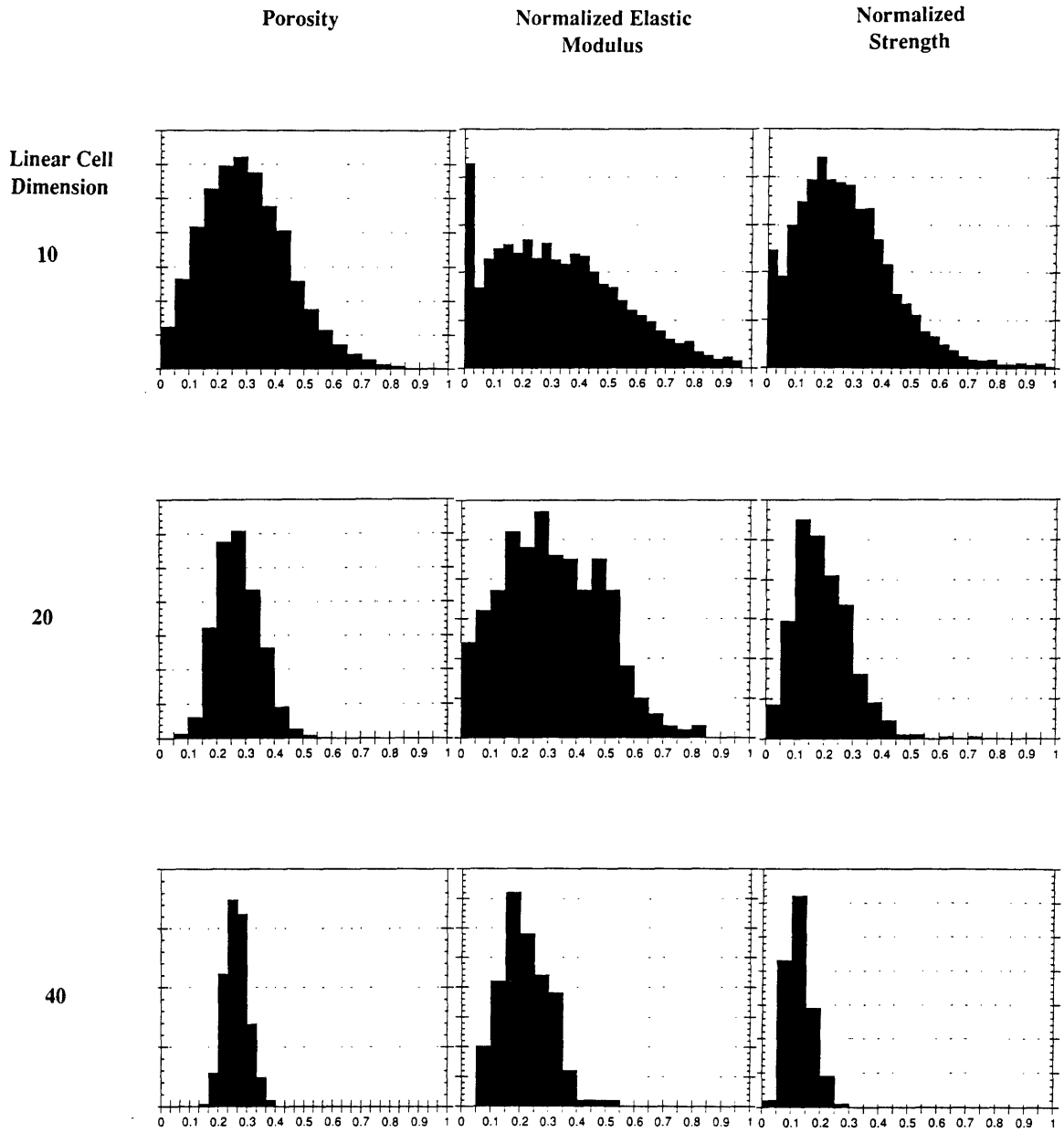

Figure 4-15: The scale effect of the measurement of local strength and stiffness. The cell dimension of 10 was chosen as the length scale appropriate for obtaining the local strength and stiffness of the interpore ligament.

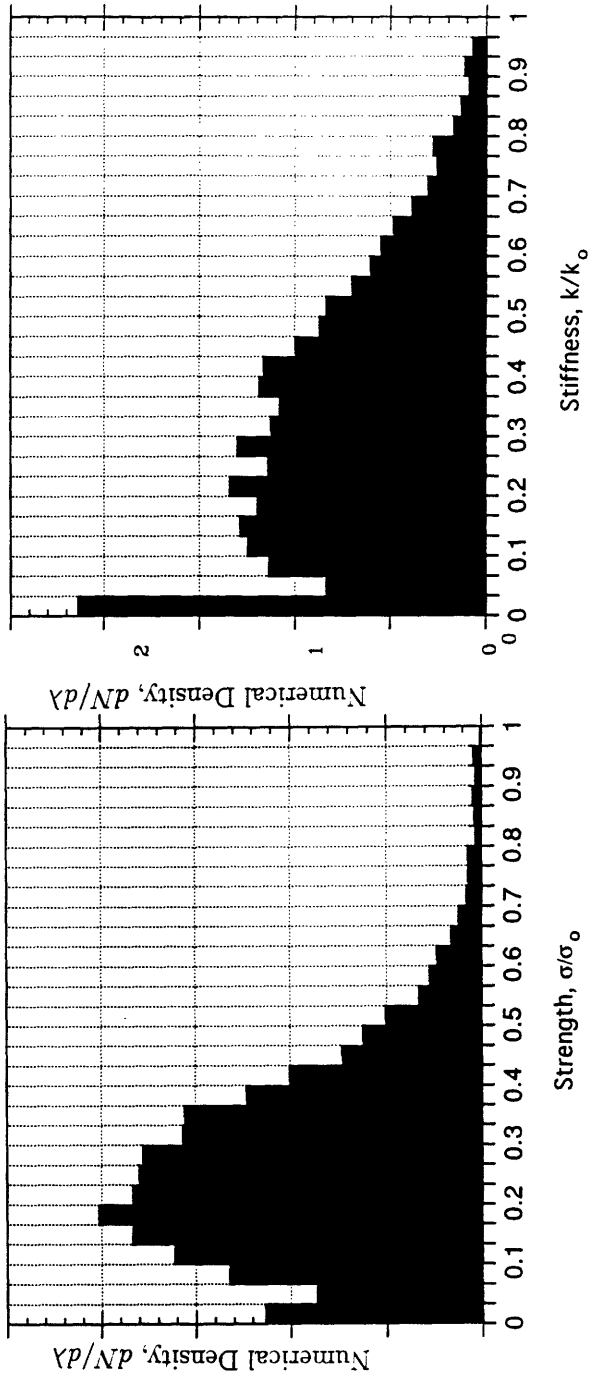

Figure 4-16: Strength and stiffness distributions obtained by probing representative volume elements of the large simulated microstructure which spans 10,000 RVEs.

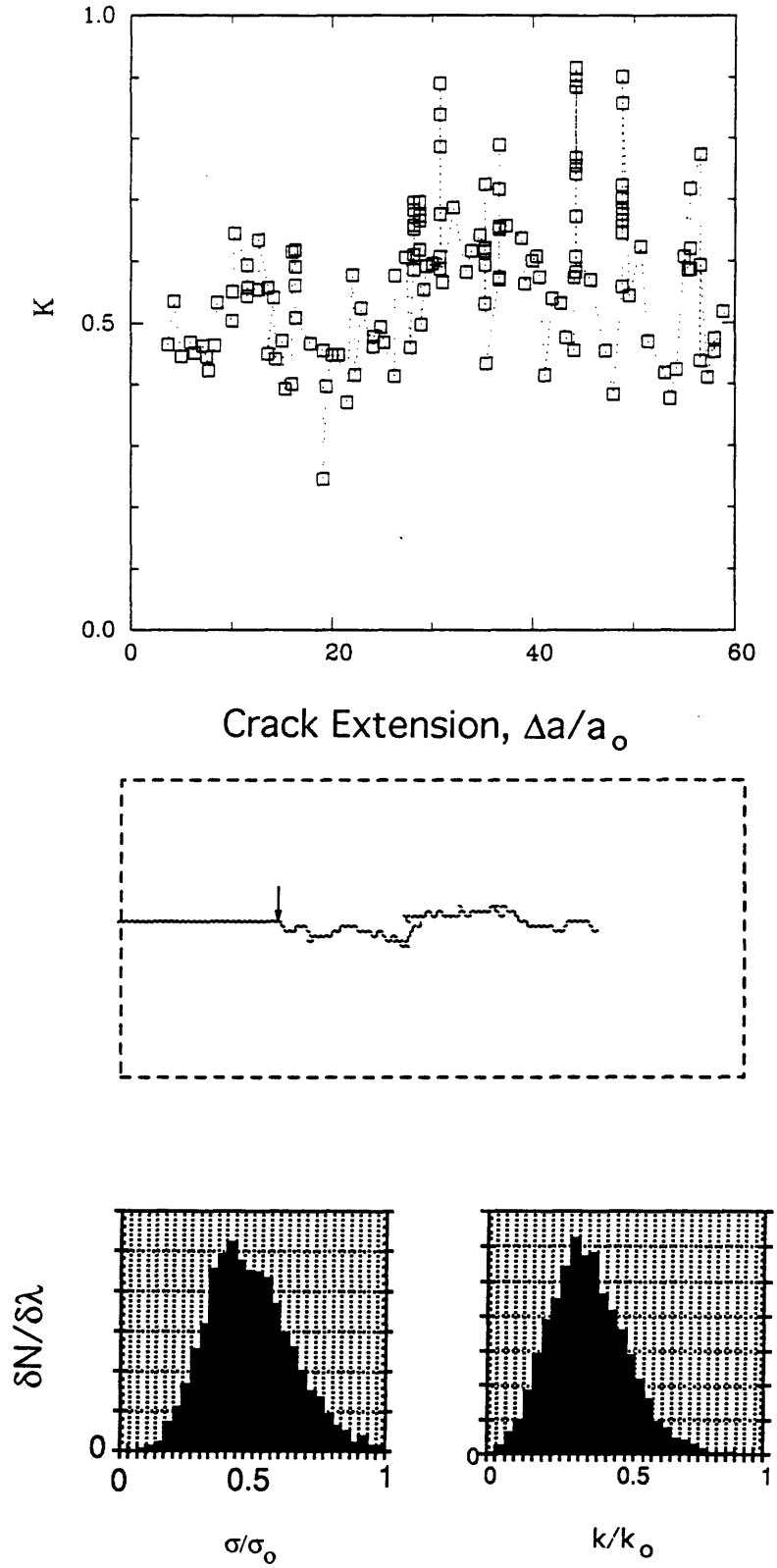

Figure 4-17: Effective 3 dimensional strength and stiffness distributions obtained by probing simulated microstructure.

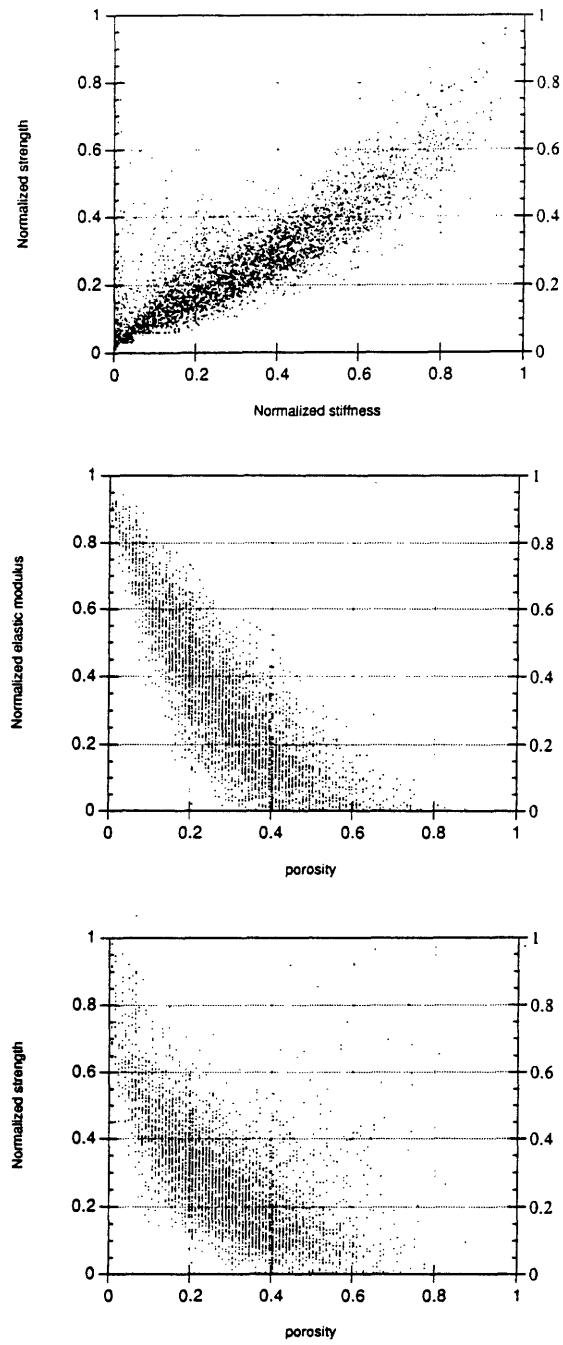

Figure 4-18: Correlation between strength, stiffness and local porosity for a simulated microstructure (c).

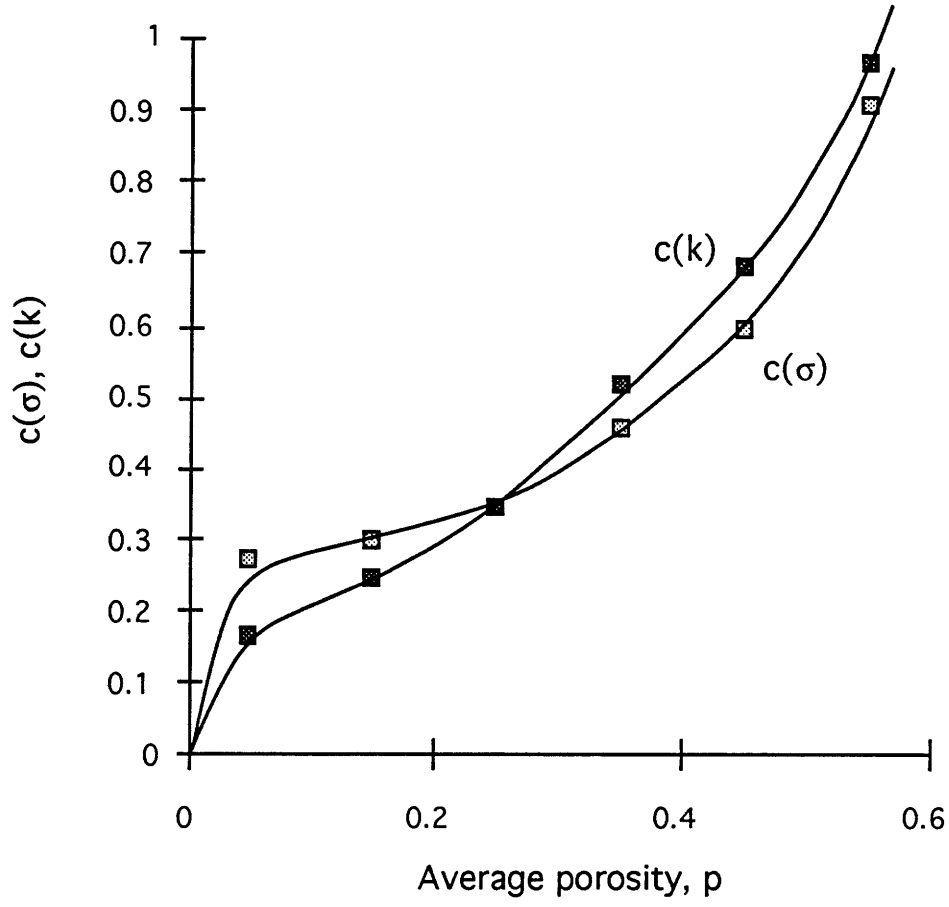

Figure 4-19: The coefficient of variability of strength and stiffness on a length scale of the interpore ligament as a function of porosity for a typical simulated structure.

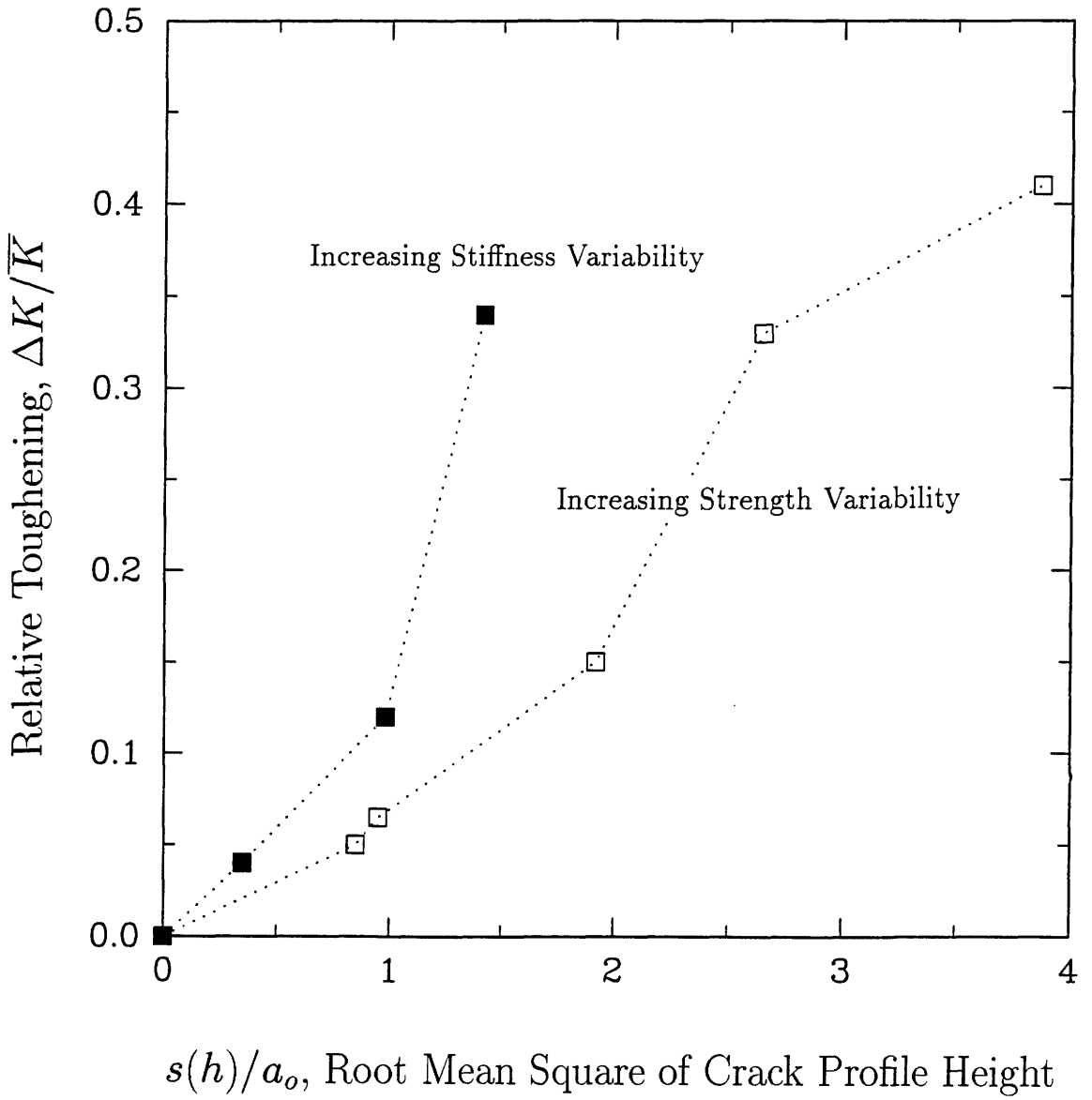

Figure 4-20: Correlation between crack profile height root mean square and relative toughness for modified fracture criterion.

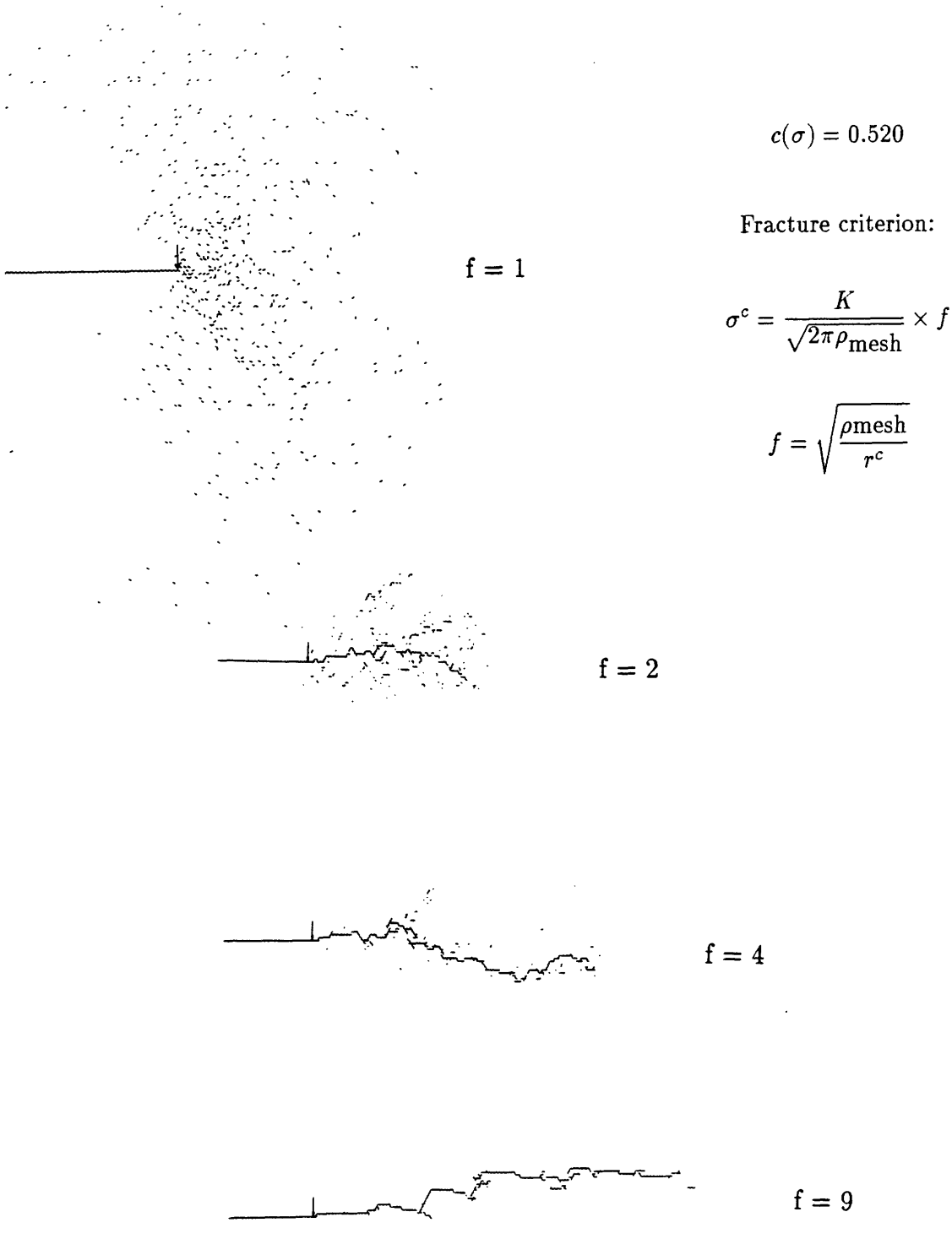

Figure 4-21: Crack configurations with increasing crack tip potency.

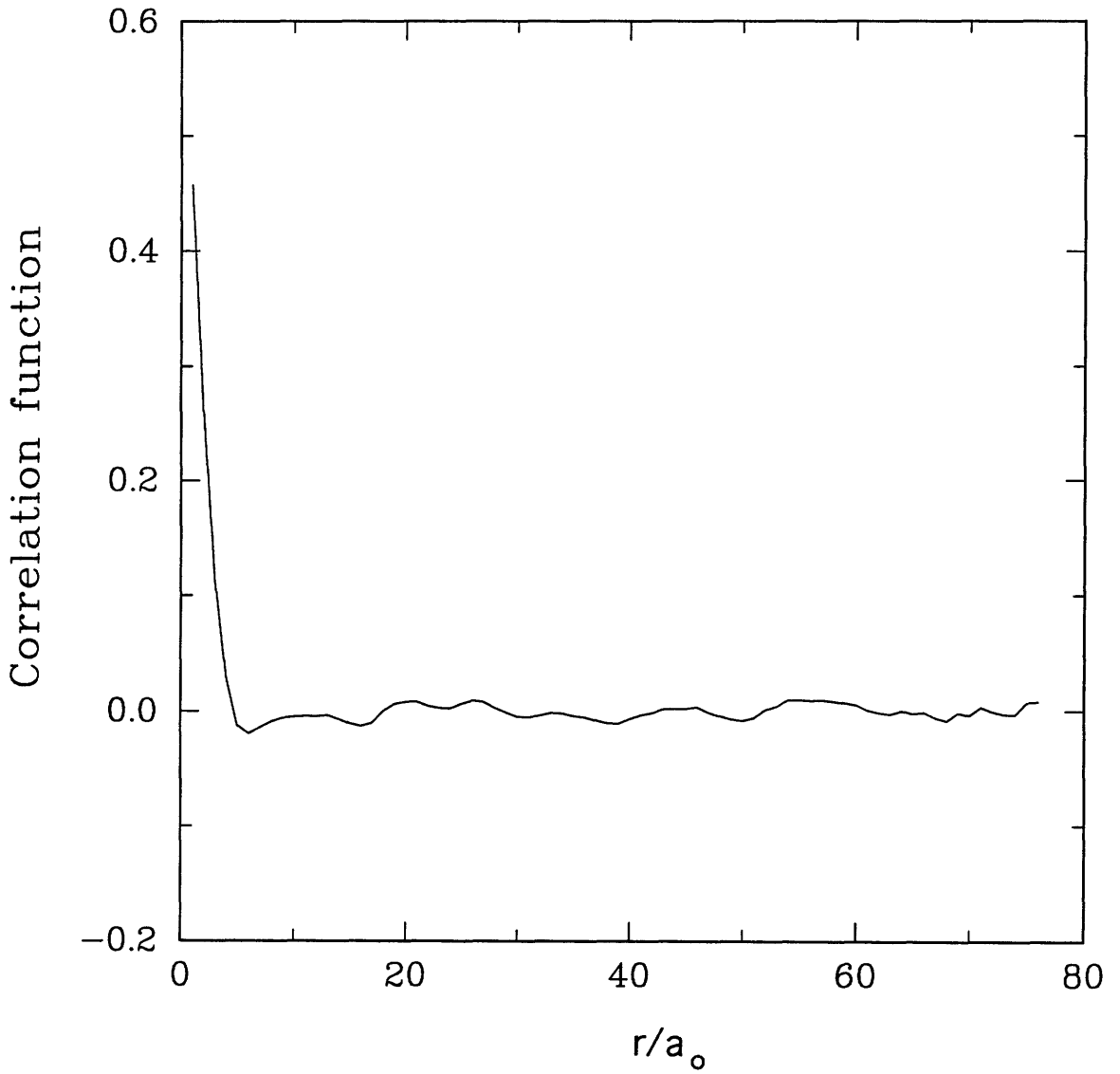

Figure 4-22: The radial correlation function of porosity in the simulated microstructure shows the lack of porosity fluctuations on scales larger than the representative volume element.

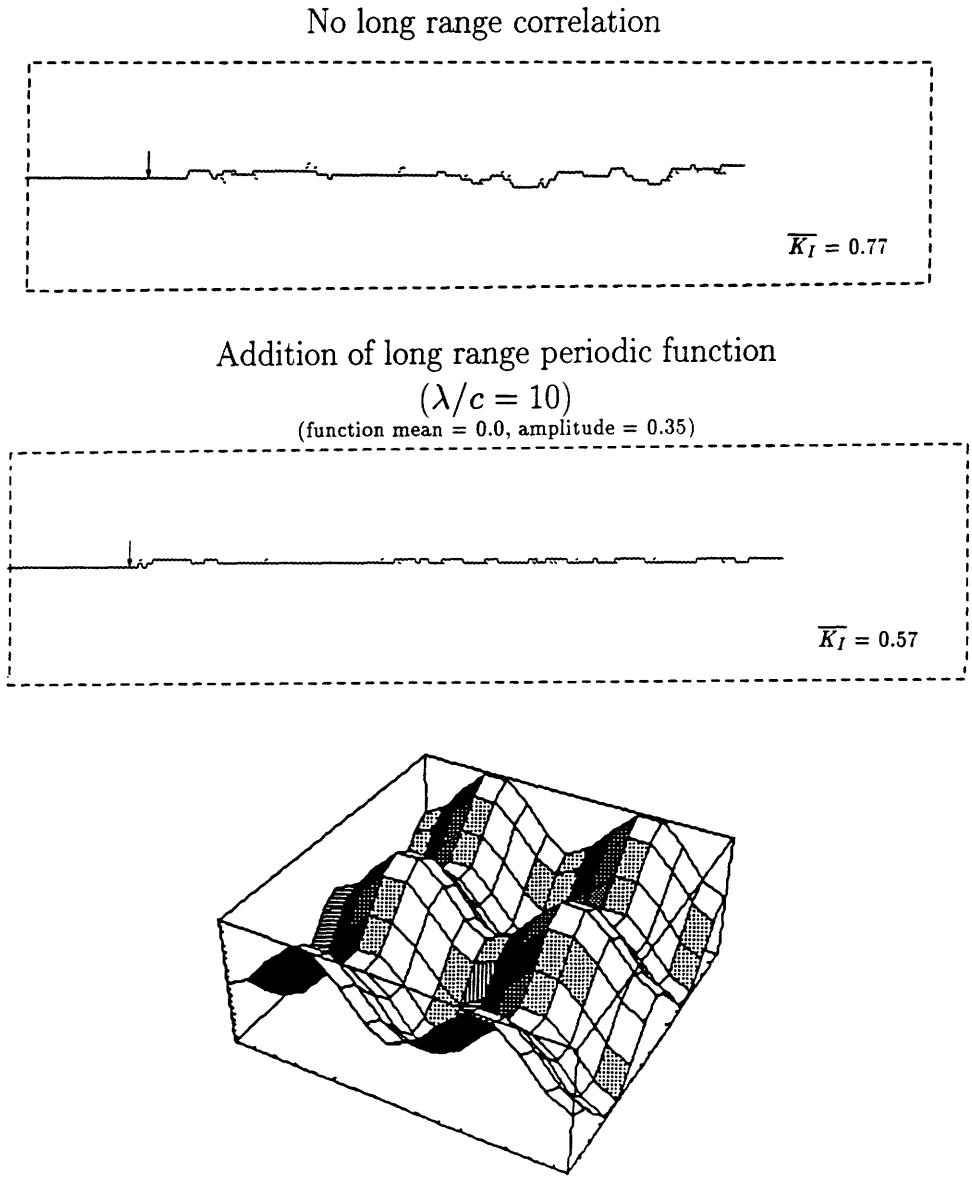

Figure 4-23: The superposition of a long range periodic function on a prescribed variability structure.

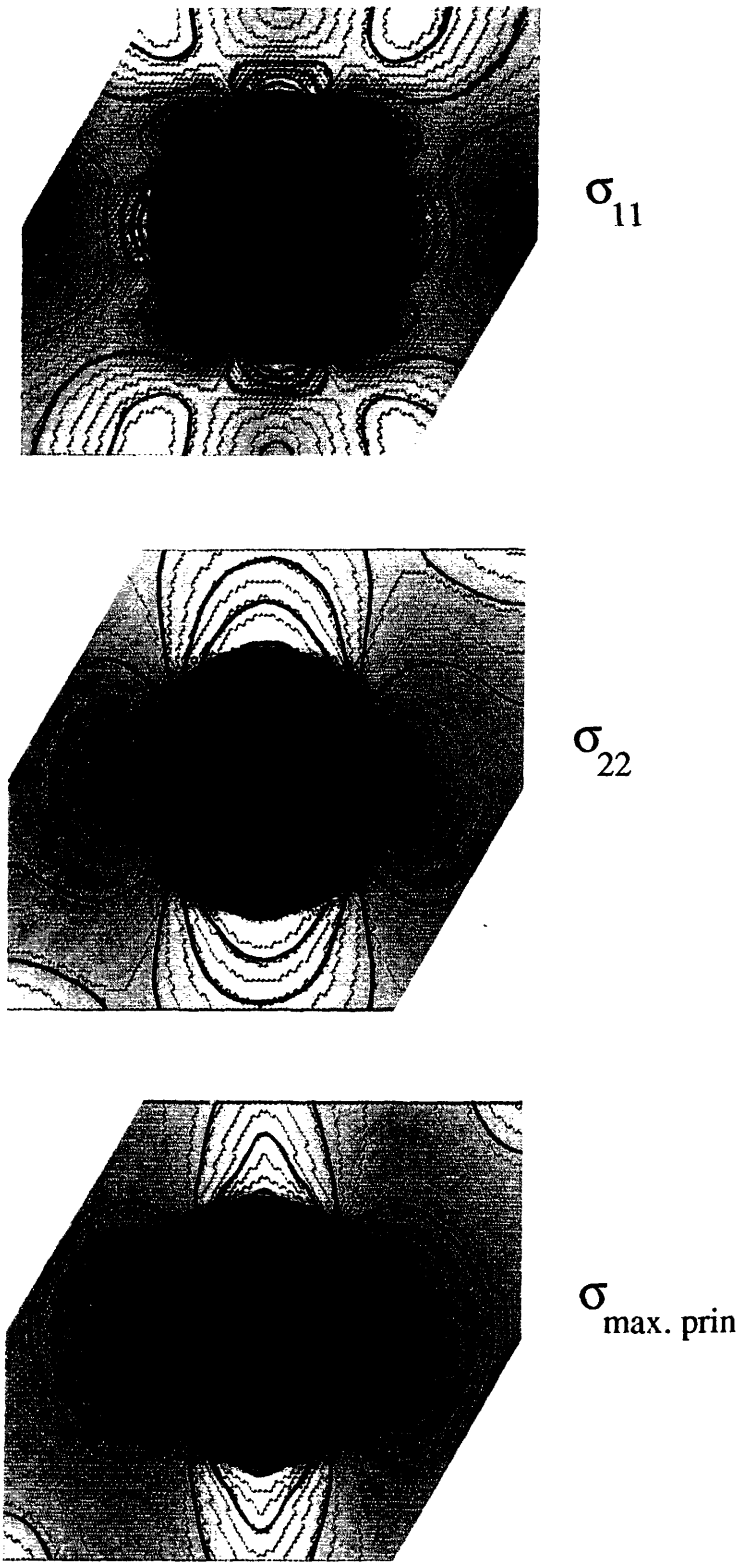

Figure 4-24: Stress field solution comparison between a finite element generated solution and the discrete spring network model for an infinite hexagonal array of pores with spacing to diameter ratio of 4 under uniaxial strain.

Chapter 5

Fracture toughness measurements

5.1 Introduction

In order to complete the evaluation of the cause-effect relationship between microstructure and the fracture properties of an experimental material, in most instances, a material with a given microstructure is studied by probing it with a number of more or less conventional tests. The findings of the microstructure-property connection, can then be used to create microstructures which should have better properties. In the case of the design of ceramic materials for improved crack propagation resistance, however, the measurement of fracture toughness is typically fraught with difficulties.

In this Chapter, an experimental technique is described for measuring fracture toughness by using the crack opening displacement dimension of Vickers microhardness indentation induced cracks. The motivation for developing this technique is to obtain fracture toughness data of sufficient resolution to make a connection with microstructural features. Previous attempts to measure small variations in fracture toughness in certain RBSN specimens have proven unsuccessful with existing indentation crack length methods [80]. This new technique is shown to correspond to accepted values for reference materials for which toughness values are known, and reveals variations in toughness previously too small to measure.

In the last Section, this measurement technique is applied to the porous RBSN

material, and the observations of cracks emanating from Vickers indentations are observed for qualitative indications of toughening mechanisms [94,108], as well as for the average interaction with porosity.

5.1.1 Measuring Fracture Toughness

When a small risk of a component failure is acceptable, statistical methods are often used to predict strength, such as the use of the Weibull distribution, among other methods. However, the knowledge of the flaw population of actual components is required, as serious errors can be made if laboratory specimens are formed by different methods. Therefore, in critical applications, a flaw tolerant approach is taken, in which the maximum flaw dimension of an in-service component determines the maximum service stress through the material fracture toughness, K_{Ic}.

In this light, significant emphasis has been placed recently by the ceramics community on the *toughening* approach to microstructure design, in contrast to the *flaw control* approach which accepts the inherent material brittleness and seeks to control the flaw population. A natural consequence of the progress in making structural ceramics tougher is the need for accurate measurement of fracture toughness.

There are many schemes for measurement of fracture toughness for brittle materials under fast fracture conditions, including standard tests which are used for less brittle materials, such as bending tests on straight-notched specimens [3]. However, the difficulty in producing a sharp crack tip for brittle ceramic materials give rise to uncertainties in the accuracy of fracture toughness. The use of techniques such as fatigue pre-cracking and the use of the chevron notch specimen overcome some of these considerations by providing for stable growth of the initial crack, and produces toughness values which are more representative of the true material behavior [76]. Another important consideration is the machining of large, complex ceramic specimens, which is expensive, and time-consuming.

Another concern relating to most of the measurement techniques for fracture toughness are environmental effects. The flaw tolerent design concept which relies on the connection between fracture toughness and critical crack length is valid only

in inert environments and for short times. Cracks in most silicates and oxides will propagate at stress intensities below the fast fracture values, and is called static fatigue. This is a result of reaction at the crack tip between the highly stressed bonds and the presence of water vapor or other molecules with similar electronic structure and size, which causes the fracture of the stressed bonds. Knowledge of the slow crack growth behavior of ceramic materials is important in assessing the long-term strength of a ceramic component. In the following discussion, the measurement of fracture toughness in the absence of static fatigue will be considered.

5.1.2 Indentation Methods

The development of indentation techniques have allowed ready access to damage resistance data for new ceramics, and have contributed to the advancement of modern high toughness ceramics. The first generation of indentation tests were used to measure a generic deformation resistance parameter, hardness. Various models have been proposed to relate hardness to tensile strength, ease of plastic flow, surface energy, and chemical bond strength[71,96,56,101,23,36]. More recently, there has been work done to directly measure the fracture toughness. These techniques fall into the categories of the Vickers microhardness indentation crack length and the indentation-strength techniques. These methods have the advantage of practicality and that the fracture properties are determined in the small crack dimension regime where engineering failures are likely to occur. In addition, because there are no practical specimen dimension limitations, measurements can be made on laboratory scale specimens. This is a beneficial aspect for the case of measurement of ceramic materials for which the details of producing material specimens, whether for large testing specimens or on a smaller developmental scale, may alter the key microstructural features.

Indentation strength methods are conceptually advantageous, due to the well characterized flaw that grows in a prescribed stress field. However considerations must be made for the effects of the unknown residual stress magnitude from the indentation and the limitation of the amount of data extractable from available specimens in comparison to the nearly unlimited data available from indentation crack length

method.

The effort by Charles and Evans in 1976[27] was the first to produce a model to relate toughness to the *applied load and the length of the radial cracks* emanating from the indentation. An exhaustive list of the many similar models that have been developed to date are summarized and reviewed in references [74] and [44].

The consensus among some authors [25], however, is that these methods do not provide the fracture data of sufficient sensitivity necessary to relate microstructure to the sources of toughness. The methods of this type are empirical in nature and estimates of the differences in measured values among the variety of techniques are of the order of 100% [74,59,44,72]. Many assumptions are made, for example that the material response under indentation is volume conserving. Questions arise as to the accuracy of this assumption since it is possible for material to flow to form ridges around indents in fully dense materials, and for the case of porous materials in which crushing damage is likely. Also, friction between the surface and the indenter strongly affects the stress state at the crack tip. Therefore, the nature of the surface and the ratio of the surface area in contact to the indented volume come into play (i.e. the indentation size effect)[65], and strongly affects the error. In addition, some investigators have questioned the authenticity of the hardness measurement, which is a central parameter in the crack-length models, when radial cracks are present. The variety of possible crack initiation sequences and final crack configurations suggest additional complexity[19]. The nature of these problems makes it difficult to make a clear and simple connection between the applied load and the stresses at the crack tip.

5.2 The Measurement of Fracture Toughness by Vickers Indentation Crack COD

From basic considerations of crack mechanics the shape of the open radial cracks emanating from indentations in brittle substances can be related to the stress state at the crack tip and the material fracture toughness, without consideration of the load

applied, provided that the crack is held open at a state of impending propagation. The requirement for the crack to be at critical stress intensity, and the impossible case for the crack tip to be at higher stress intensities than K_{Ic} implies that this method is a physically based lower bound. The key difference of this approach is that the load used to generate cracks is not explicitly used in the analysis. The stress state is obtained only from the measure of separation between the crack faces as a function of distance from the crack tip. Thus, the accuracy of this method relies on the fundamental connection between observable crack shape and the stresses at the crack tip. Through computed crack shapes obtained by finite element solutions for boundary loading conditions appropriate to the indentation process, crack opening shapes obtained by SEM, it is possible to determine high quality data for the fracture toughness.

5.2.1 Theoretical Background

Kinematics of crack nucleation

First, we note that upon indenting a surface of sufficient thickness[1], with a sharp indenter of material harder than the brittle specimen, such as a Vickers diamond stylus, radial cracks can be grown in a stable fashion. The sequence of events which occur during the Vickers indentation process are as follows. High Herztian contact stresses develop beneath the diamond tip in the half space of material, analogous to the Boussinesq stress solution, where even some pastic deformation may occur under the high hydrostatic stresses[2] around the indenter contact area. Stress analyses for simple elastic/plastic models indicate that with sufficient applied load, high stresses develop necessary for nucleation of subsurface cracks [74]. These cracks form directly below the indenter and at the elastic/plastic boundary, where the maximum tensile stress occurs. Analysis by Lawn and Swain[62] indicates that the minimum load for

[1]The thickness of the specimen should be several multiples of the crack depth. Typical crack dimensions are 10-100 microns

[2]Typical hydrostatic stress can be approximated by a first order analysis, stress = P/A $\sim$ 10N/(10 microns)^2 $\sim$ $100GPa$

nucleating a subsurface median crack is,

$$P_c = \frac{34.67 K_c^4}{\phi^2 \theta^4 H_v^3} \tag{5.1}$$

where ϕ and θ are dimensionless proportionality constants relating the radius of the plastic zone to the indenter size, and the hardness to yield strength respectively[3]. The terms K_c and H_v are the material fracture toughness and indentation hardness. Table 5.1 shows critical loads for nucleation of cracks in some ceramics[74]. Numerous observations from experiments on crack growth in transparent media[61,19] verify this nucleation mechanism qualitatively.

Experimental observations also indicate that for a larger applied load, the subsurface median crack 'pops-in' to the surface, and become visible as surface traces[62,82]. These cracks have an approximate half-penny shape. Table 5.2 shows predicted and observed loads to generate median and radial cracks for Vickers indentations.

For high loads, the tensile stress on planes parallel to the surface reach a critical value and nucleate 'lateral' cracks, typically upon unloading [19]. The development of these cracks and their extension to the surface greatly alters the stress state around the radial cracks and should be avoided for the purposes of data collection.

The connection of crack shape to the crack tip stress field

The link between the crack opening displacements and the stress intensity (or stress state) at the crack tip can be established by a number of methods. In the case of elastic, brittle material behavior, the connection of the crack opening displacement at any point on the crack surface with the stress intensity can be obtained by finite element techniques, given the geometry and loading boundary conditions. The stress intensity for loading along the interior surface of a crack appropriate for the indentation process has the following form:

$$K_I = \frac{E \Delta V(r)}{F(r/a)\sqrt{a}} \tag{5.2}$$

[3] ϕ and θ are typically 1 and 0.2 respectively for reasonable estimates.

Here, $\Delta V(r)$ is the distance between the crack faces at a distance r from the crack tip, $F(r/a)$ is a non-dimensional shape factor, E is the Young's Modulus, and a is the total crack length, from crack tip to center of indentation. Figure 5-1 shows the shape factor F(r) derived from the finite element solution with data obtained for soda lime glass.

There are some approximations associated with this finite element solution. First, the precise three dimensional shape of the embedded, approximately elliptical, surface crack emanating from the Vickers indentation is not well characterized for all loading scenarios. Although the half-penny shape is assumed in some analyses of fracture toughness for the radial cracks, there is evidence that in some materials with loads up to 200N, the cracks are of the Palmqvist type [99]. A Palmqvist crack is a surface localized crack, such that instead of a single penny shaped crack, an approximately elliptical embedded crack exists at each corner of the indentation impression. Other models incorporate this specific shape and although the details are different, the forms of equations relating fracture toughness to crack length and applied load are the same [44].

The criticality of the stress field

The final consideration that relates the crack opening displacements to fracture toughness is evidence that the stress intensity is at the critical level for impending propagation of the crack after removal of the load. There is considerable evidence, including experimental observations which indicate that this is likely to be the case in many instances. This evidence can be divided into observations of crack nucleation and growth during the indentation process and solutions for the stress state throughout the indentation process and particularly after load removal.

- The Boussinesq stress field solution for point loading of an elastic half space results in substantially compressive hoop stresses in the plane of the surface around the point of loading. This serves to restrict crack growth when the full load is applied, as seen in figure 5-2. Upon removing the indentation load, this surface stress component increases, thus causing additional crack growth.

The crack grows until the stress intensity, K_I, levels off at K_{Ic}, the material toughness or crack propagation resistance.

- Mathematical modelling of the indentation process which include modifications of the Boussinesq stress field solution due to irreversible processes during indentation predict that stresses to drive the radial cracks exist on *both the loading and unloading cycle* and to be very strongly surface localized. The inclusion by Chiang, Marshall and Evans [13] of the expanding cavity formulation derived by Hill [42] for an elastic-plastic solid, shows that the stresses increase on the unloading cycle, raising the possibility of crack extension during unloading. The stresses which drive radial crack growth upon unloading are increased with materials with large ratios of E/H, where E is the elastic modulus and H is the hardness parameter. This model further accounts for various cracking sequences as observed by Pharr and Cook [19]

- Evidence of the growth of cracks *during unloading* in a range of materials has been well documented [19,61]. Experimentally, Lawn observed that in zinc sulfide and soda lime glass, upon unloading, there is additional radial crack growth[61]. This indicates again a super charged crack upon unloading until the natural stability of the internally loaded crack causes crack arrest at K_{Ic}. The review of Pharr and Cook surveys a much larger sample of materials, and the majority of observations are of crack growth upon removal of the load, for materials with high values of E/H, (>10).

- In porous materials such as RBSN ceramic, significant residual stresses are present after removal of the load as was concluded by Nair et. al. [80] for indentations of RBSN, and as demonstrated in this Chapter by the fact that observed cracks induced by indentation remain propped open. The expectation of crack growth upon load removal and thus crack arrest at K_c is based upon the relatively high value of E/H for the RBSN material studied here (E/H = 25).

5.3 Experimental Procedures

5.3.1 Method of Observation

Examination of crack morphology can be accomplished by electron microscopy, light microscopy or by radiography. While light microscopy is often used as a ready means of observation and some x-ray micro-radiography has shown the complex three dimensional nature of cracks in heterogeneous microstructures, the electron microscope provides the necessary resolution to observe the sub-micron crack opening displacements.

5.3.2 Measurement of the COD

The implementation of the measurement technique involves the preparation of the surface for micrographical observation, as described in Chapter 2, the indentation of the surface with the Vickers microhardness technique and generation of high resolution micrographs of the produced cracks. The microhardness technique is well known, and references can be obtained which describe the various techniques[74].

Prior to indentation, a standard microscopy gold coating is applied for the purpose of obtaining optimal micrographs. Indentations are made with standard Vickers microhardness apparatus with loads ranging from 2 to 10 N. The choice of load is important to the generation of radial cracks which are large enough for observation, however, care must be taken not to exceed the load for which lateral cracks nucleate, as described in Section 5.2.1. The load is held for 20 seconds, and removed. Microscopy was performed within several minutes of indentation. Microscopy is performed with sufficient resolution to clearly resolve the crack edges.

Crack opening displacements are obtained directly from the micrograph images with standard micrometer measurements. Care was taken to estimate the uncertainty of crack opening displacement measurement by providing upper and lower bounds, as observed from the micrographs. The upper bound was determined by the criterion such that contrast gradients were uniform beyond this dimension and similarly for

the lower bound.

5.3.3 Elastic Solution for Crack Shape

A linear elastic solution was generated for a two dimensional crack in an infinite medium with the finite element code ABAQUS. The resulting non-dimensionalized crack opening displacement, F,

$$F = \frac{\Delta V(r) E}{K\sqrt{a}} \tag{5.3}$$

is shown in figure 5-1 where $\Delta V(r)$ is the crack opening displacement, E is Young's modulus, K is the applied stress intensity, and a is the crack length. The data compare well with the data from glass, for which a toughness value of 0.55 MPa$\sqrt{\text{m}}$ was measured.

Because the exact nature of the residual stress state is not well characterized, four possible loading scenarios are considered, and compared to typical data in figure 5-3. One extreme is that the load from the residual stress field is applied at the center of the indentation as a concentrated load (1). Another possibility is that the load is distributed equally over the width of the indent(2). We have found that the data fit with the loading scheme in which the concentrated load is applied at the edge of the indent (3). Curve (4) is the shape for a shorter crack (c/a = 0.35). The interaction of the two neighboring, perpendicular radial cracks has been included in the crack shape analysis.

The effective difference between the shape of a three dimensional penny shaped crack and the two dimensional analysis here is a factor of small magnitude, as seen in figure 5-4. The 2D FEM analysis for the non-dimensionalized crack opening displacement, F, is 9% less than the analytical solution for the crack face separation of a fully imbedded three dimensional penny crack at $r/a = 0.5$. Both solutions converge and are consistent with the Irwin K-field plane strain displacement solution for crack face separation, $u(r)$, near the crack tip,

$$u(r) = \frac{2K(1-\nu^2)}{E}\sqrt{8r/\pi} \tag{5.4}$$

where ν is Poisson's ratio, r is the distance from the crack tip and $u(r)$ is the is the Young's modulus and K is the applied stress intensity.

5.4 Results

5.4.1 Fracture Toughness Measurement

In order to determine the accuracy of the method of relating crack opening displacements produced by Vickers indentations to fracture toughness, data was gathered for soda lime glass, single crystal Al_2O_3 and single crystal Si for which fracture toughness values are known. Figures 5-1, 5-5, 5-6 show the agreement of data superimposed on the calculated crack shape. The measured fracture toughness values are shown in Table 5.3 and compare well with accepted values from the literature. The fracture toughness of the γ alumina has an additional approximation that the produced cracks were not oriented perpendicular to the top surface. The preferred fracture plane was oriented off axis as determined by laue back reflection, and is included here for comparative purposes only.

5.4.2 Crack Length Sensitivity

In the analyses which correlate fracture toughness with applied load and crack length, the sensitivity to the crack length is strong, usually as $K \sim 1/a^{3/2}$, where a is the crack length. In the technique presented here, there is also a sensitivity to total crack length, but with sensitivity of $K \sim 1/a$. This somewhat lower sensitivity to crack length, and the ability to extrapolate COD data to an estimate of the crack length imply a reduced fracture toughness sensitivity to crack length and less uncertainty.

The measurement of crack length is typically made with optical microscopy from the observation of surface crack traces and is inherently approximate in nature. Limitations from the resolution of the microscopy method and the subjective nature of

determining the point at which the gradually narrowing crack trace ends are inherent in the measurement. With careful technique, such as in reflected polarized light with the use of an oil-immersion objective as was undertaken for the original study correlating toughness with crack length by Antis, et. al. (1981), the position of the crack tip can be better estimated, but the possibility of error remains. Other studies have recognized this sensitivity and that higher resolution observations typically reveal longer cracks [76,3].

In order to estimate uncertainty in crack length, systematic observations were made of cracks emanating from an indentation in RBSN at a range of magnifications, as seen in figure 5-7. Measurements of crack length were taken from micrographs generated from optical and SEM images for a range of magnifications. It can be seen that sizable errors can be made on the order of 50% in underestimating the crack length, which will correspondingly overestimate fracture toughness values. In the range of observation along the crack where crack opening displacements are large enough for measurement ($r/a > 0.2$), and far enough away from the indentation where the influence of the loading creates strong deviation from linearity ($r/c < 0.75$), the COD data is observed to be approximately linear. In the cases observed, a linear extrapolation to zero opening displacement agreed with or overestimated the best-guess crack length from observations of micrographs at 20,000 magnification by no more than 10%, typically. These observations are used to verify crack length measurements.

5.4.3 Load Sensitivity

Typically, load sensitivity of indentation hardness measurements arise at low loads due to a higher contact surface to indented volume relative ratio and thus increased effect from frictional tractions at the indenter/surface interface. Because the hardness parameter enters the fracture toughness calculation for crack length/toughness models, this effect is a relevent source of error. This surface friction may affect the measurement of toughness through the COD method by an alteration of the stress state during the indentation process. To the extent that this effect alters the nature of

the crack growth process during the unloading cycle so that the cracks close to some degree, then this effect may be important. However, fracture toughness measurements on RBSN material K at 4 and 10N show differences comparable with expected uncertainty or slightly higher at low load, $K_{Ic} = 1.63$ and 1.46 MPa$\sqrt{\text{m}}$ respectively.

5.5 Application to RBSN

5.5.1 Measurement of Fracture Toughness

Detailed examination of Vickers indentation induced cracks in RBSN demonstrates a relatively small variation in measured fracture toughness, in the range of 1.0 to 2.0 MPa$\sqrt{\text{m}}$, as seen in Table 5.4. Most observed cracks displayed a strongly planar character, implying an average sampling of the porosity, and a functional dependence of fracture toughness on porosity of $K_c/\sqrt{G_{co}E_o} = \exp(-bp)$, which is undesirable for fracture toughness optimization. The measured fracture toughness exhibited the predicted decrease consistent with the planar character of the fracture paths, with a value of b of 2.3. In comparison, fracture toughness values found in the literature [86] fall between 1.1 to 3.6 MPa$\sqrt{\text{m}}$ for silicon nitride produced with a variety of processing techniques in the range of porosity comparable to the materials examined here, and the pre-exponential factor b for these materials is measured to be 2.4 [89].

The values, in figure 5-9, represent the range of measured values from the four cracks emanating from one indentation. The uncertainty for one value is based upon the standard deviation of the mean of multiple measurements of the COD at different locations along the crack and is typically 1%. Therefore the range of values is representative of the variation in fracture toughness.

The energy release rate, $G = K^2/E$, was found to follow a similar trend, as seen in figure 5-10. The trend reported in the literature for dilute porosity in silicon nitride [89] is for decreasing energy release rate,

$$G_{\text{Si}_3\text{N}_4} = 20e^{-4p}[\text{J/m}^2] \tag{5.5}$$

and extrapolates to the lower values obtained for the MIT material. This observation confirms the measurements of both fracture toughness and elastic modulus which come into the calculations. The specimens with highest porosity exhibited energy release rates comparable to those at the lowest levels of porosity indicating a change in the fracture character at the highest porosity levels.

5.5.2 Observation of Crack Shapes

Figures 5-11, and 5-12 shows the typical planar character of the observed cracks, indicating an average sampling of porosity, and weak crack/pore interaction for producing crack deflection and tortuosity. Estimates of the sampling of the porosity by the crack in the majority of samples indicate an average sampling of the microstructure in agreement with the qualitative observation of the planar character of the crack paths. This proportion was obtained by examining the crack path at high magnifications, and summing lengths of the crack path which were deemed to be passing through solid material.

Comparing two nominally identical specimen batches, materials G and H for which there was a statistically significant difference in the fracture toughness revealed that the lower toughness microstructure contained the previously mentioned bi-modal distribution of pore size. Obervation in the environmental SEM, which allows the probing of some depth into the material, of the uncoated microstructure with an indentation crack revealed interaction with the larger pore structure in material G, as seen in figure 5-13. Although the crack was more tortuous than the cracks in the homogeneous microstructure, the crack is observed to propagate along the weak pore channels. The proportion of the crack path through solid material is measured to be 88% of the relative density indicating a higher than average sampling of the porosity and a reduced toughness, in comparison with the crack propagating through the more homogeneous microstructure, which sampled the average cross section of the microstructure (99% of the solid present). The cracks in the lower toughness material however did not have the tortuosity of the pore channels which are seen to have cell-like morphology as described in Section 2.4.1, and may be explained in part by

some restriction on the amount of crack deflection due to the three dimensionality of the crack.

Specimens A and B, as seen in figures 5-14 and 5-15 at the high end of the porosity range displayed increased crack roughness and evidence of bridging ligaments in the crack wake. These bridging ligaments appear to be of the dimension between 0.5 and 1 micron, so are not likely to be single grain bridging, as the grain size has been determined to be approximately 0.1 micron or less. Other possible mechanisms for this ligament bridging include crack blunting and renucleation ahead of the crack tip, or a more complex three dimensional crack propagation effect in which a local segment of the crack front is pinned and neighboring segments rejoin imperfectly, leaving behind a bridging ligament. These specimens exhibited slightly higher fracture toughness and energy release rate than the general decreasing trend with porosity, as seen in figures 5-9 and 5-10. This is consistent with other experimental evidence that the presence of increased crack complexity occurs with increasing porosity[108].

Observations of the fracture surface of material H (see figure 5-16), reveals a wave-like roughness on the length scale of 1-2 microns which is oriented in grooves and ridges parallel to the crack propagation direction. In an analogous manner, crack tails form ridges behind an initiating heterogeneity parallel with crack propagation direction. Although no crack tail bridging was directly observed in profile for this relatively tough microstructure, this evidence suggests some degree of deviation from average sampling of porosity and the potential for crack tortuosity and bridging behavior in these porous microstructures.

5.6 Discussion

In this chapter, a method for measuring fracture toughness in brittle materials was described which is based on crack opening displacement measurements of cracks produced with the Vickers microhardness indentation technique and a physical basis of relating these dimensions to the stress field at the crack tip. Unlike more accepted methods of measuring fracture toughness with Vickers indentation cracks, which are

based upon empirical fits with crack length and applied load, the residual stresses created by the displaced material under the indenter serve as a driving force to prop open the radial/Palmqvist cracks, and thereby provide directly observable evidence of crack propagation resistance. Although the uncertainties associated with making measurements of submicron crack face opening displacements, and the lack of certainty of the precise character of the residual stress field suggest improvements in methods and analysis, the potential of this technique is for providing data based upon sound physical principles. This and the lower bounding character of these data, which approach accepted values under conditions for which the crack is expected to extend upon load removal, suggests this method for measurement of high precision toughness data and as a superior measurement technique for component design data.

The criticality of the stress field after unloading in fully dense materials is suggested not only by considerable evidence for crack extension upon unloading, but also by the measurements of monocrystal data for the Si [110] cleavage plane, and the more approximate γ alumina and soda lime glass. The value of E/H for Si (E/H = 13) is close to the value suggested as the value for transition to crack extension upon unloading, and the close agreement with accepted data for fracture toughness buttresses these concepts.

In the porous RBSN, the existence of a residual stress field is demonstrated by the observations of propped open cracks, and is the conclusion of another study on the same RBSN material [80]. In addition, the relatively high E/H measured for RBSN here (E/H = 25) which is significantly above the value for which cracks are expected to extend upon unloading, as observed by Pharr and Cook [19], and predicted by the CME analysis [13], suggests accuracy of the data in these porous materials. An estimate of the ratio of volume of the induced cracks, V_c, assuming half penny shaped cracks, to the indentation impression volume, V_i, is 0.23, 0.21 and 0.17 for fully dense Si and Al_2O_3 and soda lime glass, and is considerably larger than values for porous RBSN of 0.03. However, this reduction in the amount of stress relief due to the formation of shorter cracks is compensated for by the expected growth of the crack upon removal of the load, and thus crack arrest at K_c.

The comparison of the generated data by the crack opening displacement method of measuring fracture toughness with the crack-length/applied load methods reveals that although for the fully dense materials the obtained values compare well with accepted values, the measurements for the porous RBSN material are comparable with the low end of the range of crack-length models. Figure 5-17 shows this and the relatively large scatter from the choice of crack length - toughness model. The differences may be explained by the lower bounding character of the COD method or by an overestimation in the crack length/load methods due to the likelihood of the lack of volume conservation and some degree of densification during indentation and thus shorter cracks, which produce overestimation. However, the correlation between the COD method and the other techniques as measured by the two variable correlation parameter, χ as defined in equation 4.8, varies between 0.33 and 0.53, indicating that the COD technique has some empirical fit with the other methods.

Comparisons of measured toughness can also be made with values obtained by evaluating the fracture origin mirror constant in ball on ring strength measurements [66]. Fracture toughness measurements based upon the mirror constant rely on the observations that upon fracture initiation, characteristic patterns are made on the fracture surface near the site of the strength controlling flaw. Although these measurements contain some degree of subjectiveness in obtaining the strength controlling flaw size and shape, there is some agreement with data from the COD method, as seen in Table 5.5. Similar to the comparison of the fracture toughness obtained from crack length methods to the COD method, the fracture toughness values obtained from mirror constants are larger and reinforce the notion of the COD method as a lower bound. This technique registers the difference in fracture toughness previously noted between materials G and H and there is a general correlation between the two data sets with a few exceptions reinforcing the trends in toughness.

The relative agreement of toughness values between the crack length-load, fractographic mirror constant method and the COD method suggests a high degree of residual stress remains after the indentation of RBSN to prop open the crack at or close to critical stress intensity. However, the proof that stress intensity at the crack

tip in the porous material is at the critical value in order to relate the stress intensity to fracture toughness is not obtained with the data presented here. Nevertheless, the circumstancial evidence discussed above in Section 5.2.1 suggest crack growth upon unloading and thus crack arrest at K_c.

5.7 Conclusions

- The fracture toughness measurement by crack opening displacement of cracks induced by Vickers indentations is shown to be an alternate method for obtaining high quality lower bound data. For indentations produced under conditions in which the crack driving stresses increase upon unloading, the data is expected to be an accurate measure of fracture toughness. This is expected to be likely for materials with high E/H ratios, as is the case for RBSN. Agreement is obtained for the measurement of materials with known fracture toughness values.

- In similarly produced reaction bonded silicon nitride over the range of porosity 17-31%, the fracture toughness exhibited a decrease with average porosity, which is consistent with the planar character of the fracture profiles. In addition, energy release rates at the highest levels of porosity (p = 31%) are comparable to those values found for specimens with the lowest levels of porosity (p = 17 %). This is consistent with increased crack complexity for specimens at higher porosity as observed elsewhere [108,89], and specifically increased crack tortuosity and crack bridging ligaments as observed here.

- The comparison of two nominally identically produced microstructures revealed that the material with large pore channels had lower toughness due to the easy fracture path provided as evidenced by the higher sampling of the porosity, and lower elastic modulus.

Material	P^* (N)	C^* (μm)
Si	0.003	0.2
SiO_2 (silica)	0.02	0.6
MgO	0.06	0.8
SiC	0.8	2
Al_2O_3	3	5
Si_3N_4	3	4
WC-Co	96	22

Table 5.1: Critical loads as measured for nucleation of cracks in some ceramics. From McColm (1991)

		Prediction		Observed	
Material	Crack type	P^* (N)	C^* (μm)	P^* (N)	C^* (μm)
Soda-lime-silica	Radial	0.4	1		
glass	Median	0.6	1.1	5.0	17
$\beta = 2.2^a$	Lateral	2.0	3		
Ge (crystal)	Median	0.014	0.16	0.02	0.25
$\beta = 2.5$					
SiC (polycrystal)	Radial	5	3		
$\beta = 2.8$	Median	14	4		
	Lateral	40	7		
Si (crystal)	Median	0.05	0.36	0.03	0.65
$\beta = 2.65$					
Si_3N_4 (polycrystal)	Radial	30	7		
$\beta = 2.8$	Median	80	12		
	Lateral	210	20		
Al_2O_3	Median	0.4	0.6	0.25-0.5	3
$\beta = 2.5$					

Table 5.2: Predicted and observed loads required to generate median, radial (palmqvist) and lateral cracks for Vickers indentations. From McColm (1991)

Material	Measured Value	Accepted Value
Soda Lime Glass	0.55 MPa $\sqrt{m}$	0.4-0.8 MPa $\sqrt{m}$
Si single crystal [110] fracture plane	0.87 $\pm$ 0.08	0.89
Alumina single crystal cleavage plane	2.56 $\pm$ 0.1	2.1

Table 5.3: Measured fracture toughness values for model materials

Specimen	E	Kc	G
A	135 GPa	1.27 GPa /m	11.9 J/m^2
B	157 GPa	1.30	10.8
C	149 GPa	1.23	10.2
D	169 GPa	0.93	5.2
E	161 GPa	1.31	10.7
F	168 GPa	1.28	9.8
G	164 GPa	1.17	8.3
H	193 GPa	1.40	10.2
I	175 GPa		
J	182 GPa	1.39	10.6
K	193 GPa	1.46	11.0
L	185 GPa	1.52	12.5
M	215 GPa	1.97	18.1
N	182 GPa	1.29	9.1

Table 5.4: Summary of mechanical properties.

Material	K(fractography)	K(COD)
A	1.8 MPa $\sqrt{m}$	1.27 MPa $\sqrt{m}$
D	2	0.93
G	2	1.17
H	2.7	1.40
J	1.9	1.39
K	1.6	1.46
L	2.6	1.52

Table 5.5: Comparison between fracture toughness data between methods of fractographic analysis of mirror constants and the COD method.

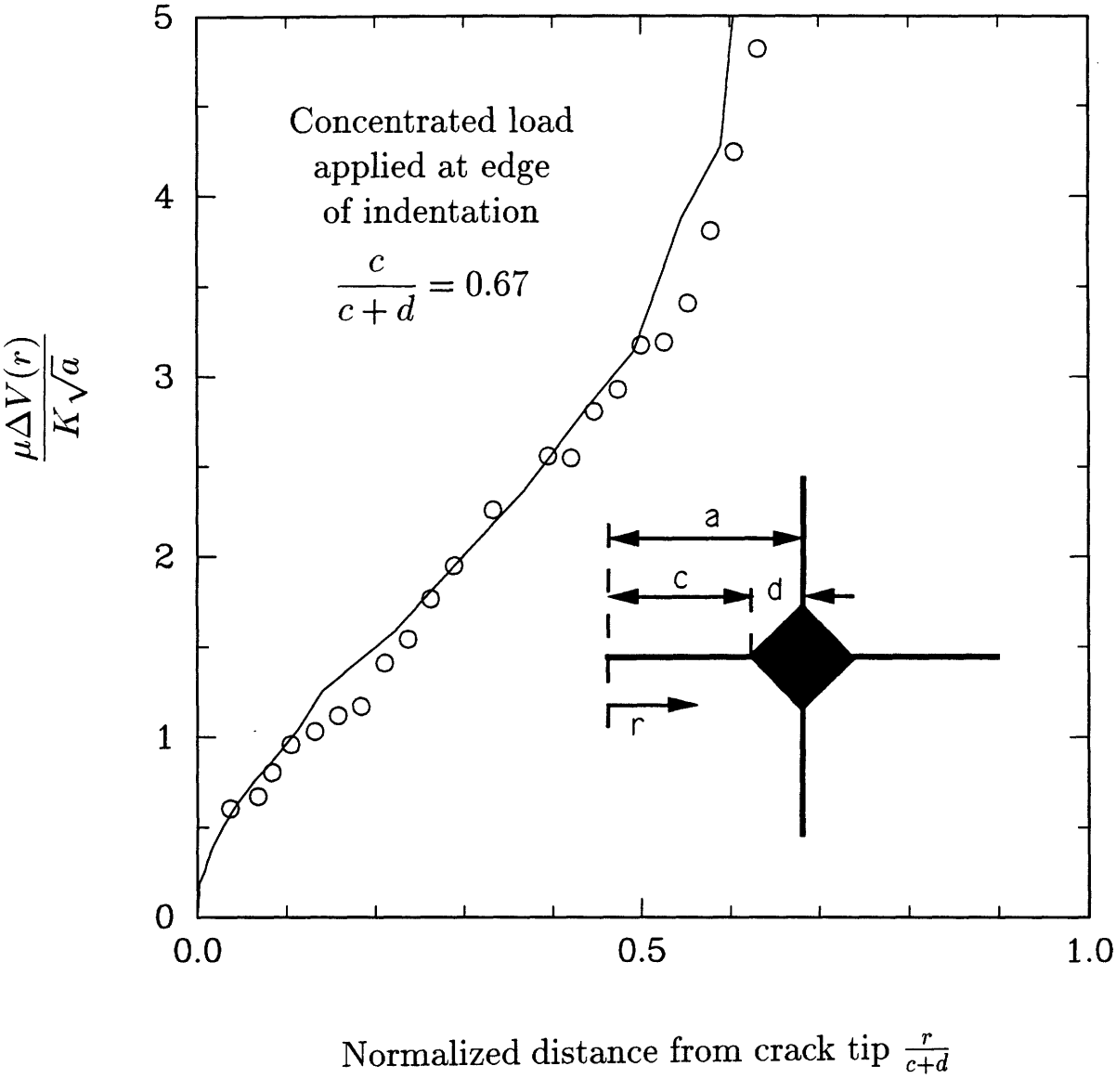

Figure 5-1: Shape factor F(r) and data from soda lime glass. The toughness value calculated is 0.55 MPa$\sqrt{\text{m}}$.

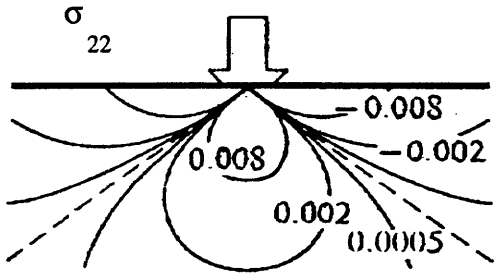

Figure 5-2: The hoop stress component of the stress field for a point load on an elastic half space from the treatment by Love (1952) based on the solutions by Boussinesq (1885).

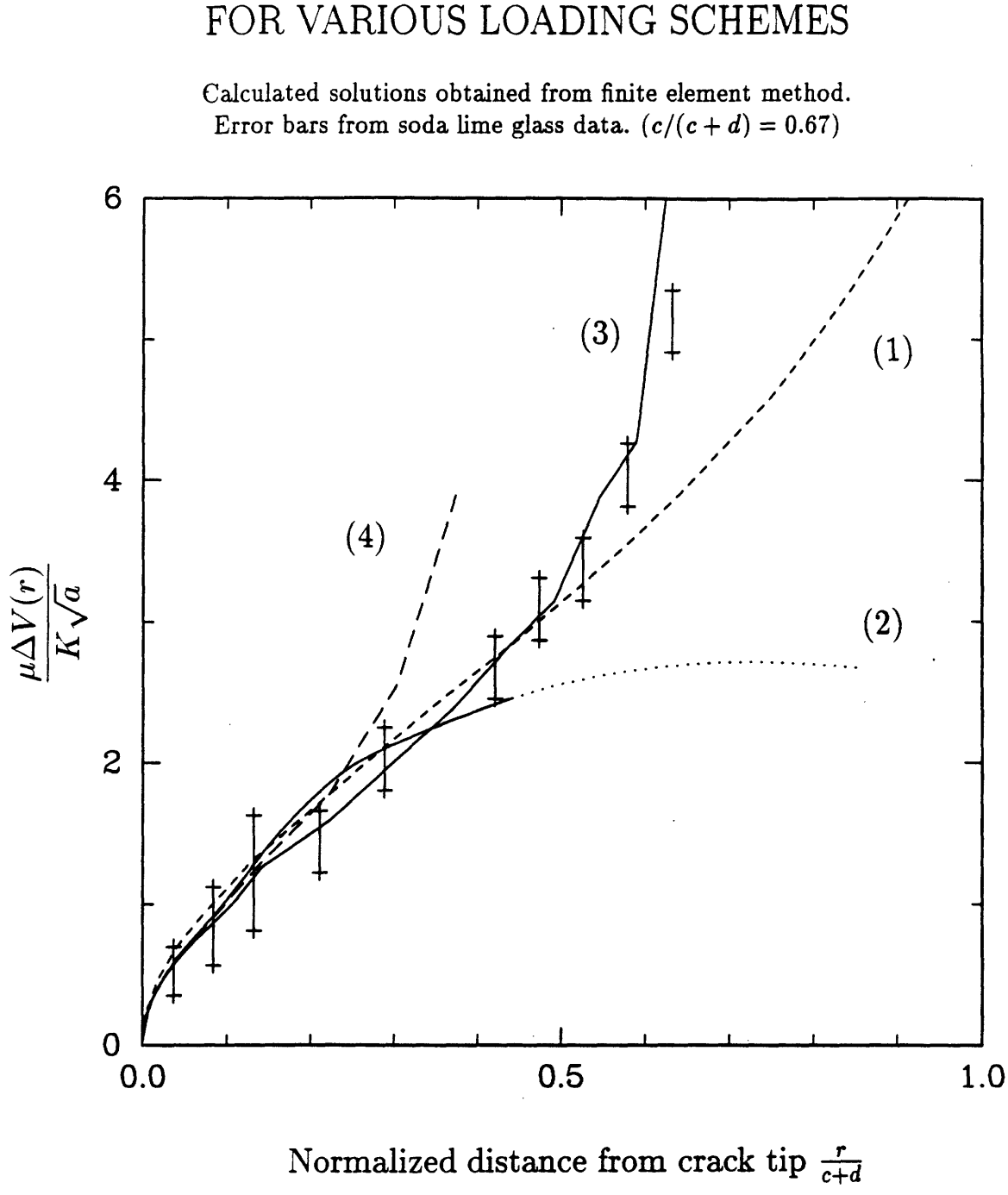

Figure 5-3: Shape factor F(r) for various loading schemes. (1) Concentrated load at center of indent d << c, (2) distributed load over length of indent, d, (3) Concentrated load at edge of indent, c/a = 0.65, (4) c/a = 0.35. Error bars are from soda lime glass data for which c/a = 0.67.

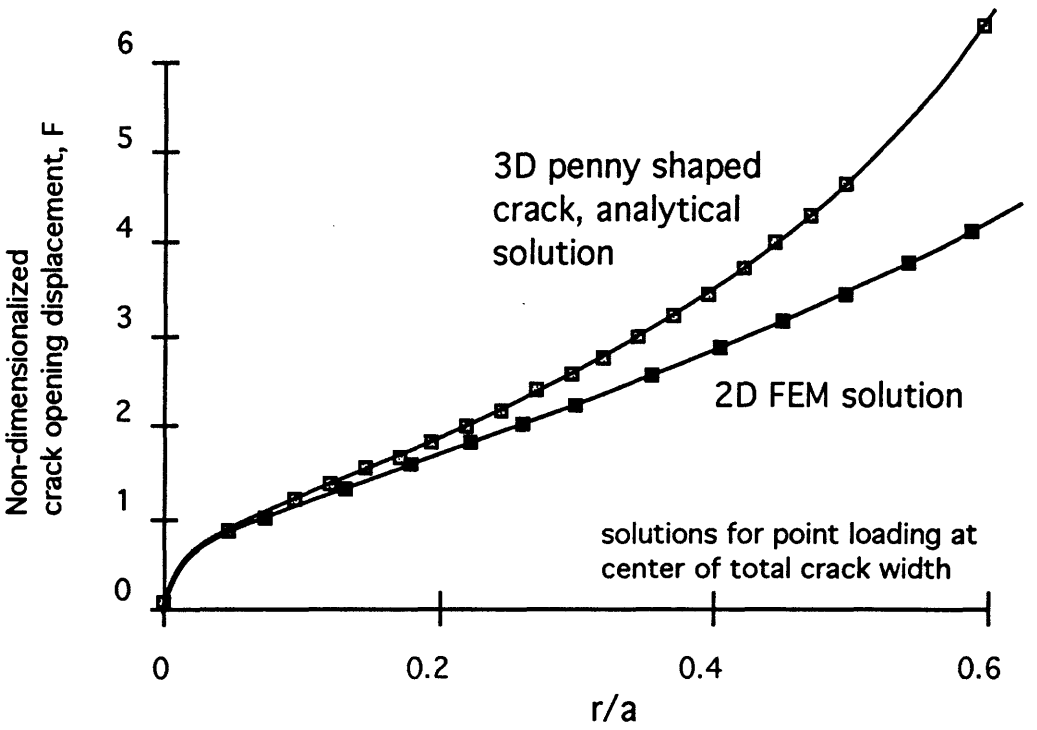

Figure 5-4: The sensitivity of the crack shape to the three dimensional nature of the indentation crack is measured through the comparison of the 2D FEM solution and the 3D analytical solution for the penny shaped crack loaded at the center.

CRACK SHAPE FROM ALUMINA SINGLE CRYSTAL

Calculated solutions obtained from finite element method.
Error bars from alumina data. ($c/a = 0.61$)

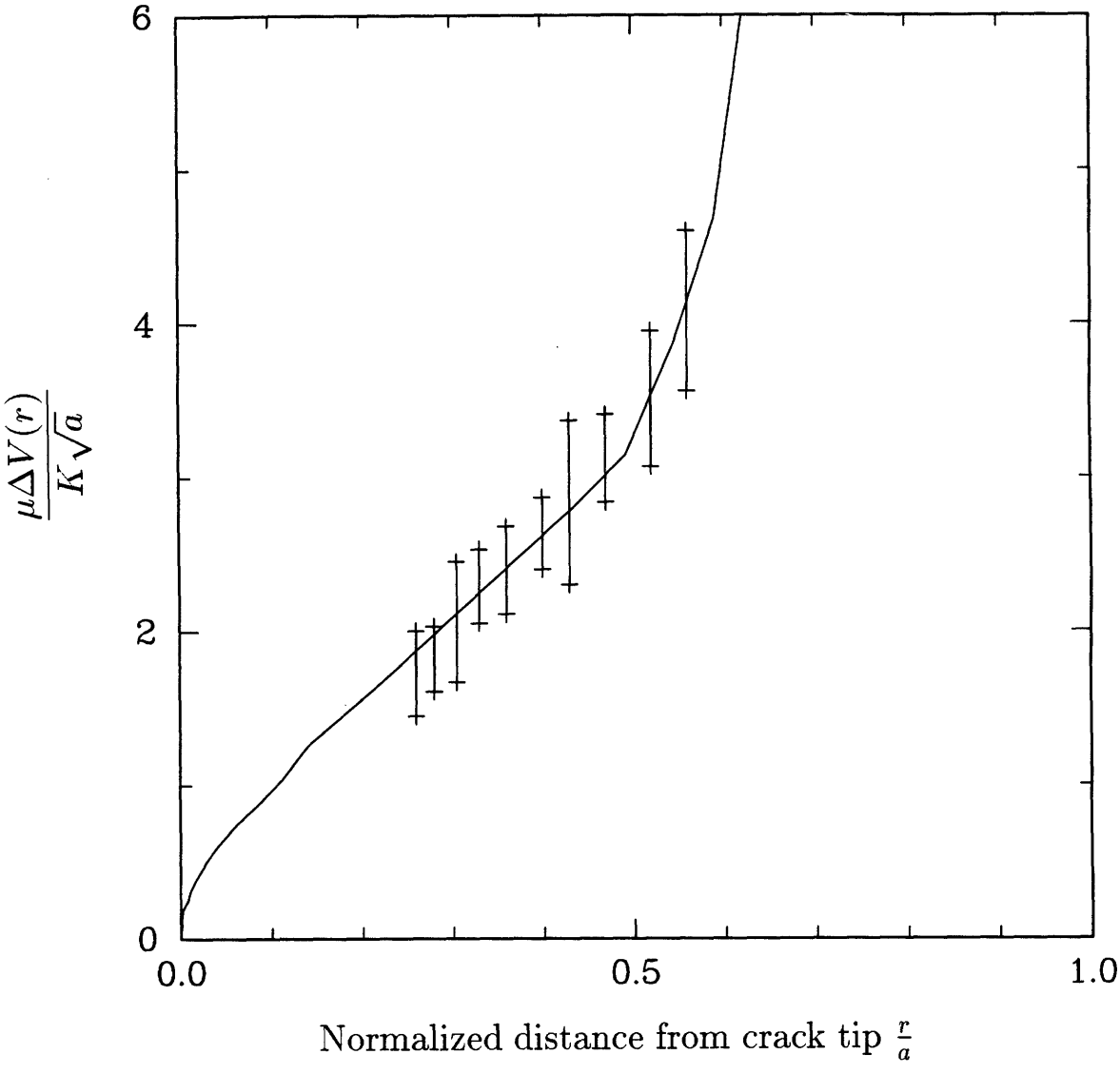

Figure 5-5: Shape factor F(r) and data from alumina single crystal (sapphire). The toughness value calculated is 2.56 MPa/m .

CRACK SHAPE FROM SILICON SINGLE CRYSTAL

Calculated solutions obtained from finite element method.
Error bars from silicon data. ($c/a = 0.71$)

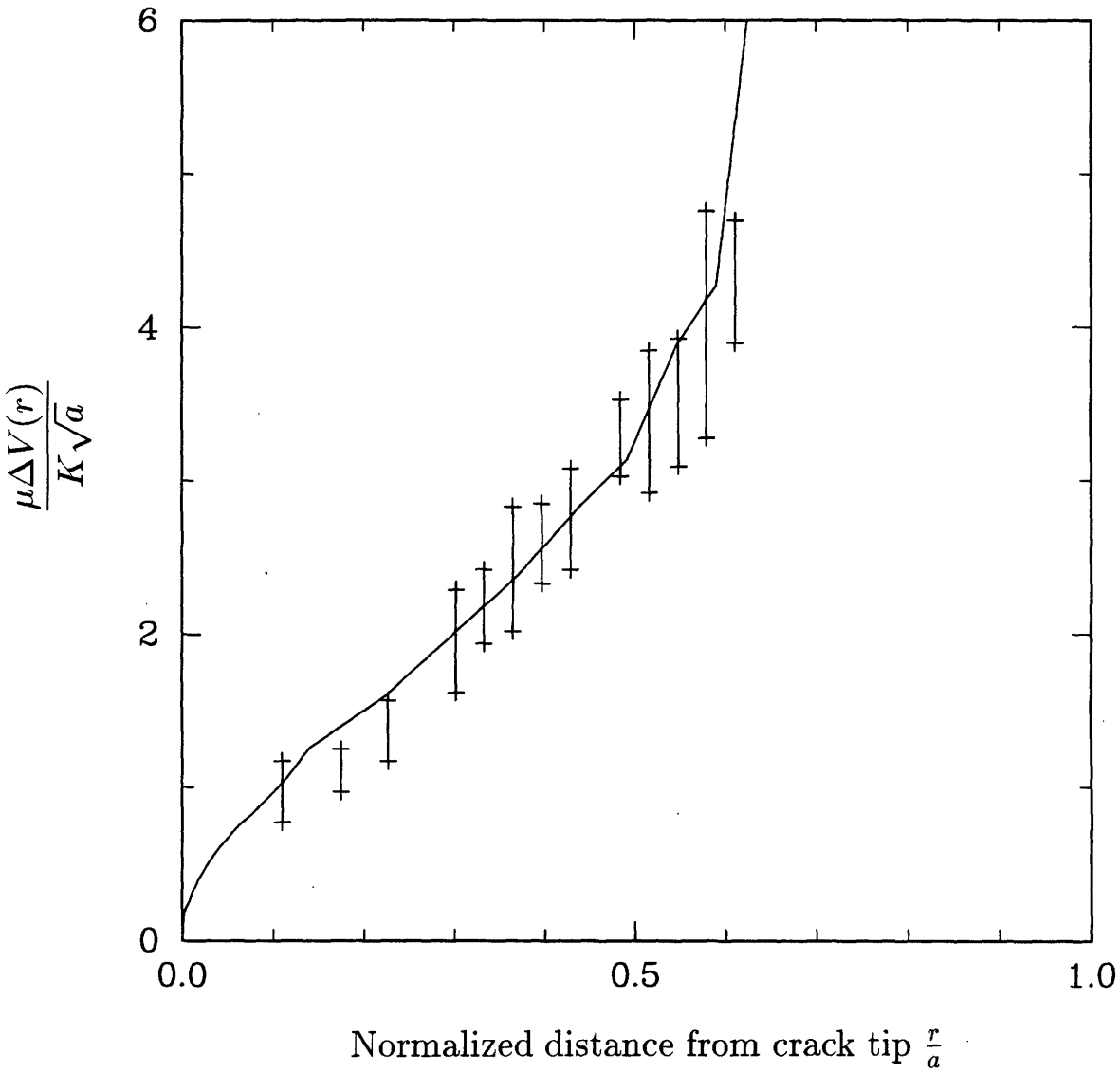

Figure 5-6: Shape factor F(r) and data from silicon single crystal. The toughness value calculated is 0.87 MPa/m.

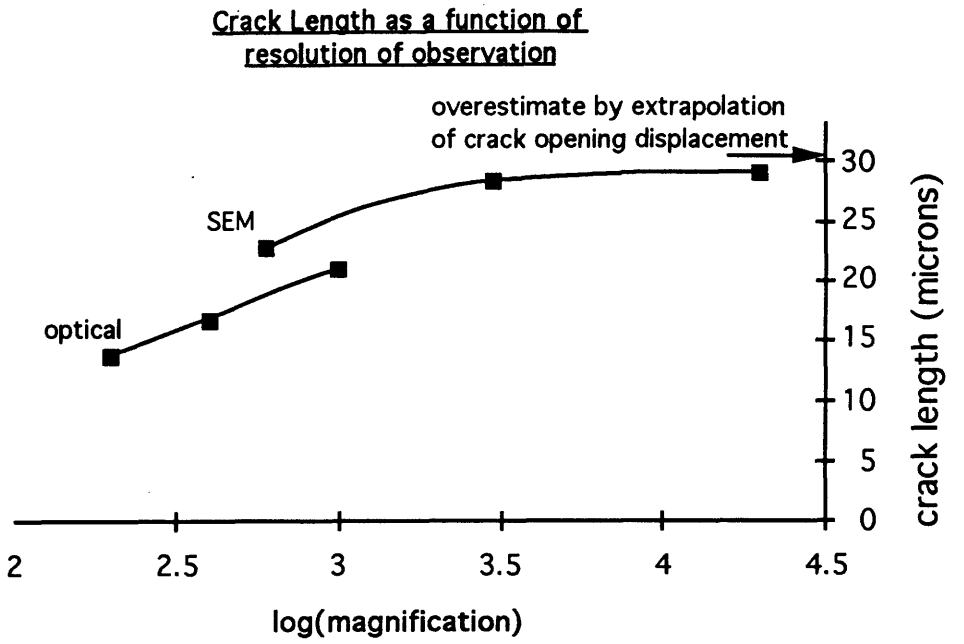

Figure 5-7: The measurement of crack length is affected by the method and resolution of observation.

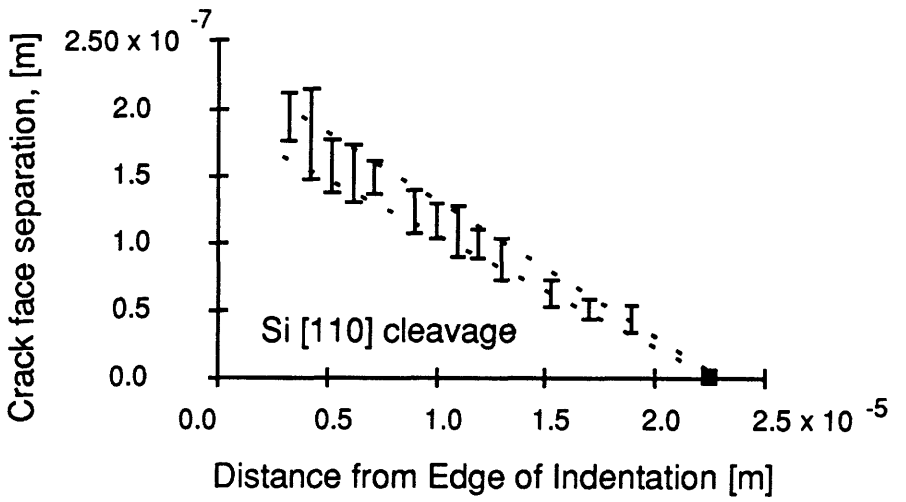

Figure 5-8: The crack opening displacement data is approximately linear in the range of measurement.

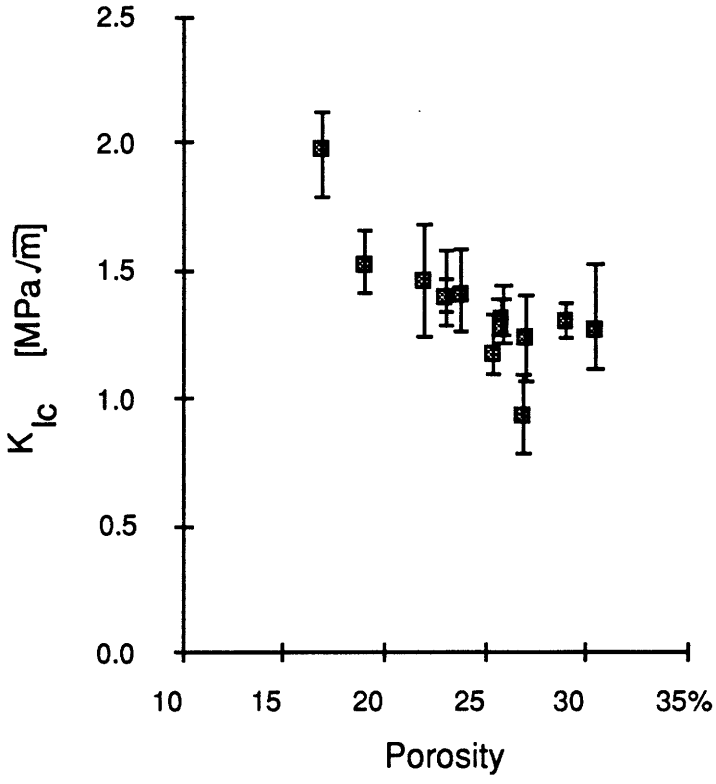

Figure 5-9: Fracture toughness ranges for specimens of RBSN as a function of porosity. Note that the range of values are not error bars but are representative of the toughness variations. Each computed toughness value has an uncertainty of 1%.

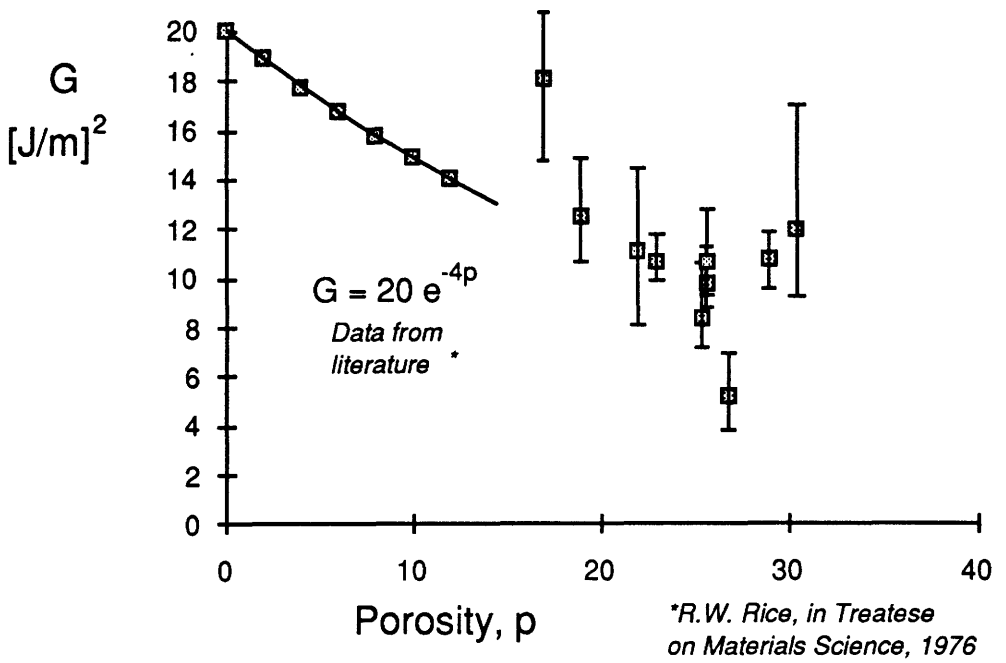

Figure 5-10: The energy release rate, G, as a function of average porosity. Note that the range of values are not error bars, but are representative of the material variation. Each computed fracture energy value has an uncertainty of 2%.

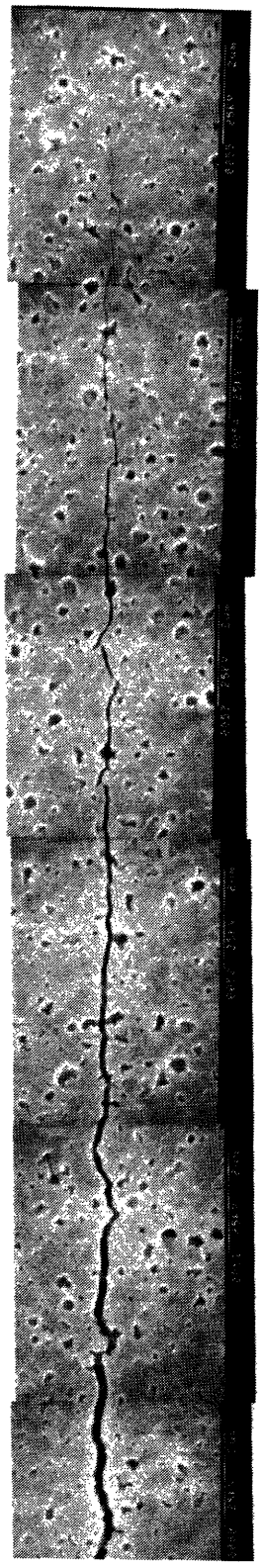

Figure 5-11: The typical planar crack path morphology of the Vickers microhardness indentation crack. (Material F).

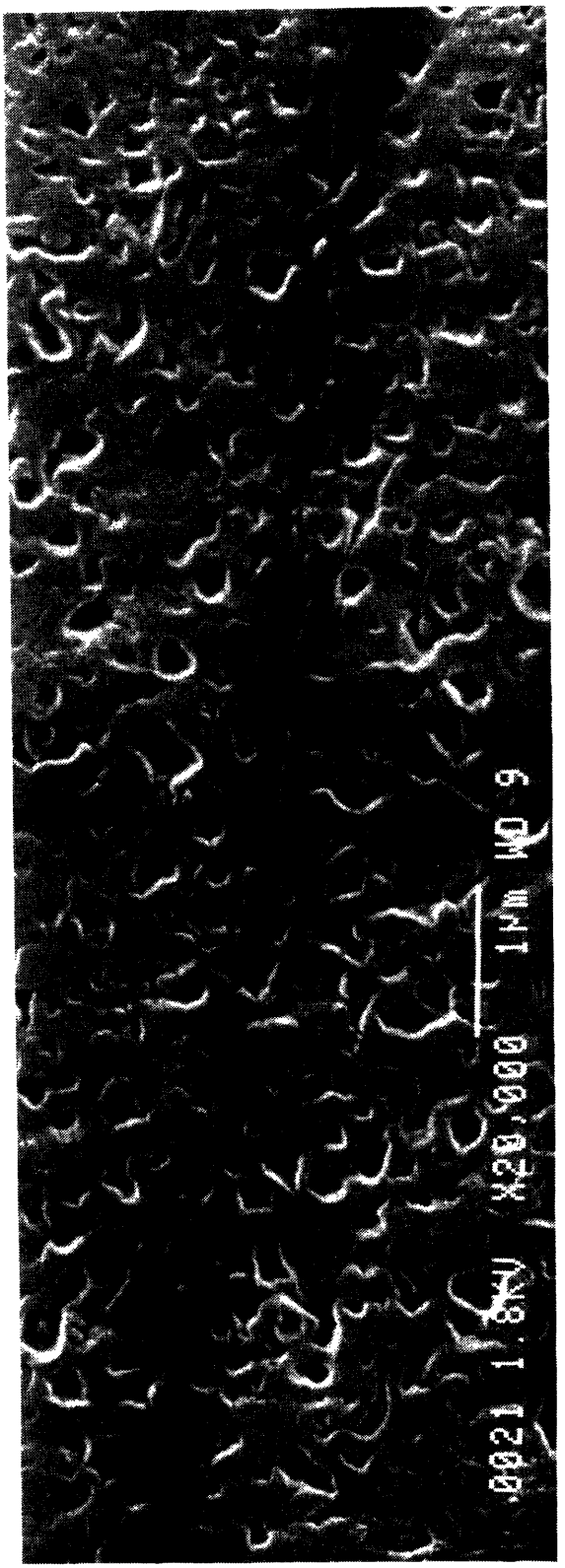

Figure 5-12: High resolution image of the Vickers indentation crack propagating through the RBSN microstructure. (Material D).

Material H

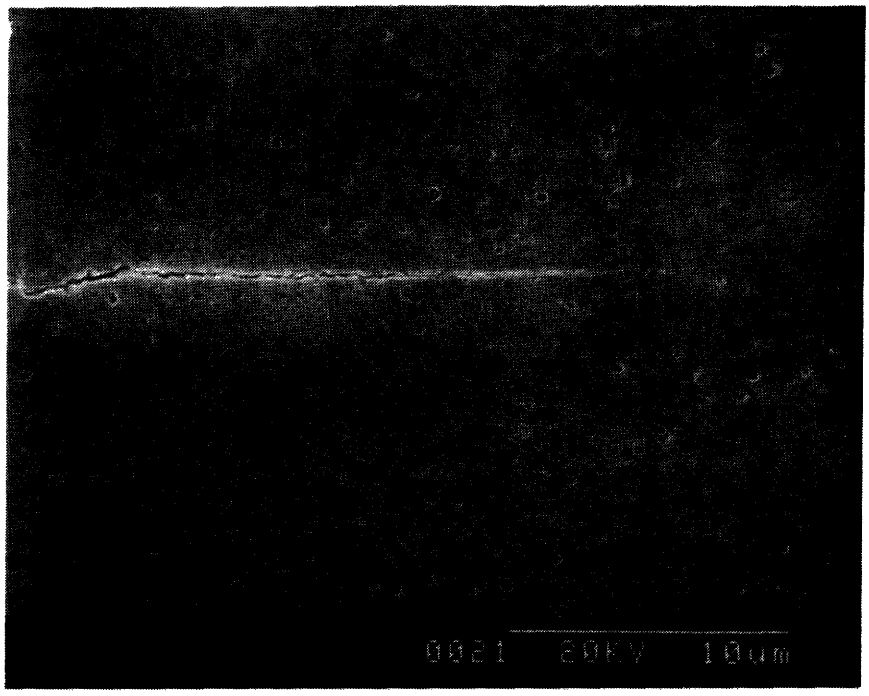

Material G

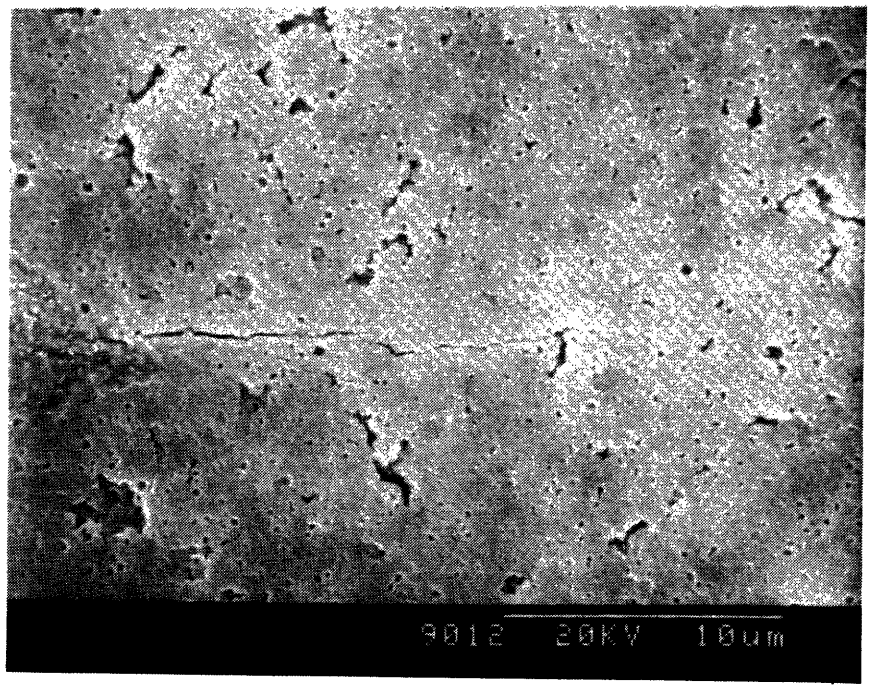

Figure 5-13: Vickers indentation cracks in nominally identially processed material. Material G has a lower Young's modulus, and fracture toughness.

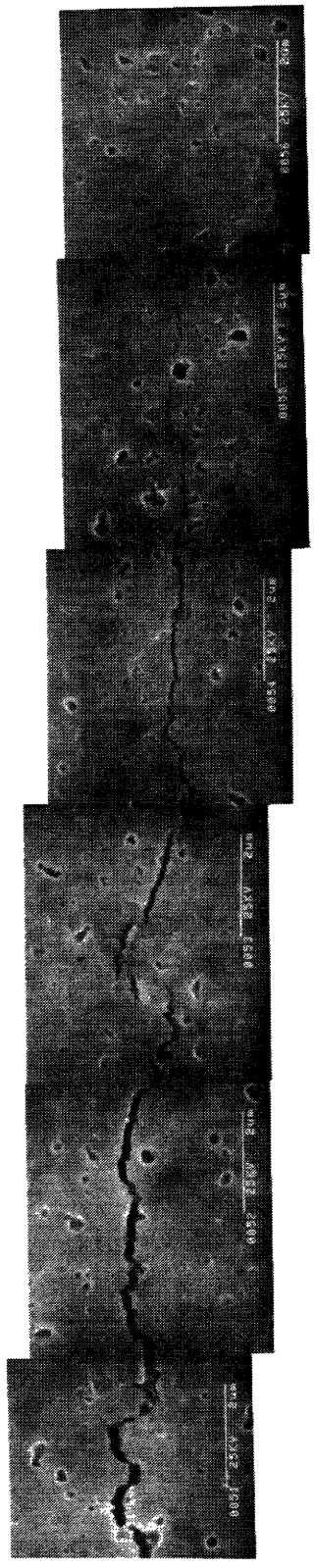

Figure 5-14: High porosity specimen exhibited increased roughness and evidence of bridging ligaments. (Material A).

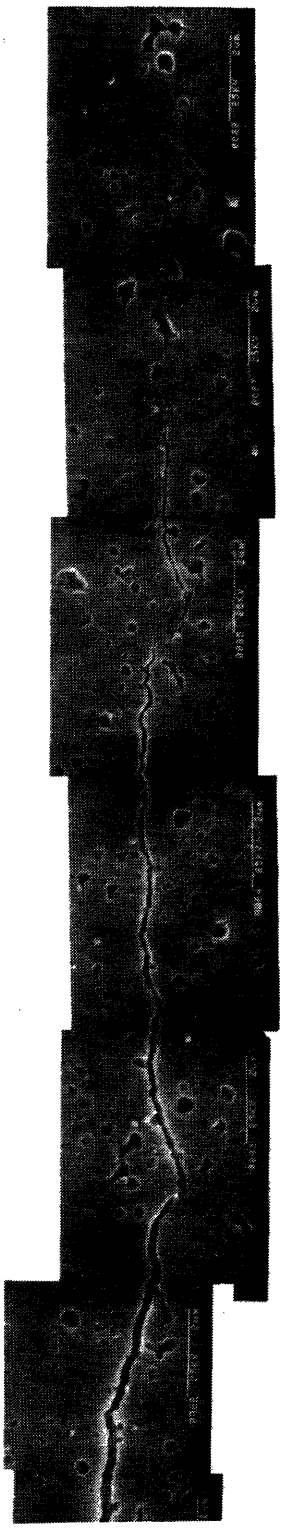

Figure 5-15: High porosity specimen exhibited increased roughness and evidence of bridging ligaments. (Material B).

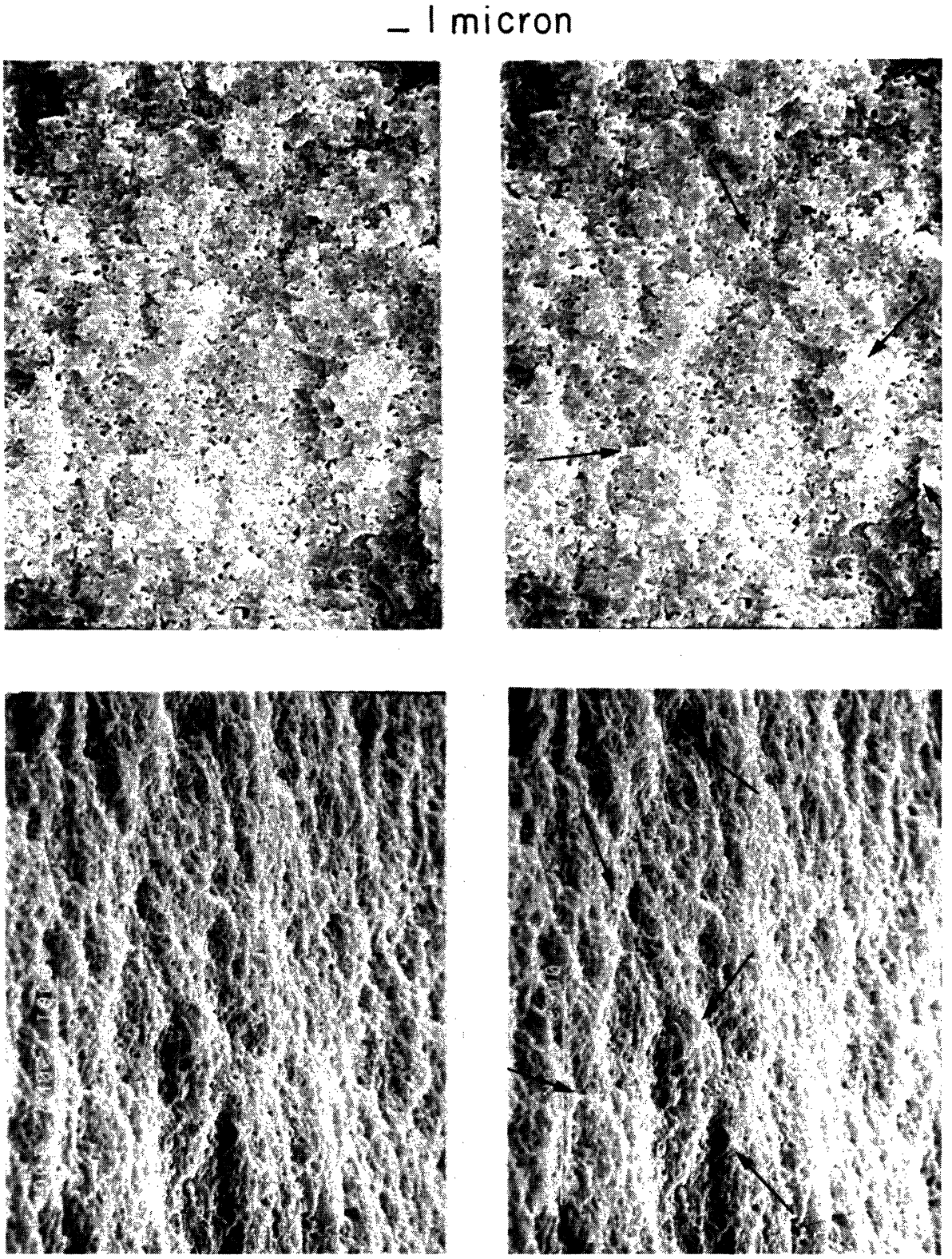

Figure 5-16: Stereo pair micrographs of the fracture surface of material H. The crack propagation direction is vertical from top to bottom.

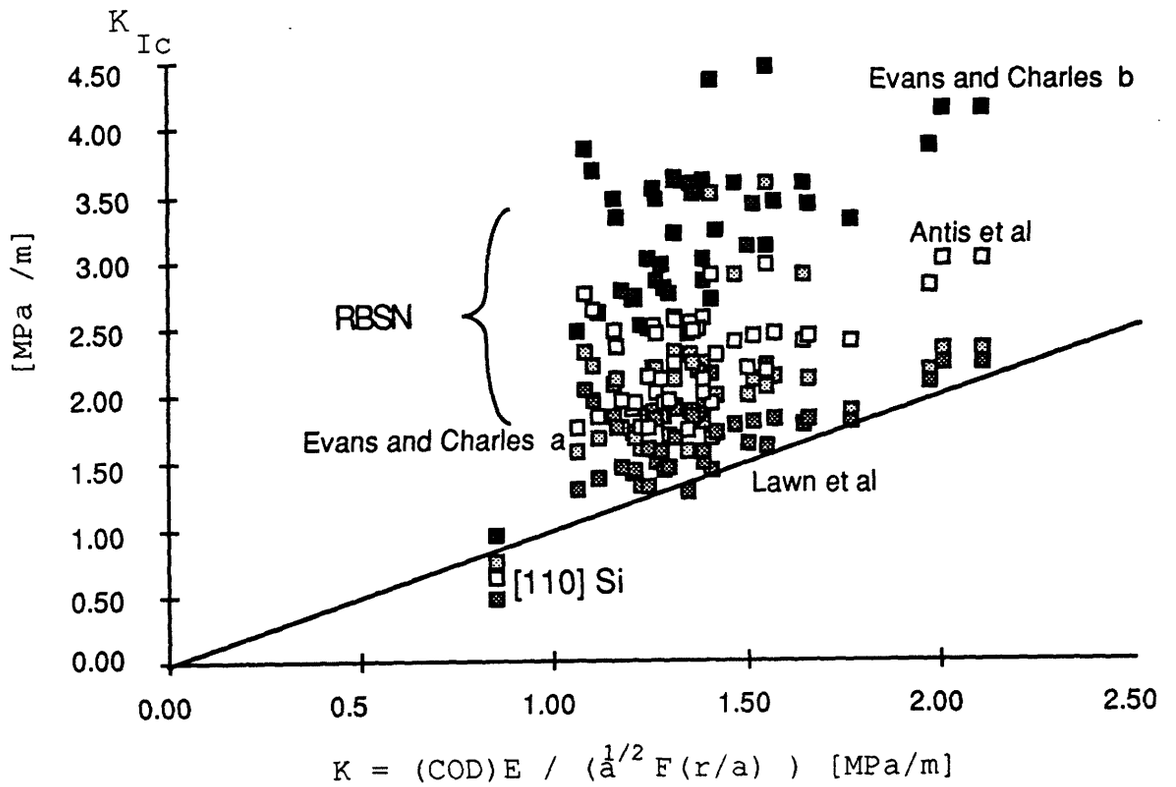

Antis et al: (1981)	$K = 0.016(E/H)^{1/2}(P/a^{3/2})$
Lawn et al: (1980)	$K = 0.028(E/H)^{1/2} H\, d^{1/2} (d/a)^{3/2}$
Evans and Charles: (1976)	$K = 0.16\, H\, d^{1/2} (d/a)^{3/2}$
	$K = 0.0732(E/H)^{1/2} H\, d^{1/2} (d/a)^{3/2}$

Figure 5-17: The comparison of four other crack-length toughness models indicating the conservative measure of the COD technique the approximate correlation between the methods, and the general scatter arising from the choice of model.

Chapter 6

Conclusions

The brittle nature of ceramic materials has provoked numerous studies to explore means of toughening these materials. The prevalent philosophy of microstructural design is to isolate the dominant mechanism of toughness through material production and evaluation and to optimize the material processing steps accordingly. The conception of new microstructures is typically based upon existing models which should lead to superior performance. The justification of this approach is usually the inadequacy of the available degrees of freedom in processing to achieve the sought after microstructures.

In the approach taken here to microstructure design, the microstructure-property connection is studied experimentally while in a parallel computer simulation the processes that control the microstructure and the mechanisms that control the property are modelled. This is ideally pursued until a close correspondence is reached with the actual experimentally probed system through a systematic variation of the available parameters that control the simulated microstructures. Once a proven cause-effect relationship is reached in the simulations that parallel the experimental one, it becomes possible to use the computer simulations to explore other microstructure-property connections and determine the possible benefits of pursuing new developments in processing to achieve such microstructures. In this final chapter the results of the preceding chapters are drawn together in order to summarize the degree to which a connection is made between the cause-effect relationships in the experimentally

probed system and the simulations.

6.1 Summary of Thesis Results

Simulations

The modelling of the reaction kinetics and subsequent fracture of the intermediate porosity reaction bonded silicon nitride mirrors many of the key features of the experimentally observed materials. In the first phases of the modelling, the reaction kinetics model in its simple form succeeds in producing microstructures which have many of the features of the observed microstructure, such as pore size and shape distributions, and average grain to particle size. As important is the allocation of such specific microstructural details which are difficult to obtain experimentally, such as the grain boundary configurations in relation to the porosity. The fracture simulations which are based on the elastic network of central and angular force bonds are then used to sample the properties of these simulated microstructures.

Crack nucleation simulations, in the first case, were performed to observe and quantify the damage accumulation processes. The observed 'clustered' nature of the fracture cascades which comprise the stable fracture of interpore ligaments is central to the high energy absorption displayed by these microstructures. However, the various microstructures generated produced, in general, small differences in mechanical properties. The average porosity was found to be the largest influence.

These observations were then extended to the growth of a crack in a stress gradient such that the criterion of fracture was made to match the length scale of the fracture cascades corresponding to the interpore ligament dimension. The primary result of this study is that for highly heterogeneous microstructures there are optimal distributions of strength and stiffness variability. In the ideal case, the strength and stiffness are uncorrelated and that high variability is beneficial by increasing crack tortuosity and bridging by tough ligaments, to the extent that generalized microcracking and excessive reduction in the average strength are avoided. As the variability of local properties increased from zero for the homogeneous case, redundant cracking

and increased tortuosity were observed, followed by the bridging of locally tough elements. As variability further increased the toughness peaked followed by the general microcracking case, characterized by the unbounded growth of the microcrack cloud.

Within the confines of the allowable distributions of local micromechanical properties imposed by the structure of the porous microstructure, the strength and stiffness are typically correlated through the common parameter of local porosity. Therefore from a microstructural design perspective, any effects which de-couple strength and stiffness and increase variations are advantageous, such as the introduction of variations in strength through tailoring of grain boundary strength.

These simulation results are trends of mechanical behavior in simplified models of spring networks, and the degree of realism is limited by the two dimensionality and the discreteness of the mesh. Further, the issue of nucleation ahead of the crack tip in competition with the macroscale crack propagation gives rise to artificial effects such as occasional microcrack nucleation ahead of the crack tip and subsequent joining with the main crack. Also, at high variabilities frequent bridging by crack blunting at strong elements discounts the possibility of crack growth around such an obstacle in the third dimension. The utility of these models, therefore, is as a sensitivity test of the pertinent factors which are available to vary.

Measuring Fracture Toughness

As important to the process of microstructural design as any other stage in the iterative process of material production and evaluation, is the accurate measurement of the toughness parameter, K_{Ic}. Although the Vickers indentation crack length / toughness methods provide comparitive trends, they do not provide a high degree of sensitivity to small variations. The results of Chapter 5 demonstrate the degree of success of measuring fracture behavior of laboratory scale specimens by making use of the observations of cracks produced by Vickers microhardness indentations. Unlike other methods of measuring fracture toughness with Vickers indentation cracks, which are based upon empirical fits with crack length and applied load, the residual stresses created by the displaced material under the indenter serve as the driving

force to prop open the radial/Palmqvist cracks, and thereby provide directly observable evidence of crack propagation resistance. The simple physics which relate crack opening displacements with the fracture toughness, the lower bounding character of the measurement and the fact that the indentations produced are analogous to in service and machining damage suggest this method as a superior measurement technique for component design data. Although the uncertainties associated with making measurements of submicron crack face opening displacements, and the lack of certainty of the precise character of the residual stress field suggest improvements in methods and analysis, the potential of this technique is for providing data based upon sound physical principles.

The existance of residual stresses after removal of the indentation load in well characterized materials is shown to make possible the connection of the crack shape and the stress state at the crack tip. Although no direct evidence or proof is given that the cracks generated are at impending fracture, or at critical stress intensity, nevertheless, the circumstancial evidence discussed in Section 5.2.1 suggests crack growth upon unloading and thus crack arrest at K_c.

Comparisons of real and simulated mechanical behavior

The simulation results are then compared with the fracture behavior of experimentally produced porous RBSN ceramic, as described in Chapter 2, which was produced by Haggerty and co-workers. These high purity, highly homogeneous microstructures over the porosity range of 17 to 31% were produced in nominally the same manner. Variations in porosity were obtained by different packing procedures and by the addition of binders and therefore the various materials may be unique and not directly comparable with the other specimens. For example, the lowest porosity specimen was produced with a binder which reacted to form additional silicon nitride phase, instead of the normal binder burn out. However, the results of the fracture simulations indicate that for similarly homogeneous materials, without long range order beyond the intrinsic pore dimension, the porosity morphology does not play a significant role in the fracture behavior. The average porosity was the key determinant. This

appears to be evidenced in the fracture trends for the experimentally produced material, which are highly correlated with average porosity, despite the range of processing procedures.

The simulation of fracture in a microstructure with variability of strength and stiffness obtained from simulated microstructures produced similarly planar cracks and sparse redundant cracking. Distributions of strength and stiffness obtained from other variations in microstructure such as the grain to pore size produced similar measured fracture toughness. In addition, variations in tensile toughness was most strongly influenced by the average porosity, and other microstructural variations, produced relatively small variations. The observations of the strong planar character of the cracks in the RBSN material also suggest that minimal microcracking occurs, in light of the result in Chapter 4 that increased redundant cracking implies increased crack deflection and tortuosity. There were no observations of significant microcrack clouds in the simulated fracture without strong deflections and bridging ligaments left in the crack wake. In addition, the acoustic microscopy images, however coarse the resolution, did not display any evidence for microcracking.

Detailed examination of Vickers indentation induced cracks in RBSN demonstrates a relatively small variation in measured fracture toughness. Most observed cracks displayed a strongly planar character with average sampling of the porosity, indicating a functional dependence of fracture toughness on porosity of $K_c/\sqrt{G_{co}E_o} = \exp(-bp)$ which is not desirable if one wishes to overcome the weakening effects of increased amounts of porosity. The measured fracture toughness exhibited the predicted decrease consistent with the planar character of the fracture paths.

In the probing the elastic modulus of both large sections of microstructure and on the representative volume element scale, as defined in Section 4.2.5, the initial modulus was found to have a particularly strong dependence on average porosity. This same dependence on average porosity was found in the experimentally measured values, indicating a similar degree of microstructural homogeneity in both simulated and real material.

There were some cases for which the fracture properties stood out. For the high-

est porosity RSBN specimens, some evidence of bridging ligaments in the crack wake was observed, which is surmised to be a result of three dimensional crack tortuosity producing crack-tail like behavior. These observations are consistent with the relatively high energy release rates of these materials, and with other studies of crack propagation in porous media that higher crack complexity occurs at higher porosity [89]. These observations are also consistent with the result of higher variability in local strength and stiffness at higher porosity, which implies increased crack tortuosity, redundant cracking and ligament bridging.

In addition, the simulation of microstructures with anisotropic grain growth, which produced a microstructure with elongated grains, was stronger than other materials of the same porosity, and tougher as measured by the tensile toughness by a factor of 1.27. The improvement in fracture toughness derived from elongated grains has been typically associated with grain bridging and pull out in the crack wake in the literature, however in this case the increase in the toughness of the material is attributed to increased strength and microcrack stability.

The consideration of the weakening effect of the large scale, narrow pore channels, which were observed to reduce the toughness, is approximately explained by the simulations in Chapter 4. The result of the simulated fracture toughness measurement of a structure with a given artificial long range spacial correlation produced lower toughness, in general agreement with the fracture of the real materials containing long pore channels. In essence, with long range spacial correlation, the possibility exists for providing for a preferential fracture path, and this is consistent with both simulation and real observations. However, the comparison of the fracture modelling is best compared with the homogeneous microstructures. The inherent difficulty of simulating a wide range of dimension in the structure of micromechanical properties is well recognized, and specialized techniques such as using the renomalization concept for incorporating processes on multiple length scales are available.

A final comparison of the results of the simulation results with real material behavior is that the analysis in Chapter 4 agrees with the analysis of Lawn [60] that the conditions for producing large microcrack process zones is difficult without creating

the condition of general microcracking. Over a narrow range of variability in the simulation population strength, (i.e. $0.46 < c(\sigma) < 0.52$ for a uniform distribution) the fracture behavior transformed into behavior consistent with generalized microcracking (i.e. unbounded microcrack cloud radius growth and no crack advance). No evidence was found for generalized microcracking in the RBSN material, and sparse evidence exists in the literature for such observations.

6.2 Statistical Distributions of Strength and Stiffness as Design Tools

The tools for designing microstructure in complex systems such as RBSN may come directly from material processing parameters or alternatively from more intermediate micromechanical parameters such as local strength and stiffness, and the connection of strength and stiffness with processing variables can then be made through an approximate way such as the model in Chapter 3. The microstructural feature size and shape distributions, as described in Chapter 2, serve as useful comparative devices such as pore size and shape, however, these lack the predictive capacity for guiding the processing. The spacial distribution of pores, which is a complex quantity as it relates to the higher order functions of strength and toughness, is as important in these complex microstructures as the pore size and shape. In intermediate porosity microstructures where porosity cannot be considered as defect, but as an integral part of the microstructure, the usual measure of the stress concentrating ability of an elliptical pore, $(\sigma/\sigma_{max} = 1 + 2\sqrt{a/\rho})$, is questionable, where a is half the pore major axis and ρ is the minimum radius of curvature, is for an isolated pore in an infinite medium, so that its applicability to the high porosity case is limited.

Instead, the measures of local elastic and strength properties obtained from probing the microstructure reflect the influence of spacial distribution of porosity. From the results in Chapter 4 of sampling simulated and real microstructures at a length scale corresponding to a small multiple of the average pore diameter, the local elastic modulus and strength are highly correlated with the average porosity. This result

implies that the bounds on the properties by the microstructural morphology of the RBSN impose constraints on the local strength and stiffness available for microstructural design.

The choice of the dimension for probing local properties is an important effect to the measured distribution. As the volume increases, the ensemble average for the elastic properties approaches the continuum average. The variability of strength will tend to narrow as the sampled volume increases, however the naturally occuring flaw population, consisting here of multiple contiguous pores, may exist over a range of dimensions and the average strength will tend to decrease, as predicted by the strength size effect of brittle fracture.

The appropriate choice of length scale must then necessarily include consideration of the scale of the microstructure, and the length scale of discrete fracture events. One of the key results of Chapter 4 is that microfractures nucleate at pore surfaces and grow in cascades which make up interpore ligaments. For this reason, the dimension of the interpore ligament was chosen to represent the dimension for sampling local strength and stiffness properties. In this way, the fracture criterion of maximum principal tensile tractions is made compatible with the consequence of fracture, the breaking of the bond on the same scale as the interpore ligament. In-situ observations of crack growth in other strongly heterogeneous material, reinforce this notion of 'clustered' crack propagation. For the case of coarse grained alumina, discontinuous crack growth was observed over distances as small as one grain diameter [103].

6.3 Strategies to Produce Tough Material

6.3.1 Overview

From the results summarized above, the potential for increasing fracture toughness is somewhat limited in high purity, highly homogeneous porous ceramic material, however, other strategies may exist to increase toughness. The results of simulated crack growth in controlled variability microstructures suggests there exists an optimal

amount of variation for fracture toughness, which corresponds to a peak toughness crack morphology with frequent crack bridging by locally tough elements and a co-operative microcracking contribution localized around the bridging ligaments with otherwise minimal microcracking. The observations of the highly planar crack paths in the majority of RBSN microstructures sampled indicate that higher variability in the microstructure on the length scale of the average pore size would increase crack tortuosity and toughness. In addition, effects which would produce independent variations in strength or stiffness will produce additional toughening.

6.3.2 Sources of Variability

One of the main sources of variability is associated with the average local porosity. The coefficient of variability increases for stiffness and strength from zero for perfectly uniform material to relatively high values with increasing amount of porosity in the two dimensional structures studied. Higher porosity structures exhibit higher variability in part because higher porosity structures naturally have a larger number of permutations to realize the structure. The experimentally observed cracks produced by Vickers indentations in the highest porosity RBSN materials which exhibited bridging ligaments, tortuous cracks and a higher energy release rate, are consistent with increased variability producing higher complexity crack paths and increased toughness.

In the case of the simulated reaction bonded silicon nitride, the correlation parameter of elastic modulus with the average porosity is -0.84 ± 0.01 over a range of simulated microstructures, indicating a high correlation. The strong dependence of elastic properties on the average porosity, as obtained experimentally and in the simulations, implies that the stiffness may not be an easy parameter to vary independently from the strength. Similarly, the majority of the dependence of local strength is on the local porosity. The correlation parameter obtained between the strength and porosity is typically -0.73 ± 0.08, indicating increased variability and de-coupling from local porosity as compared with the stiffness. Local strength may therefore be an easier parameter to use to induce variability.

Other than local density, other sources of variability for local strength which were not accounted for here, are thermal and elastic anisotropy misfit stresses. Thermal misfit stresses which are equivalent to producing strength variability are particularly potent, as they impose variability in strength independently from the local stiffness and do not shift the mean level of strength. However the potency may be lost at high temperatures where the misfit may be partly recovered. Similarly, elastic anisotropy misfit between grains produces stress concentrations, and do not affect the mean level of microstructure strength. Stiffness variability may also naturally arise from elastic anisotropy, and was not accounted for in the models presented here.

Other routes to obtain increased variability may be possible by incorporating a second phase material into the microstructure. In accord with the modeling framework with no spacial correlation larger than the average pore dimension, it can be said that the inclusion of a second phase of a well bonded population of particles with size corresponding to the average pore size and with another composition with chosen elastic properties, for example, would allow for controlled variation of elastic properties, and a likely increase in toughness.

6.4 Conclusions and Suggestions for Future Work

The general philosophy for the design of homogeneous ceramic microstructures originally derives from the desire to produce clean material with small strength controlling flaws. This pursuit in fully dense materials can and has been realized in many cases by high purity microstructures with residual porosity eliminated. In the case of microstructures with significant porosity, homogeneity is realized by producing highly uniform pore and grain dimensions, and the RBSN as produced by Haggerty and co-workers is evidence of the sophistication of the processing routes to achieve these microstructures.

However, the production of highly homogeneous microstructures may frequently produce planar character of flaw propagation, as evidenced by the behavior of the RBSN materials examined here, and low toughness. The homogeneity of materials

is beneficial in terms of reducing the flaw severity of the largest flaw and increasing the strength. Yet the result of the insensitivity of fracture behavior to pore size and spacial distribution, at the low end of the intermediate porosity range, suggests that highly homogeneous structures cannot be substantially improved through alterations of the pore size and shape through standard processing techniques. Other means which do not rely on toughness optimization based upon the rearrangement of the pore spacial structure should be addressed.

Recently, researchers in the ceramics community have realized the potential for designing in complexity for optimal performance, as described by M.P. Harmer [39], and this is increasingly accepted in light of the growth of theoretical models for toughening mechanisms in otherwise britte media. Although the application to fully dense systems is being made in such manners as introducing residual stresses through controlled thermal expansion mismatch, these same concepts should apply to highly porous microstructures. The benign neglect of porous materials is a result of the lack of recognition of the qualitatively different role of porosity in the intermediate regime where pores are not strength controlling defects, but are integral components of the microstructure. Controlled microstructural complexity in intermediate porosity materials under the guidance of appropriate fracture models, such as in Chapters 3 and 4, are useful with the production techniques that have been developed to produce high strength, uniform microstructures.

Finally, the design of porous microstructures which exhibit linear elastic behavior must include more consideration than the design of tough elements at the crack tip. Without the benefit of transformation toughening or frictional sliding effects which are potent sources of toughening, the effect of toughening by processes which are only effective at the crack tip are transitory. A microstructure which consists of homogeneously distributed tough elements will not be as tough as a microstructure with crack wake phenomenon, with associated R-curve behavior. Therefore considerations must be made in the design of highly heterogeneous material for the possibility of controlled variability microstructures which are likely to produce exceptionally tough material.

Extensions of this work into the design of composite structures which may provide tailored variability is possible with the groundwork laid here. Such considerations should be made also for the control of grain boundary strength, residual stresses, and spacial variability of density. In addition, the method for measuring fracture toughness by crack opening displacements induced by the Vickers indentation technique remains to be fully explored. The nature of the pertinent parameters which produce the residual stress field of Vickers indentations are not known.

Bibliography

[1] J.C. Amazigo and B. Budiansky. Interaction of particulate and transformation toughening. *J. Mech. Phys. Solids*, 36:581–595, 1988.

[2] M.P. Anderson, G.S. Grest, and D.J. Srolovitz. Computer simulation of normal grain growth in three dimensions. *Phil. Mag.*, 59:293, 1989.

[3] R.M. Anderson. Testing advanced ceramics. *Advanced Materials and Processes*, 3:31, 1989.

[4] E.A. Barringer and H.K. Bowen. Formation, packing and sintering of monodispersed TiO_2 powders. *J. Am. Ceram. Soc.*, 65:C199, 1982.

[5] P.F. Becher. Recent advances in whisker-reinforced cerammics. *Annu. Rev. Mater. Sci.*, 20:179, 1990.

[6] R. Bidaux, N. Boccara, and H. Chate. Cellular automata approach to diffusion problems. In P. Manneville, N Boccara, G.Y. Vichniac, and R. Bidaux, editors, *Cellula Automata and Modeling of Complex Physical Systems, Vol. 46*, page 73, Springer Proceedings in Physics, 1990.

[7] M.A. Biot. Theory of propagation of elastic waves in a fLuid-saturated porous solid. Parts I and II. *The Journal of the Acoustical Society of America*, 28:168 - 191, 1956.

[8] H. E. Bommel and K. Dransfeld. Attenuation of hypersonic waves in quartz. *Phys. Rev. Letters*, 2:298, 1959.

[9] A.F. Bower and M. Ortiz. Solution of three-dimensional crack problems by a finite perturbation method. *Journal of the Mechanics and Physics of Solids*, 38:443, 1990.

[10] M. Born and K. Huang. *Dynamical Theory of Crystal Lattics.* Clarendon, Oxford, 1966.

[11] B. Budiansky, J.W. Hutchinson, and A.G. Evans. *J. Mech. Phys. Solids*, 34:167, 1986.

[12] B. Budiansky, J.W. Hutchinson, and J.C. Lambropoulos. *Inter. J. Solids and Struct.*, 19:337, 1983.

[13] S.S. Chiang, D.B. Marshall, and A.G. Evans. The response of solids to elastic/plastic indentation. *J. Appl. Phys.*, 53:298, 1982.

[14] B. Chopard and M. Droz. Cellular automata approach to diffusion problems. In P. Manneville, N Boccara, G.Y. Vichniac, and R. Bidaux, editors, *Cellula Automata and Modeling of Complex Physical Systems, Vol. 46*, page 130, Springer Proceedings in Physics, 1990.

[15] T.S. Chow. Effect of particle shape at finite concentration on the elastic moduli of filled polymers. *Journal of Polymer Science: Polymer Physics Edition*, 16:959, 1978.

[16] D.R. Clarke. A simple calculation of process-zone toughening by microcracking. *J. Amer. Ceram. Soc.*, 67:255–260, 1984.

[17] N. Claussen. Fracture Toughness of Al_2O_3 with an Unstabilized ZrO_2 Dispersed Phase. *J. Am. Cer. Soc.*, 59:49, 1976.

[18] N. Claussen, J. Steeb, and R.B. Pabst. Effect of induced microcracking on the fracture toughness of ceramics. *Amer. Ceram. Soc. Bull.*, 56:559–562, 1977.

[19] R.F. Cook and G.M. Pharr. Direct observation and analysis of indentation cracking in glasses and ceramics. *J. Am. Ceram. Soc.*, 73:787–817, 1990.

[20] W.A. Curtin and K. Futtumura. *Acta Met. Mat.*, 38:2051–2058, 1990.

[21] D. Dab and J.P. Boon. Cellular automata approach to reaction-diffusion systems. *Phil. Mag.*, 59:257, 1989.

[22] E.A. Dean. Elastic moduli of porous sintered materials as modeled by a variable-aspect-ratio self-consistent oblate-spheroidal-inclusion theory. *Journal of the American Ceramic Society*, 66:847, 1983.

[23] S.P. Denker. *J. Less Common Metals*, 14:1, 1968.

[24] A.G. Evans. On the formation of a crack-tip microcrack zone. *Scripta Met.*, 10:93–97, 1976.

[25] A.G. Evans. Perspective on the development of high-toughness ceramics. *J. Am. Ceram. Soc.*, 73:187, 1990.

[26] A.G. Evans and R.M. Cannon. *Acta. Met.*, 34:7761, 1986.

[27] A.G. Evans and E.A. Charles. *J. Am. Ceram. Soc.*, 59:371, 1976.

[28] A.G. Evans and K.T. Faber. Crack growth resistance of microcracking brittle materials. *J. Am Ceram. Soc.*, 67:255, 1984.

[29] A.G. Evans and Y. Fu. *Acta. metall.*, 33:1525, 1985.

[30] A.G. Evans and R.M. McMeeking. On the toughening of ceramics by strong reinforcements. *Acta. metall.*, 34:2435, 1986.

[31] A.G. Evans, M. Ruhle, B.J. Dalgleish, and P.G. Charalambides. The fracture energy of bimaterial interfaces. *Materials Science and Engineering*, A126:53, 1990.

[32] W.A. Fate. High-temperature elastic moduli of polycrystalline silicon nitride. *Journal of Applied Physics*, 46:2375, 1975.

[33] H.J. Frost. Cavities in dense random packings. *Acta. metall.*, 30:889–904, 1982.

[34] P.A. Gennari. Masters thesis, U. Mass. at Amhearst, Dept. of Mechanical Engineering. 1988.

[35] L.J. Gibson and M.F. Ashby. *Cellular Solids, Structure and Properties.* Pergamon Press, 1988.

[36] J.J. Gilman. The science of hardness testing and its research applications. page 51, American Society for Metals, 1973.

[37] J. E. Gubernatis, E. Domany, J.A. Krumhansl, and M. Huberman. The Born approximation in the theory of the scattering of elastic waves by flaws. *J. Appl. Phys.*, 48:2812, 1977.

[38] J.S. Haggerty, A. Lightfoot, J.E. Ritter, P.A. Gennari, and S.V. Nair. Oxidation and fracture strength of high purity reaction bonded silicon nitride. *J. Am. Ceram. Soc.*, 72:1675, 1989.

[39] M.P. Harmer. Recent progress and remaining critical issues in the understanding of the sintering of ceramics. In *Proceedings of the 1991 Fall MRS Symposium*, Materials Research Society, 1991.

[40] F. Haubensak, J.S. Haggerty, L. Ewart, and A.S. Argon. Microstructural influences of the mechanical properties of RBSN. *to be published.*

[41] F.G. Haubensak, V.V. Bulatov, and A.S. Argon. The simulation of fracture in porous brittle media. *submitted to J. Computer-Aided Materials Design*, 1994.

[42] R. Hill. *The Mathematical Theory of Plasticty.* Oxford University Press, London, U.K., 1950.

[43] R.G. Hoagland, J.D. Embury, and D.J. Green. On the density of microcracks formed during the fracture of ceramics. *Scripta Met.*, 9:907–909, 1975.

[44] L. Huang, A. Ghosh, A.S. Kobayashi, and R.C. Bradt. Indentation fracture toughness of sintered Silicon Carbide in the Palmqvist crack regime. *J. Am. Ceram. Soc.*, 72:904, 1989.

[45] J.W. Hutchinson. Crack tip shielding by micro-cracking in brittle solids. *Acta. metall.*, 35:1605–1619, 1987.

[46] D. Lewis III. Ceramic matrix composites, advanced concepts. In *Microstructure Dependence of Mechanical Behavior of Ceramics*, 1988.

[47] A. Jagota and S.J. Bennison. Spring-network and finite-element models for elasticity and fracture. In K.K. Bardhan, B.K. Chakrabarti, and A. Hansen, editors, *Breakdown and non-linearity in soft condensed matter*, Springer Verlag, Berlin, 1993.

[48] L. Kadanoff. *Physics Today*, 39:7, 1986.

[49] J.L. Kardos. *Crit. Rev. Solid State Sci.*, 3:419, 1973.

[50] P.N. Keating. *Phys. Rev.*, 152:774, 1966.

[51] A. Kelly. *Strong Solids.* Volume 2nd, Clarendon, 1973.

[52] A.S. Kenyon and H.J. Duffy. *Polym. Eng. Sci.*, 7:1, 1970.

[53] E.H. Kerner. *Proc. Phys. Soc.*, 69B:808, 1956.

[54] K. Kijima and S. Shirasaki. Nitrogen self-diffusion in silicon nitride. *J. Chem. Phys.*, 65:2668, 1978.

[55] J.G. Kirkwood. *J. Chem. Phys.*, 7:506, 1939.

[56] D.L. Kohlstedt. *J. Mater. Sci.*, 8:777, 1973.

[57] A.J.C. Ladd and D Frenkel. Dynamics of colliodal dispersions via lattice-gas models of an incompressible fluid. In P. Manneville, N Boccara, G.Y. Vichniac, and R. Bidaux, editors, *Cellula Automata and Modeling of Complex Physical Systems, Vol. 46*, page 243, Springer Proceedings in Physics, 1990.

[58] J.C Lambropoulos. Shear, shape and orientation effects in transformation toughening. *Int. J. Solids Structures*, 22:1083, 1986.

[59] J. Lankford. Indentation microfracture in the Palmqvist crack regime: Implications for fracture toughness evaluation by the indentation method. *J. Mater. Sci. Lett.*, 1:493, 1982.

[60] B.R. Lawn. Fundamental condition for the existance of microcrack clouds in monophase ceramics. *J. European Ceramic Society*, 7:17–20, 1991.

[61] B.R. Lawn, A.G. Evans, and D.B. Marshall. Elastic/plastic indentation damage in ceramics: the median/radial crack system. *J. Am. Cer. Soc.*, 63:574, 1980.

[62] B.R. Lawn and M.V. Swain. *J. Mater. Sci.*, 10:113, 1975.

[63] R. LeSar, A.D. Rollett, and D.J. Srolovitz. *Mat. Sci. Engng.*, A155:267–274, 1992.

[64] L.C. Lev and A.S. Argon. Development of oxide coatings for matching oxide fiber-oxide matrix composites. *Ceram. Eng. and Sci. Proc.*, 18:743, 1994.

[65] H. Li, A. Ghosh, Y.H. Han, and R.C. Bradt. The frictional component on the indentation size effect in low load microhardness testing. *J. Mater. Res.*, 8:1028, 1993.

[66] A. Lightfoot, H.L. Ker, J.S. Haggerty, and J.E. Ritter. Properties of RBSN and RBSN-SiC composites. *Ceramic Engineering and Science Proceedings*, 11:842, 1990.

[67] A. Lightfoot, J. Sigalovsky, and J.S. Haggerty. Analyses of RBSN having high and low fracture toughnesses. *submitted to the Journal of the American Ceramic Society*, 1994.

[68] A. Lightfoot, J. Sigalovsky, and J.S. Haggerty. Relationship between toughness and microstructure of reaction bonded Si_3N_4. *Ceram. Eng. Sci. Proc.*, 13:1024, 1992.

[69] J.F. Lutsko. The determination of the elastic properties of inhomogeneous systems by computer simulation. In M. Meyer and V. Pontikis, editors, *Computer*

Simulation in Material Science, pages 349–363, Kluwer Academic Publishers, 1991.

[70] J. Marrow, V. Luprano, and S. Roberts. Scanning acoustic microscopy observations of high-temperature crack-bridging mechanisms in alumina. *J. Am. Ceram. Soc.*, 76:2915, 1993.

[71] D.M. Marsh. *Proc. Roy. Soc. London Ser. A*, 279:420, 1964.

[72] R.L.K. Matsumoto. Evaluation of fracture toughness determination methods as applied to ceria-stabilized tetragonal zirconia polycrystals. *J. Am. Cer. Soc.*, 70:C–366, 1987.

[73] F.A. McClintock and A.S. Argon. *Mechanical Behavior of Materials.* Addison-Wesley Publishing Co. Inc., 1966.

[74] I.J. McColm. *Ceramic Hardness.* Plenum Press, 1990.

[75] R.M. McMeeking and A.G. Evans. *J. Am. Ceram. Soc.*, 65:242, 1982.

[76] I. Merkel and U. Messerschmidt. Fracture toughness of sintered SiC ceramics: A comparison between different methods. *Materials Science and Engineering*, A151:131, 1992.

[77] D. Messier and W. Croft. *Army Materials and Mechanics Research Center review paper*, 1980.

[78] L. Monette, M.P. Anderson, S. Ling, and G.S. Grest. *J. Mat. Sci.*, 27:4393–4405, 1992.

[79] A.J. Moulson. Reaction-bonded silicon nitride: It's formation and properties. *J. Mat. Sci.*, 14:1017–1051, 1979.

[80] S.V. Nair, Z.Q. Cai, J.E. Ritter, A. Lightfoot, and J.S. Haggerty. Indentation residual stresses in RBSN and RBSN composites. *Proc. 16th Annual Conf. on Composites and Advanced Ceramics, American Ceramic Society, Cocoa Beach, FL*, Jan, 1992.

[81] G.L. Nutt and W.E. King. Comments on the Bond Strength Measurements of Gupta et. al. *to be submitted for publication*, 1994.

[82] S. Palmqvist. Occurance of crack formation during vickers indentation as a measure of the toughness of hard metals. *Arch. Eisenhuettenwes*, 33:629, 1962.

[83] C. Pierre and E.H Dowell. Localization of vibrations by structural irregularity. *Journal of Sound and Vibration*, 114:549, 1987.

[84] P. Popper and S.N. Ruddlesden. The preparation, properties, and structure of silicon nitride. *Trans. Brit. Ceram. Soc.*, 60:603–626, 1961.

[85] W.R. Rhodes. Agglomerate and particle size effects on sintering Yttria-stabilized Zirconia. *J. Am. Ceram. Soc.*, 64:19, 1981.

[86] R. W. Rice. Microstructure dependence of mechanical behavior of ceramics. In R.K. MacCrone, editor, *Treatise on Materials Science and Technology, Vol. II*, page 199, Academic Press, N.Y., 1977.

[87] R.W. Rice. Extension of the exponential porosity dependence of strength and elastic moduli. *J. Am Ceram. Soc.*, 59:536, 1976.

[88] R.W. Rice and D. Lewis III. Limitation and challenges in applying fracture mechanics to ceramics. *Fracture Mechanics of Ceramics*, 5, 1981.

[89] R.W. Rice, K.R. McKinney, C.Cm. Wu, and S.W. Freiman. Fracture energy of Si_3N_4. *Journal of Materials Science*, 20:1392, 1985.

[90] F. Riley. Preparation and properties of silicon nitride based materials. *Materials Science Forum*, 47:70, 1989.

[91] J.E. Ritter, S.V. Nair, P.A. Gennari, J.S. Haggerty, and G.J. Garvey. High strength reaction bonded silicon nitride. *Advanced Ceramic Materials*, 3:415, 1988.

[92] L.R.F. Rose. Toughening due to crack front interaction with a second phase dispersion. *Mechanics of Materials*, 6:11, 1987.

[93] S. Roux. Continuum and discrete description of elasticity and other reological behaviour. In H.J. Herrmann and S. Roux, editors, *Statistical Models for the Fracture of Disordered Media*, chapter 3, pages 87–114, Elsevier Science Publishers, 1990.

[94] M. Ruhle, A.G. Evans, R.M. McMeeking, and P.G. Charalambides. Microcrack toughening in alumina/zirconia. *Acta Metall.*, 35:2701, 1987.

[95] E. Schlangen and J.G.M. Van Mier. *Int. J. Dam. Mech.*, 1:435–454, 1992.

[96] G.M. Schwab and A. Krebs. *Planseeber. Pulvermetall.*, 19:91, 1971.

[97] B.W. Sheldon and J.S. Haggerty. The nitridation of high purity, laser-synthesized silicon powder to form reaction bonded silicon nitride. *Ceramic Engineering and Science Proceedings*, 9:1061, 1988.

[98] B.W. Sheldon and J.S. Haggerty. The Formation of Reaction Bonded Si_3N_4 at Low Temperatures and in Short Times. *Proc. 13th Annual Conference on Composites and Advanced Ceramics, Engineering Ceramics Division Meeting, American Ceramic Society, Cocoa Beach, Fl.*, Jan. 1989.

[99] D.K. Shetty, A.R. Rosenfield, and W.H. Duckworth. Indenter flaw geometry and fracture toughness for a glass-ceramic. *J. Am. Ceram. Soc.*, 68:C282, 1985.

[100] D. Sornette. Acoustic waves in random media. II. Coherent effects and strong disorder regime. *Acustica*, 67:251, 1989.

[101] M.V. Swain, R.M. Latanision, and A.R.C. Westwood. *J. Amer. Ceram. Soc.*, 58:372, 1975.

[102] P.L. Swanson. Crack-interface traction: a fracture-resistance mechanism in brittle polycrystals. In *Advances in Ceramics, Fractograpy of Glasses and Ceramics*, pages 135–155, American Ceramics Society, Columbus, Ohio, 1988.

[103] P.L. Swanson, C.J. Fairbanks, B.R. Lawn, Y. Mai, and B.J. Hockey. Crack-interface grain bridging as a fracture resistance mechanism in ceramics: Experimental study on alumina. *J. Am. Ceram. Soc.*, 70:279, 1987.

[104] R.G.F. Taylor and A.J. Pointon. Microwave Ultrasonics. *Contemp. Phys.*, 10:159, 1969.

[105] B.R. Tittmann and H. E. Bommel. Simple scheme for hypersonic measurements over broad frequency range. *Rev. Sci. Instruments*, 39:614, 1968.

[106] M. S. Triantafyllou and G.S. Triantafyllou. Frequency coalesence and mode localization phenomena: a geometric theory. *Journal of Sound and Vibration*, 150:485, 1991.

[107] H.Y. Wang, R. Najafabadi, D.J. Srolovitz, and R. Lesar. Segregation effects on intergranular fracture, an atomistic simulation study of Ni-Cu alloys. *Met. Trans. A*, 23:3105, 1992.

[108] C. Wu, S.W. Freiman, R.W. Rice, and J.J. Mecholsky. Microstructural aspects of crack propagation in ceramics. *J. Mat. Sci.*, 13:2659, 1978.

[109] C. Cm. Wu, R.W. Rice, and P.F. Becher. The character of cracks in fracture toughness measurements of ceramics. In S.W. Freiman and E.R Fuller, editors, *Fracture Mechanics Methods for Ceramics, Rocks, and Concrete, ASTM STP 745*, pages 127–140, American Society for Testing and Materials, 1981.

[110] C.F. Ying and R. Truell. Scattering of a plane longitudinal wave by a spherical obstacle in an isotropic elastic solid. *J. App. Phy.*, 27:1086, 1956.

[111] J.M. Zimon. *Models of Disorder.* Cambridge University Press, Cambridge, U.K., 1979.

Appendix A

Microcracking Model from Hutchinson

A model for microcrack toughening from Hutchinson, 1987, is summarized here. The effective reduction in driving force $K - K_{tip}$ for a microcrack nucleated in a particle of radius b with the same modulus as the matrix, has the following form,

$$\frac{K_{tip}}{K} = 1 + (k_1 - \frac{5}{8})\delta_1 + (k_2 + \frac{3}{4})\delta_2 + \frac{1}{3}\left(\frac{2}{\pi}\right)^{\frac{1}{2}} \frac{E\theta^T}{(1-\nu)K} \int_0^\pi [R(\theta]^{\frac{1}{2}} \cos(\frac{3}{2}\theta) d\theta$$

where,

$$k_1 = \frac{1}{32\pi} \int_0^\pi (11\cos(\theta) + 8\cos(2\theta) - 3\cos(3\theta)) \ln[R(\theta)] d\theta$$

$$k_2 = -\frac{1}{2\pi} \int_0^\pi (\cos(\theta) + \cos(2\theta)) \ln[R(\theta)] d\theta$$

$$\delta_1 = \frac{1}{1-\nu}\left[\frac{\overline{\overline{G}}}{\overline{G}} - 1\right]$$

$$\delta_2 = \frac{1}{1-\nu}\left[\overline{\nu}\frac{G}{\overline{\overline{G}}} - \nu\right]$$

$$\theta^T = \frac{16}{3}(1-\nu^2)\epsilon\frac{\sigma_R}{E}$$

Here, ϵ is the volume fraction of microcracks ($\epsilon = N < \lambda^3 >$). The terms k_1 and k_2 are the integrals which account for the process zone shape which is represented by $R(\theta)$, and δ_1 and δ_2 are dimensionless moduli which vanish for no change in modulus for the transformation.

Appendix B

Volumetric Expansion Parameter used in the Reaction Kinetics

The appropriate stoichiometric volume expansion parameter used in the reaction kinetics simulation is calculated here. To produce 1 'unit' (volume of 1 cell) of silicon nitride, we need:

$$3Si + 4N- > Si_3N_4$$

Mass balance: (V_o = volume of 1 cell, N = # cells)

$$m_{Si} + m_N = m_{Si_3N_4}$$

Mass of silicon evaporated from $\frac{1}{N}$ cells to produce one cell of silicon nitride:

$$m_{Si} = \frac{1}{N} \times V_o \cdot \rho_{Si}$$

where $\rho_{Si} = 2.33[\text{g/cm}^3]$, $\rho_{Si_3N_4} = 3.18[\text{g/cm}^3]$

$$m_N = \frac{4}{3} \times \frac{AMU(N)}{AMU(Si)} m_{Si} = \frac{2}{3} m_{Si}$$

$$m_{Si_3N_4} = V_o \cdot \rho_{Si_3N_4}$$

Substituting the above 3 equations into mass balance:

$$\frac{5}{3} \cdot \frac{1}{N} m_{Si} = V_o \cdot \rho_{Si_3N_4}$$

$$\hookrightarrow N = \frac{5}{3} \cdot \frac{\rho_{Si}}{\rho_{Si_3N_4}} = 1.22$$

Appendix C

Surface Tension in Reaction Kinetics Model

The consideration is made for surface tension in the reaction kinetics model of Chapter 3 for the reason that micrographs of RBSN appear to have smooth pore surfaces. The thermodynamic driving force is a function of the curvature of the surface, and the surface tension:

$$\Delta E = \sigma \cdot (K) \cdot \Delta V,$$

where σ is the surface tension, K is the curvature and ΔV is the volume of 1 cell.

For grain boundary motion, like grain coarsening, the silicon nitride cells with neighboring cells of silicon nitride of another grain orientation are given a finite probability to transform to the other grain's orientation. The curvature K has been taken to be a function of the number of surrounding cells of other grain material, such that three surrounding cells, being a straight line boundary, has a stable configuration. If we assume a linear relation between interfacial velocity and the driving force, then,

$$P_{transform} = C_{diff} \times \sigma \exp\left[N - 3\right]$$

where N is the number of neighbors of other grain orientations, and σ is the surface tension of silicon nitride grain boundaries. In all simulations performed here, $C_{diff} = 0.1$.

In the case of the free surface, a single surface cell is allowed the possibility of translating to a neighboring empty site that is adjacent to the same grain of silicon nitride. Here, the probability is related to an Arrhenius term such that the fewer the number of nearest neighbors of solid, the larger the probability of translating,

$$P_{translate} = C_o \exp A(NN)$$

where $C_o = 0.1$ and $A = 5$ were found to provide sufficient smoothing of Si_3N_4 free surfaces, and NN is the number of nearest neighbors which are classified as pore. Therefore a single cell of Si_3N_4 surrounded by few neighbors of solid has a greater chance of translating to another surface site.

Figure 3-16 shows two microstructures, one with and one without surface tension.

Appendix D

Si_3N_4 Nuclei Density Calculation

In order to approximate the simulation of the RBSN microstructure, the appropriate silicon nitride nuclei density must be accounted for in the two dimensional model. We would like to relate the 2D equivalent nuclei density, $(N^g/N^p)^{2D}$, to the 3D experimentally measured density,$(N^g/N^p)^{3D}$ where p stands for the Si particle, and g stands for the reacted Si_3N_4 grain.

By standard sterology, when we cut through the 3D packing of particles,

$$\frac{A^p}{A^{tot}} = \frac{V^p}{V^{tot}}$$

where *tot* indicates the total section area and volume.

Similarly for the grains in the fully reacted structure,

$$\frac{A^g}{A^{tot}} = \frac{V^g}{V^{tot}}$$

Thus,

$$\frac{A^g}{A^p} = \frac{V^g}{V^p}$$

In the 2D section through the unreacted Si green structure and fully reacted structure,

$$A^p = N^p \overline{a}^p$$

$$A^g = N^g \overline{a}^g$$

where N^p and N^g are the number of particles and grains respectively, A^p and A^g are the total areas of the particles and grains respectively, and $\overline{a}^p$ and $\overline{a}^p$ are the average area in the sectioned layer of the particles and grains.

Thus,

$$\left(\frac{N^g}{N^p}\right)^{2D} = \frac{\overline{a}^p}{\overline{a}^g}\frac{A^g}{A^p} = \frac{\overline{a}^p}{\overline{a}^g}\frac{V^g}{V^p} \qquad (1)$$

Using the approximation of spherical grains and Si particles,

$$r^p = \left(\frac{3v^p}{4\pi}\right)^{1/3}$$

$$r^g = \left(\frac{3v^g}{4\pi}\right)^{1/3}$$

Then, the maximum cross sectional areas of Si particles and grains are,

$$a^p = \left(\frac{3\sqrt{\pi}v^p}{4}\right)^{2/3}$$

$$a^g = \left(\frac{3\sqrt{\pi}v^g}{4}\right)^{2/3}$$

Since,

$$\frac{\overline{a}^p}{\overline{a}^g} = \frac{a^p}{a^g} = \left(\frac{v^p}{v^g}\right)^{2/3} \qquad (2)$$

and we use the relations,

$$V^g = N^g v^g$$

$$V^p = N^p v^p$$

where v^g and v^p are the volume of Si particles respectively,

$$\frac{v^p}{v^g} = \frac{V^p}{V^g}\frac{N^g}{N^p} \qquad (3)$$

When we combine equations (1), (2) and (3) we obtain the result,

$$\left(\frac{N^g}{N^p}\right)^{2D} = \left[\left(\frac{N^g}{N^p}\right)^{3D}\right]^{2/3} \times \left(\frac{V^g}{V^p}\right)^{1/3} \qquad (4)$$

The term $(\frac{V^g}{V^p})^{1/3}$ is the ratio of the total volume of the reacted grains to the total volume of the initial Si particles, or simply the reaction volume expansion parameter 1.22.

For an average grain size of 100nm and initial particle size of 250nm, we obtain a 3D nuclei density of 18.9 per Si particle and using equation (4) we obtain a 2D nuclei density of 7.6.

Appendix E

Stress Calculation

Elastic Solutions for a 2D Hexagonal Array of Pores - A Comparison of Stresses Computed in the Spring Network with the Finite Element Technique

In order to demonstrate the generality of the conjugate gradient equilibration method (CGM) and the calculation of the node level stress tensor in the spring network model, we present here a comparison between the stress field solution in the spring network model of an infinite two dimensional hexagonal array of pores with a solution obtained with the finite element technique. For each node point environment consisting of the Voronoi hexagon constructed around each point, the 2-D analog of the atomic level stress tensor is computed here by the use of the generalized definition of the stress tensor for site 'i':

$$\Omega_i \cdot \Pi_i^{\alpha\beta} = \frac{1}{2}\left(\vec{r} \otimes \frac{\partial \Phi}{\partial \vec{r}} + \frac{\partial \Phi}{\partial \vec{r}} \otimes \vec{r}\right)$$

which modifies the earlier definition used by Born and Huang [10] based on central forces alone, by introducing non-central forces by virtue of the dependence of the total elastic energy potential Φ on the angular flexure bonds. In the expression above, α and β stand for the usual tensorial subscripts (1,2) for a tensor of rank 2, Ω_i is the hexagonal Voronoi area allocated to a nodal point.

The stress fields of the spring network superimposed on the finite element stress

contours (dark, heavy lines) reveal a close comparison with some small differences due to such effects as the discreteness of the node spacing near the surface of the pore, as can be seen in Fig. 4-24. The conjugate gradient method is a commonly used equilibration technique, and is particularly adapted to equilibrating the many body interaction system of the spring mesh. Obtaining perfect equilibration, such that all unbalanced forces are eliminated, is an approximate incremental procedure, and equilibration is obtained by setting an appropriately low tolerance for unbalanced force.